

Observing seasonal to decadal variability related to the Atlantic meridional overturning circulation at 11°S

Dissertation
zur Erlangung des Doktorgrades
der Mathematisch-Naturwissenschaftlichen Fakultät
der Christian-Albrechts-Universität zu Kiel

vorgelegt von

Josefine Herrford

Kiel, 2021

Josefine Herrford (2021): *Observing seasonal to decadal variability related to the Atlantic meridional overturning circulation at 11°S.*

Dissertation zur Erlangung des Doktorgrades der Mathematisch-Naturwissenschaftlichen Fakultät der Christian-Albrechts-Universität zu Kiel.

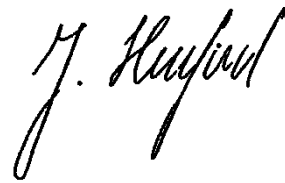
Erster Gutachter: Prof. Dr. Peter Brandt
Zweiter Gutachter: Prof. Dr. Arne Biastoch
Datum der mündlichen Prüfung: 07.04.2021

Prof. Dr. Kempken, Dekan

Eidesstattliche Erklärung

Hiermit erkläre ich, dass ich die vorliegende Arbeit - abgesehen von der Beratung durch den Betreuer - selbständig erarbeitet und verfasst habe. Sie ist unter Einhaltung der Regeln guter wissenschaftlicher Praxis der Deutschen Forschungsgemeinschaft entstanden. Ich versichere außerdem, dass ich die vorgelegte Arbeit nur in diesem und keinem anderen Promotionsverfahren eingereicht habe und, dass diesem Promotionsverfahren keine endgültig gescheiterten Promotionsverfahren vorausgegangen sind.

Berlin, 29.01.2021

A handwritten signature in black ink, appearing to read "J. Haupt". The signature is written in a cursive style with a large, looped initial "J".

Publications

- Chapter 2 was accepted for publication in Ocean Science in December 2020.

Herrford, J., Brandt, P., Kanzow, T., Hummels, R., Araujo, M., and Durgadoo, J. V.: Seasonal variability of the Atlantic Meridional Overturning Circulation at 11°S inferred from bottom pressure measurements, Ocean Sci., doi:10.5194/os-2020-55, 2021.

The candidate designed the study and performed all analyses. She processed the bottom pressure measurements, and further developed and conceptualized a methodology that was first proposed by Prof. Dr. Torsten Kanzow. The candidate produced all figures and authored the manuscript from the first draft to the final version.

- Chapter 3 represents a manuscript in preparation for submission to Ocean Science.

Herrford, J. et al.: A systematic evaluation of global wind products: Implications for the variability of the large-scale circulation in the Tropical South Atlantic, manuscript in prep.

The candidate designed the study, collected the different datasets and performed all analyses. She produced all figures and drafted this manuscript.

- Chapter 4 builds on the methods and results presented in Herrford et al. (2017), but presents new results based on an extended data set.

Herrford, J., Brandt, P., and Zenk, W.: Property Changes of Deep and Bottom Waters in the Western Tropical Atlantic, Deep Sea Res. I, 124, pp. 103-125, doi:10.1016/j.dsr.2017.04.007, 2017.

This publication presents results from work started during the candidate's Master Thesis, which was substantially revised, finalized and published during the first year of the candidate's PhD. The candidate's contribution to the publication included designing the study, synthesizing the historic ship-based data, performing all analyses, producing the figures and drafting the manuscript.

Abstract

The Atlantic Meridional Overturning Circulation (AMOC) plays a significant role in modulating the global climate by redistributing large amounts of heat, freshwater and carbon. It is projected to weaken under a continuously warming climate. Understanding the mechanisms that control its structure and variability on different timescales is, therefore, a key priority for oceanographers and climate scientists.

This thesis presents the first estimate of AMOC variations for the tropical South Atlantic – based on bottom pressure observations from the TRACOS array at 11°S. Over the observed period (2013-2018), the AMOC and its components are dominated by seasonal variability, with peak-to-peak amplitudes of 12 Sv for the upper-ocean geostrophic transport, 7 Sv for the Ekman and 14 Sv for the AMOC transport. The observed seasonal variability of the geostrophic contribution to the AMOC in the upper 300 m is controlled by pressure variations at the eastern boundary, while at 500 m depth contributions from the western and eastern boundaries are similar. The respective mechanisms are investigated with the ocean general circulation model INALTO1. In the model, seasonal AMOC variability at 11°S is governed, besides the Ekman transport, by the geostrophic transport variability in the eastern basin, which is modulated by oceanic adjustment to local and remote wind forcing. Seasonal transport variability in the western basin interior is instead mainly compensated by the Western Boundary Current. These analyses showed, that uncertainties in the wind forcing are particularly relevant for the resulting uncertainties of AMOC estimates at 11°S.

A collection of different gridded surface wind products widely used within the oceanographic community is evaluated regarding the mean wind field and variability in the tropical Atlantic. While all of the wind products capture the mean, large-scale atmospheric circulation in this region, their ability to reproduce the wind variability observed with moored buoys depends on the considered timescale as well as wind regime. For example, the CORE II forcing dataset does not reproduce the observed intra-seasonal variability at any of the buoy locations, scatterometer winds show low correlations on interannual timescales and most of the products have problems to reproduce the wind variability in the eastern tropical South Atlantic. The differences between the wind products translate into estimates of the large-scale circulation in the tropical Atlantic. Additionally, the uncertainties from using different wind stress parametrizations can make up 15 % of the momentum flux into the ocean. For integral variables like the Ekman or Sverdrup transports across a certain latitude, the choice of wind product results in uncertainties of 15- 40 % depending on the latitude and timescale. Older, coarser products produce spurious wind stress variations, especially on decadal timescales. The small-scale information contained in scatterometer winds, but not in the coarser reanalysis products, is emphasized in indices involving spatial derivatives like the wind stress curl. Substantial inconsistencies exist regarding the seasonal variability of the wind stress curl in the eastern and western boundary regions at 11°S. Together, these results highlight the importance of testing the sensitivity of derived estimates of the wind-driven circulation to the choice of wind product as well as careful consideration or incorporation of large uncertainties in wind forcing products into ocean simulation experiments.

The AMOC is closely linked to the formation, transformation and advection of water masses. Changes in the major water masses of the Atlantic Ocean are related to variations in the oceanic heat and freshwater transports and can influence basin-wide zonal pressure gradients, thus, the large-scale ocean circulation. Two full-depth transatlantic sections in the tropical South Atlantic, separated by 24 years, are analyzed regarding water mass property distributions and long-term water mass changes along 11°S. The vertical and horizontal distributions of typical property extrema in the Brazil and

Angola Basins are in agreement with previous studies. Temperature differences between 1994 and 2018 confirm a warming of the central and lower intermediate waters in the western boundary region off Brazil, also extending eastward into Angola Basin after 1994. Dissolved oxygen distributions along 11°S support a vertical expansion of the tropical South Atlantic oxygen minimum zone, but also showed a reduced westward extent between 1994 and 2018. Abyssal temperature changes in the Brazil Basin are in agreement with previous studies, showing a warming of the Antarctic Bottom Water (AABW) and cooling of the lower North Atlantic Deep Water (NADW) to be mainly caused by volume changes. However, decadal temperature variations on isopycnals to also contribute to the observed signals. An oxygen increase of 2-3 $\mu\text{mol kg}^{-1}\text{dec}^{-1}$ within the AABW layers of the Brazil Basin has not been observed before and could hint towards a dominance of local mixing processes over changes in the source waters. A similar oxygen increase is also observed above the western flank of the Mid-Atlantic Ridge and in the abyssal Angola Basin below 2000 m.

Overall, the results from this thesis contribute to the understanding of AMOC-related variability as well as possible uncertainties in the estimates of different AMOC components derived from observations in the tropical South Atlantic. When continued into the future and combined with other programs or AMOC arrays, the observations of the TRACOS array at 11°S have great potential for further investigations of the mechanisms relevant for tropical Atlantic variability, as well as meridional coherence and long-term changes of AMOC variability.

Zusammenfassung

Die Atlantische Meridionale Umwälzbewegung (AMOC) spielt eine signifikante Rolle in der Modulierung des globalen Klimas durch die Umverteilung großer Mengen an Wärme, Frischwasser und Kohlenstoff. Prognosen zufolge wird sie sich durch die globale Erwärmung abschwächen. Es ist daher von hoher Priorität für Ozeanographen und Klimawissenschaftler, die Mechanismen zu verstehen, die die Struktur und Variabilität der AMOC kontrollieren.

Diese Dissertation präsentiert die erste Abschätzung der AMOC-Schwankungen im tropischen Südatlantik – basierend auf Bodendruckbeobachtungen des TRACOS-Arrays bei 11°S. Innerhalb der Beobachtungsperiode (2013-2018) dominiert die saisonale Variabilität der AMOC und ihrer Komponenten mit Signalamplituden von 12 Sv für den geostrophischen Transport oberhalb von 1100 m, 7 Sv für den lokalen Ekman-Transport und 14 Sv für den AMOC-Transport. Die beobachtete saisonale Variabilität im geostrophischen Anteil der AMOC wird in den oberen 300 m von Druckvariationen am Ostrand des Beckens kontrolliert, bei 500 m sind dagegen die Beiträge von West- und Ostrand ähnlich. Die entsprechenden Mechanismen wurden mit dem Ozeanzirkulationsmodell INALT01 untersucht. Im Modell wird die saisonale Variabilität der AMOC, neben dem Ekman-Transport, von der Variabilität des geostrophischen Transports im Ostbecken bestimmt. Dieser wird durch die Reaktion des Ozeans auf den lokalen Windantrieb aber auch über Fernwirkungen durch Wind in entfernten Regionen moduliert. Die saisonale Transportvariabilität im inneren Westbecken wird dagegen durch den lokalen Wind angetrieben und hauptsächlich durch den Westlichen Randstrom kompensiert. Diese Analysen haben gezeigt, dass Unsicherheiten im Windantrieb besonders relevant für die resultierenden Unsicherheiten der AMOC-Abschätzung bei 11°S sind.

Eine Kollektion verschiedener gerasterter Windprodukte, die in der Ozeanographengemeinschaft weitverbreitet sind, wird hier in Bezug auf die mittleren Windfelder und die Windvariabilität im tropischen Atlantik ausgewertet. Während alle Produkte die mittlere, großskalige, atmosphärische Zirkulation in der Region erfassen, ist ihr Vermögen die von verankerten Bojen beobachtete Windvariabilität zu reproduzieren stark von der Region und der betrachteten Zeitskala abhängig: Der CORE II-Modellantrieb schafft es zum Beispiel nicht, die intra-saisonale Variabilität an irgendeiner der Bojenpositionen zu reproduzieren, Scatterometer-Winde zeigen abnehmende Korrelationen auf inter-annualen Zeitskalen und alle Produkte haben Probleme die Windvariabilität im östlichen Südatlantik zu erfassen. Die Unterschiede zwischen den Produkten wirken sich auf jegliche Abschätzungen der großskaligen Zirkulation im tropisch Atlantik aus: Die Unsicherheiten, die durch die Benutzung verschiedener Windstress-Parametrisierungen entstehen, können bis zu 15% des Impulseintrags in den Ozean ausmachen. Für integrale Größen, wie den Ekman- oder Sverdrup-Transport über einen bestimmten Breitengrad, kann die Wahl des Windprodukts, je nach Region oder Zeitskala, eine Unsicherheit von 15-40% mit sich bringen. Ältere gröber aufgelöste Windprodukte produzieren künstliche Windstressvariationen, insbesondere auf dekadischen Zeitskalen. Kleinskalige Informationen, die in den Scatterometer-Winden, aber nicht in den gröber aufgelösten Reanalyseprodukten, enthalten sind, werden in Indizes wie dem Windstresscurl, die räumliche Ableitungen erfordern, noch verstärkt. Außerdem gibt es substantielle Widersprüche in der saisonalen Variabilität des Windstresscurls in den östlichen und westlichen Küstenregionen bei 11°S. All diese Ergebnisse zeigen, wie wichtig es ist, sowohl die Empfindlichkeit abgeleiteter Abschätzungen der windgetriebenen Zirkulation auf die Wahl eines bestimmten Windprodukts hin zu prüfen als auch die Unsicherheiten der Windprodukte bei der Analyse von Ozeansimulationen zu berücksichtigen.

Die AMOC ist eng an die Bildung, Transformation und Advektion von Wassermassen gekoppelt. Veränderungen in den großen Wassermassen des Atlantischen Ozeans sind mit Variationen im ozeanischen Wärme- und Frischwassertransport verbunden und können beckenweite zonale Druckgradienten, also die großskalige Ozeanzirkulation, beeinflussen. Zwei tiefe transatlantische Schiffsschnitte im tropischen Südatlantik, gemessen im Abstand von 24 Jahren, werden hier hinsichtlich der Verteilung von Wassermasseneigenschaften und langfristiger Wassermassenveränderungen entlang von 11°S analysiert. Die vertikale und horizontale Verteilung typischer Temperatur-, Salzgehalts- und Sauerstoffextrema im Brasil- und Angolabecken stimmt mit früheren Studien überein. Temperaturdifferenzen zwischen 1994 und 2018 bestätigen eine Erwärmung des Zentralwassers und unteren Zwischenwassers in der Region vor der Brasilianischen Küste. Diese Signale sind nach 1994 auch im Angolabecken zu finden. Die Sauerstoffverteilungen entlang von 11°S unterstützen die Theorie einer sich vertikal ausdehnenden Sauerstoffminimumzone im tropischen Südatlantik, aber zeigen auch eine reduzierte westwärtige Ausdehnung zwischen 1994 und 2018. Temperaturveränderungen im tiefen Brasilbecken stimmen mit früheren Studien überein, die gezeigt haben, dass sowohl die Erwärmung des Antarktischen Bodenwassers (AABW) als auch die Abkühlung des Nordatlantischen Tiefenwassers (NADW) im nördlichen Brasilbecken hauptsächlich durch Volumenänderungen verursacht werden. Aber auch dekadische Temperaturschwankungen auf Dichteflächen tragen zu den beobachteten Signalen bei. Ein Sauerstoffanstieg von 2-3 $\mu\text{mol kg}^{-1} \text{dek}^{-1}$ in den tiefen AABW-Schichten des Brasilbeckens wurde hier zum ersten Mal dokumentiert und könnte auf die Dominanz lokaler Vermischungsprozesse gegenüber Veränderungen in den Quellwassermassen hindeuten. Ein ähnlicher Sauerstoffanstieg ist auch über der westlichen Flanke des Mittelozeanischen Rückens und im tiefen Angolabecken unterhalb von 2000 m zu beobachten.

Insgesamt tragen die Ergebnisse dieser Dissertation zum Verständnis der mit der AMOC verbundenen Variabilität im tropischen Südatlantik sowie der Unsicherheiten der Variabilität verschiedener aus Beobachtungen abgeleiteter AMOC-Komponenten bei. Wenn das Beobachtungsprogramm des TRACOS-Arrays bei 11°S fortgeführt und mit anderen Programmen oder AMOC-Arrays kombiniert wird, hat es großes Potenzial für weitere Untersuchung zu den Mechanismen der Variabilität im tropischen Atlantik, aber auch zur meridionalen Kohärenz und langfristigen Veränderungen der AMOC-Variabilität.

Table of Contents

Eidesstattliche Erklärung	3
Publications	5
Abstract	7
Zusammenfassung.....	9
Table of Contents	11
List of figures.....	13
List of tables.....	18
1. Introduction.....	19
1.1. The AMOC and its role in climate	19
1.2. AMOC observations and discoveries	20
1.3. The observational program and circulation at 11°S	24
1.4. Research questions	27
2. Seasonal variability of the Atlantic Meridional Overturning Circulation at 11°S inferred from bottom pressure measurements.....	29
Abstract	29
2.1. Introduction	29
2.2. Observational Data	31
2.2.1. Bottom pressure time series	31
2.2.2. Sea level anomalies	33
2.2.3. Wind stress	33
2.2.4. NBUC transport time series.....	34
2.3. Model Data.....	34
2.4. Methods.....	35
2.4.1. Computation of AMOC transport variations from BP observations	35
2.4.2. Using the OGCM INALT01 as a ‘testing area’	37
2.5. Results.....	38
2.5.1. Ocean pressure variability at 11°S.....	38
2.5.2. Wind stress variability	41
2.5.3. Seasonal variability of the AMOC components at 11°S.....	43
2.5.4. Dynamics of the seasonal cycle at 11°S.....	47
2.6. Summary and discussion.....	50
2.7. Acknowledgements.....	52

3. A systematic evaluation of global wind products: Implications for the variability of the large-scale circulation in the Tropical South Atlantic.....	53
Abstract	53
3.1. Introduction	53
3.2. Gridded wind fields	55
3.2.1. Reanalysis products	56
3.2.2. Wind observation products	57
3.2.3. Model forcing products	60
3.3. Wind data processing and derived quantities	61
3.4. Auxiliary data sets	62
3.4.1. Wind stress output from the INALT01 OGCM	62
3.4.2. In-situ wind measurements at PIRATA buoys	62
3.5. Results and discussion	63
3.5.1. Differences in the mean wind fields	63
3.5.2. Comparison of variability in the gridded products to directly observed wind data	66
3.5.3. Assessment of different wind-stress parameterizations	68
3.5.4. Differences in wind-derived variables and implications for the large-scale circulation in the tropical South Atlantic.....	71
3.5.4.1. The mean Ekman transport across 11°S	71
3.5.4.2. The seasonal cycle of the Ekman transport across 11°S.....	74
3.5.4.3. Interannual to decadal variations in the Ekman divergence between 11°N and 11°S.....	76
3.5.4.4. The seasonal cycle of the wind stress curl along 11°S.....	78
3.5.4.5. Interannual to decadal variations in the tropical South Atlantic wind stress curl.....	81
3.6. Summary and conclusions	84
3.7. Acknowledgements.....	87
4. Water mass changes along 11°S from two transatlantic hydrographic sections occupied in 1994 and 2018.....	89
Abstract	89
4.1. Introduction	89
4.1.1. Review	90
4.2. Data and methods.....	94
4.3. Water mass distribution along 11°S.....	95
4.4. Water mass property changes at 11°S.....	100
4.5. Summary and conclusions	106
5. Summary and suggestions for future research.....	109
References	119
Acknowledgements.....	139

List of figures

- Figure 1** (a) Meridional ocean heat transports (positive northward) in PW (1015 W) for the global ocean (black), the Indo-Pacific (green), and the Atlantic (blue) from NCEP atmospheric reanalysis (Trenberth and Caron, 2001). (b) Atlantic meridional ocean heat transports from NCEP atmospheric reanalysis (blue) compared to several direct estimates: Ganachaud and Wunsch (2003; black diamonds), Talley (2003; cyan circles), Lumpkin and Speer (2007; green stars), the RAPID-MOCHA array at 26.5°N (red square; Johns et al., 2011), Hobbs and Willis (2012; orange diamond), and Garzoli et al. (2013; magenta cross). The vertical bars indicate the uncertainty range for the direct estimates. [Adapted from Buckley & Marshall, 2016]..... 19
- Figure 2** Schematic of the Atlantic Meridional Overturning Circulation. Red arrows indicate the flow of relatively warm surface waters, blue arrow the flow of relatively cold deep waters. Yellow and green colors represent transitions between depths. White lines mark the locations of moored arrays, which currently monitor the basin-wide AMOC or important components of it..... 22
- Figure 4** Bottom pressure (BP) anomalies measured at 11°S off Angola at 300 m (pink) and 500 m (red), as well as off Brazil at 300 m (light blue) and 500 m (blue) depth. (a) Instrument drifts that are removed from, as well as the sum of the drift and the combined annual and semi-annual harmonics fitted to the individual BP anomaly time series. (b) Daily time series of BP anomalies after de-tiding and de-drifting (see text for details)..... 33
- Figure 5** Time series of SLA over the period 2013-2018 – chosen close to the western (purple; (a)) and eastern boundaries (magenta; (b)). Phases of the minima of the annual (solid curve) and semi-annual (dashed curves) harmonics as function of longitude near the western (c) and eastern (d) boundaries. In (c, d), the black dashed lines represent the zonal grid spacing of the SLA data and grey areas mark land. Light blue (c) and pink (d) lines mark the locations of the 300 m BPRs at the western (c) and eastern (d) boundaries. 34
- Figure 6** Experimental setup and strategy to estimate TG' showing the location of the BPRs (reddish & blueish circles) and the vertical sampling of VG' . VG' is derived from measurements of sea level anomaly and with bottom pressure at 300 m and 500 m depth. A level of no motion is prescribed to be at $z=1130$ m. Two methods are used to approximate $VG'(z)$: i) piecewise linear interpolation of VG' between the 4 data points (black profile), ii) regression of the 1st and 2nd dominant vertical structure functions of $VG \text{ SIM } P(z)'$ from INALT01 onto the data points at 0 m, 300 m and 500 m depth relaxing the no-flow condition at 1130 m depth (grey profile). $VG'(z)$ is then vertically integrated from 1130 m to the surface to derive TG' 36

Figure 7 Periodograms of (a, b) SLA, (c, d) BP at 300 m and (e, f) BP at 500 m depth –from observations (colored), and from the INALTO1 model (grey). In (a, b) bold solid curves show periodograms calculated from SLA data over the period 2013-2018. The transparent envelopes are an estimate for interannual variations, specifically, the minimum and maximum ranges of periodograms calculated for 5-year windows running through the full available period 1993-2018. In (c, d, f) bold solid curves show periodograms calculated from the individual BP time series available at 11°S. In (e) the solid curve represents KPO 1135 and the dashed curve KPO 1109 (two co-located sensors covering different periods; see Table 1). Grey shading in all panels gives the minimum and maximum ranges of periodograms for SLA and BP time series derived from the INALTO1 model calculated for 5-year windows running through the full available period 1978-2007. Frequency is given in ‘cycles per year’. Black vertical lines mark the frequencies of the annual and semi-annual cycles, as well as periods of 120 and 90 days in (b) or 70 days in (c, d, e, f). 39

Figure 8 Combined annual and semi-annual harmonics calculated for (a, b) SLA, (c, d) BP at 300 m and (e, f) BP at 500 m depth. Line styles and color coding are the same as in Fig. 7. Additionally, dashed envelopes around the solid curves give uncertainties for the amplitudes of the harmonics. These are calculated by 170-days low-pass filtering the pressure time series and then subsequently the 95th percentile of the deviations from the derived annual and semi-annual harmonics for every day of the year..... 40

Figure 9 (a) Amplitudes and (b) phases of the minima of the annual (pluses and black curves) and semi-annual (crosses and grey curves) harmonics of the pressure anomalies at the eastern boundary along 11°S. Markers represent estimates from the observations (2013-2018) at 0m, at 300m, 500m, the curves show estimates calculated from INALTO1 for 5-year windows running through the period of available data (1978-2007). 41

Figure 10 (a, b) Periodograms of the Ekman transport at 11°S, derived from ASCAT (a) and INALTO1 (b) wind stress. The bold curve in (a) is calculated for the period 2013-2018. Transparent envelopes in (a, b) give an estimate for interannual variations, specifically the minimum and maximum ranges of periodograms calculated for 5-year windows running through the full available time series of ASCAT (2008-2018) and INALTO1 (1978-2009). Frequency is given in ‘cycles per year’. (c, d) Hovmöller diagrams of the ASCAT (c) and INALTO1 (d) zonal wind stress anomalies along 11°S for the overlapping years 2008-2009. Red (blue) colors in (c, d) imply eastward (westward) wind stress anomalies. 42

Figure 11 Anomaly time series at 11°S of (a) the upper-ocean geostrophic transport ($TG EOFs'$), (b) the Ekman transport derived from ASCAT wind stress ($TEK ASCAT'$), and (c) the resulting AMOC transport ($TAMOC'$). Thin lines represent daily values in (a) and 5-daily values in (b, c), bold curves represent monthly averages. Different colors in (a) indicate transport calculations for different sets of BPRs – 4 BPRs (petrol), 3 BPRs (500 m WB, 300 m EB, 500 m EB; purple) and 2 BPRs (300 m & 500 m WB; magenta) combined with the annual and semi-annual harmonics derived from the fully equipped period (05/2014-10/2015; see section 2.4.1). 43

Figure 12 Mean seasonal cycles of TG' (a, b), TEK' (c, d) and $TAMOC'$ (e, f) from observations (a, c, e) and the INALT01 model (b, d, f). Upper-ocean geostrophic transport anomalies, $TG Points'$ (cyan curve) and $TG EOFs'$ (petrol curve), are derived from SLA and BP observations (as described in section 2.4.1) and averaged over the period 2013-2018, while $TG SIM'$, is derived from the INALT01 model velocity fields (as described in section 2.4.2) and averaged over the period 1978-2007. $TAMOC'$ in (e) was derived using $TG EOFs'$. For the 30-year INALT01 run (b, d, f) and the 12-year ASCAT wind time series (c), transparent envelopes represent an estimate for interannual variations, specifically, the minimum and maximum range of mean seasonal cycles calculated for 5-year windows running through the respective available periods. The dashed curves in all panels show the absolute range of possible minima and maxima per months. 44

Figure 13 Mean seasonal cycles of the geostrophic transport per unit depth, $VG SIM'$ (a, c, e) and the upper-ocean geostrophic transport $TG SIM'$ (pink curves; (b, d, f)) from INALT01. $VG SIM P(z)'$ (a) and $TG SIM P(z)'$ (blue curve; (b)), were calculated using the full vertical profiles of BP. $VG SIM Points'$ (c) and $TG SIM Points'$ (cyan curve; (d)) were reconstructed by piecewise linear interpolation of VG' between the 4 supporting points at 0, 300, 500, and 1130 m depth (black dashed lines in (c)) mark the depths of the BPRs); $VG SIM EOFs'$ (e) and $TG SIM EOFs'$ (petrol curve; (f)) by using the dominant vertical structure functions from INALT01. In (a, c, e) red (blue) colors show northward (southward) anomalies..... 46

Figure 14 Mean seasonal cycle of the geostrophic transport per unit depth, VG' , over the period 2013-2018, derived from observations at 11°S with two methods: (a) Piecewise linear interpolation between the 4 supporting points at 0, 300, 500 and 1130 m depth (black dashed lines mark the depths of the BPRs). (b) Reconstruction of VG' by regression of the dominant vertical structure functions from the INALT01 model onto the values at the 3 depth levels of pressure observations at 0 m, 300 m, 500 m depth thereby relaxing the no-flow condition at 1130 m depth. Red (blue) colors show northward (southward) anomalies. 47

Figure 15 Mean seasonal cycle of the geostrophic transport per unit depth, $VG SIM'$ (a, c, e) and the upper-ocean geostrophic transport $TG SIM'$ (b, d, f) from INALT01. In all panels, VG' and TG' were calculated from the full vertical profiles (from the surface down to 1130 m) of the simulated pressure, but from pressure differences across different regions along 11°S: across the whole basin ($TG SIM P(z)'$; blue curves in (b, d, f)); between the Brazilian continental slope and 34.55°W ($VG SIM 'NBUC$ in (a); $TG SIM 'NBUC$ orange curves in (b); between 34.55°W and 10°W ($VG SIM 'Western Basin Interior$ in (c); $TG SIM 'Western Basin Interior$ red curves in (d); between 10°W and the Angolan continental slope ($VG SIM 'Eastern Basin$ in e; $TG SIM 'Eastern Basin$ light blue curve in (f). Transparent shading and dashed curves are the same as in Fig. 12..... 48

Figure 16 (a) Time series of NBUC transport anomalies (5-daily as thin curve, and monthly averages as bold curve) based on moored observations off Brazil (see section 2.2.4) updated from Schott et al. (2005) and Hummels et al. (2015). (b) Mean seasonal cycles of the NBUC transport anomalies averaged over the periods 2013-2018 (orange curve) and 2000-2004 (black curve). The thin dashed curves show the absolute range of possible minima and maxima per months for the periods 2013-2018 (orange) and 2000-2004 (black), respectively..... 49

Figure 17 Amplitudes of the annual (solid curves) and semi-annual (dashed curves) harmonics of the vertically integrated upper-ocean geostrophic velocity in INALT01 (blue curves; left axis) and the INALT01 wind stress curl (green curves, right axis) along 11°S. Transparently shaded boxes highlight different regions – the NBUC (orange), the western basin interior (red) and the eastern basin (blue).	49
Figure 18 Bathymetric map (ETOPO1; doi:10.7289/V5C8276M) of the tropical Atlantic including the positions of 13 PIRATA buoys (red dots). The inlays show daily time series of 4m-wind speeds measured at each PIRATA buoy.	63
Figure 19 Wind speed (filled contours) and direction (arrows; plotted for every 25 th grid point) of the ensemble mean of all 8 wind products for the overlapping year 2008.	64
Figure 20 Deviations of mean wind speed (filled contours) and direction (arrows; plotted for every 25 th grid point) from the ensemble mean of all 8 wind products for the overlapping year 2008.	66
Figure 21 Correlation between the meridional wind components from the gridded products (ENWs at 10m) and measured at the PIRATA buoys (actual wind at 4m) shown for different timescales (<i>tc</i> ; in days). The correlation coefficients are calculated based on time series that were band-pass filtered for the frequency bands 10-50, 50-90, 90-150, 150-210, 300-430, 430-660 and 660-960 days. Vertical lines mark the timescale, for which the length of the overlapping time series allow 5 repetitions. Horizontal lines mark correlation coefficients of ± 0.5	68
Figure 22 Mean zonal wind stress τ_x along 11°S in 2008– a) calculated for the 8 different wind products always using the same drag coefficient formulation LY04, b) calculated from QUIKSCAT 10m wind using drag coefficient formulations from LP81 (dashed black curve), CONST (grey curve), YT96 (dotted black curve) and LY04 (thin solid blue curve), as well as the wind stress provided complementarily with the product (thick solid blue curve; QUIKSCAT prov; see section 3.2.2), c) calculated from CORE II wind using the same set of drag coefficient formulations as in b), as well as the wind stress derived with the INALT01 model (thick solid pink curve; INALT01; see section 3.4.1).	70
Figure 23 Density functions of the daily Ekman transports at 11°S calculated for the 8 wind products (solid colored curves) and for the INALT01 wind stress output (dashed pink curve), over the respective available periods for each product. Vertical lines mark the mean (thick lines) and $\pm 2\sigma$ (thin lines) of the derived Ekman transports. b) Daily time series of the Ekman transports shown for the period 05/2008-08/2008.	73
Figure 24 Mean seasonal cycles of the Ekman transport across the four latitudes 11°N (a), 26.5°N (b), 11°S (c), 34.5°S (d). These are averaged over the period 2013-2018 and calculated for the 6 wind products covering this period. Error bars give standard errors.	75
Figure 25 Transport timeseries of the Ekman transport across 11°N (a), the Ekman transport across 11°S (b), the difference between both representing the basin-wide Ekman divergence between both latitudes (c), derived from the 8 gridded products presented above. After removing the respective annual and semi-annual harmonics, all the time series have been 270-days low-pass filtered. Colored lines in (c) show linear ten-year (08/2008-07/2018) trends fitted to the Ekman divergence time series derived from 6 of the wind products.	77

Figure 26 Amplitudes of the annual harmonic of the wind stress curl along 11° S as a function of longitude. These are derived from the 8 wind products (solid colored curves) and from the INALT01 wind stress output (dashed pink curve), and calculated over the respective available periods for each product.	79
Figure 27 Phases (timing of the minimum) of the annual harmonic of the wind stress curl derived from the 8 wind products (a-g) and from the INALT01 wind stress output (h). The horizontal black lines mark 11°S.	80
Figure 28 Hovmoeller diagrams of 700 days low-pass filtered wind stress curl anomalies from the time mean along 11°S.	82
Figure 29 Basin-wide Sverdrup transport across 3°S (a) and 11°S (b). The transport time series were 700-day low-pass filtered to extract variations on interannual to decadal timescales.	84
Figure 30 Bathymetric map showing the hydrographic sections occupied in April 1994 (cyan) and June 2018 (magenta) at 11°S. Every single dot marks the position of a CTD profile.	95
Figure 31 θ -S-diagrams for the western (a) and eastern (b) basin. Cyan dots mark measurements from cruise M28 (1994) and magenta dots from cruise M148 (2018).	96
Figure 32 Vertical sections of θ (a, b; in °C) and S (c, d) at 11°S – occupied during the transatlantic cruises M28 in April 1994 (left panels) and M148 in June 2018 (right panels).	98
Figure 33 Vertical sections of O ₂ (a, b; in $\mu\text{mol kg}^{-1}$) at 11°S – occupied during the transatlantic cruises M28 in April 1994 (a) and M148 in June 2018 (b).	99
Figure 34 Vertical sections of property difference between the two sections at 11°S occupied during M28 in April 1994 and M148 in June 2018. Shown are the differences in (a) potential temperature (Θ) and (b) dissolved oxygen (O ₂) on isobars, as well as (c) in-situ temperature (T) on and (d) pressure (P) of isopycnal surfaces. Red (blue) contours denote positive (negative) anomalies. Note, that positive anomalies of $P(\gamma^n)$ mean a downward displacement of isopycnals.	103
Figure 35 Zonal section of the phase of the annual harmonic of the meridional velocity in INALT01 along 11°S. White hatching overlays part of the section, where the harmonics have an amplitude $< 0.0025 \text{ m s}^{-1}$. The white line marks the level of no motion (at 1130 m) assumed for the calculation of the AMOC in INALT01.	112
Figure 37 Vertical section of meridional velocity [m s^{-1}] along 11°S measured during METEOR cruise M148/1 in 2018. Red (blue) colors show northward (southward) velocity.	115
Figure 38 Evolution of θ [°C] of the coldest AABW found in the Equatorial Channel (a), at the western boundary along 11°S (b) and within the Vema Channel (c). Linear fits are shown as black solid lines and their 95% confidence estimates (the standard error of the slope of the fit multiplied by 1.96) as black dashed lines. This figure is an update of Fig. 11 in Herrford et al. (2017) as well as adapted from Fig. 18 in Zenk (2019). Linear Black circles mark new temperature measurements from recent cruises – from M159 (2019) in (a) and from M119 (2015), M130 (2016), M148 (2018), M159 (2019) in (b). Please note, that in (c), the 2016 proxy was calculated from a downstream observation at 27° S under the assumption of a given averaged horizontal temperature gradient. The data point from May 2018 was taken during Polarstern cruise PS113 and declared preliminary (Zenk, 2019).	117

List of tables

- Table 1** Collection of available BP measurements at 11°S. Acronyms used throughout this article are given in the 1st column, official mooring IDs and instrument types are listed in the 2nd and 3rd columns. Columns 4-6 give the positions, depths and deployment periods for each BP measurement. The BP data can be found at <https://doi.org/10.1594/PANGAEA.907589>. *These sensors were re-deployed in 2018 and are currently in place. 32
- Table 2** Information on and availability of 8 different gridded wind products. The first column gives the product IDs used throughout this study, their official names and related references, column 2 the data sources. The original temporal and spatial resolutions, as well as the available periods are listed in columns 3-5. * The CCMP and JRA55-do data sets used here do not or not fully cover the year 2019. They have not been updated due to a lack of time. ** CERSAT-IFREMER does also provide wind stress estimates for QUIKSCAT (and ASCAT), which we use to compare different wind stress parametrizations in section 3.5.3. 59
- Table 3** Mean Ekman transports across 11°S, 11°N, 26.5°N and 34.5°S, derived from the gridded wind products listed in the 1st column. At 11°S, the mean Ekman transports are calculated for the full available periods of each product (2nd column), the overlapping year 2008 (4th column) or the period 2013-2018 (column 3). At the other latitudes, mean transports are also calculated for the period 2013-2018 (column 5, 6, 8) as well as for other periods, for which Ekman transports were published as part of an AMOC estimate. *This period was chosen to compare the Ekman transports with results from Rayner et al. (2011). ** This period can roughly be compared to Meinen et al. (2018). 72
- Table 4** Linear trends in Ekman divergence between 11°N-11°S for 6 different wind products with 95% confidence intervals – after Brandt et al., (2021). * The trend from CORE II was calculated for a slightly different period – 01/1999 – 08/2009. 78
- Table 5** New hydrographic measurements along four repeated ship sections with in the tropical Atlantic, which are going to full-depth and were conducted after 2014. This table represents an update of table 2 in Herrford et al. (2017). 116

1. Introduction

1.1. The AMOC and its role in climate

As part of the global overturning circulation, the Atlantic Meridional Overturning Circulation (AMOC) plays a significant role in modulating the global climate. The AMOC connects warm surface currents and colder deep currents across all latitudes through localized deep water formation and upwelling. This complex circulation system transports large amounts of heat and freshwater from the South to the North Atlantic, and carbon from the surface to the deep ocean (e.g. Buckley & Marshall, 2016).

The AMOC represents the strongest mode of northward heat transport by the ocean – it contributes about 25% to the total global heat transport of 5 PW of the coupled ocean-atmosphere system (e.g. Bryden & Imawaki, 2001). The northward heat transport accomplished by the AMOC is largest in the tropical and subtropical North Atlantic with observational estimates at 26.5°N ranging from 1.0-1.5 PW (e.g. Ganachaud & Wunsch, 2003; Talley, 2003; Lumpkin & Speer, 2007; Johns et al., 2011; see Fig. 1 b). Because of the AMOC, there is also a substantial northward heat transport throughout the South Atlantic and across the equator (e.g. Talley et al., 2011). This is unique among global oceans (cf. Fig. 1 a) and responsible for an inter-hemispheric sea surface temperature gradient contributing, for example, to the northward shift of the mean annual position of the Atlantic Inner Tropical Convergence Zone (ITCZ; e.g. Marshall et al., 2014).

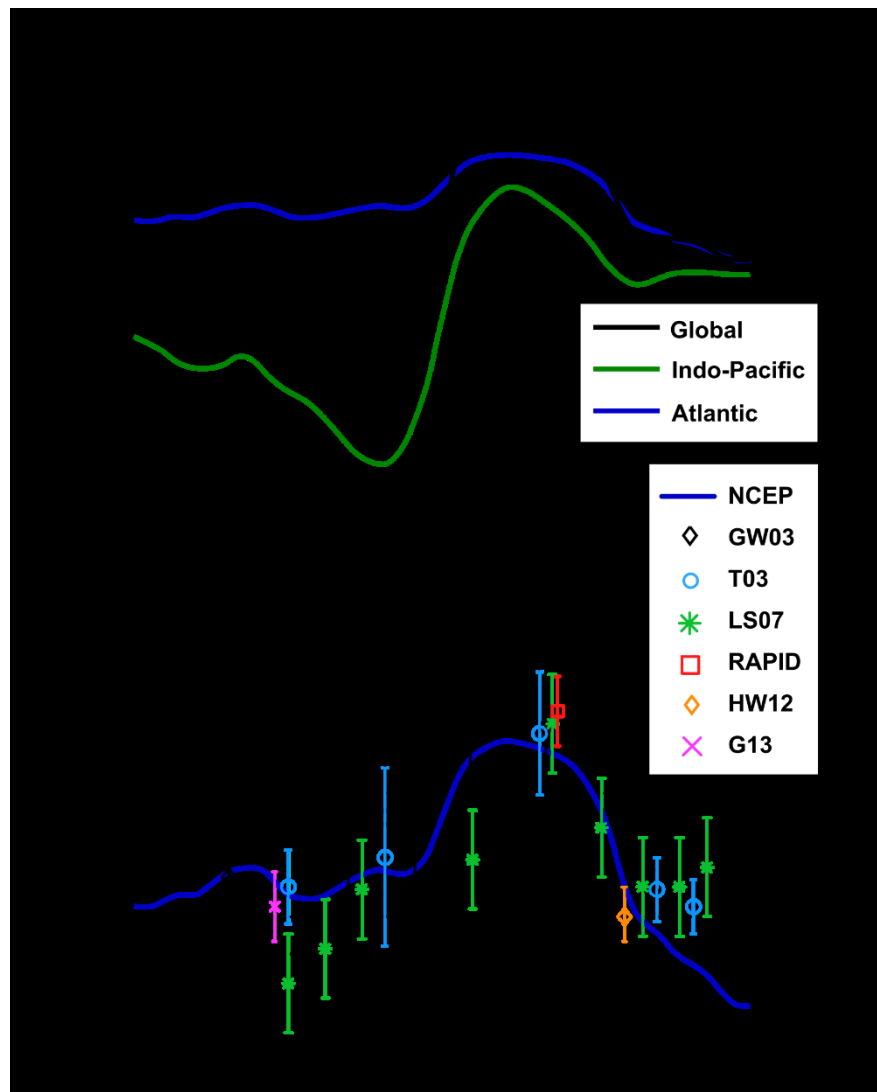


Figure 1 (a) Meridional ocean heat transports (positive northward) in PW (10¹⁵ W) for the global ocean (black), the Indo-Pacific (green), and the Atlantic (blue) from NCEP atmospheric reanalysis (Trenberth and Caron, 2001). (b) Atlantic meridional ocean heat transports from NCEP atmospheric reanalysis (blue) compared to several direct estimates: Ganachaud and Wunsch (2003; black diamonds), Talley (2003; cyan circles), Lumpkin and Speer (2007; green stars), the RAPID-MOCHA array at 26.5°N (red square; Johns et al., 2011), Hobbs and Willis (2012; orange diamond), and Garzoli et al. (2013; magenta cross). The vertical bars indicate the uncertainty range for the direct estimates. [Adapted from Buckley & Marshall, 2016].

Paleoclimatic reconstructions (Clark et al., 2002; Alley, 2007; Barker et al., 2011) suggest that, prior to the Holocene, the AMOC may have been much more variable than today by changing its mode of

operation on decadal timescales and driving or being indicative of abrupt shifts in the climate system (e.g. Srokosz et al. 2012). The Holocene, on the other hand, has been characterized by a relatively stable climate and dampened AMOC variability. However, recent studies discuss a steady weakening of the AMOC strength since the mid-20th century, which could be related to an accumulated freshening in the subpolar North Atlantic (Rahmstorf et al., 2015; Böning et al. (2016); Caesar et al., 2018).

On decadal to centennial timescales, variations in the AMOC-related heat and freshwater transports have been associated with the climate or ocean “bipolar seesaws”, which describe antiphase relationships between the Arctic and Antarctic sea surface temperature or deep water formation (e.g. Rahmstorf, 2002; Swingedouw et al., 2009). Multidecadal variations in sea surface temperatures, like the Atlantic Multidecadal Variability (AMV), which have been linked to the AMOC (e.g. Zhang & Delworth, 2006; Danabasoglu et al. 2012; Kim et al, 2020), can also influence climate variability over the adjacent continents (e.g. Zhang et al., 2019).

The exact mechanisms affecting the AMOC are still unclear and possible long-term changes in the AMOC are a key source of uncertainty for the prediction of future climate change. Climate models within the 5th Coupled Model Intercomparison Project (CMIP5) predict that the AMOC is very likely to also weaken over the 21st century under a continuously warming climate, while a shutdown was found to be unlikely (e.g. Stocker et al., 2013; Bakker et al., 2016). A strong weakening or shutdown of the AMOC is hypothesized to result in a reduced oceanic heat and carbon transport into the North Atlantic leading, for example, to an equatorward shift of the ITCZ (e.g. Zhang & Delworth, 2005; Stouffer et al., 2006), a strengthened relationship between the tropical Atlantic and Pacific Oceans with implications for the El Niño–Southern Oscillation phenomenon (e.g. Timmermann et al., 2005; Svendsen et al., 2014), a reduced ocean uptake of atmospheric CO₂ in the North Atlantic (e.g. Steinfeldt et al., 2009), a strengthening of the boreal winter North Atlantic storm track over western Europe (e.g. Brayshaw et al., 2009) or a slowing of the sea ice loss in the Arctic (e.g. Liu et al., 2020).

Given the importance of the AMOC for the climate system, providing the observational evidence of the mechanisms that control its structure and variability seems essential in order to understand the present-day climate, validate climate simulations and improve predictions.

1.2. AMOC observations and discoveries

The growing number of AMOC observations over the last decades has continuously led to new insights, thereby, challenging existing paradigms again and again.

Early estimates of the AMOC strength and structure were based on a few zonal hydrographic sections (e.g. Richardson, 2008), which mainly focused on establishing the mean AMOC and related heat transport. Significant contributions to the understanding of the AMOC came from, for example, a series of zonal hydrographic sections in the South Atlantic measured during the German Atlantic expedition (1925-1927; Wüst, 1935) or the collection of systematic hydrographic sections and analysis of global circulation performed during the World Ocean Circulation Experiment (WOCE; 1990-2002; e.g. Ganachaud and Wunsch, 2003).

Single AMOC estimates can be derived from hydrographic sections by applying the thermal wind balance, which relates the vertical gradient of the horizontal velocity to the horizontal gradient of density under the geostrophic approximation. The main uncertainty of this method results from the choice of a reference level velocity. The solutions range from assuming a level of no motion, imposing constraints of a zero-mass transport or fixed throughflow on estimates from basin-wide hydrographic sections to using direct velocity estimates from ship or lowered Acoustic Doppler Current Profilers (e.g.

McCarthy et al., 2020). Meridional heat and freshwater transport can then be calculated using the temperature and salinity measurements from the hydrographic sections.

McCarthy et al. (2020) nicely describe, how early estimates of the heat transport in the South Atlantic derived from zonal hydrographic sections measured during the German Atlantic expedition (Wüst, 1935) were not published, as the heat transport appeared to be working against global heat redistribution. Today, we know that the heat transport in the South Atlantic, unlike in all other major ocean basins, is equatorward because of the northward heat transport of the AMOC (e.g. Talley et al., 2011).

Efforts have been made to also use repeated hydrographic sections to detect changes in the AMOC. For example, Bryden et al. (2005) estimated a 30% decline in the overturning circulation since the 1950s from five hydrographic sections along 24.5°N (1957, 1981, 1992, 1998, 2004). The concept of a trans-basin array continuously measuring the temporal variability of the AMOC only arose in the 2000s. Soon, the RAPID/MOCHA transport mooring array was set up at 26.5°N. Using a combination of different techniques (current meter and dynamic height moorings, bottom pressure measurements, an old submarine telecommunications cable) the RAPID-array provides continuous full-depth measurements of AMOC transport as well as the related heat flux since 2004 (Cunningham et al., 2007; Rayner et al., 2011; McCarthy et al., 2015). The first results from the RAPID-array at 26.5°N showed surprisingly large variability of the AMOC on daily to seasonal time scales, stressing that the range of AMOC change discussed by Bryden et al. (2005) could easily be observed within a couple of weeks of the measured AMOC transport time series (Cunningham et al. 2007; Srokosz & Bryden, 2015 for a review). Identifying a strong seasonal cycle in the AMOC at 25.6°N, Kanzow et al. (2010) demonstrated that the bias induced by the seasonal anomalies leads to aliasing, when estimating the AMOC strength from single hydrographic sections. If seasonally-corrected, the section-based AMOC estimates at 24°N no longer support a near-monotonic AMOC decline (e.g. Frajka-Williams et al., 2019). While these results highlight the importance of continuous observations from purposefully designed arrays in order to monitor long-term AMOC changes, there is, however, potential in using hydrographic for estimating AMOC variability in other regions or on longer timescales. Results from the OVIDE repeat hydrography project have shown that it is possible to detect decadal AMOC variations in the subpolar North Atlantic, where the circulation is believed to have a more pronounced decadal component than in the Subtropics, using biennially repeated hydrographic ship sections combined with satellite altimetry and Argo data (Mercier et al., 2015).

Today, there are five trans-basin observational arrays in place to monitor the AMOC at selected latitudes (see Fig. 1), such as - the OSNAP array in the subpolar North Atlantic (since 2014; Lozier et al., 2019), the NOAC array at the southern boundary of the subpolar North Atlantic at 47°N (Roessler et al., 2015; extended in 2016), the RAPID array in the subtropical North Atlantic at 26°N (since 2004; Cunningham et al., 2007; McCarthy et al., 2015) or the SAMBA array in the subtropical South Atlantic at 34.5°S (since 2009; Meinen et al., 2018). Other intensive programs measure vital components of the overturning, such as - the deep overflow observations through Denmark Strait (Jochumsen et al., 2017) and Faroe Bank Channel (Hansen et al., 2016) or the Western Boundary Current arrays at 53°N (since 1997; Zantopp et al. 2017), at 39°N (Line W; 2004-2014; Toole et al., 2017), at 16°N (MOVE; since 2001; Kanzow et al., 2008; Send et al., 2011; Frajka-Williams et al., 2018) and at 11°S (2000-2004 and since 2013; Hummels et al., 2015).

The TRACOS array in the tropical South Atlantic aims at observing the **TRopical Atlantic Circulation & Overturning at 11°S** (Herrford et al., 2021). It was extended from the Western Boundary array off Brazil across the basin in 2013 (see section 1.3) and represents a link between North and South Atlantic MOC variability.

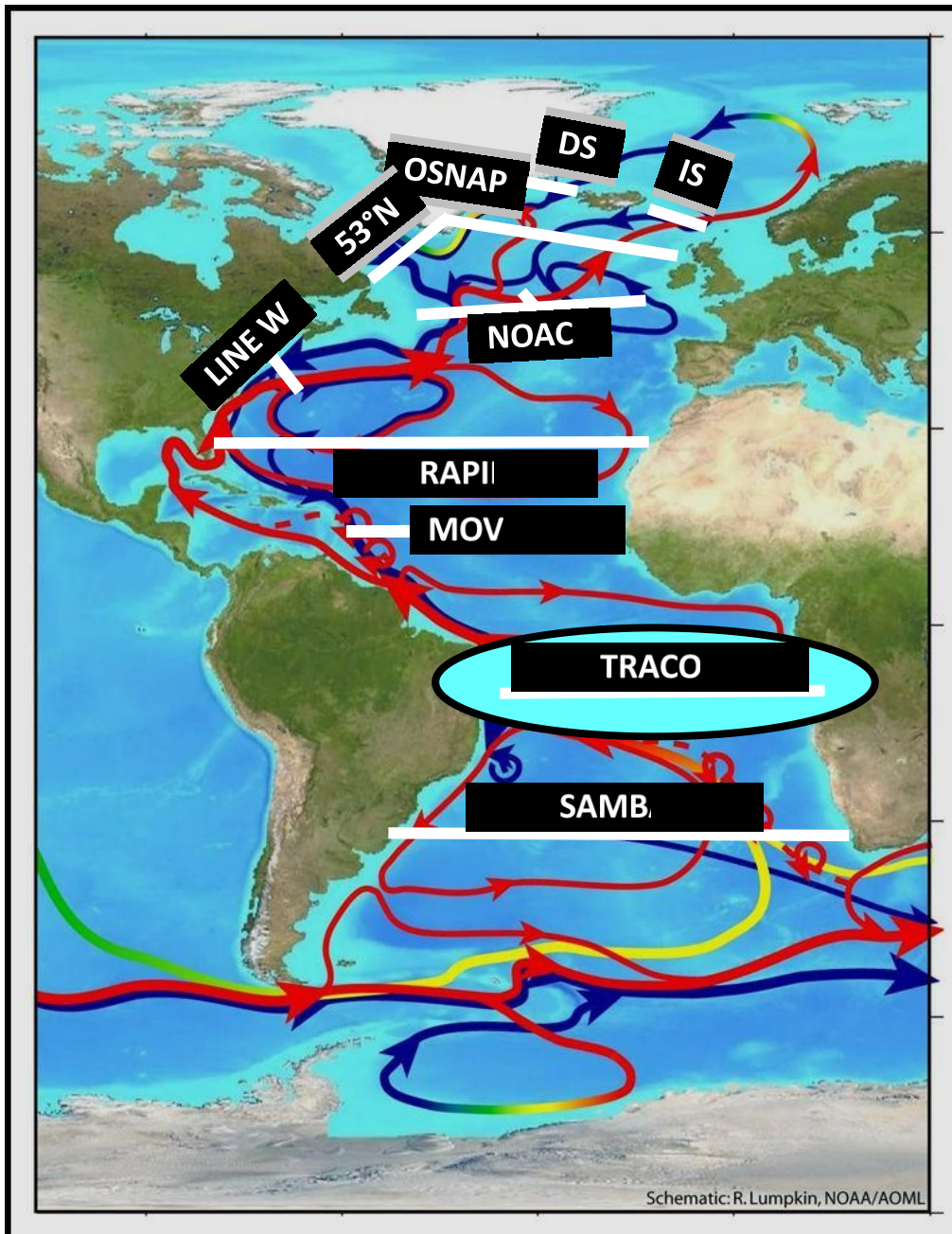


Figure 2 Schematic of the Atlantic Meridional Overturning Circulation. Red arrows indicate the flow of relatively warm surface waters, blue arrow the flow of relatively cold deep waters. Yellow and green colors represent transitions between depths. White lines mark the locations of moored arrays, which currently monitor the basin-wide AMOC or important components of it.

Most of the trans-basin AMOC arrays built on existing long-term observations of western boundary currents, which are one component of the AMOC but not representative of the basin-wide transport. To derive the basin-wide overturning, Western Boundary Current observations are typically combined with estimates of the geostrophic transport in the basin interior derived from density or pressure differences across the basin and estimates of the Ekman transport across the corresponding latitude calculated from surface wind products. However, the approaches and techniques can vary substantially between the different latitudes and programs. Several white papers have been published within the framework of the OceanObs'19 conference in 2019, nicely summarizing and reviewing all the AMOC observations (e.g. Frajka-Williams et al., 2019; McCarthy et al., 2020). These studies also elaborate on the aims, strengths and limitations of the different AMOC observing arrays and make suggestions for how they can be sustained and improved into the future. While the strategies of long-

standing arrays – like the RAPID or MOVE arrays – have already been tested regarding the accuracy and efficiency of their AMOC observing approaches (e.g. Kanzow et al., 2008; Stepanov et al., 2016; Sinha et al., 2018), this has not been sufficiently done for the newer programs. Frajka-Williams et al. (2019) also suggest that testing of the different observational strategies in models as well as incorporating alternative observational methods may be required to improve the accuracy of AMOC estimates and efficiency of the individual programs. Alternative approaches to monitor the AMOC use a combination of Argo float observations with sea surface height observations from radar altimetry (e.g. Willis, 2010; Schmid, 2014) or bottom pressure measurements along the western and eastern continental slopes (e.g. Bingham & Hughes, 2008; Hughes et al., 2018). Both approaches have their caveats: Willis (2010) noted that his method would not work in regions where significant meridional transport lies above the continental shelf or the upper part of the continental slope as Argo floats dive to approximately 2000 m to obtain temperature and salinity profiles. The difficulties of bottom pressure observations are thoroughly described in sections 2.2.1 and 2.6.

Traditionally, the AMOC was often simplified as a ‘conveyor belt’, which carries warm surface waters from the tropics into the North Atlantic, exports cold deep waters from the North Atlantic to the tropical and South Atlantic and is controlled by the production or upwelling of those deep waters. Almost two decades of continuous AMOC observations, predominantly in the North Atlantic, have replaced this simplified view of the AMOC with a more detailed understanding of the differing AMOC dynamics in different ocean basins (McCarthy et al., 2020). The basin-wide transport across a certain latitude can be dynamically decomposed into an Ekman and a geostrophic contribution (e.g. Hirschi & Marotzke, 2007), which are controlled by different mechanisms and dominate on different timescales. In contrast to the long-standing paradigm that intra-seasonal to interannual AMOC variability was mostly driven by the variability in the Ekman component (e.g. Bryden and Imawaki, 2001), early results from the RAPID array in the subtropical North Atlantic showed surprisingly large fluctuations in the upper-ocean interior geostrophic transport on periods as short as 20 days (Cunningham et al., 2007; Srokosz & Bryden, 2015 for review). Fluctuations in the geostrophic contribution to the AMOC at 26.5°N exceeded those in the Ekman contribution on intra-seasonal and seasonal time scales (Kanzow et al., 2007; 2010). Kanzow et al. (2010) and Chidichimo et al. (2010) found the seasonal cycle of the geostrophic AMOC component to be primarily driven by density anomalies at the eastern boundary and related it to strong seasonal variability in the near-coastal wind stress curl. Later, Yang (2015) found the seasonal AMOC variability at 26.5°N to not only be forced by the wind stress curl at the eastern boundary but also strongly influenced by wind stress forcing from other latitudes, especially from the subpolar North Atlantic. Subsequent modelling studies have confirmed that seasonal AMOC variability is primarily wind-driven in the subtropics as well as in the tropics (e.g. Zhao & Johns, 2014a; Xu et al., 2014). They suggest the seasonal cycle of the AMOC in the subtropics to be determined by both, the Ekman transport being directly driven by surface wind forcing and the upper-ocean geostrophic transport resulting from oceanic adjustment to local and remote wind forcing, and in the tropics to be dominated by the Ekman contribution. Remote wind forcing can cause local oceanic adjustment to either boundary waves propagating around ocean basins (e.g. Elipot et al., 2013) or planetary waves propagating westward from the basin interior (e.g. Zhao and Johns, 2014b). Modelling studies have also shown that wind-driven dynamics can explain most of the interannual changes in the AMOC at 26.5°N and may even play an important role on longer timescales by modulating the decadal time-scale response to buoyancy forcing (Bjastoch et al., 2008a; Zhao & Johns, 2014b; Polo et al., 2014). However, on decadal time scales, variations in surface buoyancy fluxes are generally thought to dominate variability of the AMOC (e.g. Polo et al., 2014). Buoyancy-forced AMOC changes are suggested to have large amplitudes in the subpolar North Atlantic (e.g. Bjastoch et al., 2008a), where the OSNAP array aims at assessing the link between deep water mass formation and AMOC variability (Lozier et al., 2019).

While a large part of the observed AMOC variability is locally or regionally driven, for climate research, it is particularly important to understand the meridional coherence of AMOC signals between different ocean basins. As some of the AMOC observations in the North Atlantic span several years now, efforts have recently been made to link AMOC variability at 26.5°N with observations at 41°N and 16°N. For example, Mielke et al. (2013) evaluated observed AMOC variability in the subtropical and subpolar North Atlantic and found the phases of the annual cycles of the geostrophic contributions to the overturning at 26°N and 41°N to be 180° out-of-phase. As seasonal and interannual variations in the geostrophic AMOC contribution are thought to be mainly wind-driven, phased variability between the tropical, subtropical and subpolar gyres is expected on these timescales (e.g. Xu et al., 2014; Elipot et al., 2017). Zhao & Johns (2014a) analyzed an ocean general circulation model regarding the individual contributions from the eastern and western boundaries as well as interior basin to the basin-wide upper-ocean geostrophic transport in the Atlantic. Their results suggest that the seasonal cycle of the AMOC in the subtropics is controlled mainly by local boundary effects, with either the western or eastern boundary being dominant at different latitudes, while in the tropical North Atlantic it is controlled interior flow and a lagged compensation by the western boundary current. However, these results also strongly depend on the choice of wind product used to force their model. The ability of different wind products to capture the seasonal wind variability in the tropical Atlantic is evaluated in section 3.5.2 of this thesis. On interannual timescales, AMOC variability in the North Atlantic was also reported to be coherent over some but not all latitudes (Xu et al., 2014) and has been associated with the North Atlantic Oscillation (Elipot et al., 2017). While it is still discussed how the meridional coherence of AMOC signals on shorter timescales breaks down, it is commonly accepted that the AMOC is meridionally coherent on decadal or longer timescales. At 26°N and 16°N, however, long-term AMOC changes show incoherent tendencies - with a weakening at 26°N and a strengthening at 16°N (Frajka-Williams et al., 2018). Diagnosing the origins of these different tendencies, Frajka-Williams et al. (2018) found consistent low frequency deep density changes at the western boundaries occurring first at 26°N and 7 months later at 16°N, but also discrepancies in the methodologies (e.g. addressing the geostrophic reference level) to contribute to low-frequency variability of the derived AMOC time series.

The meridional coherence of observed AMOC transport variations in the South Atlantic has, to my knowledge, not been investigated in detail yet. Results from the SAMBA array indicate that the AMOC in the subtropical South Atlantic highly energetic with strong variations on time scales from a few days to years (Meinen et al., 2013; 2018). Meinen et al. (2018) found AMOC variability at 34.5°S to be more complicated than in the subtropical North Atlantic with the dynamical control of AMOC variations being more broadly spread across the basin. They report baroclinic and barotropic changes at both boundaries to be important for AMOC variations on seasonal timescales, but eastern boundary density variations to be most important at interannual timescales. They argue, that the latter reflects the impact of interocean exchanges between South Atlantic and the Indian Ocean. Results from the TRACOS array at 11°S can contribute to the understanding of the meridional coherence of AMOC signals across the equator or within the South Atlantic.

1.3. The observational program and circulation at 11°S

Parts of the observational program in the western tropical South Atlantic already started in the early 1990s during the WOCE (World Ocean Circulation Experiment) program and were continued during 2000-2004 within the German CLIVAR (climate variability and predictability) program with repeated ship-sections along 5°S and 11°S. Also, in 2000-2004, a mooring array consisting of five tall moorings was deployed at 11°S (Fig. 3) to observe the variability of the western boundary current regime off the Brazilian coast. While the main objective of this mooring array was to observe variability of the North Brazil Undercurrent (NBUC) that might potentially be related to variability of the shallow thermohaline

subtropical cell (STC; Schott et al., 2002), it was also instrumented to observe the deep flow within the Deep Western Boundary Current (DWBC). A number of important discoveries have been made from that mooring period: Based on observations from the WOCE and CLIVAR programs, Schott et al. (2005) described the local water mass distribution as well as the mean state and seasonal variability of the western boundary circulation at 11°S. They found the NBUC to transport + 25 Sv northward on average and to exhibit strong seasonal cycle, which seems to be out of phase with the seasonal variations in the DWBC. Analyzing a large-scale survey off the coast of Brazil in 2000, Stramma et al. (2005) observed a relatively weak NBUC at 11°S compared to 5°S and a stronger than normal inflow from the east between both latitudes. Rhein & Stramma (2005) found seasonal variations in the upper North Atlantic Deep Water (NADW) layers based on chlorofluorocarbon (CFC) measurements. Note, that the seasonal cycle of the NBUC, calculated from an updated transport timeseries, is described in more detail and compared to the output of the INALT01 model in section 2.5.4 of this thesis.

On intra-seasonal timescales, Dengler et al. (2004) noticed a spectral peak at a period of 60-70 days in the moored time series at deep water levels and concluded that the DWBC transport at 11° S is not accomplished by a continuous boundary current but by a sequence of migrating eddies. Later, Veleda et al. (2012) related NBUC variability at periods of 2-3 weeks to coastal trapped waves (CTWs) propagating equatorward along the Brazilian coast.

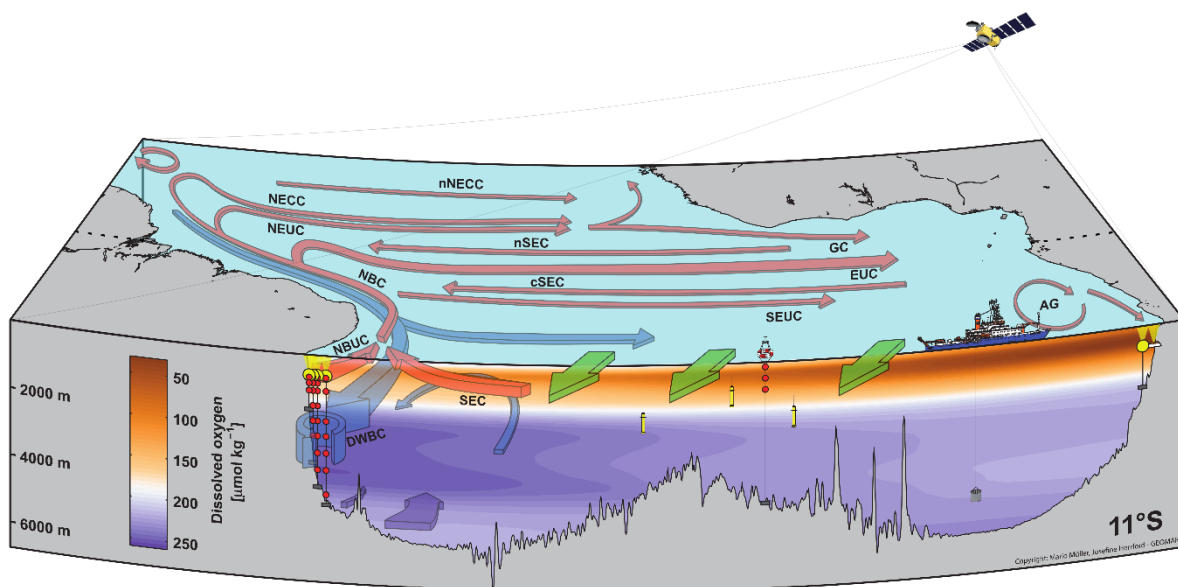


Figure 3 Schematic of the large-scale circulation in the tropical Atlantic and of the observational program at 11°S. Red arrows represent surface and thermocline currents (after Hahn et al., 2017; Burmeister et al., 2019), blue arrows the NADW circulation, purple arrows the spreading of AABW (only in the Brazil Basin; both after Herrford et al., 2017) and green arrows the Ekman transport across 11°S. The front panel shows the dissolved oxygen distribution along 11°S measured during Meteor cruise 28/1 (see chapter 4).

In July 2013, a similar mooring array was again deployed off Brazil as part of the BMBF projects RACE I, RACE II & RACE synthesis. While Hummels et al. (2015) did not find significant changes in the averaged NBUC and DWBC transports between the two observational periods 2000-2004 and 2013-2015, they found interannual NBUC variability to be consistent with the output from the forced ocean general circulation model INALT01 (Durgadoo et al., 2013). Decadal variability in INALT01 (Hummels et al., 2015) was also found to be similar to transport estimates based on historical hydrographic observations from Zhang et al. (2011). Zhang et al. (2011) reported multi-decadal variability of the NBUC to be of similar order as its seasonal cycle and suggested that the NBUC could serve as an index

for AMOC variations on these time scales. A related model study by Rhs et al. (2015) found decadal to multi-decadal buoyancy-forced changes in the AMOC transport to the manifest themselves in NBUC transport (at 6° S), however, this relation to be also masked by interannual wind-driven variability.

Ship-based hydrographic measurements collected during the cruises within the WOCE, CLIVAR and RACE programs allowed for the investigation of long-term water mass changes in the western tropical Atlantic. A salinification of the central and intermediate waters within the NBUC could be related to an increasing Agulhas leakage (e.g. Biastoch et al., 2008a; Kolodziejczyk et al., 2014). A Freshening of the NADW layers in the tropical Atlantic was shown to be related to fresher overflows in the North Atlantic in the 1980s to 1990s (e.g. Hummels et al., 2015; Fu et al., 2018). The prominent signal of Antarctic Bottom Water warming, observed all around the Southern Hemisphere, was found to reach the equatorial Atlantic and to be the result of a decreasing volume of its densest component (Herrford et al. 2017). A more comprehensive review of the water mass distribution as well as long-term property changes observed at 11°S is provided in section 4.1.1.

With the resumption of the mooring array at 11°S in 2013, the observational program was also extended: Another mooring array for direct velocity measurements was installed across the continental slope off Angola (Fig. 3) within the German SACUS (Southwest African Coastal Upwelling System and Benguela Nios) project. Studies based on the moored observations off Angola showed that the circulation there is weak and dominated by seasonal variability associated with remotely forced waves (Kopte et al., 2017; 2018). They benefited from the extensive oceanographic data set off repeated ship surveys acquired since 1983 within the EAF-Nansen program (Tchipalanga et al., 2018). PIES (Pressure Inverted Echo Sounders) or single bottom pressure recorders (BPRs) were deployed on both sides of the Atlantic. At the eastern boundary off Angola, two SBE 26plus sensors (single or attached to an ADCP shield) measured pressure at 300 m and 500 m depth from 07/2013 to 11/2015. The instruments were re-deployed, but could not be recovered again - they were probably lost due to extensive fishing in the region. An overview of the availability and processing of the bottom pressure measurements at 11°S can be found in section 2.2.1 of this thesis.

The observational program of the TRACOS array at 11°S, as it is today, allows for estimating AMOC variations on intra-seasonal to interannual timescales and investigating mechanisms relevant for tropical Atlantic variability. Any AMOC signal that is understood in terms of regional forcing can be removed from the observed AMOC timeseries, which is important for estimating the significance of long-term AMOC changes and, thus, for the detectability of its meridional coherence. If continued into the future, this array has great potential for understanding meridional coherence and long-term changes of AMOC variability.

1.4. Research questions

As discussed above, there is a need for sustained and widespread observations of the AMOC - in order to better understand the mechanisms that control its structure and variability. The western tropical South Atlantic is a key region for the exchange of water masses, heat and salt between the Southern and Northern Hemispheres. Therefore, 11°S is considered to be a good place to monitor water mass signals, changes in the Western Boundary Current system and changes in the AMOC strength. In this thesis, I investigate different aspects of the observed seasonal to decadal variability in the tropical South Atlantic related to the AMOC at 11°S by answering the following questions:

- Chapter 2: How can bottom pressure observations at 11°S be utilized to construct an AMOC transport timeseries? How does the observed seasonal variability along 11°S compare to the output of the OGCM INALTO1? What are the mechanisms that control the seasonal cycle of the AMOC at 11°S?
- Chapter 3: To which extent do different wind products agree on the large-scale wind patterns and wind variability in the tropical Atlantic? How can the differences among wind products translate into estimates of the large-scale circulation in the tropical Atlantic and its variability on different timescales?
- Chapter 4: How have water mass properties in the tropical South Atlantic changed over the last 25 years? Are the observed temperature trends caused by intrinsic water mass or volume changes?

The results from my thesis contribute to the overall understanding of AMOC-related variability in the tropical Atlantic as well as possible uncertainties in the variability of different AMOC components derived from observations. Chapter 5 provides a summary of the main results and a list of suggestions for further research.

2. Seasonal variability of the Atlantic Meridional Overturning Circulation at 11°S inferred from bottom pressure measurements

Abstract

Bottom pressure observations on both sides of the Atlantic basin, combined with satellite measurements of sea level anomalies and wind stress data, are utilized to estimate variations of the Atlantic Meridional Overturning Circulation (AMOC) at 11°S. Over the period 2013-2018, the AMOC and its components are dominated by seasonal variability, with peak-to-peak amplitudes of 12 Sv for the upper-ocean geostrophic transport, 7 Sv for the Ekman and 14 Sv for the AMOC transport. The characteristics of the observed seasonal cycles of the AMOC and its components are compared to results from an ocean general circulation model, which is known to reproduce the variability of the Western Boundary Current on longer timescales. The observed seasonal variability of zonally integrated geostrophic velocity in the upper 300 m is controlled by pressure variations at the eastern boundary, while at 500 m depth contributions from the western and eastern boundaries are similar. The model tends to underestimate the seasonal pressure variability at 300 and 500 m depth, especially at the western boundary, which translates into the estimate of the upper-ocean geostrophic transport. In the model, seasonal AMOC variability at 11°S is governed, besides the Ekman transport, by the geostrophic transport variability in the eastern basin. The geostrophic contribution of the western basin to the seasonal cycle of the AMOC is instead comparably weak as transport variability in the western basin interior related to local wind curl forcing is mainly compensated by the Western Boundary Current. Our analyses indicate, that while some of the uncertainties of our estimates result from the technical aspects of the observational strategy or processes being not properly represented in the model, uncertainties in the wind forcing are particularly relevant for the resulting uncertainties of AMOC estimates at 11°S.

2.1. Introduction

The Atlantic Meridional Overturning Circulation (AMOC) plays a major role in the global oceanic heat budget. About 88 % of the maximum heat transport in the subtropical North Atlantic (1.3 PW; e.g. Lavin et al., 1998) are carried by the AMOC (Johns et al., 2011). Because of the AMOC, there is substantial northward heat transport across the Atlantic equator (e.g. Talley, 2003), which is unique among global oceans. Simplifying the circulation in the Atlantic to a two-dimensional latitude-depth plane, the AMOC connects warm waters flowing northward in the upper ocean and cold waters flowing southward at depth across all latitudes through water mass transformation, for example, in the subpolar North Atlantic or near the Southern Ocean (e.g. Buckley & Marshall, 2016). With the AMOC representing the strongest mode of northward heat transport by the ocean, it is essential to provide the observational evidence of the mechanisms that control its structure and variability in order to understand the present-day climate, validate climate simulations and improve predictions. Historically, the strength and structure of the AMOC was estimated based on shipboard hydrographic sections establishing the mean AMOC strength and related heat transport (e.g. Richardson, 2008). The first trans-basin mooring array - the RAPID/MOCHA transport array at 26°N - continuously measures the temporal variability of the AMOC since the early 2000s (Hirschi et al., 2003). Those observations showed that large AMOC variations can occur on a range of timescales - from weeks to decades (e.g. Srokosz & Bryden, 2015). Kanzow et al. (2007) showed, that not only the Ekman, but even more the geostrophic contribution to the AMOC, exhibit pronounced high-frequency variability with periods up to few weeks. Kanzow et al. (2010) demonstrated that the strong seasonal cycle in the AMOC strength

at 26°N leads to aliasing, when estimating the AMOC strength from single hydrographic sections. They also found the upper-ocean geostrophic AMOC contribution to dominate on seasonal time scales, while Chidichimo et al. (2010) discovered those to be primarily driven by processes at the eastern boundary.

Today, there are several ongoing international efforts monitoring the AMOC at selected latitudes (e.g. Frajka-Williams et al., 2019), such as - the OSNAP array in the subpolar North Atlantic (since 2014; Lozier et al., 2019), the RAPID array in the subtropical North Atlantic at 26°N (since 2004; Cunningham et al., 2007; McCarthy et al., 2015), the MOVE array in the tropical North Atlantic at 16°N (since 2001; Kanzow et al., 2008; Send et al., 2011; Frajka-Williams et al., 2018), the SAMBA array in the subtropical South Atlantic at 34.5°S (since 2009; Meinen et al., 2018) – as well as other programs measuring important components of the overturning, such as - the Western Boundary Current (WBC) arrays at 53°N (since 1997; Zantopp et al. 2017), at 39°N (Line W; 2004-2014; Toole et al., 2017) and at 11°S (2000-2004 and since 2013; Hummels et al., 2015), the array across the North Atlantic Current at 47°N (NOAC array; Roessler et al., 2015), the deep overflow observations through Denmark Strait (Jochumsen et al., 2017) or Faroe Bank Channel (Hansen et al., 2016). In this study, we will present the first estimate of basin-wide AMOC variations in the tropical South Atlantic - from the TRACOS (Tropical Atlantic Circulation and Overturning at 11°S) array.

The western tropical South Atlantic constitutes a key region for the exchange of water masses, heat and salt between the Southern and Northern Hemispheres (Biaostoch et al., 2008a; Schmidtko & Johnson, 2012; Kolodziejczyk et al., 2014; Hummels et al., 2015; Lübbecke et al., 2015; Herrford et al., 2017). Several observational and modelling studies (e.g. Rühls et al., 2015; Zhang et al., 2011) suggest that 11°S is a good place to monitor water mass signal propagation, changes in the WBC transports and, with that, changes in the AMOC transport. At 11°S the WBC regime is comprised of the northward North Brazil Undercurrent (NBUC) with a subsurface velocity maximum at about 200 m and the southward Deep Western Boundary Current (DWBC) below 1200 m (e.g. Schott et al., 2005). The NBUC is known to originate from the southern branch of the South Equatorial Current (da Silveira et al., 1994), which transports subtropical waters towards Brazil and bifurcates between 14-28°S (Stramma and England 1999; Boebel et al. 1999; Wienders et al., 2000). From 2000 to 2004, a first mooring array was deployed at 11°S to observe the variability of the WBC and its components –the NBUC and the DWBC below. Schott et al. (2005) found the NBUC to carry 25 Sv northward on average. The NBUC showed a strong seasonal cycle, which seems to be out of phase with the seasonal variations in the DWBC. Intra-seasonal signals could also be observed: Dengler et al. (2004) described a spectral peak in the velocity time series at a period of 60-70 days, which was observed in most of the moored records, but was strongest within the DWBC. They concluded that the DWBC transport at 11°S is mainly accomplished by migrating eddies. Further, Veleza et al. (2012) could relate variability at periods of 2-3 weeks to coastal trapped waves (CTWs) propagating from 22-36°S equatorward along the Brazilian coast. In July 2013, a similar mooring array was again deployed at 11°S (Hummels et al., 2015), and is still in place. Comparing the two observational periods, Hummels et al. (2015) did not find significant changes in the averaged NBUC and DWBC transports. Furthermore, they could show that the interannual NBUC variability observed between 2000-2004 is consistent with the output of a forced ocean general circulation model (OGCM) named INALT01. Decadal variability in INALT01 was also found to be similar to transport estimates based on historical hydrographic observations from Zhang et al. (2011). To date, Zhang et al. (2011) provide the only NBUC time series derived from hydrographic observations spanning several decades. They estimated multi-decadal variability of the NBUC to be of similar order as its seasonal cycle and, because of the connection to the Atlantic Multidecadal

Variability, suggested the NBUC to serve as an index for AMOC variations on these time scales. In a model study, R hs et al. (2015) found decadal to multi-decadal buoyancy-forced changes in the AMOC transport to manifest themselves in NBUC transport (at 6 S), however these changes are also masked by interannual wind-driven variability.

With the resumption of the mooring array at 11 S in 2013, the observational program was also extended by installing a mooring array for direct velocity measurements across the continental slope off Angola. Studies based on these observations showed that the circulation there is weak and dominated by seasonal variability associated with remotely forced waves (Kopte et al., 2017; 2018). As shown in several model studies, most of the intra-seasonal ($T > 120$ days) to interannual variability in that region is induced by a wave response to equatorial wind forcing that generates equatorial Kelvin waves propagating eastward and, while reaching the eastern boundary, transferring a part of their energy as CTWs further to the south towards 11 S (Illig et al., 2004; Illig et al., 2018; Bach lery et al., 2016; Imbol Koungue et al., 2017).

Besides the moored observations at 11 S, PIES (Pressure Inverted Echo Sounders) or single bottom pressure recorders (BPRs) were deployed on both sides of the Atlantic. Within some of the other programs targeting AMOC fluctuations – such as RAPID (Kanzow et al. 2010, Meinen et al. 2013, McCarthy et al., 2015), MOVE (Kanzow et al., 2006, 2008) and SAMBA (Meinen et al., 2018; Kersal  et al., 2020) – bottom pressure (BP) measurements are used to estimate the time-varying portion of a barotropic reference velocity which is then combined with the internal geostrophic velocity derived from differences in dynamic height derived from full-depth dynamic height moorings or the PIES travel times. But, circulation changes in z -coordinates can also be estimated using only a series of bottom pressure measurements installed at different depths on the western and eastern continental slopes. In a model study, Bingham and Hughes (2008) showed that this works well down to around 3000 m, even with only western boundary measurements. In our study, we use the BP differences across the basin at 300 m and 500 m depth to estimate the geostrophic contribution to AMOC variations in the tropical South Atlantic over the period 2013-2018 and investigate its seasonal variability.

2.2. Observational Data

2.2.1. Bottom pressure time series

Over the period 2013-2018 five BPRs were deployed at 11 S (Table 1). In May 2013, together with the WBC mooring array, two bottom-mounted PIES were installed across the Brazilian continental slope at 300 m and 500 m depth. PIES measure the acoustic travel time to the surface, as well as bottom pressure. In this study, we only used the BP time series. One year later another set of PIES was deployed at the same locations. While of the first set only the 500 m sensor could be recovered, the second set was maintained in September 2016 and spring 2018. Note, that the two PIES at 500 m, KPO 1109 and KPO 1135 (Table 1), were located only ~ 1 km away from each other over the period 05/2014 – 10/2015. At the eastern boundary off Angola, two SBE 26plus sensors (single or attached to an ADCP shield) measured pressure at 300 m and 500 m depth from 07/2013 to 11/2015. The instruments were re-deployed, but could not be recovered again. We assume, that they were lost due to extensive fishing in the region.

Table 1 Collection of available BP measurements at 11°S. Acronyms used throughout this article are given in the 1st column, official mooring IDs and instrument types are listed in the 2nd and 3rd columns. Columns 4-6 give the positions, depths and deployment periods for each BP measurement. The BP data can be found at <https://doi.org/10.1594/PANGAEA.907589>. *These sensors were re-deployed in 2018 and are currently in place.

Acronym	Mooring ID	Instrument	Position	Depth	Deployment period
P _{WB 500m a}	KPO 1109	PIES	10.2367°S 35.8633°W	500m	05/2013 - 10/2015
P _{EB 300m}	KPO 1110	Single SBE 26plus sensor	10.6830°S 13.2250°E	300m	07/2013 - 11/2015
P _{EB 500m}	KPO 1106	ADCP shield with SBE 26plus sensor	10.7090°S 13.1855°E	500m	07/2013 - 10/2015
P _{WB 300m}	KPO 1134	PIES	10.2320°S 35.8780°W	300m	05/2014 - 09/2016 09/2016 - 03/2018*
P _{WB 500m b}	KPO 1135	PIES	10.2430°S 35.8700°W	500m	05/2014 - 09/2016 09/2016 - 02/2018*

For our analyses, the available BP records were de-spiked, interpolated from an original sampling rate of 10 minutes to hourly values and de-tided using harmonic fits with tidal periods shorter than 35 days. All tidal harmonics were calculated performing a classical harmonic analysis (Codiga, 2011). The tidal models for $T < 35$ days capture between 97.0-99.6 % of the total variance in the original BP time series. After removing these higher-frequency tides, the remaining variance is mainly related to seasonal variations and low-frequency instrument drifts. Instrument drifts vary substantially between the five instruments: While KPO 1106 shows almost no drift, all other sensors exhibit a combination of exponential and linear behaviour, but with different signs and at different rates (Fig. 4 (a)). Unfortunately, we were not able to directly relate individual drift behaviour to pressure effects or material creep. Earlier studies (e.g. Watts & Kontoyiannis, 1990; Johns et al., 2005; Kanzow et al., 2006; Cunningham et al, 2009) found subtracting a least-squares exponential-linear fit of the form $P_{Drift}(t) = a[1 - e^{-bt}] + ct + d$ from the pressure time series to be the procedure that works best for the PIES. As the SBE26plus recorders were also equipped with Quartz pressure sensors, we decided to “de-drift” all five sensors similarly by subtracting exponential-linear fits as described above. Kanzow et al. (2006) also discussed the problem of this empirical de-drifting not being able to distinguish between the instrumental drift and ocean signals of the order of or longer than the time series. This means that, for example, seasonal signals can leak into the fit and its removal from the time series can reduce seasonal signals in return. We attempted to solve this problem by iteratively fitting an exponential-linear drift as well as annual and semi-annual harmonics. The first guess of the exponential-linear drift was removed from the original time series and annual and semi-annual harmonics were fitted to the de-drifted time series. This first guess was iteratively improved by calculating new exponential-linear fits after subtracting the iteratively improved annual and semi-annual harmonics from the original data. After three repetitions the fits tended to converge. Both fits from the third repetition are shown in Fig. 4 (a). For further analyses, we removed the derived instrument drift from the original BP time series and averaged to daily values (Fig. 4 (b)).

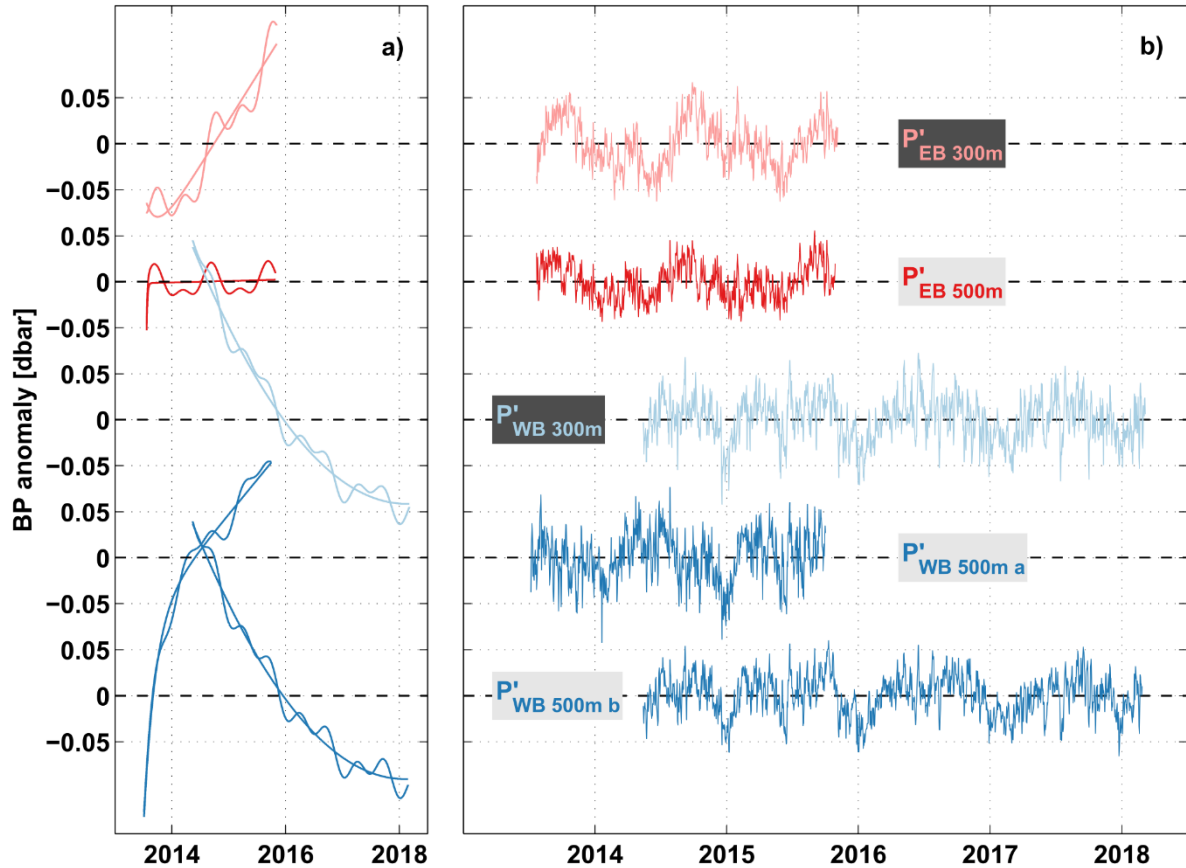


Figure 4 Bottom pressure (BP) anomalies measured at 11°S off Angola at 300 m (pink) and 500 m (red), as well as off Brazil at 300 m (light blue) and 500 m (blue) depth. (a) Instrument drifts that are removed from, as well as the sum of the drift and the combined annual and semi-annual harmonics fitted to the individual BP anomaly time series. (b) Daily time series of BP anomalies after de-tiding and de-drifting (see text for details).

2.2.2. Sea level anomalies

To estimate pressure variability at the surface, we used sea level anomalies (SLA) from the delayed-time “all-sat-merged” data set of global sea surface height, produced by Ssalto/Duacs and provided by the Copernicus Marine Environment Monitoring Service (CMEMS). The multi-satellite altimeter sea surface heights are mapped on a $0.25^\circ \times 0.25^\circ$ grid (e.g. Pujol et al., 2016) and are available for the period 1993-2018 at daily resolution. To obtain pressure variation near the boundaries, SLA grid points were chosen closest to the Brazilian and Angolan coasts at 11°S, respectively. The sensitivity of our results to SLA changes with distance to the coast (Fig. 5 (c, d)) was tested: At the western boundary, off Brazil, the phase of the annual harmonic slightly changes with distance to the coast – about 30 days over 0.5° longitude. At the eastern boundary, off Angola, the phases of both annual and semi-annual harmonics are constant over the distance between the location of the 300 m BPR and the coast.

2.2.3. Wind stress

In order to estimate the Ekman contribution to AMOC variability at 11°S we used gridded daily wind stress fields from Metop/ASCAT scatterometer retrievals. Those are available for the period 2007-2018 and with a spatial resolution of $0.25^\circ \times 0.25^\circ$ (Bentamy & Croizé-Fillon, 2012). The near-surface Ekman transport was estimated as the zonal integral of the zonal wind stress component between 10.5-11°S (see Eq. (7) in section 2.4.1).

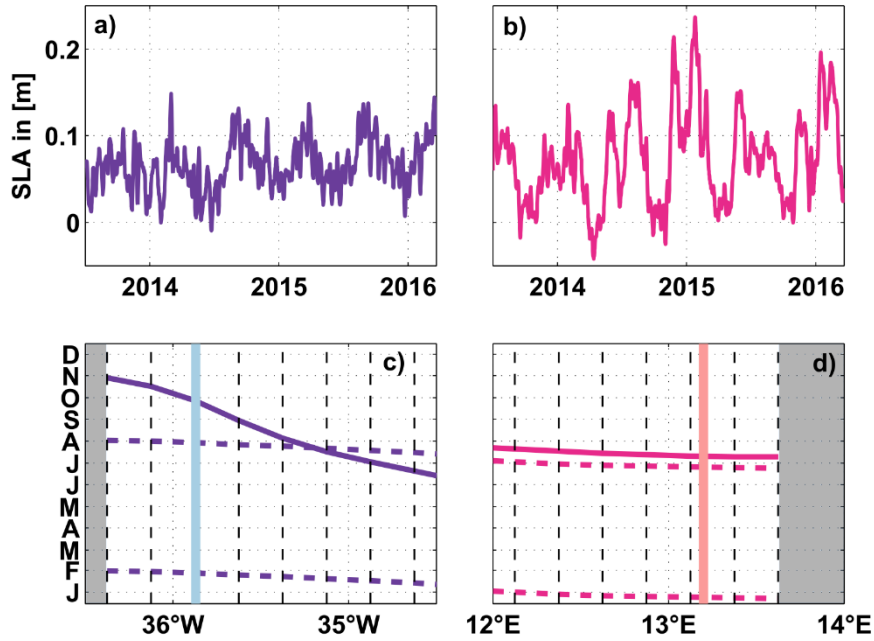


Figure 5 Time series of SLA over the period 2013-2018 – chosen close to the western (purple; (a)) and eastern boundaries (magenta; (b)). Phases of the minima of the annual (solid curve) and semi-annual (dashed curves) harmonics as function of longitude near the western (c) and eastern (d) boundaries. In (c, d), the black dashed lines represent the zonal grid spacing of the SLA data and grey areas mark land. Light blue (c) and pink (d) lines mark the locations of the 300 m BPRs at the western (c) and eastern (d) boundaries.

2.2.4. NBUC transport time series

To estimate the western boundary current transport, we computed a transport time series of the NBUC (section 2.5.4), which is derived from four current meter moorings spanning the width of the NBUC at 11°S and represents an update from previous studies (Schott et al., 2005; Hummels et al., 2015). Record gaps were filled with empirical orthogonal functions (EOFs) derived from the mooring data. Moored time series were finally mapped into sections every 2.5 days using a Gaussian-weighted interpolation with horizontal mapping scales of 20 km with a cutoff radius of 150 km and vertical mapping scales of 60 m with a cutoff radius of 1500 m. The NBUC transport was computed by integrating the total flow (including northward and southward flow) within a predefined box (see Hummels et al. (2015) for further details).

2.3. Model Data

To validate the observational strategy, we used the 5-daily output from a hindcast experiment with the global ocean/sea-ice Ocean General Circulation Model configuration `INALT01`. It is based on the NEMO (Nucleus for European Modelling of the Ocean v3.1.1; Madec, 2008) code and developed within the DRAKKAR framework (The DRAKKAR Group, 2014). INALT01 is a global 1/2° configuration with a 1/10° refinement between 70°W-70°E and 50°S-8°N, improving the representation of the western boundary current regime in the South Atlantic and extended Agulhas region (Durgadoo et al., 2013). It uses a tripolar horizontal grid, 46 vertical levels with increasing grid spacing and is forced by interannually varying air-sea fluxes (1948-2007) from the CORE2b data set (Coordinated Ocean-ice Reference Experiments; Large & Yeager, 2009). Sea surface elevation and wind stress are then prognostic variables: INALT01 uses the filtered free surface formulation for the surface pressure gradient and calculates surface wind stress from relative winds using the CORE2b bulk formulae. This particular model configuration has been previously used in the region. South of Africa it was used for

validating a method of determining Agulhas leakage from satellite altimetry (Le Bars et al., 2014). Hummels et al. (2015) found interannual variability of the NBUC as assessed from moored observations to be consistent with the INALTO1 model output as well as decadal variability in INALTO1 to be similar to geostrophic transport estimates from Zhang et al. (2011). Further, the simulated overturning streamfunction (in neutral density classes) at 11°S is in good agreement with the vertical structure and amplitude of an estimate based on shipboard observations conducted in 1994 (Lumpkin & Speer, 2003). Our analysis employs 2-dimensional (longitude-depth) sections of temperature, salinity and velocity, as well as surface elevation and wind stress fields along 11°S for the simulated period 1978-2007. Surface wind stress fields are additionally shown for the years 2008-2009.

2.4. Methods

2.4.1. Computation of AMOC transport variations from BP observations

The structure of the AMOC is often described using the overturning transport stream function $\psi(y, z, t)$, which is derived from integrating the meridional velocity component, v , zonally (from the western (x_{WB}) to the eastern boundary (x_{EB})) and vertically:

$$\psi(y, z, t) = \int_z^0 \int_{x_{WB}}^{x_{EB}} v(x, y, z', t) dx dz' \quad (1)$$

with x being longitude, y latitude, z the vertical coordinate pointing upward and t time. This reduces a complex three-dimensional circulation system to a two-dimensional one. The AMOC strength or transport is commonly defined as the maximum of ψ over depth and typically expressed in Sverdrups [$1 \text{ Sv} = 10^6 \text{ m}^3 \text{ s}^{-1}$]. At any chosen latitude, Ψ_{MAX} can be decomposed into Ekman and geostrophic components (thereby generally neglecting small ageostrophic, non-Ekman components):

$$\psi_{MAX}(y, t) = T_{AMOC}(y, t) \approx T_G(y, t) + T_{EK}(y, t) \quad (2)$$

Variations in the basin-wide upper-ocean meridional geostrophic transport T_G at a certain latitude can be derived from the differences between the bottom pressure at the eastern (P_{EB}) and western (P_{WB}) basin boundaries. At 11°S, we use bottom pressure measurements on both sides of the basin at 300 m and 500 m depth. Figure 6 displays the observational strategy.

Our method is limited by the fact that the depth levels of the instruments with respect to equipotential surfaces are not known and, thus, only velocity anomalies can be determined (e.g. Donohue et al., 2010). However, the differences between eastern and western boundary pressure anomalies from BPRs have successfully been used to estimate temporal fluctuations of the geostrophic contribution to AMOC variability (e.g. Kanzow et al., 2007).

At the BPRs depths, anomalies of the geostrophic transport per unit depth $V'_G(z, t)$ were calculated as:

$$V'_G(z, t) = \frac{1}{\rho_0 \cdot f} \cdot (P'_{EB}(z, t) - P'_{WB}(z, t)) \quad (3)$$

P'_{EB} and P'_{WB} are the pressure anomalies at the eastern and western boundary with respect to the time mean, respectively, f the Coriolis parameter and ρ_0 a mean sea water density.

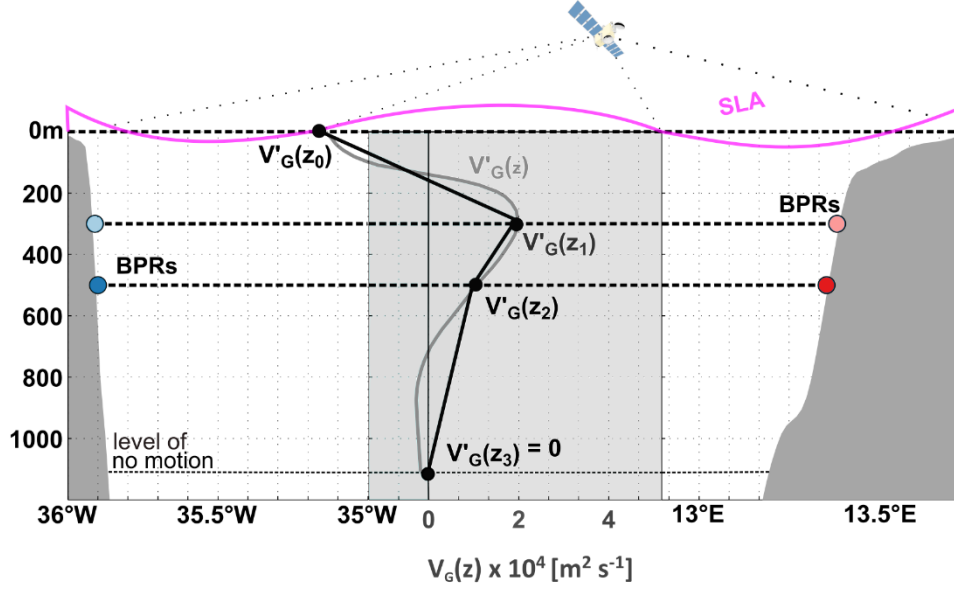


Figure 6 Experimental setup and strategy to estimate T'_G showing the location of the BPRs (reddish & blueish circles) and the vertical sampling of V'_G . V'_G is derived from measurements of sea level anomaly and with bottom pressure at 300 m and 500 m depth. A level of no motion is prescribed to be at $z_3=-1130$ m. Two methods are used to approximate $V'_G(z)$: i) piecewise linear interpolation of V'_G between the 4 data points (black profile), ii) regression of the 1st and 2nd dominant vertical structure functions of $V'_{G \text{ SIM P}(z)}$ from INALT01 onto the data points at 0 m, 300 m and 500 m depth relaxing the no-flow condition at 1130 m depth (grey profile). $V'_G(z)$ is then vertically integrated from 1130 m to the surface to derive T'_G .

At the surface, $V'_G(z = 0, t)$ can be calculated accordingly from sea level anomalies, η' :

$$V'_G(z = 0, t) = \frac{g}{f} \cdot (\eta'_{EB}(t) - \eta'_{WB}(t)) \quad (4)$$

with g being the acceleration of gravity. Additionally, a level of no motion is prescribed at 1130 m, such that $V'_G(z = -1130 \text{ m}, t) = 0$ at all times. This 'level of no motion' is based on the velocity field from the INALT01 model configuration and defined as the local zero-crossing depth of v , averaged across the basin and over time. The maximum of the corresponding stream function averaged over time is located at $z=-1072$ m. Earlier studies in this region, used a level-of-no-motion at the depths of $\sigma_1 = 32.15 \text{ kg m}^{-3}$ (at about 1150 m; e.g. Stramma et al., 1995; Schott et al., 2005). The sensitivity to the choice of the level of no motion was tested between 800-1300 m and the obtained AMOC transport changed by less than 10%.

We use two different methods to approximate the vertical structure of V'_G :

1. Piecewise linear interpolation of V'_G between the 4 data points at 0 m, 300 m, 500 m and 1130 m depth – denoted as $V'_{G \text{ Points}}$ or $T'_{G \text{ Points}}$ throughout the study.
2. Regression of the 1st and 2nd EOFs, i.e. the two dominant vertical structure functions of the geostrophic transport per unit depth derived from density and sea level anomalies in INALT01, $V'_{G \text{ SIM P}(z)}$ (see section 2.4.2), onto the 3 data points at 0 m, 300 m and 500 m depth thereby relaxing the no-flow condition at 1130 m depth. The first (second) dominant vertical structure function explains 90.3 % (9.6 %) of the variance contained in $V'_{G \text{ SIM P}(z)}$. The resulting transport variations are denoted as $V'_{G \text{ EOFs}}$ or $T'_{G \text{ EOFs}}$.

Upper-ocean geostrophic transport variations, T'_G , were then calculated by vertically integrating the approximated V'_G profile from $z_3=-1130$ m up to the surface.

$$T'_G(t) = \int_{z_3}^0 V'_G(z, t) dz \quad (5)$$

Using the first method, z_3 is defined as the ‘level of no motion’ ($V'_G(z_3) = 0$), whereas for the second method $V'_G(z_3)$ might vary with time.

Finally, AMOC transport variations (T'_{AMOC}) can be derived by adding local Ekman transport anomalies T'_{EK} .

$$T'_{AMOC}(t) = T'_G(t) + T'_{EK}(t) \quad (6)$$

The latter can efficiently be estimated from the zonal component of the wind stress, τ_x , at 11° S according to

$$T_{EK}(t) = - \int_{x_{WB}}^{x_{EB}} \frac{\tau_x(x, t)}{\rho_0 \cdot f} dx \quad (7)$$

and subtracting the temporal average.

In the following, all mean transports are presented together with the standard error $SE = \sigma / \sqrt{N/n_d}$, where σ is the standard deviation and n_d the decorrelation time scale of the respective time series of length N .

Annual and semi-annual harmonics for all pressure time series (section 2.5.1) are presented together with uncertainties for their amplitudes, which were derived by low-pass filtering the pressure time series with a cutoff of 170 days and subsequently calculating the 95th percentile of the deviations from the derived annual and semi-annual harmonics for every day of the year.

Following the observational strategy (Fig. 6), BPRs at least at four different locations (two depth levels) are required to derive basin-wide geostrophic transport variations in the upper 1130 m of the water column. While five recorders were in place over the period 05/2014-10/2015, no BP measurements at 300 m depth off Brazil are available before 05/2014 and none at all off Angola since 11/2015. In this study, we found combined annual and semi-annual cycles explaining 44-61 % of the variance in the daily BP time series at the eastern boundary and 18-24 % of the variance at the western boundary (see section 2.5.1). Despite the smaller numbers at the western boundary, the annual and semi-annual cycles are still the dominant signals in all pressure time series at 11° S. Therefore, we decided to “replace” the missing sensors with the combined annual and semi-annual harmonics derived from the available BP time series. This means, for example, that the geostrophic transport after 11/2015 is derived from the differences between measured BP variations at the western boundary and repeated annual and semi-annual harmonics – as derived from earlier years – at the eastern boundary. We derive confidence in our method from the comparison of the observed BP variations with variations in the simulated BP time series and in the SLA time series off Angola, both covering longer periods.

2.4.2. Using the OGCM INALT01 as a ‘testing area’

To validate our strategy for the computation of AMOC variations from the BP observations and to better understand the observed seasonal variability, we simultaneously analyzed the output of the

OGCM INALT01 (see section 2.3). In INALT01 we can diagnose AMOC variations, $T'_{AMOC\ SIM}$, from the velocity field using Eq. (1) and Eq. (2), i.e. by directly integrating the simulated meridional velocity component at 11°S horizontally across the basin and vertically from 1130 m to the surface. The zonally integrated Ekman transport $T'_{EK\ SIM}$ at 11°S is derived with Eq. (7) from INALT01 wind stress. According to Eq. (6) the simulated upper-ocean geostrophic transport anomaly $T'_{G\ SIM}$ is then $T'_{AMOC\ SIM} - T'_{EK\ SIM}$.

Alternatively, we can derive $T'_{G\ SIM\ P(z)}$ according to our observational strategy based on BP fields from the modelled hydrographic fields and sea level. The model pressure field is given by

$$p(x, z, t) = g \cdot \int_z^0 \rho(x, z', t) dz' + g \cdot \rho_0 \cdot \eta(x, t) \quad (8)$$

with g being the acceleration of gravity, ρ the seawater density as function of z and η the sea level. Taking the BP along the continental slopes (at each depth level) of Brazil and Angola from Eq. (8), the simulated upper ocean geostrophic transport anomalies, $V'_{G\ SIM\ P(z)}$ and $T'_{G\ SIM\ P(z)}$, can be derived from the pressure differences across the basin using Eq. (3) and Eq. (5), respectively. Under the assumption, that ageostrophic non-Ekman velocities are negligible, $T'_{G\ SIM}$ and $T'_{G\ SIM\ P(z)}$ should agree and particularly should show the same seasonal cycles.

Additionally, we test the two methods used to approximate the vertical structure of V'_G from the observations (see section 2.4.1): 1. Piecewise linear interpolation between values of $V'_{G\ SIM\ P(z)}$ at 0 m, 300 m, 500 m depth and a level of no motion at 1130 m depth –denoted as $V'_{G\ SIM\ Points}$ or $T'_{G\ SIM\ Points}$ in the following, and 2. Regression of the 1st and 2nd EOFs of $V'_{G\ SIM\ P(z)}$ onto the values $V'_{G\ SIM\ P(z)}$ at 0 m, 300 m, 500 m depth – deriving $V'_{G\ SIM\ EOFs}$ or $T'_{G\ SIM\ EOFs}$. These different transport estimates from INALT01 were used to validate the methods applied to the observations (see section 2.5.3). In section 2.5.4, we use INALT01 to identify relevant mechanisms of the seasonal AMOC variability at 11°S, including specifically a comparison of the seasonal variability of the NBUC transport derived from observations and INALT01. For the sake of simplicity, in INALT01, unlike for the calculations from observations, the NBUC transport was calculated above a fixed depth of 1130 m and west of 34.55°W.

2.5. Results

2.5.1. Ocean pressure variability at 11°S

All of the ocean pressure time series in this study, i.e. at the surface from SLA (Fig. 5 (a, b)), at 300 m and 500 m depth from the BPRs (Fig. 4 (b)), at the western or eastern boundary, are dominated by seasonal variability. The corresponding periodograms all exhibit pronounced peaks at periods of the annual and semi-annual cycles (colored curves in Fig. 7).

The main focus here is on seasonal variability, however there are some other interesting peaks in the periodograms indicating energy on intra-seasonal and interannual time scales. Off Brazil, variability at a period of 70 days (Fig. 7 (c, d)) is very likely related to the DWBC eddies described by Dengler et al. (2004), which are thought to dominate the DWBC flow at 11°S and influence the upper water column as well (e.g. Schott et al., 2005). The periodograms of SLA at the eastern boundary (Fig. 7 (b)) exhibit peaks at 90 days, 120 days and 2 years. Variability at periods of 90 days and 120 days were also observed by Kopte et al. (2018) in velocity time series from moored observations off Angola and are likely associated with the passage of CTWs. Based on numerical experiments, Bachèlery et al. (2016) showed that SLA variability along the African coast is on intra-seasonal time scales ($T < 105$ days)

primarily driven by local atmospheric forcing, while at periods >120 days it can mostly be explained by equatorial forcing. Further, Polo et al. (2008) suggested that part of the intra-seasonal variability is related to year-to-year variations of the seasonal cycle. Interestingly, the OGCM INALT01 does reproduce the spectral peaks at 2 years, 120 days and 90 days in the SLA off Angola, but not the 70 days period observed in any of the BP time series.

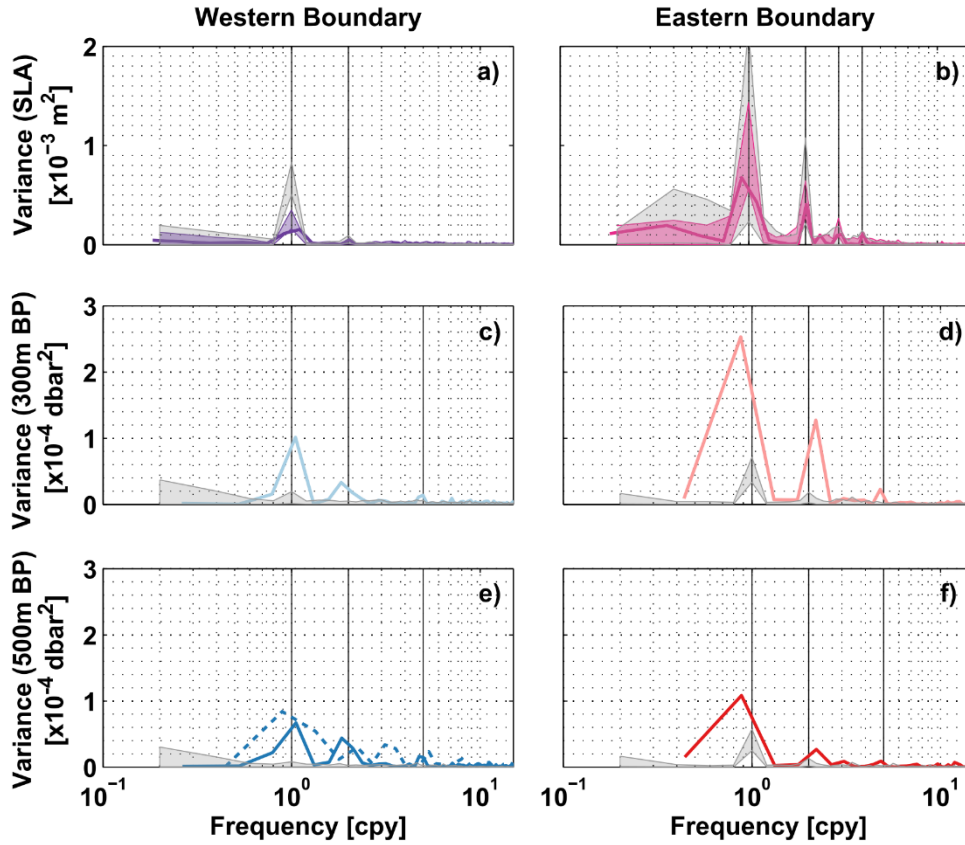


Figure 7 Periodograms of (a, b) SLA, (c, d) BP at 300 m and (e, f) BP at 500 m depth –from observations (colored), and from the INALT01 model (grey). In (a, b) bold solid curves show periodograms calculated from SLA data over the period 2013-2018. The transparent envelopes are an estimate for interannual variations, specifically, the minimum and maximum ranges of periodograms calculated for 5-year windows running through the full available period 1993-2018. In (c, d, f) bold solid curves show periodograms calculated from the individual BP time series available at 11°S. In (e) the solid curve represents KPO 1135 and the dashed curve KPO 1109 (two co-located sensors covering different periods; see Table 1). Grey shading in all panels gives the minimum and maximum ranges of periodograms for SLA and BP time series derived from the INALT01 model calculated for 5-year windows running through the full available period 1978-2007. Frequency is given in ‘cycles per year’. Black vertical lines mark the frequencies of the annual and semi-annual cycles, as well as periods of 120 and 90 days in (b) or 70 days in (c, d, e, f).

We found the relative importance of seasonal variability to be most pronounced near the surface off Angola in both, the observations and the model (Fig. 7). The combined annual and semi-annual harmonics of the observed pressure time series explain most of the variance there – 61 % at the surface, 58 % at 300 m depth, 44 % at 500 m depth – and their amplitudes decrease with depth. To make this statement we converted SLA variance into pressure variance using the hydrostatic equation. The combined annual and semi-annual harmonics at the eastern boundary (Fig. 8 (b, d, f)) show a similar structure at different depth with maxima in austral autumn and spring, and a minimum in winter. Nevertheless, the phases of the annual and semi-annual cycles change with depth at different rates (Fig. 9). With a phase shift of about 5 months, the annual harmonics at the surface and 500m depth are almost out-of-phase. The semi-annual harmonic is rather in-phase peaking about 1.5 month earlier at depth. This difference in the phase changes with depth can be associated with CTWs of certain

baroclinic modes. Kopte et al. (2018) associated the annual and semi-annual cycles of the alongshore velocity from the mooring at 11°S with basin-mode resonance in the equatorial Atlantic of the fourth and second baroclinic modes, respectively (Brandt et al., 2016). Corresponding CTWs propagate along the African coast towards 11°S thereby impacting the local velocity and pressure fields.

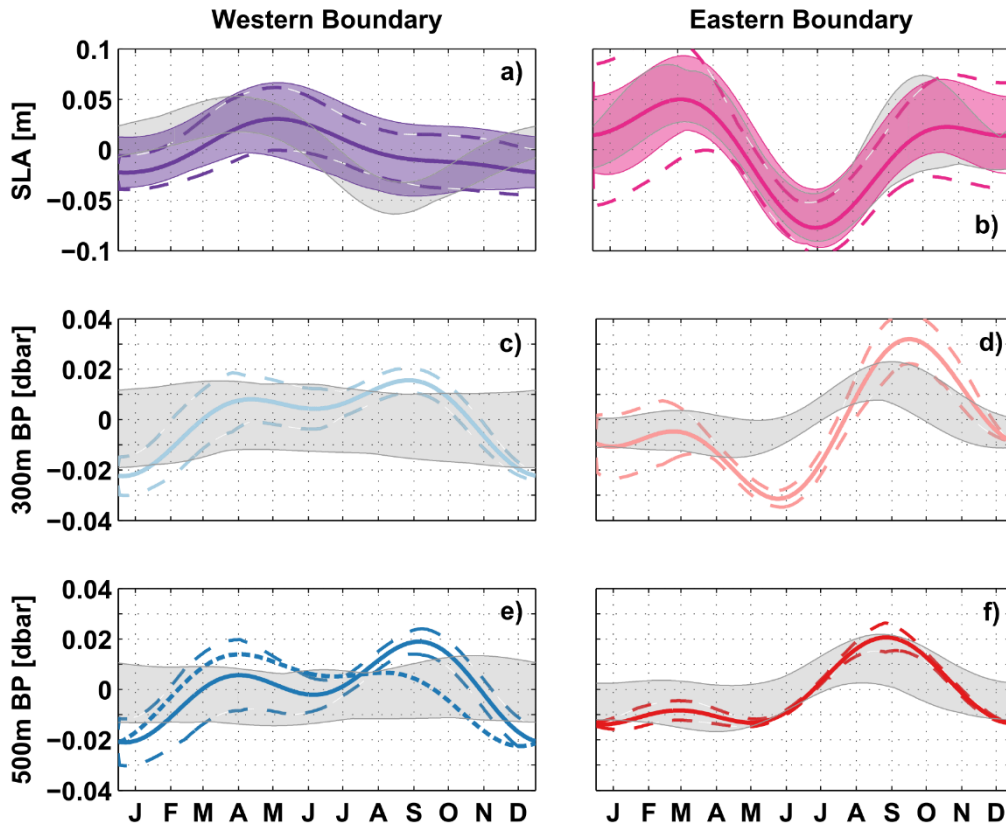


Figure 8 Combined annual and semi-annual harmonics calculated for (a, b) SLA, (c, d) BP at 300 m and (e, f) BP at 500 m depth. Line styles and color coding are the same as in Fig. 7. Additionally, dashed envelopes around the solid curves give uncertainties for the amplitudes of the harmonics. These are calculated by 170-days low-pass filtering the pressure time series and then subsequently the 95th percentile of the deviations from the derived annual and semi-annual harmonics for every day of the year.

At the western boundary (Fig. 8 (a, c, e)), the seasonal variability of the observed pressure time series is less pronounced. The combined annual and semi-annual harmonics explain only 12 % of the total variance at the surface and are barely different from zero, considering the uncertainty estimate for the amplitude. Seasonal variability of the surface pressure is decoupled from the pressure variability at depth, which supports the undercurrent character of the NBUc. The BP measurements at 300 m and 500 m depth, which are both located in the depth range of the NBUc, have annual and semi-annual harmonics of similar amplitude and phase (Fig. 8 (d, f)). The phase of the annual harmonic changes by 2 months between the surface and 300 m depth, the semi-annual harmonic by ~1 month and both peak later at depth (Fig. 8 (b, d)). At depth, seasonal pressure variations also become more important - at 500 m depth, for example, the annual and semi-annual harmonics explain up to 29%. We found similar results for 2-year subsets of the western boundary BP time series.

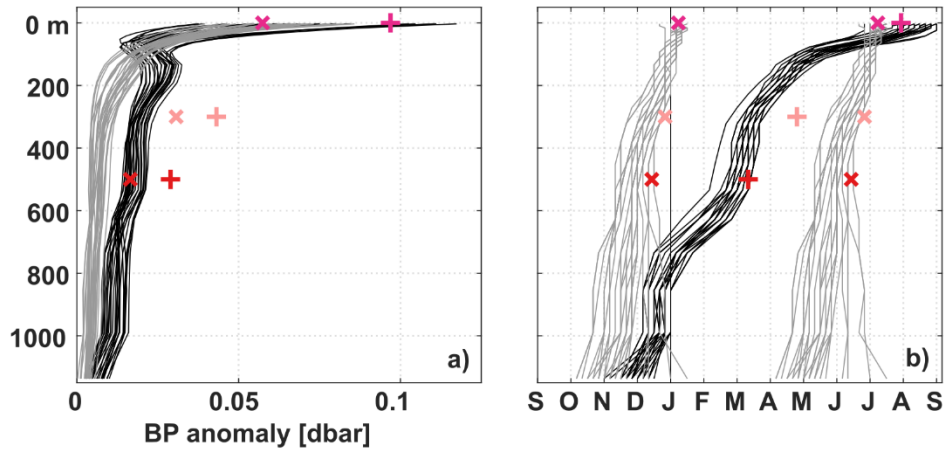


Figure 9 (a) Amplitudes and (b) phases of the minima of the annual (pluses and black curves) and semi-annual (crosses and grey curves) harmonics of the pressure anomalies at the eastern boundary along 11°S. Markers represent estimates from the observations (2013-2018) at 0m, at 300m, 500m, the curves show estimates calculated from INALT01 for 5-year windows running through the period of available data (1978-2007).

Annual and semi-annual harmonics of the individual pressure time series simulated in the INALT01 model (grey shading in Fig. 8) agree quite well with the observations regarding the timing of the maxima and minima. On the other hand, there are large differences in the amplitudes: The model tends to overestimate the annual harmonic at the surface and generally underestimate seasonal variability at depth - especially at the western boundary the seasonal cycle of the simulated BP at 300 m and 500m depth is almost non-existent.

In summary, for the seasonal variability at 11°S we observed that near the surface eastern boundary pressure variations prevail, whereas at 500 m depth the western and eastern boundary pressure variations are of similar importance. In the INALT01 model, the eastern boundary pressure variations dominate even more over western boundary ones.

2.5.2. Wind stress variability

Prevailing winds along 11°S are from southeast, which results in a mean meridional Ekman transport toward south. Using wind stress derived from ASCAT for the period 2013-2018 the mean and standard error of the meridional Ekman transport amounts to -11.7 ± 0.9 Sv and for the full available period 2007-2018 to -11.8 ± 0.6 Sv. The mean and standard error of the meridional Ekman transport derived from INALT01 wind stress amounts to -10.7 ± 0.3 Sv. Zonal wind stress in the tropical South Atlantic varies on different time scales, but is clearly dominated by seasonal variability. Periodograms of the Ekman transport based on ASCAT and INALT01 wind stress (Fig. 10 (a, b)) both show the strongest peaks at the frequency of the annual cycle. Note, that the two products cover very different periods and that their periodograms both also hint towards longer-term variability, whenever considering the full records.

The zonal wind stress anomalies at 11°S for the two analyzed wind products for the overlapping years 2008-2009 (Fig. 10 (c, d)) agree in the following characteristics: Seasonal wind stress variability is more pronounced in the western part of the basin than in the eastern part. Across the whole width of the basin, the zonal wind stress anomalies along 11°S are typically eastward (positive) in January to March – resulting in a weaker basin-wide southward Ekman transport. In austral winter zonal wind stress anomalies are rather westward (negative) and the southward Ekman transport is strongest - changing again towards the end of the year. For both wind products, the Ekman transport across 11°S is mainly

governed by the seasonal cycle of the southeasterly trade winds (e.g. Philander & Pacanowski, 1986). However, there are also recognizable differences between both products: For 2008-2009, the mean and the monthly standard deviation of the Ekman transport at 11°S (not shown) are about 0.5 Sv larger for ASCAT than for INALT01, respectively. Wind stress anomalies along 11°S reveal differences in its spatial structure, as well as in the course and amplitudes of its seasonal cycle (Fig. 10 (c, d)).

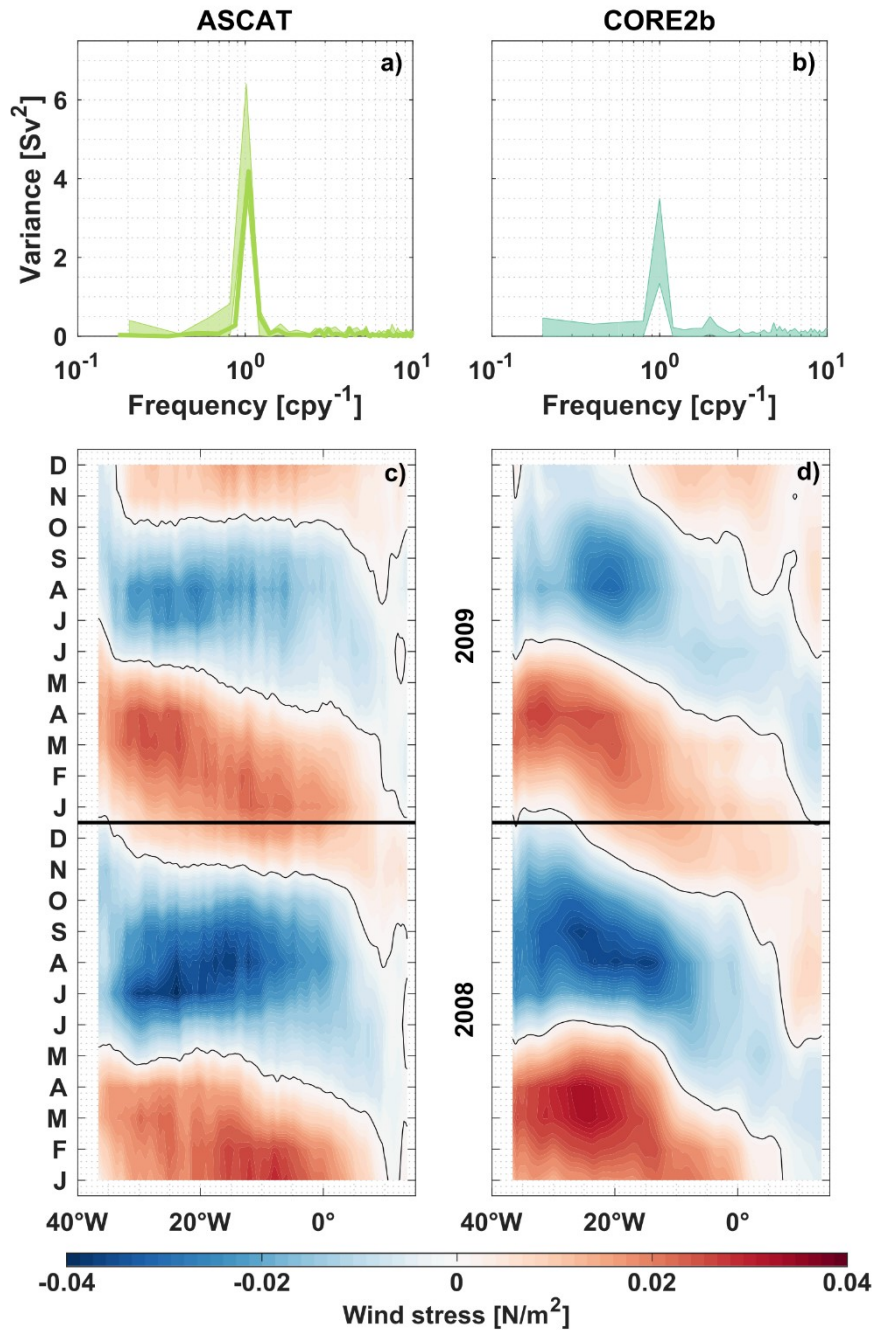


Figure 10 (a, b) Periodograms of the Ekman transport at 11°S, derived from ASCAT (a) and INALT01 (b) wind stress. The bold curve in (a) is calculated for the period 2013-2018. Transparent envelopes in (a, b) give an estimate for interannual variations, specifically the minimum and maximum ranges of periodograms calculated for 5-year windows running through the full available time series of ASCAT (2008-2018) and INALT01 (1978-2009). Frequency is given in 'cycles per year'. (c, d) Hovmöller diagrams of the ASCAT (c) and INALT01 (d) zonal wind stress anomalies along 11°S for the overlapping years 2008-2009. Red (blue) colors in (c, d) imply eastward (westward) wind stress anomalies.

2.5.3. Seasonal variability of the AMOC components at 11°S

As described in the methods, we were able to estimate AMOC transport variations in the tropical South Atlantic from BP measurements over the period 2013–2018. Figure 11 displays the derived time series of T'_G , T'_{EK} and the sum of both components T'_{AMOC} at 11°S. The different versions of T'_G derived from 4 BPRs or from 2–3 BPRs complemented with the combined annual and semi-annual harmonics (Fig. 11 (a), see section 2.4.1) show a general good agreement within the overlapping period. In the following sections, we analyzed the combined time series of $T'_{G\ EOFs\ 2\ BPRs}$ (07/2013 to 05/2014), $T'_{G\ EOFs\ 4\ BPRs}$ (05/2014 to 11/2015) and $T'_{G\ EOFs\ 2\ BPRs}$ (11/2015 to 03/2018; compare Fig. 11 (a)).

While from the BP observations we could only derive anomalies of T_G , in INALT01, however, we could also calculate mean values: The AMOC transport at 11°S based on the INALT01 velocity field averaged over the whole model run (1978–2007) is $T_{AMOC\ SIM} = 14.1 \pm 0.5$ Sv (mean and standard error). This is within the uncertainty range of 3 Sv for the AMOC estimate of 16.2 Sv derived from a hydrographic ship section along 11°S in 1994 (Lumpkin & Speer, 2007).

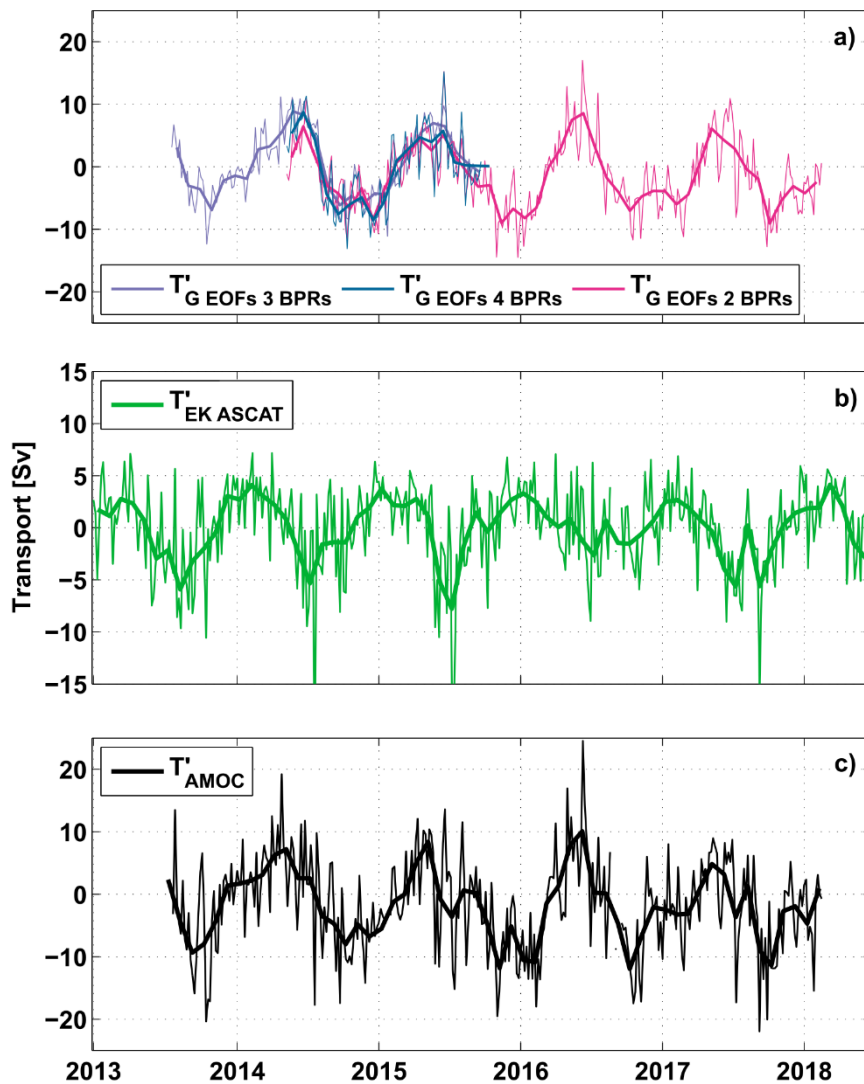


Figure 11 Anomaly time series at 11°S of (a) the upper-ocean geostrophic transport ($T'_{G\ EOFs}$), (b) the Ekman transport derived from ASCAT wind stress ($T'_{EK\ ASCAT}$), and (c) the resulting AMOC transport (T'_{AMOC}). Thin lines represent daily values in (a) and 5-daily values in (b, c), bold curves represent monthly averages. Different colors in (a) indicate transport calculations for different sets of BPRs – 4 BPRs (petrol), 3 BPRs (500 m WB, 300 m EB, 500 m EB; purple) and 2 BPRs (300 m & 500 m WB; magenta) combined with the annual and semi-annual harmonics derived from the fully equipped period (05/2014–10/2015; see section 2.4.1).

Both, the T'_G and T'_{EK} time series and, hence, also T'_{AMOC} , show variability on different time scales, but are clearly dominated by seasonal variability. Mean seasonal cycles of T'_G , T'_{EK} and T'_{AMOC} from observations and INALT01 are shown in Fig. 12.

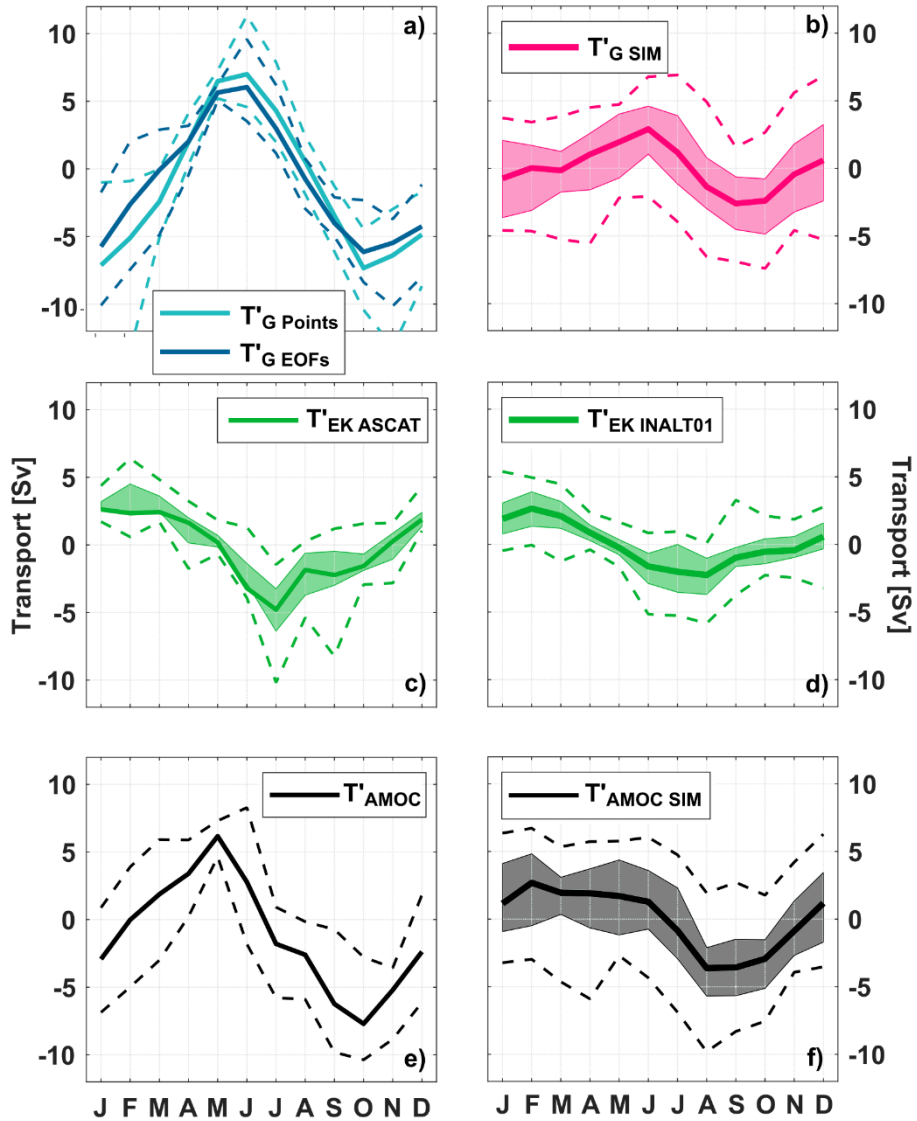


Figure 12 Mean seasonal cycles of T'_G (a, b), T'_{EK} (c, d) and T'_{AMOC} (e, f) from observations (a, c, e) and the INALT01 model (b, d, f). Upper-ocean geostrophic transport anomalies, $T'_{G\ Points}$ (cyan curve) and $T'_{G\ EOFs}$ (petrol curve), are derived from SLA and BP observations (as described in section 2.4.1) and averaged over the period 2013-2018, while $T'_{G\ SIM}$ is derived from the INALT01 model velocity fields (as described in section 2.4.2) and averaged over the period 1978-2007. T'_{AMOC} in (e) was derived using $T'_{G\ EOFs}$. For the 30-year INALT01 run (b, d, f) and the 12-year ASCAT wind time series (c), transparent envelopes represent an estimate for interannual variations, specifically, the minimum and maximum range of mean seasonal cycles calculated for 5-year windows running through the respective available periods. The dashed curves in all panels show the absolute range of possible minima and maxima per months.

T'_{EK} is characterized by a maximum southward transport in June-August and minimum southward transport in January-March, with the individual extrema slightly varying between ASCAT and INALT01 (Fig. 12 (c, d)). Note again, that both products are averaged over different periods. The peak-to-peak amplitude of seasonal Ekman transport variations is 7.1 Sv for ASCAT wind stress (2007-2018; Fig. 12 (c)) and 4.9 Sv for INALT01 wind stress (1978-2009; Fig. 12 (d)). The seasonal cycles may vary from year to year as well as on longer time scales. Here, such variations are, for example, estimated with the

range of mean seasonal cycles calculated for running 5-year subsets of the available wind stress data: While the timing of the seasonal cycle of T'_{EK} is rather stable between different periods, the peak-to-peak amplitudes have a range of 6-11 Sv for ASCAT and 2-8 Sv for INALT01.

The observed upper-ocean geostrophic transport anomaly (T'_G) shows a maximum northward transport in June, while minima occur in October and January with a weak secondary maximum in December (Fig. 12 (a, b)). The two estimates, $T'_{G\ Points}$ and $T'_{G\ EOFs}$, referring to the two different methods, agree well in the timing of minima and maxima (Fig. 12 (a)). However, the amplitude of the seasonal cycle of $T'_{G\ EOFs}$, which we consider to be the more realistic solution in the following, is about 2 Sv smaller than the corresponding amplitude of $T'_{G\ Points}$. A possible explanation for the difference between the two estimates based on observations is given below.

Nevertheless, the seasonal cycles of both estimates based on observations, $T'_{G\ Points}$ and $T'_{G\ EOFs}$, are substantially more pronounced than that of $T'_{G\ SIM}$ derived directly from the velocity fields of the 30-year model run (Fig. 12 (b)). The peak-to-peak amplitude of the seasonal cycle of $T'_{G\ SIM}$ calculated over 30 years is 5.5 Sv, while amplitudes can range between 2-10 Sv when calculated for 5-year subsets. The peak-to-peak amplitude of $T'_{G\ EOFs}$ calculated over the observed 4.5 years is 12.2 Sv and thus larger than the model range. Even when comparing the total range of possible seasonal cycles obtained by considering only single years, the observed values are just out of the range of the simulated values. Regarding the timing of minima and maxima, the observed and simulated seasonal cycles of T'_G agree quite well (cf. Fig. 12 (a, b)). The larger peak-to-peak amplitudes of the seasonal cycle of T'_G from observations (cf. Fig. 12 (a, b)) as well as the ASCAT Ekman transports (cf. Fig. 12 (c, d)) result in a larger seasonal cycle of T'_{AMOC} with a peak-to-peak amplitude of 13.9 Sv compared to $T'_{AMOC\ SIM}$ (cf. Fig. 12 (e, f)), which is 6.3 Sv calculated over 30 years and can be as large as 10.5 Sv when calculated for 5-year subsets.

In order to test our observational strategy, we compared the upper-ocean geostrophic transport anomaly derived directly from the simulated meridional velocity component ($T'_{G\ SIM}$) to the one being derived from simulated BP time series. Using the full vertical resolution of the model when deriving $T'_{G\ SIM\ P(z)}$, we obtained good agreement with $T'_{G\ SIM}$ as expected (Fig. 13 (a) and b). Reducing the vertical resolution to the depths of the pressure observations at 0 m, 300 m, 500 m depth and using piecewise linear interpolation between those and a 'level of no motion' at 1130m ($V'_{G\ SIM\ Points}$; $T'_{G\ SIM\ Points}$; Fig. 13 (c, d)), we found this method to miss certain parts of the vertical structure of $V'_{G\ SIM\ P(z)}$, and with that, to substantially overestimate the peak-to-peak amplitude of the seasonal cycle of $T'_{G\ SIM\ P(z)}$ by 6 Sv (Fig. 13 (d)). While in the model a strong seasonal cycle is confined to the near-surface ocean, linear interpolation between the surface and 300m artificially increases the seasonal signal in the layer from 50 to 250 m depth. To improve the approximation, another method was applied that is based on a regression of the 1st and 2nd dominant vertical structure functions of $V'_{G\ SIM\ P(z)}$ onto the values at the 3 depth levels of pressure observations at 0 m, 300 m, 500 m depth ($T'_{G\ SIM\ EOFs}$; $V'_{G\ SIM\ EOFs}$, Fig. 13 (e, f)) thereby relaxing the no-flow condition at 1130 m depth. As the first two EOFs of $V'_{G\ SIM\ P(z)}$ explain 99 % of the variance contained in $V'_{G\ SIM\ P(z)}$, $T'_{G\ SIM\ EOFs}$ agrees well with $T'_{G\ SIM\ P(z)}$ in INALT01 (Fig. 13 (f)). However, the comparison of the observed BP time series with the BP simulated in INALT01 (Fig. 7), shows that the model tends to underestimate the seasonal pressure variability at depth (see section 2.5.1) leaving some uncertainty regarding the vertical structure of V'_G in reality.

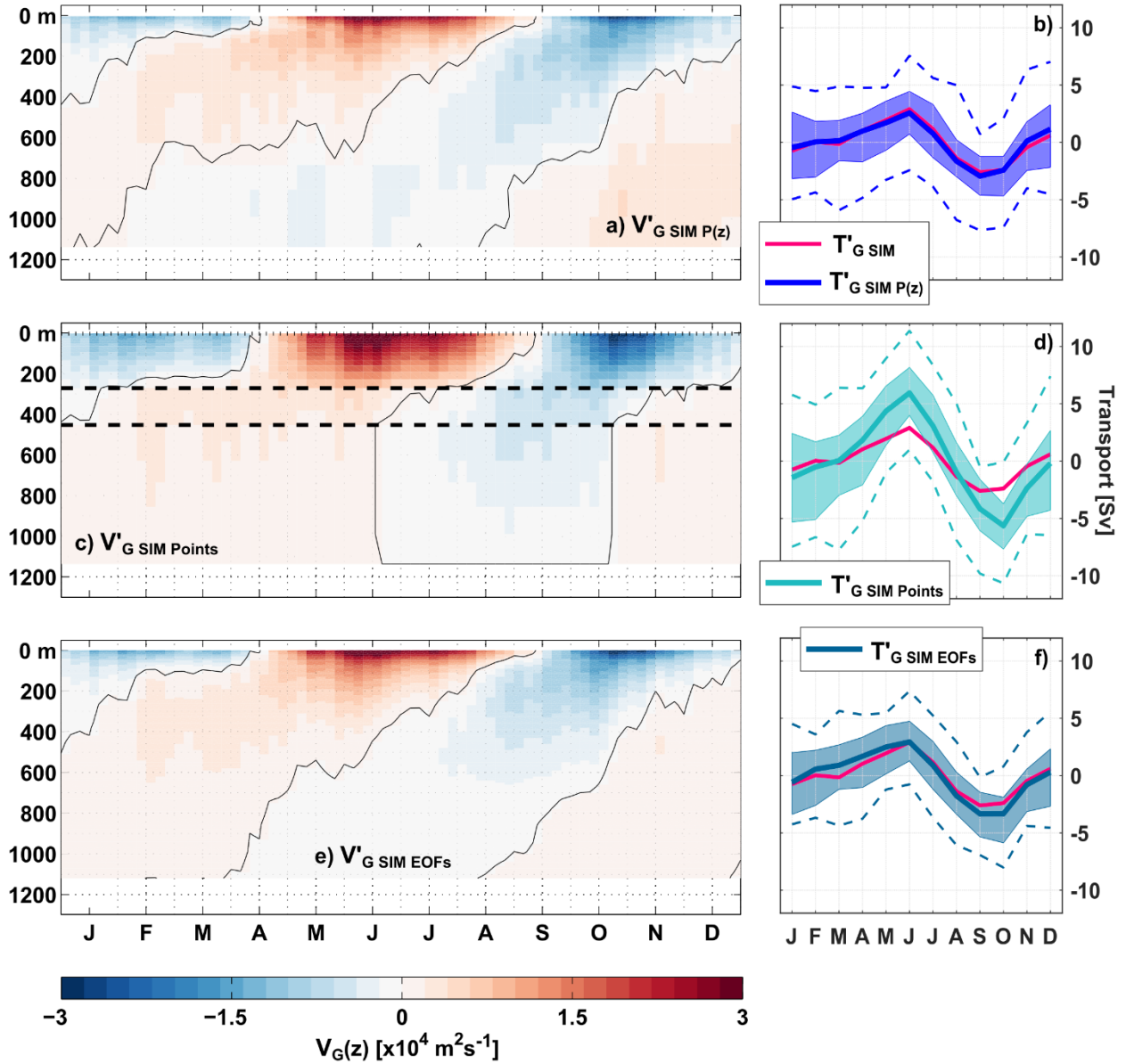


Figure 13 Mean seasonal cycles of the geostrophic transport per unit depth, V'_G (a, c, e) and the upper-ocean geostrophic transport T'_G (pink curves; (b, d, f)) from INALT01. $V'_{G\ SIM\ P(z)}$ (a) and $T'_{G\ SIM\ P(z)}$ (blue curve; (b)), were calculated using the full vertical profiles of BP. $V'_{G\ SIM\ Points}$ (c) and $T'_{G\ SIM\ Points}$ (cyan curve; (d)) were reconstructed by piecewise linear interpolation of V'_G between the 4 supporting points at 0, 300, 500, and 1130 m depth (black dashed lines in (c)) mark the depths of the BPRs); $V'_{G\ SIM\ EOFs}$ (e) and $T'_{G\ SIM\ EOFs}$ (petrol curve; (f)) by using the dominant vertical structure functions from INALT01. In (a, c, e) red (blue) colors show northward (southward) anomalies.

Figure 14 compares the mean seasonal cycles of V'_G from observations for the two different methods. Using the vertical structure from the EOFs of $V'_{G\ SIM\ P(z)}$ from INALT01 does especially reduce the amplitude of the subsurface variability (50-200 m). In this depth range the transition from negative to positive transport anomalies also shifts from April to March. At larger depths, differences between both methods are the result from $V'_{G\ Points}$ being constrained by a level of no motion at 1130 m, while $V'_{G\ EOFs}$ is not. However, independent of the applied method, the peak-to-peak amplitude of the seasonal cycle of T'_G from observations (Fig. 12 (a)) remains to be substantially larger than that from INALT01.

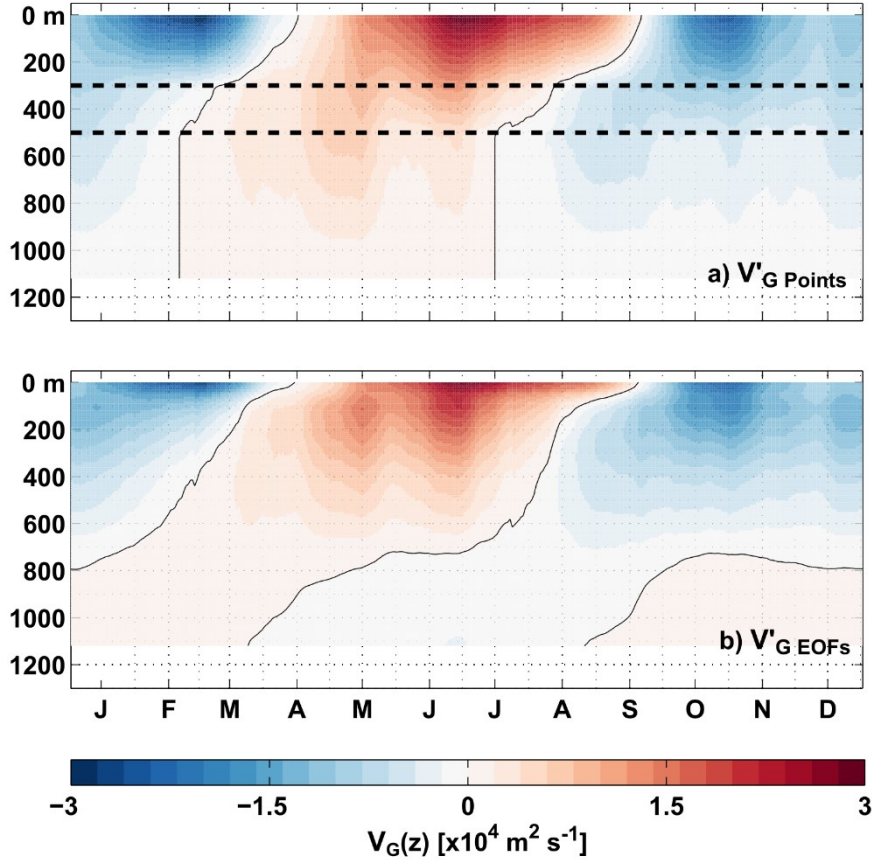


Figure 14 Mean seasonal cycle of the geostrophic transport per unit depth, V'_G , over the period 2013-2018, derived from observations at 11°S with two methods: (a) Piecewise linear interpolation between the 4 supporting points at 0, 300, 500 and 1130 m depth (black dashed lines mark the depths of the BPRs). (b) Reconstruction of V'_G by regression of the dominant vertical structure functions from the INALT01 model onto the values at the 3 depth levels of pressure observations at 0 m, 300 m, 500 m depth thereby relaxing the no-flow condition at 1130 m depth. Red (blue) colors show northward (southward) anomalies.

For the period 2013-2018, the geostrophic contribution to the seasonal cycle of the AMOC at 11°S, as we observed it, exceeds the Ekman contribution almost by a factor of 2 (cf. Fig. 12 (a, c)). In INALT01, on the other hand, averaged over the 30-year model run, the geostrophic and Ekman contributions are of similar magnitude (Fig. 12 (b, d)). The seasonal cycles of both contributions vary substantially between years (calculated for 5-year subsets of the model run) – e.g. 2-10 Sv for $T'_{G\ SIM}$ from INALT01, 2-8 Sv for T'_{EK} from INALT01 or 6-11 Sv for T'_{EK} from ASCAT - hence there is a modulation of the ratios of both contributions on interannual time scales. However, even when considering the uncertainties of the seasonal cycle of $T'_{G\ Points}$ or $T'_{G\ EOFs}$ (Fig. 12 (a)) and the range of possible mean seasonal cycles of $T'_{G\ SIM}$ calculated for subsets of the model run (Fig. 12 (b)), the observed values are significantly larger than simulated ones.

2.5.4. Dynamics of the seasonal cycle at 11°S

In order to better understand the mechanisms that set the seasonal cycle of T'_{AMOC} at 11°S, we investigated the longitudinal structure of the geostrophic velocity field and transport along that section in INALT01. We were able to distinguish three different regimes – the NBU, the Western Basin Interior and the Eastern Basin - all showing seasonal variability of similar magnitude (Fig. 15).

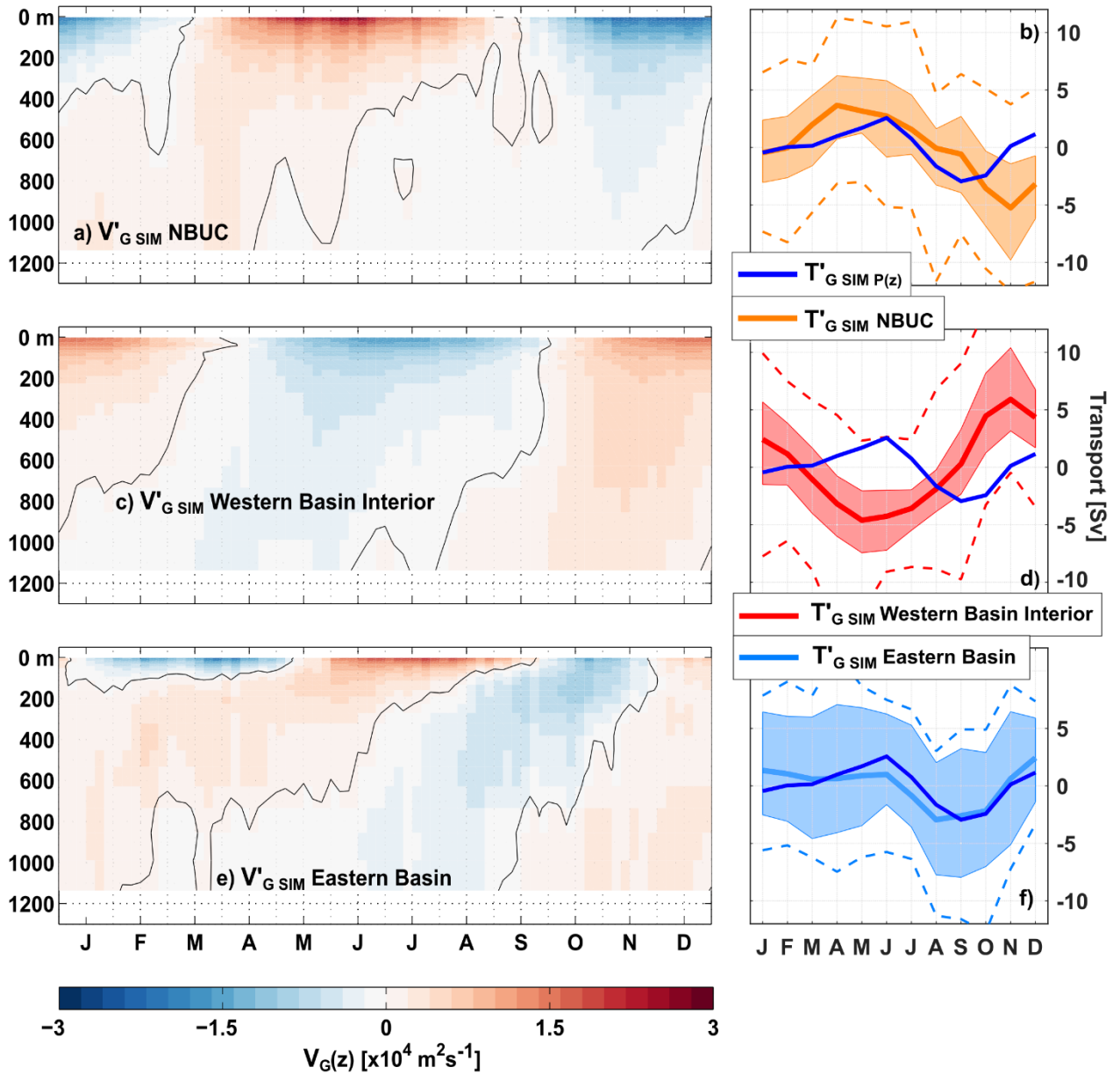


Figure 15 Mean seasonal cycle of the geostrophic transport per unit depth, $V'_{G\text{ SIM}}$ (a, c, e) and the upper-ocean geostrophic transport $T'_{G\text{ SIM}}$ (b, d, f) from INALT01. In all panels, V'_G and T'_G were calculated from the full vertical profiles (from the surface down to 1130 m) of the simulated pressure, but from pressure differences across different regions along 11°S : across the whole basin ($T'_{G\text{ SIM } P(z)}$; blue curves in (b, d, f)); between the Brazilian continental slope and 34.55°W ($V'_{G\text{ SIM } \text{NBUC}}$ in (a); $T'_{G\text{ SIM } \text{NBUC}}$ orange curves in (b)); between 34.55°W and 10°W ($V'_{G\text{ SIM } \text{Western Basin Interior}}$ in (c); $T'_{G\text{ SIM } \text{Western Basin Interior}}$ red curves in (d)); between 10°W and the Angolan continental slope ($V'_{G\text{ SIM } \text{Eastern Basin}}$ in (e); $T'_{G\text{ SIM } \text{Eastern Basin}}$ light blue curve in (f)). Transparent shading and dashed curves are the same as in Fig. 12.

The mean seasonal cycle of the NBUC, as calculated for the 30-year INALT01 model run, has its maximum in April, minimum in November and a peak-to-peak amplitude of 10 Sv (Fig. 15 (b)). Peak-to-peak amplitudes of up to 15 Sv can be found in 5-year subsets of the model time series. Having a mooring array installed off the coast off Brazil measuring the Western Boundary Current system there (e.g. Hummels et al., 2015; see section 2.2.4), allowed us to directly compare the seasonal variability of the NBUC in INALT01 with observations. The seasonal cycle of the NBUC in INALT01 agrees quite well with the seasonal cycle observed in recent years – regarding the peak-to-peak amplitude (7.6 Sv in 2000-2004 and 7 Sv in 2013-2018) and the timing of maximum and minimum transports (Fig. 16 (b)). During the earlier deployment period 2000-2004 there was a stronger semi-annual cycle creating a

secondary minimum in March, which was neither found in the observations during 2013-2018 nor in INALT01.

In INALT01, the contribution of the NBUC to the AMOC on seasonal time scales is largely compensated by the flow in the western basin interior. The seasonal cycle of the geostrophic transport per unit depth in the western basin interior is of similar strength and vertical structure, but opposing sign to the one of the NBUC (cf. Fig. 15 (a, c)). In the western basin interior, the vertically integrated upper-ocean geostrophic velocity is mainly associated with an annual harmonic and likely related to a strong seasonal cycle in the local wind stress curl (Fig. 17). The annual harmonic of the wind stress curl exhibits relatively large amplitudes over the region (10°W to 34.55°W) and a westward phase propagation (not shown).

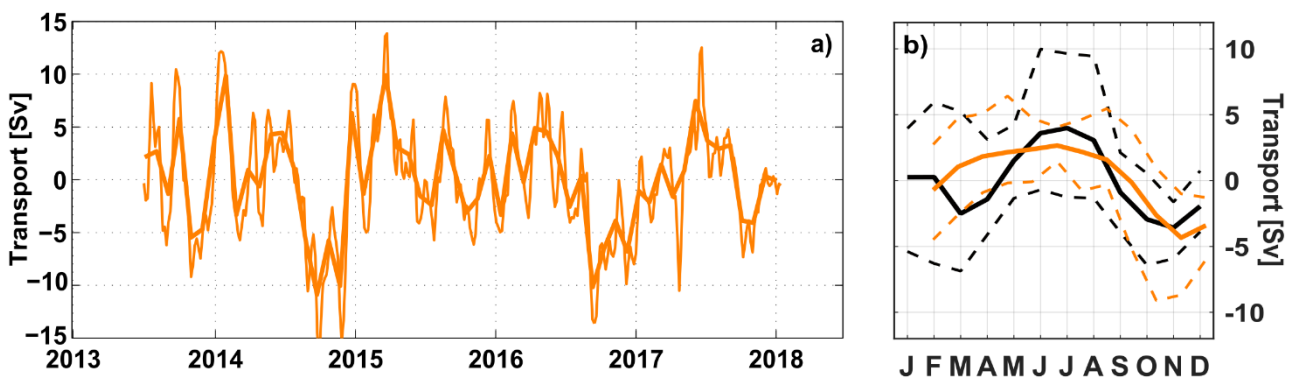


Figure 16 (a) Time series of NBUC transport anomalies (5-daily as thin curve, and monthly averages as bold curve) based on moored observations off Brazil (see section 2.2.4) updated from Schott et al. (2005) and Hummels et al. (2015). (b) Mean seasonal cycles of the NBUC transport anomalies averaged over the periods 2013-2018 (orange curve) and 2000-2004 (black curve). The thin dashed curves show the absolute range of possible minima and maxima per months for the periods 2013-2018 (orange) and 2000-2004 (black), respectively.

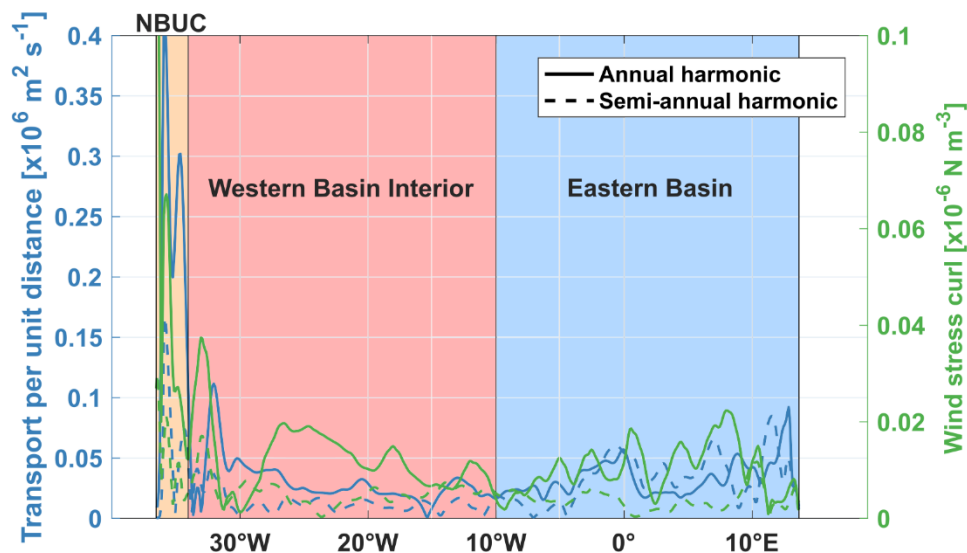


Figure 17 Amplitudes of the annual (solid curves) and semi-annual (dashed curves) harmonics of the vertically integrated upper-ocean geostrophic velocity in INALT01 (blue curves; left axis) and the INALT01 wind stress curl (green curves, right axis) along 11°S. Transparently shaded boxes highlight different regions – the NBUC (orange), the western basin interior (red) and the eastern basin (blue).

As the contributions of the NBUC and western basin interior seasonal cycles to the AMOC tend to cancel each other out, in INALT01, seasonal variability of the upper-ocean geostrophic transport at 11°S is mainly set in the eastern basin (Fig. 15 (f)). Both, the vertically integrated upper-ocean

geostrophic velocity and the wind stress curl (Fig. 17), exhibit strong seasonal variability throughout most of the eastern basin. However, the largest amplitudes of the annual and semi-annual harmonics of the vertically integrated upper-ocean geostrophic velocity are found near the eastern boundary, east of 12°E, where seasonal variability in the wind stress curl is weak.

From this analysis, we conclude that a compensation between the NBUC and western basin interior results in a major contribution of the upper-ocean geostrophic transport of the eastern basin to the AMOC transport on seasonal time scales. As described in section 2.5.1, however, the model tends to underestimate the seasonal pressure variability at 300 m and 500 m depth – especially at the western boundary. This leaves some uncertainty in the relative importance of western and eastern basin contributions to the seasonal AMOC variability in reality.

2.6. Summary and discussion

In this study, we used bottom pressure observations on both sides of the basin at 300 m and 500 m depth, combined with satellite measurements of sea level anomalies, different wind stress products and model results, to estimate the upper-ocean geostrophic and Ekman transport contributions to AMOC variability at 11°S over the period 2013-2018.

The use of bottom pressure measurements to compute basin-wide integrated northward transports is not straightforward: Firstly, the sensors experience instrumental drifts, which limits the BPRs capabilities to recover variability on longer time scales. Secondly, the deployment depth is not precisely known, which only allows the calculation of transport anomalies. We found the available BP time series at 11°S to be sufficiently long to investigate the seasonal variability in the region, but, clearly, longer time series will allow us to refine these estimates in the future.

At 11°S, seasonal variability is strong in most of the time series presented in this study. After removing tides with periods shorter than 35 days, the combined annual and semi-annual harmonics explain a large part of the variability at the eastern boundary – from 60 % at the surface to 44 % at 500 m depth. We found hints towards a baroclinic structure in the annual and semi-annual harmonics of the pressure time series at the eastern boundary (Fig. 9), which could be related to CTWs of specific baroclinic modes that can travel from the equator towards 11°S along the African coast thereby impacting the local pressure and velocity fields.

At the western boundary, seasonal pressure variability is weaker with its relative importance compared to other variability increasing with depth - the annual and semi-annual harmonics explain about 10 % of the variability at the surface and 30 % at 500 m depth. The seasonal variability of the zonally integrated geostrophic velocity anomaly in the upper 300 m is, therefore, mainly controlled by pressure variations at the eastern boundary, while at 500 m depth contributions from the western and eastern boundaries are similar. Annual and semi-annual harmonics at the western boundary also exhibit a vertical structure as seasonal variability at the surface is decoupled from the pressure variability at 300 m and 500 m depth. Based on geostrophic velocity fields from hydrographic measurements, studies like da Silveira et al. (1994) or Stramma et al. (1995) already stated that the WBC system at 11°S includes an energetic undercurrent, the NBUC, with weak or reversed flow above. From moored observations, Schott et al. (2005) showed strong gradients in the amplitude of the annual harmonic in the upper few hundred meters of the water column (their Fig. 14 (a)) suggesting a decoupling of the variability at the surface from the subsurface.

Over the period 2013-2018, the upper-ocean geostrophic transport variations derived from pressure differences across the basin, are dominated by seasonal variability – with a peak-to-peak amplitude of 12-14 Sv, depending on the method used to approximate its vertical structure. The peak-to-peak amplitude of the mean seasonal cycle of the Ekman transport is 7 Sv and of the resulting AMOC transport 14-16 Sv. For the Subtropics, recent estimates of the peak-to-peak amplitude of the mean seasonal cycle of the AMOC range from 4.3 Sv at 26.5°N (2004-2017; Frajka-Williams et al., 2019) to 13 Sv at 34.5°S (2014-2017; Kersalè et al., 2020).

The output of the OGCM INALT01 was compared to the observed characteristics of the seasonal cycles of the AMOC, its components as well as the NBUC. It reproduces the seasonal cycles of the NBUC as observed in recent years with current meter moorings and of the Ekman transport across 11°S as derived from ASCAT winds. However, this comparison also reveals model-observation discrepancies regarding seasonal variability in the bottom pressure fields and the resulting geostrophic transport variations:

- The INALT01 model tends to underestimate the seasonal bottom pressure variability at 300 m and 500 m, especially at the western boundary. This translates into the vertical structure of the simulated geostrophic transport variations, which is also used for the calculation of the observational estimate (method 2) adding to its uncertainty.
- In the observations, the geostrophic contribution to seasonal AMOC variability exceeds the Ekman contribution by almost a factor of 2, while in INALT01, averaged over the 30-year model run, or in earlier studies based on models (e.g. Zhao & Johns, 2014a), the contributions are similar. Even when considering the multi-year variations of the seasonal cycle of T'_G over 2013-2018 (Fig. 12 (a)) and the total range of possible seasonal cycles of $T'_{G\ SIM}$ calculated for subsets of the model run period 1978-2007 (Fig. 12 (b)), the observed values are significantly larger than the simulated values.
- The ratios of the NBUC and AMOC seasonal amplitudes are different between the observations (<1) and the model (>1).

In the model, seasonal upper-ocean geostrophic transport variability at 11°S is governed by the variability in the eastern basin. The seasonal cycle of the simulated upper-ocean geostrophic transport in the western basin becomes comparable small due to a compensation of the western basin interior and the NBUC transports. This could be explained by an almost equilibrium response of the circulation in the western basin at low baroclinic modes to the wind stress curl (e.g. Döös, 1999). Locally wind-forced annual Rossby waves would travel westward and after arriving at the western boundary directly force WBC variability. The seasonal variability in the eastern basin is instead forced by the local wind stress curl and, additionally, by Rossby waves radiated from the eastern boundary via poleward propagation of seasonal CTWs (e.g. Brandt et al., 2016; Kopte et al., 2018). Similar Rossby-wave radiation from the eastern boundary has been reported for the tropical North Atlantic (e.g. Chu et al., 2007) and proposed to be one of the main mechanisms for seasonal variations in the geostrophic transport there (e.g. Hirschi et al., 2006; Zhao & Johns, 2014a).

The compensation between the western basin interior and the NBUC on seasonal time scales found in INALT01 results in a minor contribution of the western basin compared to the eastern basin and limits the importance of the NBUC for AMOC variability on seasonal time scales. However, in this study we found that INALT01 tends to underestimate seasonal variability at 300m and 500m off Brazil. In two different model studies, Rodrigues et al. (2007) and Silva et al. (2009), related seasonal variability in the NBUC to seasonal variations in the bifurcation region of the South Equatorial Current. Thus, the phases of the annual and semi-annual harmonics of the NBUC may not simply be set by the response

to the local wind curl forcing in the western basin at 11°S, but may also depend on the wind curl forcing farther south and associated equatorward signal propagation along the western boundary.

We conclude that the seasonal variability of the geostrophic contribution to the AMOC at 11°S is mainly wind-forced, as it is modulated by oceanic adjustment to local and remote wind forcing. While some of the uncertainties of our analysis result from the technical aspects of the observational strategy or processes being not properly represented in the model, our results indicate, that uncertainties in the wind forcing are particularly relevant for AMOC estimates in the tropical South Atlantic. Differences between wind products are an important source of uncertainty for estimates of the AMOC and its variability. Especially, when comparing estimates of AMOC strength and variability between different projects, latitudes or from observations and models, the choice of wind product is crucial.

This study adds to the overall understanding of local and shorter-term AMOC variations, which is important for estimating the significance of long-term AMOC changes and, thus, for the detectability of its meridional coherence. To predict the long-term behavior of the AMOC and its impacts, continuous observations from purposefully designed arrays are required in different key locations. We would like to argue that the observational program at 11°S, if continued into the future, has potential for monitoring long-term AMOC changes. As the western tropical Atlantic is a crossroad for the different branches of the AMOC and a region with high signal-to-noise ratios, 11°S is a good place to monitor AMOC variations. Having a sustainable AMOC observing system there, linking northern and southern AMOC variability, would contribute to the general understanding of related mechanisms. There is potential to use the BPRs for investigating longer-term AMOC variability. While progress is made in solving the problems of bottom pressure sensors on longer time scales (e.g. Kajikawa & Kobata, 2014; Worthington et al., 2019), the advantage of our method is that the BPRs are less expensive and easier to deploy than full-height mooring arrays. Learning from the use of long-term PIES arrays at 47°N (Roessler et al., 2015) or 34.5°S (e.g. Meinen et al. 2018), we think that the travel times derived from the PIES installed off Brazil could add information to or reduce the uncertainty of our results. Additionally, we can fall back on more than 20 years of shipboard hydrographic measurements in the tropical South Atlantic – at the western (e.g. Hummels et al., 2015; Herrford et al., 2017) and eastern boundary (e.g. Tchipalanga et al., 2018). Ongoing work includes combining all of these hydrographic measurements to extend the time series of the WBC system and AMOC at 11°S back into the 1990s.

2.7. Acknowledgements

This study was funded by the Deutsche Bundesministerium für Bildung und Forschung (BMBF) as part of the projects RACE (03F0651B, 03F0729C, 03F0824C), SACUS (03G0837A) and BANINO (03F0795A), by the EU H2020 under grant agreement 817578 TRIATLAS project and by the Deutsche Forschungsgemeinschaft (DFG) through funding of Meteor cruises. We thank captains and crews of the R/V Meteor and R/V Sonne, as well as our technicians for the assistance during the shipboard and moored station work. Data sets described in section 2.2.1 are available through <https://doi.pangaea.de/> SLA data was distributed by the E.U. Copernicus Marine Service Information. INALT01 was developed at GEOMAR, with details of its configuration and access to data available at <https://www.geomar.de/forschen/fb1/fb1-od/ocean-models/inalt01>. J.V.D acknowledges funding from the Helmholtz Association and the GEOMAR Helmholtz Centre for Ocean Research Kiel (grant IV014/GH018). We would like to thank G. Krahnmann and M. Dengler for helpful discussions, and we are very grateful for the constructive comments by two anonymous reviewers.

3. A systematic evaluation of global wind products: Implications for the variability of the large-scale circulation in the Tropical South Atlantic

Abstract

Wind determines the momentum flux at the air-sea interface, wind stress, which plays a dominant role in driving the oceanic circulation. Good quality wind stress datasets are, therefore, essential to reliably analyze and simulate the ocean circulation and other climatic processes. Many different wind and wind stress products exist today - varying in their resolution or processing level and exhibiting substantial differences between them. Here, we present an assessment of a collection of different gridded surface wind products widely used within the oceanographic community. We compared their mean wind fields and variability on different timescales: All of the considered wind products capture the mean large-scale atmospheric circulation in the tropical Atlantic with overall differences among products of 10 % for wind speed and 5° in wind direction. We found regional differences in the mean wind fields to be in good agreement with previous studies. The ability of the different wind products to reproduce the tropical Atlantic Ocean variability observed with moored buoys depended on the considered timescale as well as the region or wind regime. The excessively used CORE II forcing dataset did not reproduce the observed intra-seasonal variability at any of the buoy locations, while scatterometer winds showed low correlations on interannual timescales. Most of the products revealed problems to reproduce the wind variability in the eastern tropical South Atlantic. Directly incorporating the moored buoy observations, winds derived from merging several platforms (CCMP) performed best at the buoy locations. We tested how the differences among products translate into derived variables (wind stress, wind stress curl, Ekman and Sverdrup transports) relevant for the large-scale circulation in the tropical Atlantic: The uncertainties from using different wind stress parametrizations can make up 15 % of the momentum flux into the ocean, which is of the same order of magnitude as the differences between individual products. For integral variables like the Ekman or Sverdrup transports across a certain latitude, the choice of wind product resulted in uncertainties of 15- 40 % depending on the latitude and considered timescale. The more recent, higher resolution products agreed on the seasonal to decadal wind stress variability in the tropical Atlantic, while older and coarser products (NCEPNCAR and CORE II) produced spurious wind stress variations, especially on decadal timescales. Systematic differences were found for indices involving spatial derivatives: The small-scale information contained in scatterometer winds, but not in the coarser reanalysis products, is emphasized in the spatial distribution of the wind stress curl. We found substantial inconsistencies regarding the seasonal variability of the wind stress curl in the eastern and western boundary regions at 11°S as well as multi-decadal variations of the wind stress curl throughout of the tropical South Atlantic in NCEPNCAR and CORE II compared to the other wind products. Taken together, our results highlight the importance of testing the sensitivity of derived results to the choice of wind product, an extended and more systematic validation of global products against observations, and the careful consideration or incorporation of large uncertainties in wind forcing products into ocean simulation experiments.

3.1. Introduction

The momentum flux at the air-sea interface, wind stress, plays a dominant role in driving the oceanic circulation. Surface wind stress provides energy for the ocean gyres through Ekman transport and pumping, the generation of planetary waves and vertical turbulent mixing. Good quality wind stress datasets are, therefore, essential for the investigation of many oceanographic as well as meteorological and climatic processes. However, before the late 1980s, there were no large-scale

measurements of wind stress over the ocean. Measurements of wind over the ocean, on the other hand, have been more common as they were much needed for marine weather forecast or shipping navigation.

A few decades ago, ocean surface winds were mainly derived from buoys or shipboard measurements, which were usually very sparse, unevenly distributed in time and space, suffered from long periods of missing data or a bad quality. Since the late 1950s, operational numerical weather prediction was able to provide global wind fields with a better resolution. Reanalysis products are the result of combining a numerical model with the assimilation of observations. Because of their complete space-time coverage and uniform resolutions, they are often used for global analyses or as the forcing for ocean models. However, all reanalysis products are limited by our knowledge of the physical processes represented in the underlying model and the availability of observations. While the newer generation of reanalysis products, with increased resolution and improved assimilation schemes, generally perform better than older ones (e.g. Taboada et al., 2019), there are some large differences between individual reanalysis products regarding long-term trends in wind speed (Torralba et al., 2017). Only with the advent of spaceborne scatterometers in the late 1980s it became possible to observe the ocean surface wind stress directly and on a near-global scale (e.g. Liu and Xie, 2006).

Although scatterometers measure the ocean surface roughness that is supposed to be in equilibrium with stress, they have been promoted as wind measuring instruments for the past decades (Liu et al., 2010). For further use, the inferred surface stress is typically converted into equivalent 10 m wind (e.g., Chelton and Freilich, 2005– assuming, for example, neutral atmospheric stability or neglecting the influence from ocean surface currents (e.g. Kelly et al., 2001). While over most of the ocean, the atmosphere is generally near neutral and ocean surface currents are small compared to wind speed, this can have effects on the accuracy of the wind estimates in the tropical oceans or cause spurious spatial derivatives (e.g. Kilpatrick and Xie, 2016). Efforts to synthesize wind observations from various satellite missions, although involving a number of other challenges, have been found to produce more consistent estimates of surface winds compared to buoy observations (e.g. Atlas et al., 2011).

Today, there are many different wind and wind stress products available to the scientific community. These products vary in their resolution or processing level and there are substantial differences between them. Several sources of errors and uncertainties can emerge from the process of wind field production – for example, during the assimilation of observations from different platforms or periods (e.g. Torralba et al., 2017; Hersbach et al., 2020) or from the methods used to correct towards other wind observations or to convert from one to another variable (e.g. Chelton and Freilich, 2005).

Unfortunately, in many studies, the uncertainties related to the choice of a single wind product are not discussed or the process that lead to the decision for or against a particular wind product is not clearly laid out. For example, differences between wind products can be an important source of uncertainty for estimates of the Atlantic Meridional Overturning Circulation (AMOC) and its variability. Within the AMOC observing community there is no common practice regarding the choice of wind product for estimates of the surface Ekman contribution to the AMOC (e.g. Frajka-Williams et al., 2019), which can be crucial when comparing estimates of AMOC strength and variability between different projects, latitudes or from observations and models.

Several recent studies, from the Physical Oceanography department at GEOMAR and related to the subproject TP1.1 of the BMBF projects RACE I, RACE II & RACE Synthesis, investigated different aspects of the wind-driven large-scale circulation in the Equatorial and South Atlantic: Analyzing the output of

a general ocean circulation model, Herrford et al. (2021) found the geostrophic contribution to the seasonal cycle of the AMOC at 11°S to be mainly wind-forced, as it is modulated by oceanic adjustment to local wind forcing along 11S as well as remote wind forcing on the equator. The results from their study indicate, that uncertainties in the wind forcing are particularly relevant for the resulting uncertainties of AMOC estimates in the tropical South Atlantic. The western boundary current at 11°S, the North Brazil Undercurrent (NBUC), is not only part of the basin-scale AMOC but also of the wind-driven tropical-subtropical ocean circulation (e.g. Schott et al., 2005). A model study by Rühls et al. (2015) showed that on decadal to multidecadal timescales buoyancy-forced changes in the basin-scale AMOC transport manifest themselves in the NBC farther downstream, however, found this relation also to be masked by a strong interannual to decadal wind-driven gyre variability of the NBC. Based on long-term moored observations at 23°W, Brandt et al. (2021) report the Atlantic Equatorial Undercurrent (EUC), which transports thermocline waters eastward along the equator, to have strengthened by more than 20 % over the decade 2008-2018. They related the strengthening of the EUC in the Atlantic to decadal changes in the Ekman divergence across the equator, specifically, a strengthening in the tropical North Atlantic trade winds affected by Atlantic multi-decadal variability. In agreement, Tuchen et al. (2020) found the total thermocline layer transport convergence in the equatorial Atlantic to exhibit a weakening from 2005 to 2010 followed by a strengthening until about 2015. Their analyses based on reanalysis data suggested interannual thermocline layer transport variations to be alternatingly dominated by contributions from the tropical North and South Atlantic.

Many ocean and climate models have shown to be sensitive to the choice of wind stress forcing. Differences in the wind forcing can, for example, be emphasized during the calculation of spatial derivatives, like wind stress curl and Ekman pumping, and result in discrepancies in the model output (e.g. Brahmananda Rao et al., 2008; He et al., 2016). Large systematic biases in coupled climate models such as the persistent warm sea surface temperature (SST) bias in the tropical Atlantic (e.g. Richter, 2015) have also been partly associated with biases in the wind stress. Analyzing a set of sensitivity experiments with prescribed wind stress, Voltaire et al. (2019) reported a leading role of wind stress biases in driving SST biases in the equatorial and south-eastern tropical Atlantic, even if the amplitudes of the SST biases were strongly model dependent. Variations in the tropical Atlantic SST, on the other hand, have been found to impact the climate on the adjacent continents via precipitation (e.g. Lübbecke et al., 2018) and are, therefore, of socio-economic importance. Studies comparing winds and wind stresses from different datasets are, therefore, necessary and can be very useful for several applications.

The purpose of this study is to develop a systematic evaluation of surface wind products. We compare a collection of wind products widely used within the oceanographic community regarding their mean wind fields and variability in the tropical Atlantic. Following the studies within RACE, we test how the differences between the products can translate into derived variables, which are relevant for the large-scale circulation in the region - such as the wind stress and wind stress curl, as well as Ekman transport, Ekman divergence or Sverdrup transport variations on seasonal to decadal time scales.

3.2. Gridded wind fields

In this study, we compare gridded fields of wind at 10 m (u_{10}, v_{10}) from 8 different products, commonly used within the ocean observing and modelling community. Any collection of wind datasets represents a choice from among a large number of different atmospheric data products, which all differ in their resolutions, covered periods, calibration procedures and are rarely independent of each other. Our collection of wind datasets includes reanalysis products, scatterometer winds, merged observations

and model forcing datasets. Table 2 lists these 8 products, their data sources, the periods they cover and their temporal and spatial resolutions. In the following, we review how the different wind products are derived, calibrated and connected, as well as their advantages and disadvantages.

3.2.1. Reanalysis products

Reanalysis products combine numerical models with the assimilation of several observations with the goal of creating a consistent dataset for a long period (e.g. Ramon et al., 2019). They allow for the analysis of variability in regions not at all or only sparsely covered by observations, but are limited by our knowledge of the physical processes represented in the respective model, uncertainties in the data assimilation procedure and the availability of observational data. Various institutes are generating a growing variety of useful reanalysis products, spanning longer time periods at increasing spatial and temporal resolutions.

In this study, we consider three widely used state-of-the-art global reanalysis products representing different generations of re-analysis products. One of the oldest reanalysis efforts is the National Centers for Environmental Prediction (NCEP)/National Center for Atmospheric Research (NCAR) Reanalysis 1 (**NCEPNCAR**; Kalnay et al., 1996; Kistler et al., 2001). Compared to other reanalysis products, NCEPNCAR Reanalysis 1 has the advantage of a time series of more than 70 years (1948-present). One disadvantage is the relatively low spatial resolution – it has a zonally uniform spacing of 1.875° and a meridionally nonuniform spacing that varies from 1.89° at the poles to 2.1° near the equator. NCEPNCAR Reanalysis 1 uses the NCEP global spectral model and a ‘frozen’ global data assimilation system from 1995 to produce a retroactive record of global atmospheric fields. NCEPNCAR assimilates observations from several sources such as weather stations, ships, buoys, oil rigs, radiosondes and aircrafts. Since 1979 vertical temperature soundings from television infrared satellites and cloud-tracked winds from geostationary satellites were also included (Kalnay et al., 1996). Although the NCEP model started to also assimilate ocean surface winds from scatterometers such as QUIKSCAT in 2002 – for example used for the newest NCEP product CFSR (Climate Forecast System Reanalysis; e.g. Saha et al., 2010), NCEPNCAR Reanalysis 1 was continued with the ‘frozen’ set of observations for assimilation (e.g. Fujiwara et al., 2017). The idea behind using a consistent model and methodology over the entire available period was to avoid climate jumps associated with changes in the data assimilation system which complicate analyses of longer time periods (Kalnay et al., 1996). However, NCEPNCAR Reanalysis 1 is still affected by changes in the observing systems before its setup in 1995, particularly by the introduction of the early satellite observations in 1979 (Kistler et al. 2001; Chelton & Freilich, 2005). Although relying on a model and data assimilation system that is more than 20 years old and having several major and minor problems (<https://psl.noaa.gov/data/reanalysis/problems.shtml>; latest access: 21 November 2020), NCEPNCAR Reanalysis 1 has been and is still used as ocean model forcing or for the analysis of climate variability in numerous publications.

At the same time as NCEPNCAR Reanalysis 1 was developed, other reanalysis products were conducted at the European Centre for Medium-Range Weather Forecasts (ECMWF): The early ERA15 (Gibson et al. 1997) was only run for a limited period (1979-1993) and then superseded by ERA-40 (Uppala et al., 2005), which covered a longer period (1957–2002) and also included a coupled atmospheric/wave model. ERA-Interim (**ERA-I**; Dee et al., 2011b; Berrisford et al., 2011), initially released in 2006, was conceived to provide a bridge between ERA40 and a more ambitious next-generation reanalysis envisaged at ECMWF. ERA-I covers the data-rich satellite era since 1979 and includes several corrections and improvements to the ERA40 system described in Dee et al. (2011b). A major step

forward was the use of 4-dimensional variational analysis, which makes more complete use of observations considering tendencies in the global atmospheric budgets of mass, moisture, energy, and angular momentum (Berrisford et al., 2011). ERAI is produced using a higher horizontal resolution (reduced Gaussian grid; approximately $0.7^\circ \times 0.7^\circ$), better data selection, quality control and bias correction – including a variational bias correction for satellite data. The ECMWF model started to assimilate scatterometer ocean surface winds from 1996 onwards: Data from the scatterometer onboard ERS-2 (European Remote sensing Satellites) is used from June 1996 to September 2011, data from the SeaWinds scatterometer onboard QUIKSCAT was used from February 2002 until November 2009 and data from the ASCAT instrument onboard MetOp-A is used since June 2007 (Hersbach, 2010a). Chelton & Freilich (2005), reported large improvements in the accuracies of the ERAI winds between 1997 and 2000 and only modest further improvements after 2002. However, changes in the assimilated observations or in the correction of model biases over time can introduce spurious low-frequency variations or trends in the reanalysis products that can be difficult to distinguish from actual signals of climate variability (e.g. Simmons et al., 2014, Torralba et al., 2017). More recent efforts focused on compensating for possible bias differences in ERAI resulting from model input changes since 2002 (e.g. Jones et al., 2017). In ERAI, the scatterometer winds were assimilated as equivalent neutral 10m wind vectors (ENWs), which are defined as the winds that would exist if the atmosphere were neutrally stable. As other reanalysis products employ different methodologies, this could also lead to differences in wind trends between products (e.g. Torralba et al., 2017). ERA surface winds have been found to exhibit systematic errors: They do not capture small-scale features that are dynamically important to the ocean and atmosphere - such as topographic or sea surface temperature gradients, and ocean current influences on surface winds (e.g. Risien and Chelton, 2008). Further, they are generally characterized by excessive mean zonal winds (westerlies) in the midlatitudes and too-weak mean meridional winds (trades) in the tropics (Chaudhuri et al., 2013; Belmonte Rivas & Stoffelen, 2019).

The production of ERAI stopped on 31st August 2019. About a decade after the release of ERAI, ECMWF implemented its successor **ERA5** (Hersbach & Dee, 2016; Hersbach et al., 2019). The new ERA5 reanalysis has a better representation of geophysical processes in the forecast model, more observational input into the data assimilation system, as well as a higher spatial ($0.25^\circ \times 0.25^\circ$) and temporal resolution. Compared to ERAI, ERA5 was found to perform better regarding the mean and transient wind errors described above, as well as wind divergence and wind stress curl biases (e.g. Belmonte Rivas & Stoffelen, 2019). As the total amount of data from ERA-Interim to ERA5 increased by a factor of ~80 (Hersbach et al., 2019), however, the usage of ERA5 poses a challenge to the community in, for example, downloading and maintaining copies of the data.

3.2.2. Wind observation products

We included wind data from two scatterometers - the SeaWinds scatterometer onboard **QUIKSCAT** and **ASCAT** onboard the EUMESAT Meteorological Operational (MetOP) Satellites. QUIKSCAT operated from 1999- 2009, while MetOp- A and MetOp-B were launched in 2006 and 2012, respectively, and are still in use. Spaceborne measurements made a broad-scale coverage and direct estimates of wind (stress) possible. Scatterometers directly or indirectly measure the roughness of the ocean surface, which is assumed to be in equilibrium with the surface wind stress (e.g. Liu et al., 2010). However, the different providers of scatterometer wind fields rather present ENWs at 10m. This is because direct measurements of ocean surface stress are sparse, which would be needed to develop a model function for converting radar backscatter to stress. A much larger data base exists to relate radar backscatter

to ENWs – in-situ data from moored buoys. If simultaneous measurements of air and sea surface temperatures, thus atmospheric stability, are available, it is straightforward to convert actual wind measured with anemometers attached buoys to ENWs at 10m (e.g. Chelton and Freilich, 2005), for example using the algorithms by Liu and Tang (1996) or by Fairall et al. (2003; Coare 3.0). As the atmospheric boundary layer is nearly neutrally stable over most of the world ocean, differences between the ENWs at 10 m and the actual winds at 10 m, thus, systematic errors from assuming neutral stability, are in the order of a few tenths of a meter per second or less (e.g. Mears et al., 2001; Risien & Chelton, 2008).

It is important to note that scatterometers measure winds relative to the horizontal movement of the ocean surface. Chelton et al. (2004) found timeseries from QUIKSCAT to show an influence of small-scale ocean processes on the wind stress. They identified different processes: Temperature differences between the atmosphere and the ocean can influence wind and wind stress via atmospheric boundary layer stability and turbulent mixing. Currents, which tend to have shorter length scales than winds, can have an effect on spatial derivatives such as the wind stress curl as well as the rate of wind work via differences between wind and current velocities (e.g. Duhaut & Straub, 2006). This is especially important in regions where surface current speeds are of similar order as or even exceed the surface wind speeds – like over energetic western boundary currents or in the tropical oceans (e.g. Kelly et al, 2001; Chelton & Freilich 2005). Hughes & Wilson (2008), argue that, although accounting for ocean currents results in rather small changes in wind stress, a surprisingly large effect is implied by the link between wind stress and ocean current on the wind work (about 20%) due to the effect of accounting for currents being negative definite. By analyzing the ocean current contribution to the mean differences between scatterometer and reanalysis wind products, Belmonte Rivas & Stoffelen (2019) estimate zonal mean wind biases of up to 50 % in the midlatitude westerly or trade wind regions. As scatterometers evaluate the roughness of the ocean surface, they can retrieve wind under almost all weather conditions, but are sensitive to heavy rain (e.g. Atlas et al., 2011). QUIKSCAT and ASCAT products are calculated using a model function in consistency with winds from passive satellite microwave radiometers such as the Special Sensor Microwave Imager (SSM/I), which help to determine if rain was present (e.g. Ricciardulli and Wentz, 2015). The temporal availability of wind estimates from satellites is limited by the number of overpasses of the same satellite over a certain region per day. For example, the grid points north and south of 40°N/40°S are observed by ASCAT at least once a day, while in the tropics ASCAT retrievals for each grid point are < 1 per day (Bentamy & Croize-Fillon, 2011). Since 2018, three identical ASCAT instruments are operating on satellites MetOP-A, -B & -C, which should improve the spatial and temporal coverage further. Scatterometer winds are known to be affected by the presence of land (Vignudelli et al., 2011) and can, therefore, be less reliable in coastal areas, shallow seas or regions with strong orography (e.g. Kilpatrick et al., 2019).

Here, we use the gridded fields of ENW at 10m from QUIKSCAT and ASCAT provided by the Centre de Recherche et d'Exploitation Satellitaire (CERSAT) at IFREMER, which were calculated using the same objective method for both scatterometers (e.g. Bentamy & Croize-Fillon, 2011; Bentamy & Croize-Fillon, 2012). CERSAT-IFREMER does also provide wind stress estimates for QUIKSCAT and ASCAT, which have been calculated from 10m ENWs using the coefficients for sea surface wind stress and wind profiles depending on wind speed and temperature from Smith (1988). Note, that these daily gridded wind fields of QUIKSCAT and ASCAT winds can, depending on the gridding method and wind stress parametrization, slightly differ from those provided by the Jet Propulsion Laboratory (JPL; e.g. Liu et al., 2010; Fore et al., 2014).

Table 2 Information on and availability of 8 different gridded wind products. The first column gives the product IDs used throughout this study, their official names and related references, column 2 the data sources. The original temporal and spatial resolutions, as well as the available periods are listed in columns 3-5. * The CCMP and JRA55-do data sets used here do not or not fully cover the year 2019. They have not been updated due to a lack of time. ** CERSAT-IFREMER does also provide wind stress estimates for QUIKSCAT (and ASCAT), which we use to compare different wind stress parametrizations in section 3.5.3.

Product ID & reference	Data source	Temp. resolution	Spatial resolution	Period
NCEPNCAR "NCEP/NCAR Atmospheric Reanalysis I" <i>Kalnay et al. (1996); Kistler et al. (2001)</i>	Provided by the NOAA/OAR/ESRL PSL (Boulder, Colorado, USA) and downloaded from their website: http://www.esrl.noaa.gov/psd/data/gridded/data.ncep.reanalysis.surfacefluxes.html . [Latest access: 12 June 2020].	daily	1.85°x1.90°	1948-2019
ERA-Interim "ECMWF Reanalysis Interim" <i>Dee et al. (2011b); Berrisford et al. (2011)</i>	Downloaded from the World Data Center for Climate (WDCC) at DKRZ: https://cera-www.dkrz.de/WDCC/ui/cersearch/entry?acronym=ERAIN_SFC00_6H_10U_165 _10V_166 . [Latest access: 25 May 2020].	6-hourly	0.7°x0.7	1979-2019
ERA5 "Fifth generation of ECMWF Reanalyses of the global climate." <i>Hersbach & Dee, 2016; Hersbach et al., 2019</i>	Provided by the Copernicus Climate Change Service Climate Data Store (CDS) and downloaded from: https://cds.climate.copernicus.eu/cdsapp#!/home . [Latest access: 14 July 2020]	hourly	0.25°x0.25°	1979-2019
QUIKSCAT "Gridded Mean Wind Fields from Ku-Band SeaWinds onboard QuikSCAT Level 3" <i>Bentamy & Croize-Fillon (2011)</i>	Provided by the Centre de Recherche et d'Exploitation Satellitaire (CERSAT), at IFREMER (Plouzané, France), and downloaded from: ftp://ftp.ifremer.fr/ifremer/cersat/products/gridded/MWF/L3/QuickSCAT/Daily/Netcdf/ . ** [Latest access: 20 May 2020].	daily	0.25°x0.25°	1999-2009
ASCAT "Gridded Mean Wind Fields from C-Band Advanced SCATterometer onboard MetOp-A Level 3" <i>Bentamy & Croize-Fillon (2011)</i>	Provided by the Centre de Recherche et d'Exploitation Satellitaire (CERSAT), at IFREMER (Plouzané, France), and downloaded from: ftp://ftp.ifremer.fr/ifremer/cersat/products/gridded/MWF/L3/ASCAT/Daily/Netcdf/ . [Latest access: 20 May 2020].	daily	0.25°x0.25°	2007-2019
CCMP "Cross-Calibrated Multi-Platform Reanalysis Version 2 Level 3" <i>Atlas et al. (2011); Wentz et al. (2015)</i>	Provided by Remote Sensing Systems (RSS) and downloaded from: http://www.remss.com/measurements/ccmp/ [Latest access: 16 May 2020]	daily	0.25°x0.25°	1987-2019*
CORE II "Coordinated Ocean-sea ice Reference Experiments: Corrected Inter-Annual Forcing data set Version 2.0" <i>Large & Yeager (2009)</i>	Downloaded from: https://data1.gfdl.noaa.gov/nomads/forms/core/COREv2/CIAF_v2.html . ** [Latest access: 14 May 2020].	6-hourly	1.85°x1.90°	1948-2009
JRA55-do "Japanese 55-year Reanalysis for driving ocean-sea ice models Version 1.4." <i>Kobayashi et al. (2015); Tsujino et al. (2018)</i>	Downloaded from: https://climate.mri-jma.go.jp/~htsujino/jra55do.html . [Latest access: 8 March 2019]	3-hourly	0.56°x0.56°	1958-2018*

The **CCMP** (Cross-Calibrated Multi-Platform) gridded surface vector wind product was originally developed by Atlas et al. (1996) merging satellite, moored buoy, and model wind data using a Variational Analysis Method (VAM; Hoffman et al., 2003) of data assimilation. With the VAM a gridded surface wind analysis is calculated, which minimizes the misfit of the analysis to the background wind field, the observational data and some defined constraints. Here, we use version 2 of the CCMP winds (Atlas et al., 2011), which additionally includes RSS radiometer wind speeds, QUIKSCAT (1999-2009) and ASCAT (since 2008) scatterometer wind vectors, a more comprehensive set of global ship and buoy observations, and ERAI reanalysis wind fields as the background product. For this generation of CCMP wind fields, satellite observations from various missions are synthesized, which increases the spatiotemporal coverage (Wentz et al., 2015). According to Atlas et al. (2011) approximately 25 % of the global ocean was observed in the late 1980s and the coverage increased to 60 % after 2000 at 6-hourly resolution. This conversely means that roughly 40 % of the CCMP surface winds are based on the background reanalysis winds from ERAI at the 6-hourly resolution. Incorporating the ERAI model data in this way can, for example, introduce spurious trends that may exist in the background wind fields (e.g. Torralba et al., 2017). Furthermore, as CCMP winds rely heavily on scatterometer measurements, a large fraction of the difference between CCMP and ERAI are related to effects of boundary layer stability and strong ocean currents (e.g. Atlas et al., 2011).

3.2.3. Model forcing products

As wind stress provides the main mechanical forcing for the ocean circulation, its correct computation is also crucial in ocean modeling. Here, we include 10m-winds from two data sets of atmospheric boundary conditions that are used in the ocean modelling community to force a diverse set of ocean general circulation models (OGCMs): The Coordinated Ocean Research Experiments Interannual forcing version 2 (hereafter called **CORE II**; Large & Yeager, 2009) data set consists of a globally complete set of air-sea fluxes of momentum, heat and freshwater covering the period 1948-2009. It is largely based on the atmospheric surface fields from the NCEPNCAR product, which is described above. In order to reduce biases, the NCEPNCAR fields have been corrected based on the comparison with satellite and in-situ data. Large & Yeager (2004) analyzed the ratio of the mean QUIKSCAT speed averaged over the two years 2000-2001 to that from NCEPNCAR. They found NCEPNCAR winds to have a low bias with a ratio larger than 1 everywhere except a few isolated regions off the coasts of South America and Africa. Over most of the mid-latitude oceans QUIKSCAT winds are 5 - 10 % higher, and in some regions near the equator and the poles up to 15%. To correct the NCEP wind speed bias, they multiply the wind components (u_{10}, v_{10}) from NCEPNCAR with the spatially-dependent wind speed ratio RS . Later, Large & Yeager (2009) published an updated version of the CORE II fluxes. Besides adding a 6-year extension through 2006, they also modified the wind speed factor by deriving it from 5 years of QUIKSCAT winds (2000-2004) instead of 2 years and, additionally, applied a wind rotation correction by using the unambiguous wind angles defined by wind component means and accommodating low wind regions. Unfortunately, CORE II provides no estimates of uncertainties and is available only through 2009.

With a refined horizontal grid spacing and temporal interval, as well as improved adjustment methods for the underlying atmospheric reanalysis product, **JRA55-do** (Tsujino et al., 2018) aims to replace CORE II within and reacts to feedback from the ocean modelling community. Similar to CORE II, JRA55-do is based on a reanalysis product, the Japanese 55-year Reanalysis project (JRA-55) conducted by the Japan Meteorological Agency (JMA). The reanalysis JRA-55 covers a period of more than 50 years, uses an atmospheric model with a horizontal resolution of 55 km and 4DVar for data assimilation

(Kobayashi et al., 2015). As for NCEPNCAR in CORE II, the surface fields of JRA-55 have to be bias corrected against reference fields and modified globally using a two-dimensional optimal interpolation analysis performed by JRA-55 (Tsuji et al., 2018). The reference fields for most variables are updates of those used to correct CORE II (Large and Yeager, 2009). JRA-55 winds are corrected towards the mean wind vectors from almost 10 years of QUIKSCAT (1999 - 2009) and SSM/I wind speed to cover the period before QUIKSCAT (1988–1998). Instead of applying a multiplicative like Large & Yeager (2009; CORE II), wind speed is corrected using an offset to retain the variance contained in JRA-55. To account for abrupt shift in the atmospheric fields caused by changes in the observing systems, JRA55-do applies time-dependent adjustments dividing the data set into different phases. For the wind it is especially relevant that, like the ECMWF reanalysis products, the JRA-55 reanalysis started to include scatterometer winds in the late 1990s: ERS-1 & ERS-2 from 05/1997 to 01/2001, QUIKSCAT from 07/1999 to 11/2009 and, additionally, ASCAT since 01/2008 (Tsuji et al., 2018). The JRA55-do forcing data set is currently available until and including 2019, which allows for direct model validation and comparison with observations from the RACE projects.

3.3. Wind data processing and derived quantities

The wind products in our collection vary in different aspects, e.g. resolution and time period. To avoid introducing further uncertainties, we decided to follow the same procedure to process and analyze all gridded products. Therefore, we use 10m-wind fields which are standard WMO observations and available for every wind product. All 10m-wind fields are interpolated onto the $0.25^\circ \times 0.25^\circ$ spatial grid of QUIKSCAT and ASCAT, and values over land are removed. If available, we use daily wind values. If not, data with higher temporal resolution were downloaded (see Table 2) and averaged to daily values.

Surface wind stress $\vec{\tau} = (\tau_x, \tau_y)$ is calculated from 10m-wind vectors $\vec{u}_{10} = (u_{10}, v_{10})$ using the bulk formula:

$$\vec{\tau} = \rho_a C_D |\vec{u}_{10}| \vec{u}_{10} \quad (9)$$

where $\rho_a = 1.223 \text{ kg m}^{-3}$ is the air density, $|u_{10}|$ the 10m-wind speed and C_D the bulk transfer coefficient for drag under neutrally stable atmospheric conditions. C_D was estimated as a function of only 10m-wind speed based on a formulation by Large & Yeager (2004; LY04):

$$\text{LY04: } 10^3 C_D = \frac{2.7}{U_{10}} + 0.142 + 0.0764 |u_{10}| \quad \text{for all } |u_{10}| \quad (10)$$

We test a collection of different formulations for the drag coefficient depending only on wind speed in section 3c.

The meridional Ekman transports through 11°N and 11°S are estimated from the zonal component of the wind stress, τ_x , along each latitude according to

$$T_{EK}(t) = - \int_{x_{WB}}^{x_{EB}} \frac{\tau_x(x, t)}{\rho_0 \cdot f} dx \quad (11)$$

with f being the Coriolis parameter, ρ_0 a mean sea water density of 1027 kg m^{-3} and (x_{EB}, x_{WB}) the longitudes of the eastern and western boundaries. The Ekman divergence between 11°N and 11°S was calculated as the difference between the Ekman transports through both latitudes.

Fields of the wind stress curl, $\nabla \times \vec{\tau}$, are calculated from the interpolated fields with a $0.25^\circ \times 0.25^\circ$ grid using centered derivatives. The Sverdrup transport is computed as the zonal integral of the wind stress curl between the western and eastern boundary:

$$T_{SV}(t) = \int_{X_{WB}}^{X_{EB}} \frac{1}{\beta \cdot \rho_0} (\nabla \times \vec{\tau}) \quad (12)$$

where $\beta = \frac{df}{dy}$ is the meridional gradient of the Coriolis parameter. Wind stress curl or Sverdrup transport at certain latitudes were only extracted afterwards.

3.4. Auxiliary data sets

3.4.1. Wind stress output from the INALT01 OGCM

In order to extend our assessment of different wind stress parametrizations by a formulation that also considers ocean currents, we additionally include the wind stress output of a hindcast experiment with the global ocean/sea-ice Ocean General Circulation Model configuration `INALT01` in the comparison. INALT01 is based on the NEMO (Nucleus for European Modelling of the Ocean v3.1.1; Madec, 2008) code and developed within the DRAKKAR framework (The DRAKKAR Group, 2014). It is a global $1/2^\circ$ configuration with a $1/10^\circ$ refinement between 70°W - 70°E and 50°S - 8°N and was shown to represent the western boundary current regime in the tropical and South Atlantic well (e.g. Durgadoo et al., 2013). The model is forced by the interannually varying air-sea fluxes from the CORE II data set described in section 3.4.1. In INALT01, the 10m- wind vectors from CORE II are first converted into “relative winds”, which take into account the underlying ocean surface velocities ($\vec{u}_{Current}$) scaled with the parameter α :

$$\vec{\tau} = \rho_a C_D |\vec{u}_{10} - \alpha \cdot \vec{u}_{Current}| (\vec{u}_{10} - \alpha \cdot \vec{u}_{Current}) \quad (13)$$

In this model configuration as well as in many others, α is chosen to equal 1. A set of sensitivity experiments with INALT20, the successor of the INALT01 model configurations, is performed by Schwarzkopf et al. (2019) exploring the role of ocean currents in the wind stress calculation choosing $\alpha=0.7$ (partial wind) or $\alpha=0$ (absolute wind). Observational and modelling studies have highlighted the effect of the mean ocean currents on the mean surface stress: Renault et al. (2017) showed that the current feedback can reduce the median wind stress magnitude by 20%, while a reduced energy input from the atmosphere to the ocean can, consequently, slow down mean currents and dampen meso-scale activity. Abel et al. (2017) confirmed this and stress that ocean-only simulations should include the surface current feedback to the wind.

Our analysis employs the 5-daily wind stress output for the period 1978-2009.

3.4.2. In-situ wind measurements at PIRATA buoys

In order to test the capability of 8 different wind products (section 2a) to capture the wind variability in the region of interest, we compare them to wind measurements from 13 PIRATA (Prediction and Research Moored Array in the Tropical Atlantic; Bourles et al., 2019) buoys spanning the tropical Atlantic. Figure 18 displays the positions of these 13 PIRATA buoys as well as time series of the 4m wind speed at each location, most of which are already approaching 20 years in length. In this study, we use daily time series of the wind anomalies at 4m downloaded from “<https://www.pmel.noaa.gov/tao/drupal/disdell/>” (latest access: 21 July 2020).

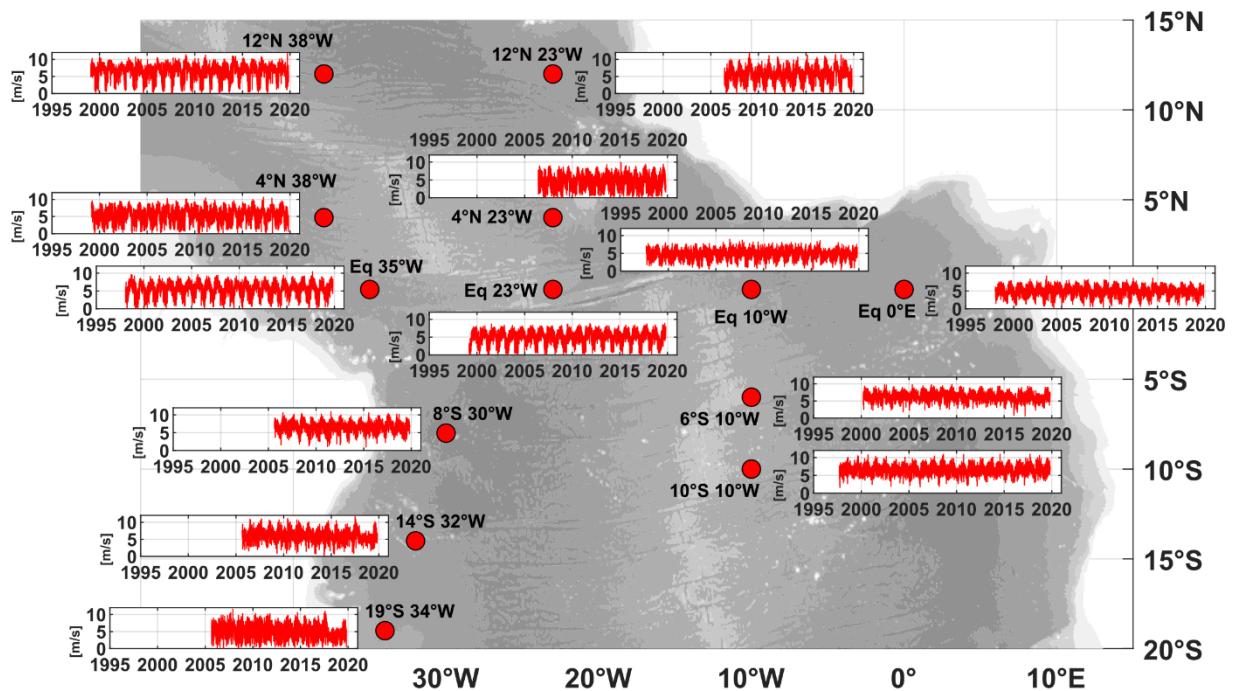


Figure 18 Bathymetric map (ETOPO1; doi:10.7289/V5C8276M) of the tropical Atlantic including the positions of 13 PIRATA buoys (red dots). The inlays show daily time series of 4m-wind speeds measured at each PIRATA buoy.

In section 3.5.2 we correlate neutral 10m wind anomalies from the gridded products with non-neutral 4m-wind anomalies from PIRATA buoys. Please note, that depending on the region and temporal resolution wind speed errors between 0.1 m s^{-1} (monthly) to 0.5 m s^{-1} (hourly) can occur when the PIRATA winds are not adjusted for stability effects (Smith, 1988; Mears et al., 2001; Fairall et al., 2003; Kara et al., 2008).

3.5. Results and discussion

In the following section, we present a variety of findings from our evaluation of the different gridded wind products. We decided to organize our results in the form of a catalogue having a segmented motivation and discussion for each of the investigated aspects.

3.5.1. Differences in the mean wind fields

The mean surface wind field in the equatorial and tropical Atlantic is governed by the northeast and southeast trade winds. These winds are known to drive westward currents – such as the different branches of the North and South Equatorial Currents, as well as equatorial and eastern boundary upwelling. Along the eastern boundaries, the winds are mainly equatorward, driving the Canary and Benguela Current Systems in the eastern tropical North and South Atlantic, respectively. South of 35°S , the mid-latitude westerlies drive the southern branch of the South Atlantic Subtropical Gyre – the South Atlantic Current (e.g. Talley et al., 2011).

All of the 8 gridded wind products resemble the mean, large-scale wind patterns described above (see Fig. 19 for the 2008 ensemble mean wind field of the 8 wind products), which means that they are all able to capture the large-scale atmospheric circulation in this region. However, we find regional differences in wind speed and direction between them (Fig. 20). Across all products, differences in wind speed and direction are less than 10 % and less than 5° almost everywhere in the tropical and South Atlantic. Major differences are only found in narrow patches collocated with regions of minimum

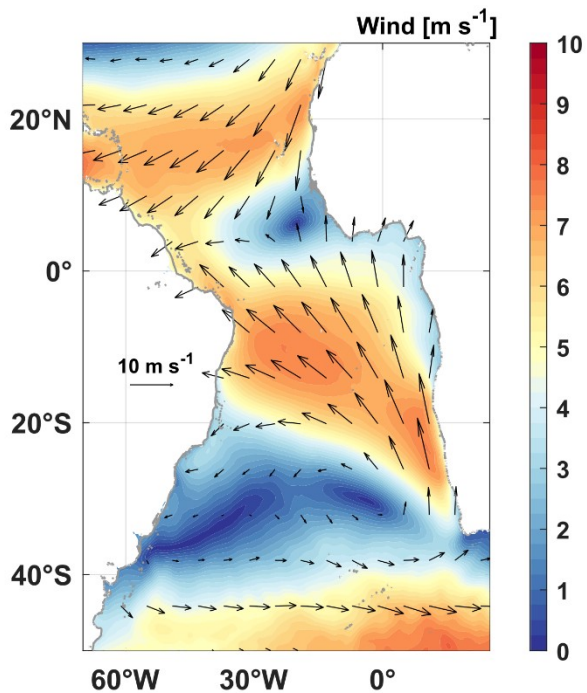


Figure 19 Wind speed (filled contours) and direction (arrows; plotted for every 25th grid point) of the ensemble mean of all 8 wind products for the overlapping year 2008.

wind speed: Along the West African coast wind direction can differ by 10° among products. Differences of up to 30 % in wind speed and 20° in direction can be found south of South Africa. Only in a patch at about 5°N off Guinea and along a zonal band (30-40°S) within the South Atlantic Subtropical Gyre differences can be as large as 60 % in wind speed and 160° in direction. These differences seem to be related to small variations in the positions of the South Atlantic Subtropical Cyclone or the convergence of the trade winds among the different wind products.

The largest deviations from the 2008 ensemble mean wind field are found in NCEPNCAR and CORE II (Fig. 20 (a, g)). These show substantial geographic variations for both products with deviations of up to $\pm 1.2 \text{ m s}^{-1}$ in the equatorial Atlantic and of $\pm 0.8 \text{ m s}^{-1}$ throughout most of the tropical and subtropical South Atlantic. NCEPNCAR has been reported to have several

shortcomings, underestimating, for example, wind speed in the equatorial Atlantic (e.g. Meissner et al., 2001; Feng et al., 2006). In comparison with ship observations, NCEPNCAR revealed a consistent low bias wind speed throughout all latitudes, which seem to be attributed to weak pressure gradient in the underlying NCEP model and becomes worse with increasing wind speed (Smith et al., 2001). Also, NCEPNCAR does not assimilate any surface winds from satellite observations (Fujiwara et al., 2017). The CORE II product is mainly based on NCEPNCAR winds, however, its production accounts for wind speed biases in the reanalysis product. The ENWs from NCEPNCAR are multiplied with a spatially-dependent factor that is defined as the wind speed ratio between NCEPNCAR and 5 years of QUIKSCAT measurements (Fig. 6 in Large & Yeager, 2004; Large & Yeager, 2009). Differences in the spatial distributions of wind anomalies from NCEPNCAR and CORE II, therefore, almost exclusively stem from this correction factor. Due to the correction factor, winds in CORE II have systematically weaker poleward components in the westerly wind belts, especially over the Southern Hemisphere, compared to NCEPNCAR. Regarding absolute values of the wind speed (not shown here), the effects of increasing the NCEPNCAR wind speed by a spatially-dependent factor are more than compensated by NCEP using a larger and constant drag coefficient (Smith et al. 2001; see also section 3.5.3). Compared to the new generation model forcing product JRA55-do, wind speed in CORE II is generally higher by 0.7-1.2 m s^{-1} . According to Tsujino et al. (2018), this is because in NCEPNCAR the actual wind speed was directly adjusted toward ENWs from QUIKSCAT, while in JRA55-do the adjustment procedures was performed in terms of equivalent neutral wind.

The other two reanalysis products, ERAI and its successor ERA5 (Fig. 20 (b, c)), show very similar spatial distributions of deviations from the ensemble mean with generally weaker trade winds and stronger westerlies. In ERAI, wind speed deviations from the ensemble mean range from -0.85 m s^{-1} in the eastern equatorial Atlantic to $+0.5 \text{ m s}^{-1}$ south of 30°S. With an increased horizontal resolution from ERAI to ERA5, the deviations from the ensemble mean wind fields have also been reduced by half over most of the tropical and South Atlantic. Exceptional positive deviations ($< 0.5 \text{ m s}^{-1}$) in ERA5 from the

ensemble mean can be found in narrow patches along the African coast (Fig. 20 (b); e.g. southern Benguela, Gulf of Guinea). The low wind speed bias in the tropics is assumed to a large extent be related to atmospheric stability effects over warm waters (e.g. Kara et al., 2008). According to Belmonte Rivas & Stoffelen (2019), the ECMWF products lack detail in the representation of surface temperature gradient effects in the vicinity of the ITCZ or Western Boundary Currents. Also, when comparing reanalysis to scatterometer winds, ocean currents can make a substantial contribution to the excessively zonal mean wind bias in the westerlies and trades (up to 50%; Belmonte Rivas & Stoffelen, 2019). The improvement from ERAI to ERA5 is also supported by Belmonte Rivas & Stoffelen (2019), who find ERA5 to perform better than ERAI not only in terms of mean wind errors, but also transient wind errors as well as wind divergence and wind stress curl biases.

The two scatterometer wind products used in this study, QUIKSCAT and ASCAT (Fig. 20 (d, e)), do also reveal substantial deviations from the ensemble mean ($\pm 1 \text{ m s}^{-1}$) as well as surprisingly large differences among their spatial distributions. QUIKSCAT winds are stronger and more northward than the ensemble mean wind with wind speed deviations of $+ 0.8 \text{ m s}^{-1}$ all along the equator, most of the African coast and in the Agulhas region (Fig. 20 (d)). ASCAT winds are weaker and more westward with wind speed deviations of $- 0.75 \text{ m s}^{-1}$ just north of the equator, $- 0.5 \text{ m s}^{-1}$ along the coasts of Angola, Namibia and South Africa, as well as deviations of $- 0.65 \text{ m s}^{-1}$ in the basin interior south of 30°S (Fig. 20 (e)). The regional differences between QUIKSCAT and ASCAT are in agreement with findings from Bentamy & Croize-Fillon (2011), who attributed most of them to differences in their operating frequencies, which can lead to biases of up to 1 m s^{-1} in QUIKSCAT. Those biases seem to depend on the rain rate, wind velocities or seas surface temperatures, and can especially affect wind estimates in the tropics. Further, the difference between QUIKSCAT and ASCAT can also increase in coastal regions where the diurnal cycle of winds is aliased by the time lag between satellites - the QUIKSCAT local equator crossing time at the ascending node (6:30 A.M.) leads the ASCAT local equator crossing time (9:30 A.M.) by 3 hours (Bentamy & Croize-Fillon, 2012).

The mean wind field from CCMP is closest to the ensemble mean of the 8 wind products used in this study. Only in the eastern equatorial Atlantic and Agulhas region, where the CCMP winds are stronger and more northward, wind deviations of $+ 0.5 \text{ m s}^{-1}$ can be found. In all other regions, CCMP wind deviations are smaller than $\pm 0.3 \text{ m s}^{-1}$ (Fig. 20 (f)). Interestingly, the spatial distribution of the CCMP wind deviations is more similar to QUIKSCAT than to ASCAT (Fig. 20 (d, e)), although both scatterometer products are incorporated into CCMP in 2008 (Wentz et al., 2015). There is also no close resemblance between the spatial distributions of CCMP and ERAI deviations from the 2008 ensemble mean although CCMP uses ERAI as the background field when no other observations are available (Atlas et al., 2011). Wind speed in CCMP is generally higher by about 0.5 m s^{-1} in the tropical Atlantic than in the ECMWF products.

Winds from the model forcing dataset JRA55-do tend to be only slightly weaker ($- 0.4 \text{ m s}^{-1}$) and more eastward in the trade wind regions compared to the ensemble mean (Fig. 20 (h)). As for most of the other products, narrow patches of strong positive and negative deviations ($\pm 0.9 \text{ m s}^{-1}$) can be found in the eastern equatorial Atlantic and all along the African coast. Compared to the other model forcing dataset, CORE II, JRA55-do winds are substantially weaker with maximum differences of $- 1.3 \text{ m s}^{-1}$. Tsujino et al. (2018) relate these differences to the different methods used to correct the underlying reanalysis winds with QUIKSCAT measurements (see section 3.2.3 for details).

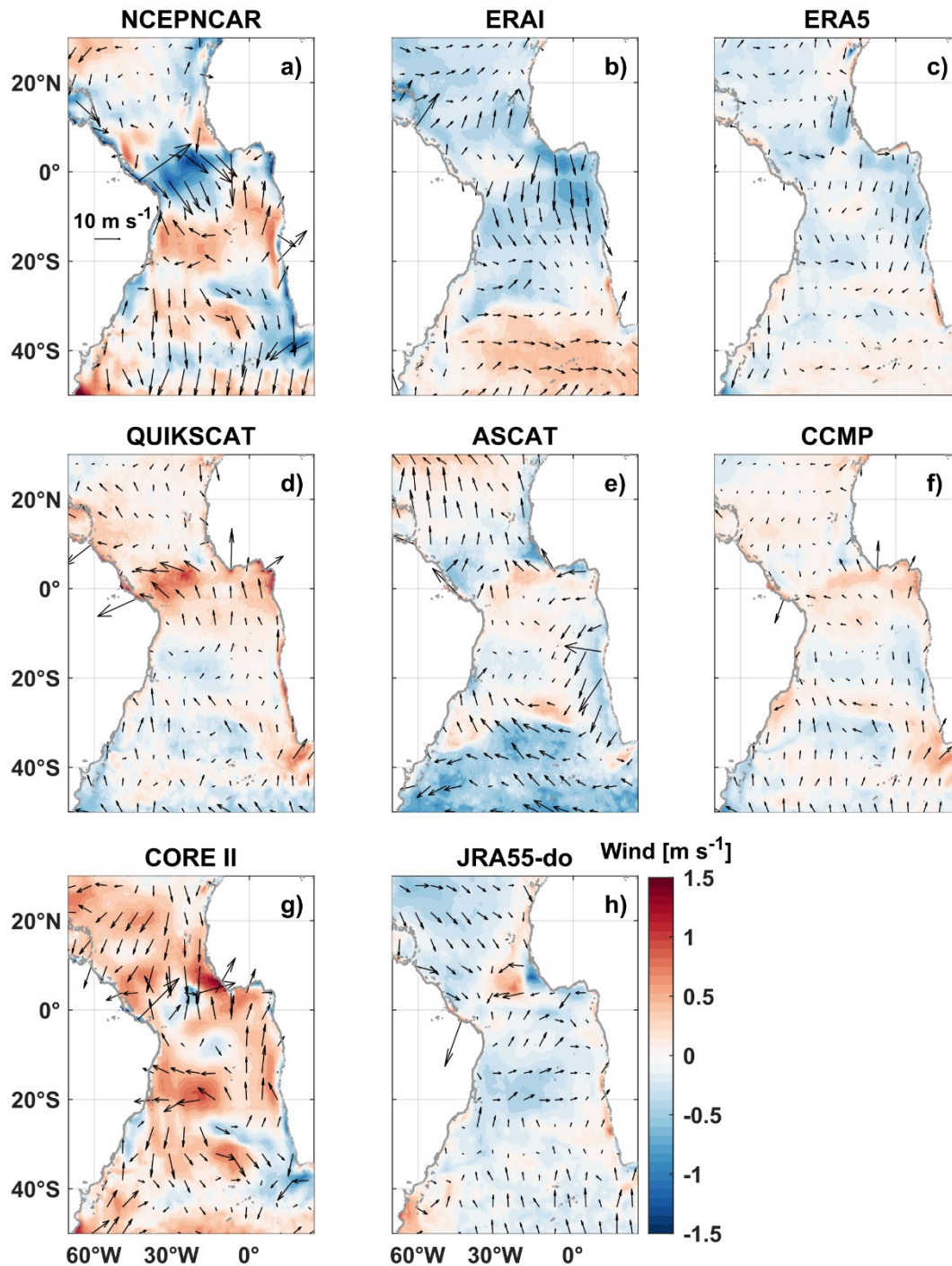


Figure 20 Deviations of mean wind speed (filled contours) and direction (arrows; plotted for every 25th grid point) from the ensemble mean of all 8 wind products for the overlapping year 2008.

3.5.2. Comparison of variability in the gridded products to directly observed wind data

Wind observations from open-ocean buoys, although having their caveats as well (e.g. Schlundt et al., 2020), can be considered to represent the ‘real world’. Here, we compare the 8 gridded wind products described above with daily time series of anemometer winds from 13 PIRATA buoys spanning the tropical and South Atlantic regarding their correlations on different timescales.

For the comparison, winds from the gridded products were interpolated linearly towards the locations of the 13 PIRATA buoys. Note, that the standard deviations of the individual time (not shown) series can be reduced by the linear spatial interpolation – for identically correlated neighbouring grid points

standard deviations could be reduced by a factor of $\sqrt{2}$. In order to compare variability on different timescales, we calculated correlations for differently filtered timeseries: For intra-seasonal to seasonal timescales, we used band-pass filters (3rd order Butterworth filter) for the frequency bands 10-50, 50-90, 90-150, 150-210 and 300-430 days. These bands were chosen around the frequencies of the most pronounced periodicities (30, 70, 120, 180, 365 days) in the PIRATA wind data (not shown). For interannual timescales, we used a low-pass filter with a gradually decreasing cut-off frequency. Correlations were calculated for each data pair, at each station and for each filter setting (Fig. 21). Instead of testing for statistical significance, here, we do only show correlations for timescales $t_c \leq \frac{N}{5}$, with N being the length of the overlapping buoy and gridded product time series in days. This means, that if there is a periodic signal with the frequency $1/t_c$, the calculation of correlation coefficients is based on at least 5 repetitions of that periodic signal.

Figure 21 shows how much the agreement of the 8 wind products with the in-situ winds depends on the considered timescale as well as the region and wind regime. The differences among the products are surprisingly large and the possible mechanisms can be manifold. Overall, we find CCMP to agree best with the PIRATA winds— at almost all buoy locations and on almost all timescales, which is expected as CCMP production incorporates them directly (see section 3.2.2). The two ECMWF reanalysis products and JRA55-do, which do not assimilate wind observations from moored buoys, also show good agreement with the PIRATA winds. Interestingly, in many cases, ERAI shows slightly higher correlations than its high-resolution successor ERA5. The four wind products mentioned above show the highest correlations with the buoy measurements in regions where the mean winds are dominantly zonal, for example at 4°N or closest to the Brazilian coast. They show the lowest correlations with PIRATA as well as the widest spread among each other at the four buoy locations in the eastern tropical Atlantic. It should also be noted, that JRA55-do has some problems to reproduce the observed intra-seasonal variability along the equator and the seasonal cycle at 0°-6°S|10°W. Besides this, the observed seasonal variability seems to be captured sufficiently.

The remaining four products include NCEPNCAR, CORE II and the two scatterometer products, all reveal problems on different timescales. What becomes immediately apparent, is that CORE II is not able to reproduce the variability on intra-seasonal timescales at all of the 13 buoy locations. On seasonal to interannual timescales the correlation between CORE II and PIRATA winds increase and we find CORE II to align with the other products. Beside performing better than CORE II on short timescales, NCEPNCAR shows only moderate to low correlations with the PIRATA data on all other timescales and at all buoy locations. The scatterometer winds, on the other hand, show better agreement with the PIRATA winds on intra-seasonal timescales – for example, comparable to JRA55-do, but lower and decreasing correlations on interannual timescales, especially in the eastern tropical Atlantic. The bad performance of the scatterometer winds in the eastern tropical Atlantic could also explain the low correlations of the CCMP or ERAI, ERA5 and JRA55 winds, as those incorporate or assimilate the scatterometer products.

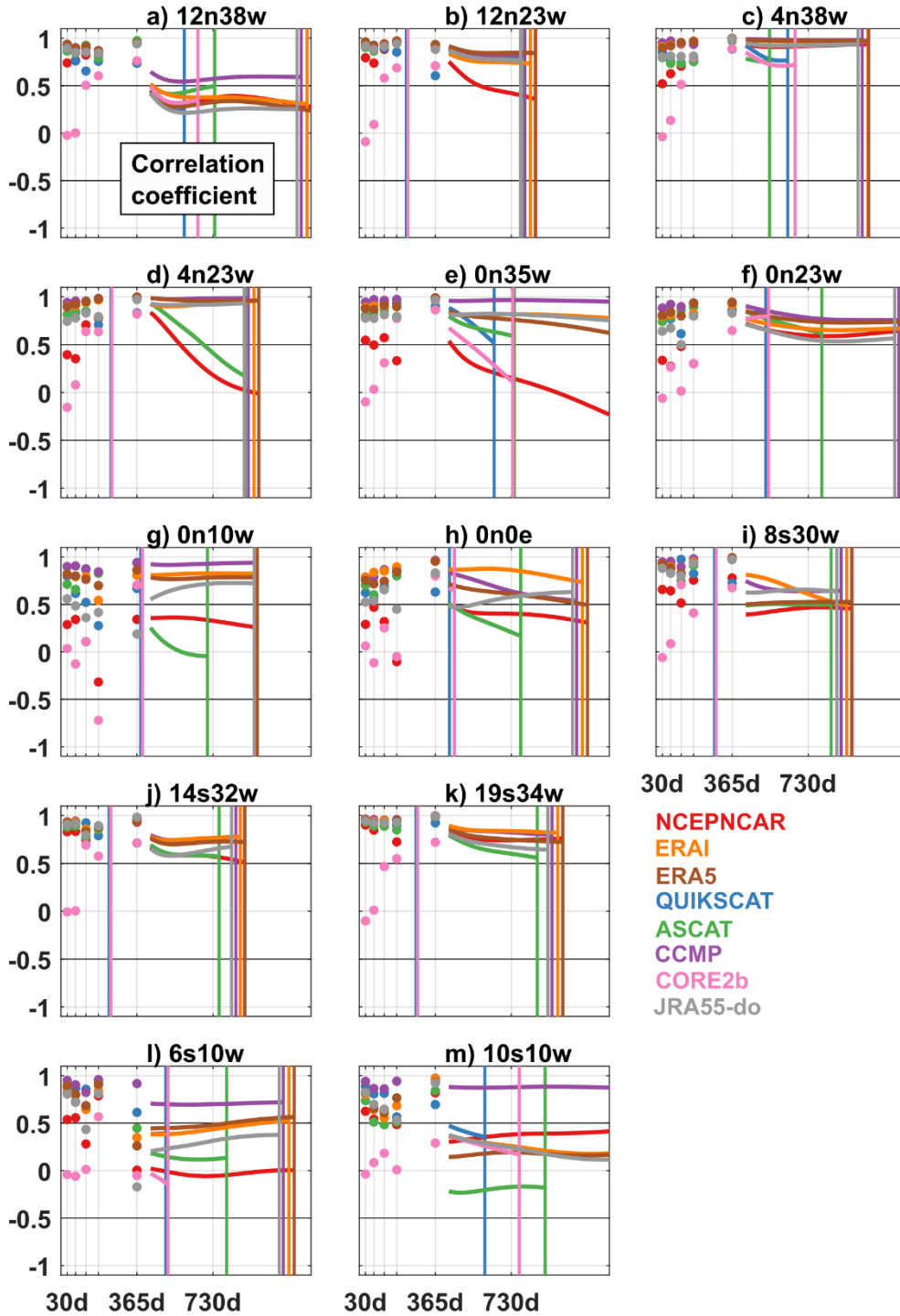


Figure 21 Correlation between the meridional wind components from the gridded products (ENWs at 10m) and measured at the PIRATA buoys (actual wind at 4m) shown for different timescales (t_c ; in days). The correlation coefficients are calculated based on time series that were band-pass filtered for the frequency bands 10-50, 50-90, 90-150, 150-210, 300-430, 430-660 and 660-960 days. Vertical lines mark the timescale, for which the length of the overlapping time series allow 5 repetitions. Horizontal lines mark correlation coefficients of ± 0.5 .

3.5.3. Assessment of different wind-stress parameterizations

To systematically evaluate the different wind products and focus on differences between them, we decided to use gridded fields of 10m-winds (\vec{u}_{10}) provided with all the products and convert them to wind stress using the same bulk transfer coefficient for drag (C_D) from Large & Yeager (2004) assuming neutrally stable atmospheric conditions (see Eqs. 1, 2 in section 3.3).

This non-linear, but simple formulation from LY04 is very popular, but tends to be referenced differently. It is a modification of a formulation presented in Large & Pond (1981; LP81),

$$LP81: 10^3 C_D = \begin{cases} 1.2 & 4 \leq |u_{10}| < 11 \frac{m}{s} \\ 0.49 + 0.065 |u_{10}| & 11 \leq |u_{10}| < 25 \frac{m}{s} \end{cases} \quad (14)$$

repeated again in Large et al. (1994), Large & Yeager (2004), Risien & Chelton (2008) or Large & Yeager (2009), and also used, for example, in the suite of CORE/OMIP projects or Brandt et al. (2021). Several formulations for calculating the drag coefficient are in common use, but there is no consensus on which formulation is the most accurate. An alternative formulation depending only on wind speed was, for example, presented in Yelland & Taylor (1996; YT96)

$$YT96: 10^3 C_D = \begin{cases} 0.29 + \frac{3.1}{|u_{10}|} + \frac{7.7}{|u_{10}|^2} & 3 \leq |u_{10}| < 6 \frac{m}{s} \\ 0.6 + 0.07 |u_{10}| & 6 \leq |u_{10}| < 26 \frac{m}{s} \end{cases} \quad (15)$$

As the formulations by LP81 and YT96 do not cover wind speeds $< 3 - 4 \text{ m s}^{-1}$, they are both complemented with a formulation by Trenberth et al. (1990), another modification of Large & Pond (1981) for weak winds:

$$10^3 C_D = \begin{cases} 0.218 & |u_{10}| < 1 \frac{m}{s} \\ 0.62 + \frac{1.56}{|u_{10}|} & 1 \leq |u_{10}| < 4 \frac{m}{s} \end{cases} \quad (16)$$

Within the investigated region, such weak wind speeds appear less than 7% of the time in all of the 8 products. Note, that for wind speeds above 30 m s^{-1} results from Donelan et al. (2004) suggest that the drag coefficient tends to converge to a constant value.

It is also common to use a constant drag coefficient to derive wind stress from wind, like for example in Tuchen et al. (2020) or for the calculation of the wind stress provided with NCEPNCAR (Kalnay et al., 1996; CONST):

$$CONST: 10^3 C_D = 1.3 \text{ for all } |u_{10}| \quad (17)$$

To understand how much the accuracy of the estimated wind stress depends on the specification of the drag coefficient, we compare the range of the mean zonal wind stress ($\bar{\tau}_x$) along 11°S between the 8 products when calculated with LY04 to the range for single products (QUIKSCAT and CORE II) when using the different drag coefficients listed above. Additionally, we include the wind stress estimates provided for QUIKSCAT by CERSAT-IFREMER (QUIKSCAT prov; Bentamy & Croize-Fillon, 2011) and the wind stress output of the OGCM INALT01 forced with CORE II winds (INALT01; Durgadoo et al., 2013).

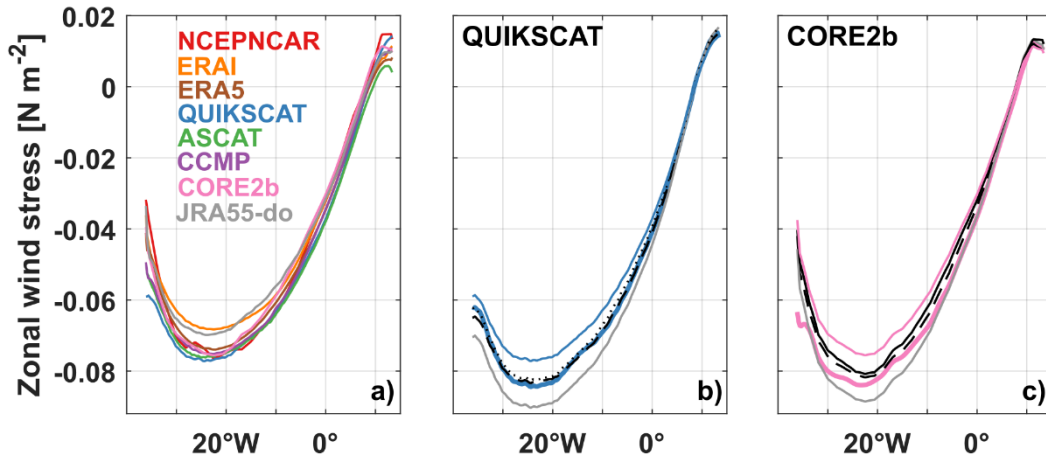


Figure 22 Mean zonal wind stress $\bar{\tau}_x$ along 11°S in 2008– a) calculated for the 8 different wind products always using the same drag coefficient formulation LY04, b) calculated from QUIKSCAT 10m wind using drag coefficient formulations from LP81 (dashed black curve), CONST (grey curve), YT96 (dotted black curve) and LY04 (thin solid blue curve), as well as the wind stress provided complementarily with the product (thick solid blue curve; QUIKSCAT prov; see section 3.2.2), c) calculated from CORE II wind using the same set of drag coefficient formulations as in b), as well as the wind stress derived with the INALT01 model (thick solid pink curve; INALT01; see section 3.4.1).

When calculated with LY04 for all 8 wind products, $\bar{\tau}_x$ along 11°S (Fig. 22 (a)) shows maximum differences of almost 0.03 N m⁻² at the western boundary, and of 0.01 N m⁻² in the western basin interior and at the eastern boundary. The difference between individual products are manifold and do also vary with longitude: At the western boundary, $\bar{\tau}_x$ calculated from the reanalysis products and model forcing data sets shows the weakest values, $\bar{\tau}_x$ derived from CCMP and ASCAT winds is slightly stronger and QUIKSCAT produces the strongest values of $\bar{\tau}_x$. Larger deviations between scatterometer and reanalysis wind stress in western boundary systems or other areas with strong currents can, as for wind speed, be partly explained by scatterometers measuring winds relative to the moving ocean surface (e.g. Kelly et al, 2001; Chelton & Freilich 2005). In the basin interior, both scatterometer wind products result in the strongest $\bar{\tau}_x$ (Fig. 22 (a)). However, they are close to the estimates from most of the other products, except for ERAI and JRA55-do, which are distinguishably weaker. At the eastern boundary, the largest differences in $\bar{\tau}_x$ can be found between the two scatterometers, with QUIKSCAT showing, together NCEPNCAR, the largest values of $\bar{\tau}_x$ and ASCAT the smallest. As described in section 3.5.1 (Fig. 20 (d, e)), ASCAT winds exhibit weaker winds along the African coasts compared to QUIKSCAT, which then also translates into the wind stress calculated with a bulk formula depending only on wind speed.

The effect of using different drag coefficients – shown here exemplarily for QUIKSCAT and CORE II (Fig. 22 (b, c)) - is rather small at the eastern boundary ($\Delta\bar{\tau}_x < 0.004$ N m⁻²), larger at the western boundary ($\Delta\bar{\tau}_x \sim 0.01$ N m⁻²) and largest in the western basin interior between 20-25°W. There, using the drag coefficient from LY04 results in the weakest and using the constant drag coefficient from Eq. (17) in the strongest mean zonal wind stress in the western basin interior. The maximum difference between those two estimates is ~ 0.015 N m⁻². Throughout the basin, the drag coefficient formulations from LP81 and YT96 produce very similar results for $\bar{\tau}_x$ along 11°S, which are within the range of the other estimates and also very close to the QUIKSCAT wind stress provided by CERSAT-IFREMER.

Interestingly, the mean zonal wind stress calculated from the output of the INALT01 model is, close to the western boundary, very different from the $\bar{\tau}_x$ derived with a variety of wind speed dependent drag coefficients (Fig. 22 (c)). West of 34°W, $\bar{\tau}_x$ derived from INALT01 is about 0.025 N m⁻² larger than the estimate derived from CORE II winds using LY04, and does not increase as steadily from the coast to

30°W. The differences between the wind stress derived from CORE II winds with LY04 and the wind stress output from the INALT01 model can mainly be related to the small but persistent wind work of the surface currents at 11°S as the INALT01 model output accounts for the underlying ocean surface velocities (e.g. Abel et al., 2017; Schwarzkopf et al., 2019). Another important effect of ocean-atmosphere coupling is the imprint of seas surface temperatures onto the wind stress. All of the formulations converting wind to wind stress listed above assume a neutrally stable atmosphere. This is a good assumption over most of the ocean, but can cause biases over, for example, warm tropical waters (e.g. Kara et al., 2008). There are several more complex formulations to convert wind to wind stress including e.g. stability effects and molecular constraints at the ocean-atmosphere-interface (Liu et al., 1979; the COARE algorithm from Fairall et al., 2003; Andreas et al., 2012). However, those formulations or algorithms require information such as the local air and sea surface temperatures, humidity, atmospheric pressure, shortwave and longwave radiation fluxes, and the height of the atmospheric boundary layer (e.g. Fairall et al., 2003). Because of the need for this additional information, accounting for the oceanic thermal feedback is not feasible within our systematic approach. However, we decided to extend our collection of wind products by one that includes a parametrization of ocean currents. Therefore, the wind stress output from INALT01 will additionally be included in all the following analyses. It should be noted, that the QUIKSCAT and ASCAT wind stress provided by CERSAT-IFREMER, which was calculated with the temperature dependent C_D from Smith (1988), should already incorporate the thermal feedback.

3.5.4. Differences in wind-derived variables and implications for the large-scale circulation in the tropical South Atlantic

3.5.4.1. The mean Ekman transport across 11°S

The tropics are governed by the persistent easterly trade winds, which are known to force strong poleward Ekman transport (e.g. Talley et al., 2011). The basin-wide Ekman transport (T_{EK}) across a certain latitude can efficiently be estimated from the zonal component of the wind stress, τ_x , following Eq. (11). In section 3.5.3, we report differences of up to 0.03 N m⁻² (~30%) between the wind stress estimates from the 8 gridded products and the output of the INALT01 model along 11°S. These differences translate into integrated or indirectly derived variables such as the Ekman transport.

Integrated across the ocean basin, the Ekman transport at 11°S is about -10 Sv on average. When considering the year 2008, which is covered by all products, the mean Ekman transports across 11°S can range from -8.8 Sv (ERA-Interim and JRA55-do) to -10.2 Sv (ASCAT) between the 8 gridded wind products (see Fig. 23 (a) and Table 3). Thus, the choice of wind product can come with an uncertainty of 1.4 Sv or ~15 % of the mean Ekman transport. This uncertainty even increases to 2.5 Sv when including the INALT01 model estimate (-11.3 Sv) and is only slightly reduced when averaging over longer periods. These differences in the mean Ekman transport across 11°S are comparable to the uncertainty introduced by the choice of wind stress parametrization (up to 1.8 Sv; see section 3.5.3).

Here, we also estimated the uncertainties of the mean Ekman transport from using different wind products for the latitudes 11°N, as well as 26.5°N and 34.5°S (Table 3). The latter represent the locations of the RAPID and SAMBA arrays. The mean Ekman transport across 11°N is + 8.8 Sv northward with the absolute value being almost as large as at 11°S and differs by 1.1 Sv between products. In the subtropics, the mean Ekman transports are considerably smaller with about 3 Sv northward across 26.5°N or about 1.6 Sv northward across 34.5°S. While in the subtropics the differences between products are also smaller compared to the tropics with 0.6-0.9 Sv for 26.5°N (depending on the

considered period) and 0.4-0.6 Sv for 34.5°S, the uncertainties can be as large as 38 % of the mean Ekman transport.

Table 3 Mean Ekman transports across 11°S, 11°N, 26.5°N and 34.5°S, derived from the gridded wind products listed in the 1st column. At 11°S, the mean Ekman transports are calculated for the full available periods of each product (2nd column), the overlapping year 2008 (4th column) or the period 2013-2018 (column 3). At the other latitudes, mean transports are also calculated for the period 2013-2018 (column 5, 6, 8) as well as for other periods, for which Ekman transports were published as part of an AMOC estimate. *This period was chosen to compare the Ekman transports with results from Rayner et al. (2011). ** This period can roughly be compared to Meinen et al. (2018).

Wind product	Ekman transport [Sv]							
	11°S			11°N	26.5°N		34.5°S	
	$\mu_{\text{full period}}$	$\mu_{2013-2018}$	μ_{2008}	$\mu_{2013-2018}$	$\mu_{2013-2018}$	$\mu_{2004-2008}^*$	$\mu_{2013-2018}$	$\mu_{2009-2017}^{**}$
NCEPNCAR	-9,3	-10,3	-10,1	8,4	3,0	2,7	1,5	1,4
ERA1	-8,9	-9,4	-8,8	8,3	2,9	2,7	2,0	1,9
ERA5	-9,5	-9,8	-9,6	8,6	3,0	2,8	1,6	1,5
QUIKSCAT	-10,0	-	-10,1	-	-	3,2	-	-
ASCAT	-10,1	-10,1	-10,2	9,4	3,4	-	1,5	1,3
CCMP	-9,7	-10,0	-10,0	9,3	3,3	3,2	1,9	1,7
CORE II	-9,2	-	-10,1	-	-	3,5	-	-
INALT01	-10,7	-	-11,3	-	-	-	-	-
JRA55-do	-8,9	-9,1	-8,8	8,8	2,8	2,6	1,7	1,6

We would like to stress, that our approach and the resulting uncertainties for the basin-wide mean Ekman transport are especially relevant for the AMOC observing community. Today, there are several international efforts to observe the AMOC and its variability at selected latitudes. The individual strategies to estimate the geostrophic or boundary current contributions to the AMOC differ substantially among programs and come with a variety of uncertainties (e.g. Frajka-Williams et al., 2019). The basin-wide Ekman contribution to the AMOC, however, is often considered to be straightforward and calculated following Eq. (11) without testing or documenting the quality of the chosen wind product in the respective region.

The uncertainties for the mean Ekman transport across 11°S, add to the results for the TRACOS array presented in Herrford et al. (2021). They used the gridded daily ASCAT wind stress fields provided by CERSAT-IFREMER (see section 3.2.2) to estimate the basin-wide Ekman transport over the period 2013-2018. Publications related to the SAMBA effort at 34.5°S used CCMP winds (Meinen et al., 2013; 2018) or SCOW (The Scatterometer Climatology of Ocean Winds; Dong et al., 2014), which is essentially a climatology of QUIKSCAT winds (Risien & Chelton, 2008). Publications related to the RAPID array at 26.5°N used different products to estimate the basin-wide Ekman transport there: QUIKSCAT (e.g. Kanzow et al., 2010; Rayner et al., 2011) or CCMP (e.g. McCarthy et al., 2012; 2015). Studies focusing on 41°N used, for example NCEPNCAR (Willis, 2010) and later QUIKSCAT (Hobbs & Willis, 2012). For the OSNAP array, we found only one publication elaborating on their choice of wind product: Zhao et al. (2018) mention to use ERA1 winds to estimate the AMOC related heat transport across the array.

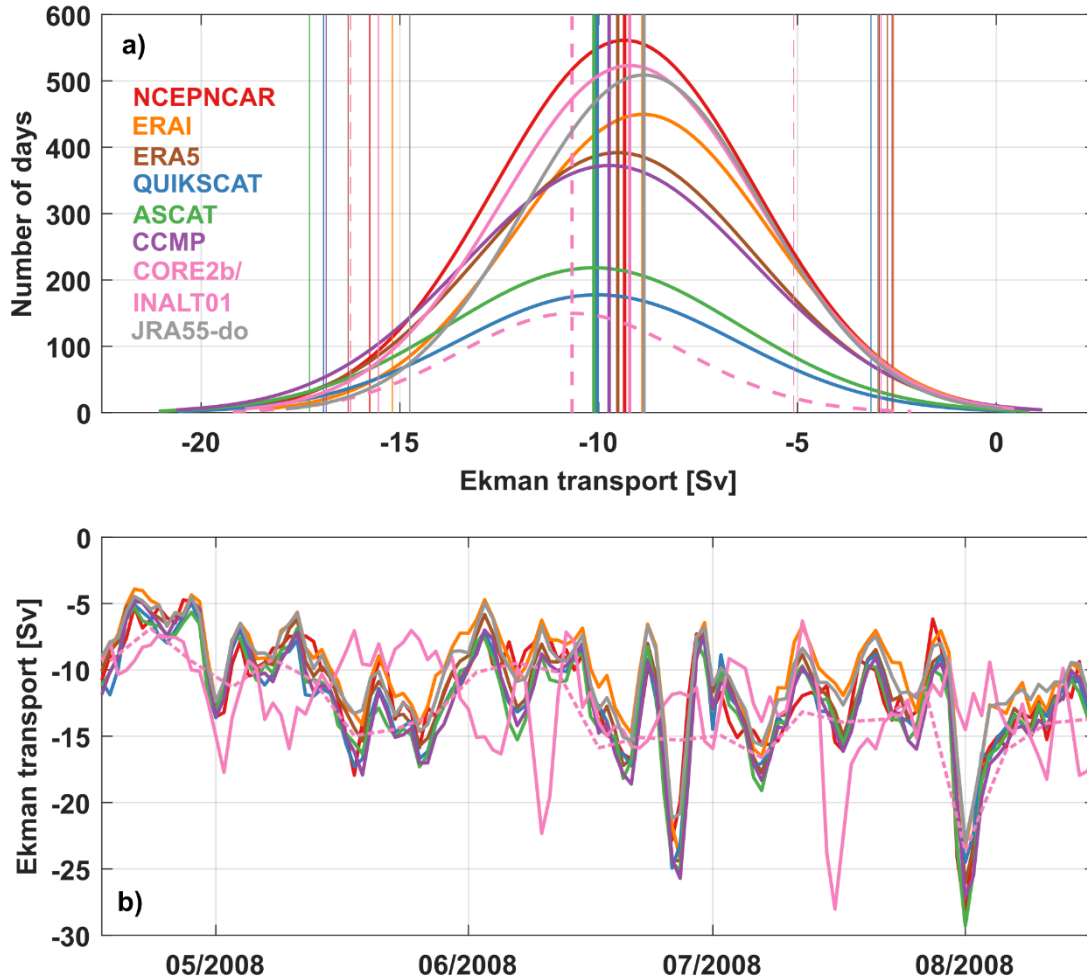


Figure 23 Density functions of the daily Ekman transports at 11°S calculated for the 8 wind products (solid colored curves) and for the INALT01 wind stress output (dashed pink curve), over the respective available periods for each product. Vertical lines mark the mean (thick lines) and $\pm 2\sigma$ (thin lines) of the derived Ekman transports. b) Daily time series of the Ekman transports shown for the period 05/2008-08/2008.

Besides the differences in the mean Ekman transports among products, we do also find their extrema to be distributed differently (Fig. 23 (a)). The 8 wind products tend to agree on the possible minimum southward Ekman transports across 11°S with the $+2\sigma$ limit varying between -2.6 Sv to -3.2 Sv. The -2σ limit, however, ranges from -17.3 Sv for ASCAT (-16.9 Sv for QUIKSCAT) to -14.8 Sv (JRA55-do). The scatterometer winds, which resolve variations with smaller spatial and temporal scales as the other products, produce more daily extreme values regarding the maximum possible Ekman transport across 11°S. The Ekman transport calculated from the 5-daily wind stress output of INALT01, does not reproduce the minima, but is just within the range of maximum Ekman transports derived from the other products. When comparing daily timeseries of the Ekman transport across 11°S (Fig. 23 (b)), the short-term variations ($T < 30$ days) in CORE II deviate strongly from those found in the other products. Although based on 5-daily model output, the short-term variations estimated from INALT01, on the other hand, agree much better with the other products. This, as well as the extremely high Ekman transport values found in the scatterometer estimates, could be a hint towards the effect of ocean current onto the wind stress playing a dominant role on these timescales.

3.5.4.2. *The seasonal cycle of the Ekman transport across 11°S*

Most of the variability in the wind forcing and surface-ocean currents has an annual periodicity with maximum amplitudes in the tropical oceans (Castellanos et al., 2015). Therefore, not only the mean Ekman transport is large in the tropics compared to other regions, its seasonal variability is as well.

Figure 24 displays the mean seasonal cycles of the Ekman transports across the same tropical and subtropical latitudes considered in section 3.5.4.1 – namely 11°S, 11°N, 26.5°N, 34.5°S. Those were all calculated over the period 2013-2018 and are shown only for the 6 wind products covering this period. Note, that the error bars give the respective standard errors per month and are indicative of the possible variations in the seasonal cycles from year to year.

The Ekman transport across 11°S (Fig. 24 (c)) is characterized by a maximum southward transport in June-August and minimum southward transport in January-March. While there is good agreement regarding the course of the year among the 6 wind products, the peak-to-peak amplitudes of the mean seasonal cycles range from 4.0 Sv (NCEPNCAR) to 5.7 Sv (ASCAT). Again, we find NCEPNCAR to show the largest deviations from the other wind products at 11°S with a more southward Ekman transport during the months September-April. When excluding NCEPNCAR from the comparison, the other products differ by 0.5 Sv in December and 1.6 Sv in July, which is just within the standard errors of the individual products for all months. When NCEPNCAR is included, differences can increase up to 2.0 Sv in April, which exceeds the standard errors. It should be noted, that Herrford et al. (2021) report a peak-to-peak amplitude of 7 Sv for the mean seasonal cycle of the Ekman transport across 11°S. That is because, their estimate was derived from the ASCAT wind stress provided by CERSAT-IFREMER, which considers atmospheric temperatures following Smith (1988). In section 3.5.3, we could show (for QUIKSCAT along 11°S; Fig. 22 (b)) that the wind stress provided with the gridded scatterometer wind products is stronger in most of the basin interior than the wind stress derived from neutrally stable 10m winds with the bulk formula by LY04.

With peak-to-peak amplitudes ranging from 12.6 Sv (ERA1) to 14.2 Sv (CCMP), the mean seasonal cycle of the Ekman transport at 11°N (Fig. 24 (a)) is even larger than that at 11°S. While, at 11°N, the estimate from NCEPNCAR is closer to the other products, we find the weakest seasonal cycle in ERA1 with less northward Ekman transport during the months January-May. The differences between products are also larger with 0.7 Sv in September and 2.3 Sv in December. As for 11°S, the differences between the 6 wind products are just within the standard errors of the individual products for all months.

At both subtropical latitudes, the mean seasonal cycles of the respective basin-wide Ekman transport are weaker compared to the tropics with peak-to-peak amplitudes ranging from 4.1 Sv to 4.6 Sv at 34.5°S (Fig. 24 (d)) and from 1.5 Sv to 2.4 Sv at 26.5°N (Fig. 24 (b)). We find the differences between the 6 wind products at 26.5°N (0.4 Sv in June and 1.3 Sv in February) to be only slightly smaller and the differences at 34.5°S to be substantially smaller (0.4 Sv in January and 0.7 Sv in May) compared to 11°S. These differences are, as for the tropical latitudes, also within the standard errors for each month, representing year to year variations of the seasonal cycles, and at 34.5°S less than half the standard errors. Regarding the course of the year, the mean seasonal cycles derived from the 6 wind products agree well with each other and with the results from other studies (e.g. Kanzow et al., 2010; Meinen et al., 2018).

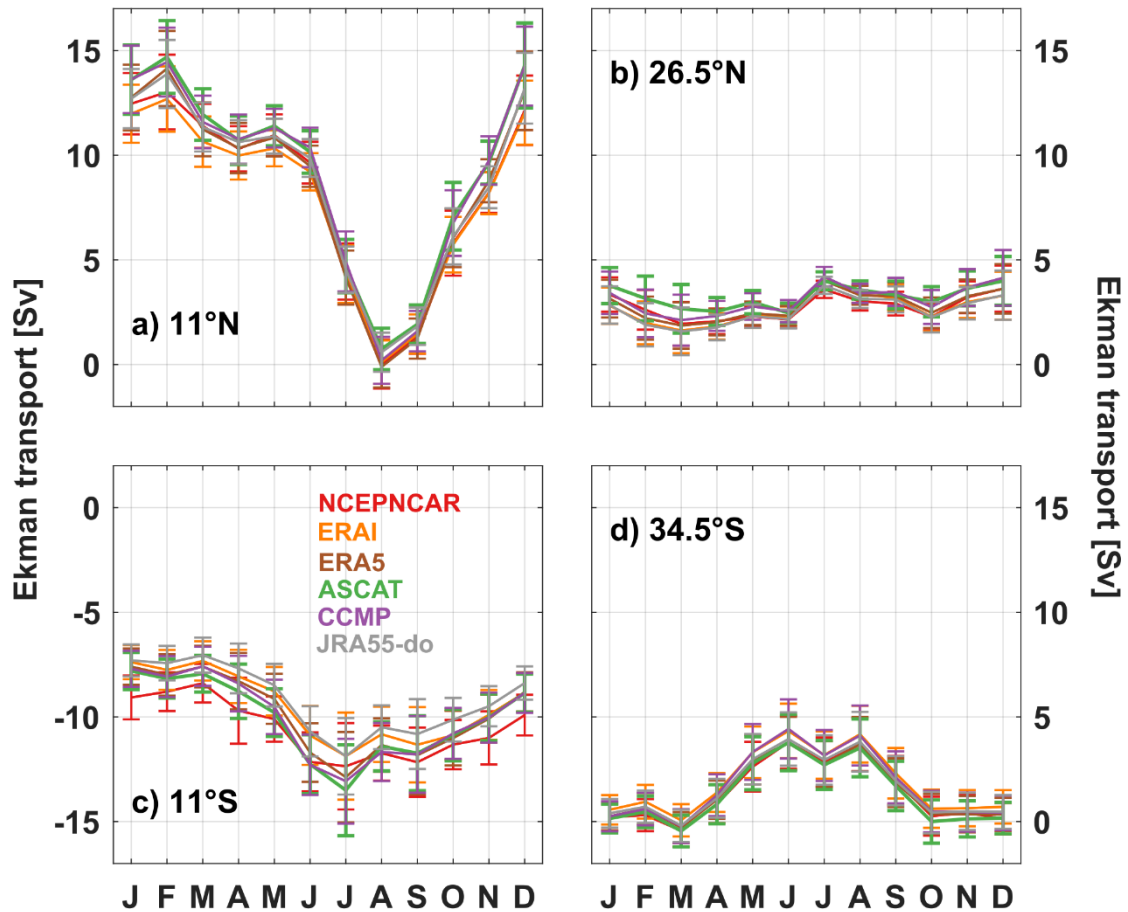


Figure 24 Mean seasonal cycles of the Ekman transport across the four latitudes 11°N (a), 26.5°N (b), 11°S (c), 34.5°S (d). These are averaged over the period 2013-2018 and calculated for the 6 wind products covering this period. Error bars give standard errors.

The uncertainties resulting from using different wind products to estimate the mean seasonal cycle of the Ekman transport are less than 20 % of the peak-to-peak amplitude for individual months at 11°N and 34.5°S. However, they can be as large as 50 % for individual months at 11°S (including NCEPNCAR), where differences between products are large, or as large as the peak-to-peak amplitude itself at 26.5°N, where seasonal variability is rather weak. As already pointed out before for estimates of the mean Ekman transport across a certain latitude, these uncertainties can translate into estimates of seasonal AMOC variability. Those can be derived by adding basin-wide Ekman transport variations to an estimate of upper-ocean geostrophic transport variations. At 11°S, for example, the uncertainties related to the Ekman transport seasonal cycle resulting from using different wind products are in some months as large as the methodological uncertainties reported for the seasonal cycle of the upper-ocean geostrophic transport there (Herrford et al., 2021). We are aware of several studies investigating the Ekman and geostrophic contributions to the seasonal cycle of the AMOC at other latitudes and using different wind products to estimate the local Ekman transport - QUIKSCAT at 26.5°N (Kanzow et al., 2010), SCOW at 34.5°S (Dong et al., 2014), CCMP at 34.5°S (Kersalè et al., 2020) – or as model forcing – NCEPNCAR (Zhao & Johns, 2014), NCEPNCAR and ERAI (Mielke et al., 2013). A more comprehensive comparison, however, is beyond the scope of this chapter.

3.5.4.3. Interannual to decadal variations in the Ekman divergence between 11°N and 11°S

The poleward Ekman transport in the tropics leads to Ekman surface convergence and subduction of water masses at subtropical latitudes as well as surface Ekman divergence and upwelling near the equator – together forming the thermocline subtropical cells (STCs; e.g. Schott et al., 2004; Tuchen et al., 2019). The Ekman surface divergence is co-located with the ITCZ, which is positioned slightly north of the equator. This results in easterly wind stress along the equator that is balanced by an eastward pressure gradient, which, for a vanishing Coriolis force, causes subsurface flow directly down the pressure gradient – the eastward EUC (e.g. Talley et al., 2011). On interannual and longer timescales the EUC was found to be connected to the strength of the STCs via the transport convergence in the thermocline layer (e.g. Rabe et al., 2008). In a recent study based on long-term observations at 23°W, Brandt et al. (2021) reported a significant increase in the EUC transport over the last decade. They could relate the strengthening of the EUC to decadal changes in the Ekman divergence across the equator between 10°N and 10°S, which in the recent decade were mainly caused by variations in the tropical North Atlantic trade winds related to the Atlantic multi-decadal variability (AMV).

Here, we test how the Ekman transports across 11°S and 11°N (Fig. 25 (b, a)) differ between the 8 wind products on interannual to decadal timescales, and whether they all reproduce the increase in Ekman divergence since 2008. To extract the variability on interannual timescales, the individual Ekman transport time series were 270-day low-pass filtered after subtracting the respective annual and semi-annual harmonics.

At 11°N, we find interannual variations of the order of up to 5.5 Sv in CORE II and 5.1 Sv in NCEPNCAR, and of 3.5-4.3 Sv in the other products. Besides the larger amplitude in variations, the CORE II estimate also deviates from NCEPNCAR by an offset of about 1.3 Sv averaged over the period 1990-2009. When excluding CORE II, the other filtered Ekman transport time series differ by 1.3 Sv on average with a maximum possible range of 2.5 Sv. At 11°S, the interannually filtered Ekman transport time series derived from CORE II and NCEPNCAR are very similar. They deviate substantially from the other products in some years – by up to ± 1.5 Sv in, for example, 1990-1994 or 2002-2003 - and agree well with the other products in other years. After 2010, when CORE II is not available anymore, NCEPNCAR shows relatively large deviations from the other products (> 1.7 Sv) in the form of a spurious decadal signal. When excluding NCEPNCAR and CORE II, the interannual variations of the Ekman transport at 11°S are comparable to those at 11°N with amplitudes of 3.3-4.5 Sv and differences between individual time series are less than 1.8 Sv. For completeness, we also added the interannually filtered Ekman transport time series at 11°S estimated from the INALT01 model output that was forced with CORE II winds (section 3.4.1). The Ekman transport derived from INALT01 is, as expected, stronger than the estimate from CORE II, however, it shows similar interannual variations as CORE II.

The Ekman divergence in the tropical Atlantic is calculated as the difference between the filtered Ekman transport time series at 11°N and 11°S. On interannual timescales, it shows possible variations of 6.8 Sv and of 5.2 Sv when excluding the NCEPNCAR and CORE II estimates. The differences between the wind products at each latitude can add up to differences in the interannually filtered Ekman divergence of 4.8 Sv and of 3.2 Sv when excluding the NCEPNCAR and CORE II estimates. Unfortunately, at the time when this analysis was done, we did not have INALT01 output at hand for regions north of the equator (see Fig. 27 (h) for covered region), therefore, we cannot provide an INALT01 estimate for the Ekman divergence for now.

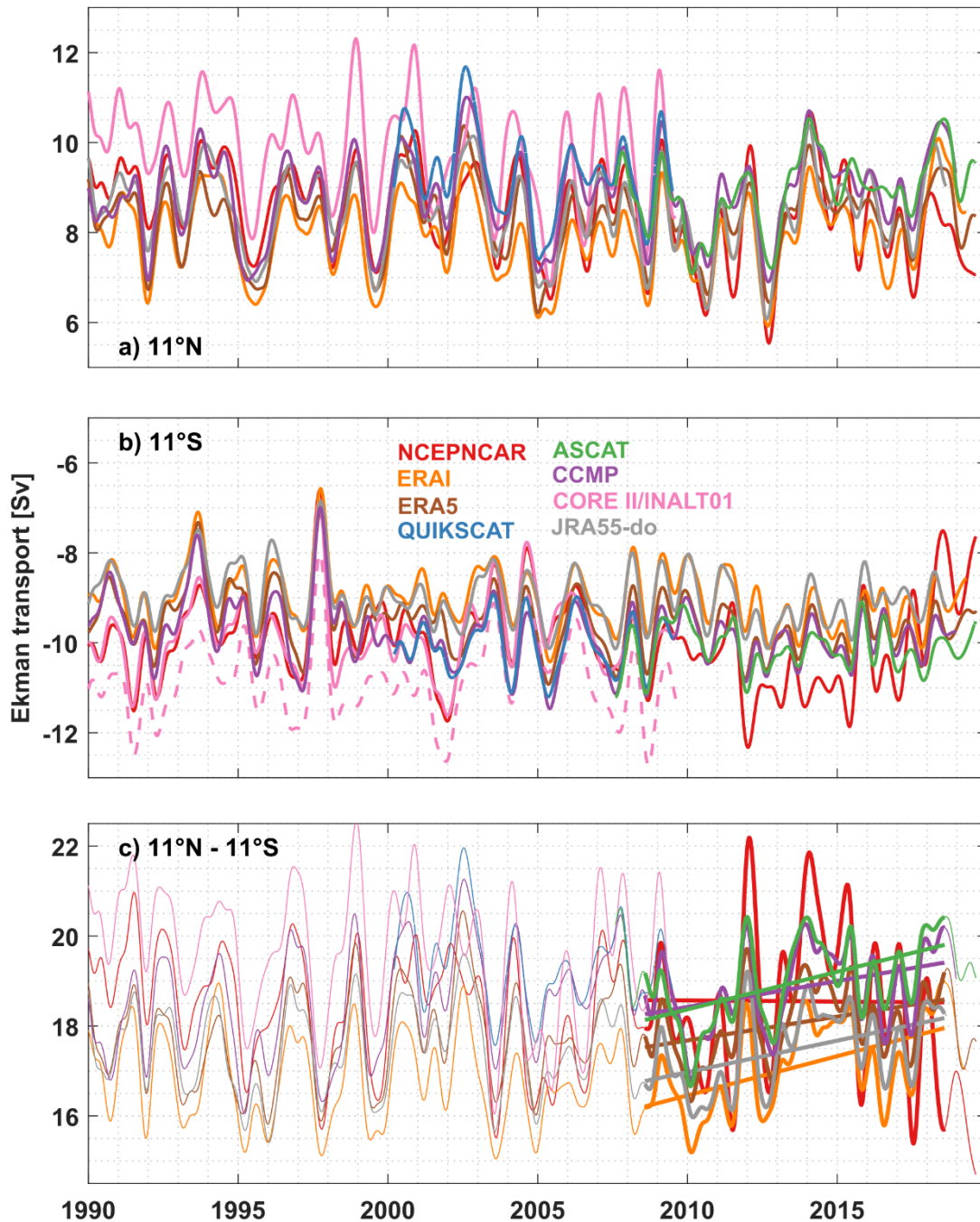


Figure 25 Transport timeseries of the Ekman transport across 11°N (a), the Ekman transport across 11°S (b), the difference between both representing the basin-wide Ekman divergence between both latitudes (c), derived from the 8 gridded products presented above. After removing the respective annual and semi-annual harmonics, all the time series have been 270-days low-pass filtered. Colored lines in (c) show linear ten-year (08/2008- 07/2018) trends fitted to the Ekman divergence time series derived from 6 of the wind products.

We derive ten-year trends (2008-2018) from 6 of the wind products (NCEPNCAR, ERAI, ERA5, ASCAT, CCMP, JRA55-do) - QUIKSCAT and CORE II do not cover the considered period. Except for the estimate from NCEPNCAR, all products agree on a general strengthening of the Ekman divergence over the last decade. NCEPNCAR shows no trend over the considered period. At the same time, the interannually filtered Ekman divergence time series derived from NCEPNCAR shows spurious decadal variations after 2010, which are mainly caused by variations in the Ekman transport across 11°S not found in the other products. Excluding NCEPNCAR, the positive linear trends can differ by about 30 % among products

ranging from + 1.0 Sv dec⁻¹ to + 1.7 Sv dec⁻¹. This uncertainty cannot be attributed to a certain type of wind product and adds to the statistical uncertainties of decadal signals.

Although we used daily values and chose slightly different latitudes, we were able to reproduce the ten-year trends in the Ekman divergence presented in Brandt et al. (2021). They calculated their trends based on monthly values of the Ekman divergence between 10°N and 10°S over the period 08/2008-07/2018 already comparing trend estimates from three different wind products – CCMP, JRA55-do as well as a different version of gridded ASCAT winds (provided by JPL; e.g. Liu et al., 2010). For all products they derived positive trends ranging from 1.1 Sv (CCMP) to 2.0 Sv (ASCAT) per decade. We derive a slightly weaker positive trend of 1.7 Sv per decade from ASCAT (Table 4;

Table 4 Linear trends in Ekman divergence between 11°N-11°S for 6 different wind products with 95% confidence intervals – after Brandt et al. (2021). * The trend from CORE II was calculated for a slightly different period – 01/1999 – 08/2009.

Wind product	Linear trends in Ekman divergence between 11°N - 11°S [Sv dec ⁻¹]	
	08/2008-07/2018	01/2000-12/2010
NCEPCAR	-0.1 ± 1.9	-1.0 ± 1.2
ERA1	1.7 ± 1.0	-1.0 ± 0.8
ERA5	1.0 ± 0.9	-1.1 ± 0.9
QUIKSCAT	-	-
ASCAT	1.7 ± 0.9	-
CCMP	1.1 ± 1.0	-1.2 ± 1.0
CORE II	-	-0.8 ± 1.6*
JRA55-do	1.4 ± 0.9	-1.5 ± 0.9

column 2). This could be due the different choice of latitudes, which, in case of the scatterometer products that resolve much smaller scales, may result in larger differences or due to using different versions of gridded ASCAT winds. The ten-year trends in the Ekman divergence calculated from the two ECMWF wind products are also within the same range as the trends presented in Brandt et al. (2021).

The decade before - here, we consider the periods 1999-2009 for CORE II and 2000-2010 for the other products - is characterized by a weakening of the Ekman transport divergence between 11°N and 11°S (Table 4; column 3). This weakening is of similar order of magnitude as the Ekman divergence strengthening from 2008-2018 with linear trends ranging from -0.8 Sv (CORE II) to -1.5 Sv (JRA55-do). Interestingly, NCEPCAR and CORE II show a weakening of the surface Ekman divergence over the respective periods 2000-2010 or 1999-2009, which is not statistically significant but comparable to the other products. Tuchen et al. (2020), discussed the northern hemisphere to dominate the strengthening of the STCs in the last decade and the southern hemisphere the weakening before 2000. These decadal variations in the Ekman transport divergence, which we find in most of the wind products, support the proposed linkage between the tropical Atlantic Ekman transport divergence and the AMV, which shifted from a warm phase before 2000 to a cold phase afterwards thereby influencing the strength of the trade winds (e.g. Knight et al., 2006).

3.5.4.4. *The seasonal cycle of the wind stress curl along 11°S*

Small differences in surface winds can lead to spurious signals in spatial derivatives like the wind stress curl $\nabla \times \vec{\tau}$, which has dynamical effects on the ocean currents. Analyzing the output of the INALT01 model, which is forced with relative winds calculated from CORE II (see section 3.4.1), Herrford et al. (2021), for example, found the geostrophic contribution to seasonal AMOC variability at 11°S to be governed by oceanic adjustment to local as well as remote wind forcing.

Here, we want to test how seasonal variability of the wind stress curl along 11°S differs among products. To investigate the annual cycle of the wind stress curl, we calculated its amplitudes (Fig. 26; only along 11°S) and phases (Fig. 27; entire tropical Atlantic) for the 8 wind products. A feature that all wind products show is a patch in the eastern basin interior, which is characterized by strong amplitudes of the annual harmonic ($0.015\text{--}0.02 \cdot 10^{-6} \text{ N m}^{-3}$) and relatively constant phase (minima in October to mid-November) over that area. Most of the products produce a minimum amplitude and an abrupt phase shift (~ 6 months) in the western basin interior (located between 15–20°W as well as a gradual increase in seasonal cycle strength from there towards western boundary related to a second patch of relatively constant phase (minimum in mid-April to May). We find a variety of small-scale features in the longitudinal distribution of the annual harmonics estimated from QUIKSCAT and ASCAT. Those are the result of small-scale information contained in the scatterometer winds, which are not resolved in the coarser reanalysis products and emphasized by the high-pass filtering through the spatial derivatives. Although these small-scale features make it harder to identify a clear separation between the two patches, the annual harmonic of the wind stress curl estimated from ASCAT exhibits minimum values between 20–25°W. Interestingly, the estimate from INALT01 does also show a more variable structure compared to all the wind products, which are based on reanalysis.

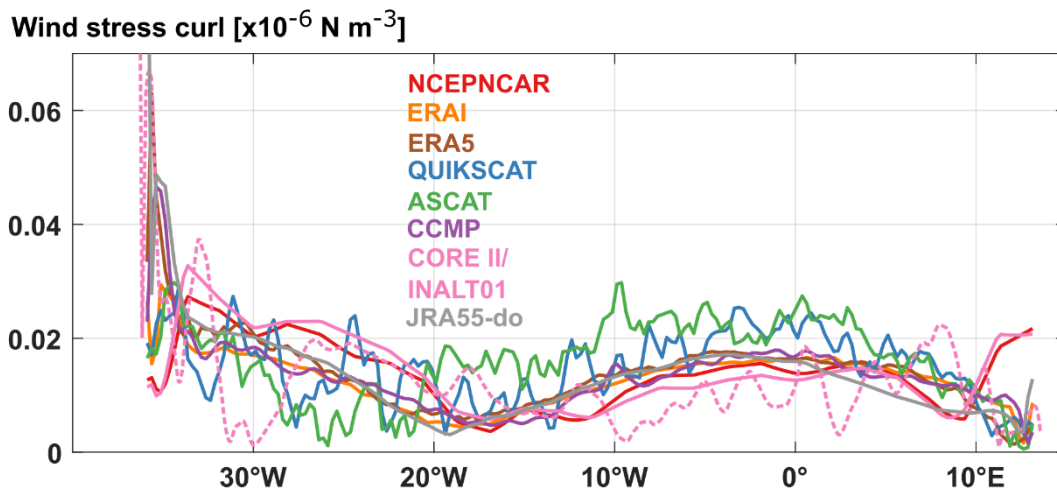


Figure 26 Amplitudes of the annual harmonic of the wind stress curl along 11° S as a function of longitude. These are derived from the 8 wind products (solid colored curves) and from the INALT01 wind stress output (dashed pink curve), and calculated over the respective available periods for each product.

While, in the basin interior of the tropical Atlantic, the different wind products tend to agree on the general large-scale pattern of the seasonal cycle in wind stress curl, the largest differences can be found at the eastern and western boundaries. At the eastern boundary, NCEPNCAR and CORE II produce strong seasonal cycles in the wind stress curl with amplitudes of up to $0.02 \cdot 10^{-6} \text{ N m}^{-3}$ (Fig. 26). The other products exhibit minimum values of less than $0.01 \cdot 10^{-6} \text{ N m}^{-3}$ east of 10°E. At the western boundary, the amplitudes of the annual harmonics of the wind stress curl estimated from NCEPNCAR and CORE II are smaller compared to the other products. They drop from more than $0.025 \cdot 10^{-6} \text{ N m}^{-3}$ at 33°W to $0.01 \cdot 10^{-6} \text{ N m}^{-3}$ at 35°W. ERAI, QUIKSCAT and ASCAT also show an abrupt decrease in the seasonal cycle amplitudes towards the western boundary, but only down to $0.017 \cdot 10^{-6} \text{ N m}^{-3}$. Interestingly, estimates from CCMP, ERA5, JRA55-do and the INALT01 model output produce very large amplitudes ($> 0.06 \cdot 10^{-6} \text{ N m}^{-3}$) of the annual harmonic of the wind stress curl close to the western boundary.

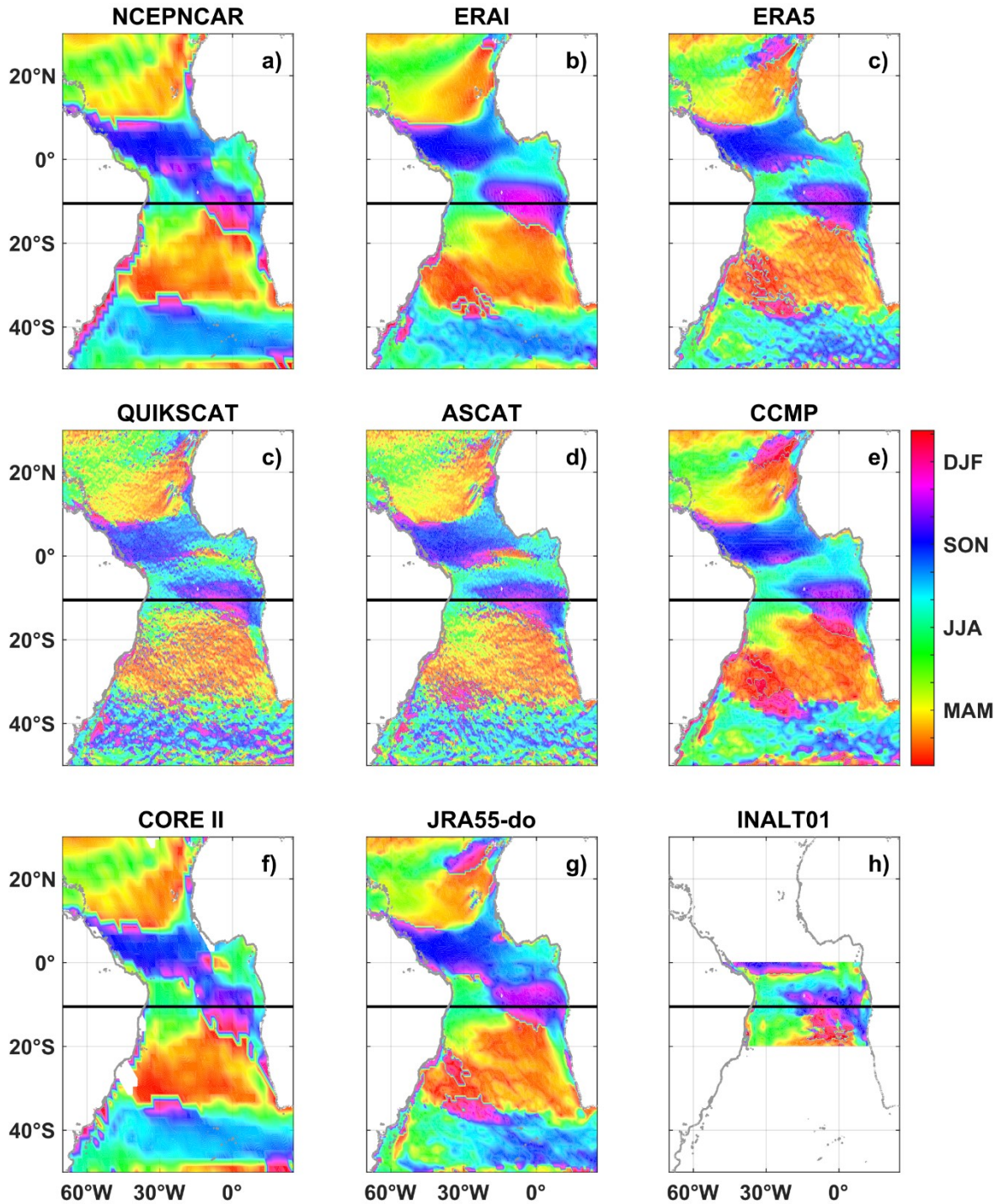


Figure 27 Phases (timing of the minimum) of the annual harmonic of the wind stress curl derived from the 8 wind products (a-g) and from the INALT01 wind stress output (h). The horizontal black lines mark 11°S.

Higher amplitudes of the annual cycle of the wind stress curl at the western boundary in CCMP, ERA5 and JRA55-do are probably related to a higher resolution of the products or the underlying models. In INALT01, on the other hand, the higher amplitudes as well as the variable longitudinal structure could also reflect the influence of ocean currents included in the wind stress formulation for the INALT01 model output. Observational and numerical studies found the effect of the ocean currents to weaken the mean surface stress, to partially control the Western boundary currents and to dampen mesoscale activity (e.g. Renault et al., 2017). The results from this analysis indicate, that the current feedback does have an influence on the spatial distribution of seasonal variability along 11°S.

When used to force an ocean model, temporal and spatial differences in the wind stress curl derived from different wind products will result in difference in the simulated ocean circulation. These differences are perturbations in the ocean dynamics and can cause a variety of model discrepancies and, therefore, mask actual model deficiencies. For example, in INALT01, seasonal AMOC variability at 11°S was found to be governed by the geostrophic transport variability in the eastern basin, which was forced by the local wind stress curl over the basin interior and, additionally, by Rossby waves radiated from the eastern boundary (Herrford et al., 2021). Concurrently, the contribution from the western basin is rather small as the transport variability in the basin interior related to local wind curl forcing is mainly compensated by the Western Boundary Current (Herrford et al., 2021). As shown in this study, the ratios of local and remote wind forcing can be very different among wind products, which adds to the uncertainties of at least seasonal AMOC variability estimated from ocean models. Furthermore, the observed differences in the seasonal wind stress curl variability at the eastern boundary, as another example, could have an influence on estimates or the simulation of coastal upwelling in that region, which is to a large extent controlled by the alongshore winds and their curl. Especially, the coarser resolution NCEPNCAR has previously been reported to produce weak winds as well as altered wind stress curl fields in all of the upwelling regions (e.g. Taboada et al., 2019). An underrepresentation of upwelling and the associated cooling are assumed to contribute to sea surface temperature biases in global climate models in eastern boundary upwelling ecosystems (Richter, 2015).

At other latitudes, the differences in seasonal wind stress curl variability can be even larger among products: NCEPNCAR and CORE II show some spurious wave-like pattern in the tropical North Atlantic (Fig. 27 (a, f)). Phase shifts in the wind stress curl seasonal harmonics - for example in the region around Cape Verde, in the central equatorial Atlantic or in the Brazil-Malvinas Confluence region - can have completely different locations (cf. Fig. 27 (a, b, e)). Only some products (e.g. QUIKSCAT and ASCAT) are able to resolve the mesoscale structures, which break up large-scale patterns of similar annual harmonic phase in the subtropical South Atlantic wind stress curl. Although it would be interesting, a more comprehensive evaluation of the effects of these differences on the large-scale circulation at other latitudes than 11°S is beyond the scope of this study.

3.5.4.5. Interannual to decadal variations in the tropical South Atlantic wind stress curl

On interannual timescales, the upper-ocean geostrophic transport contribution to the AMOC in the subtropics and tropics is assumed to be also to a large extent wind-driven (e.g. Zhao & Johns, 2014b). Analyzing a set of hindcast experiments within the INALT01 model, Rühls et al. (2015) showed that decadal to multidecadal buoyancy-forced changes in the basin-scale AMOC transport, which manifest themselves in the western boundary current of tropical South Atlantic, are also masked by strong interannual to decadal wind-driven gyre variability of the western boundary current.

Here, we want to investigate how the interannual to decadal wind-driven gyre variability differs among wind products. In accordance with the results from Rühls et al. (2015), the time series of wind stress curl anomalies from the time mean along 11°S were 700 days low-pass filtered to extract the contained interannual to decadal variations. Hovmöller diagrams of the filtered wind stress curl anomalies along 11°S (Fig. 28) reveal pronounced spatial and temporal differences among products: The high spatial resolution of QUIKSCAT and ASCAT (originally ~25 km) clearly translates into the strength of spatial gradients emphasizing small-scale features, which are not resolved in any of the reanalysis products, not even ERA5 with a horizontal resolution of ~31 km.

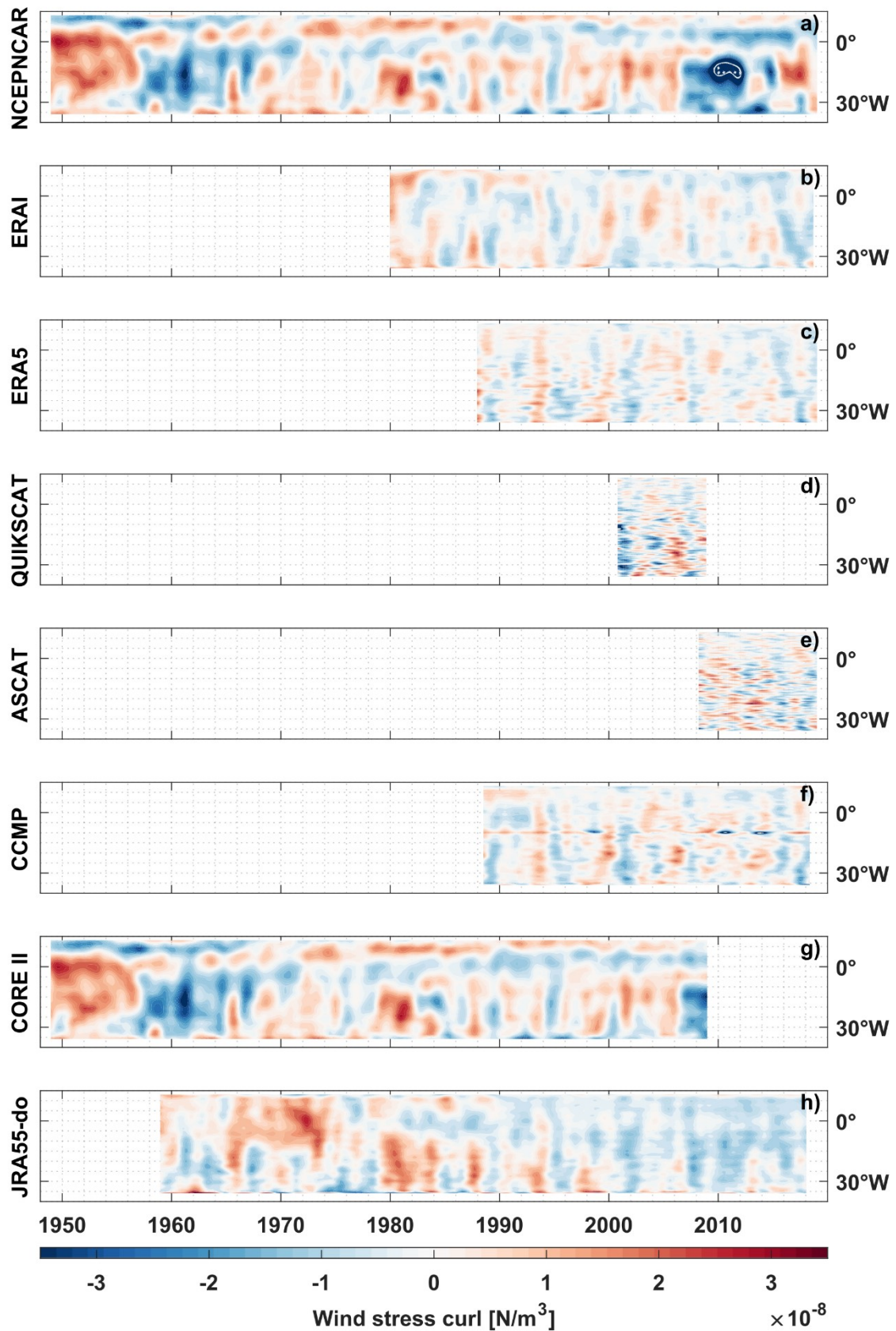


Figure 28 Hovmoeller diagrams of 700 days low-pass filtered wind stress curl anomalies from the time mean along 11°S.

Interestingly, the wind stress curl derived from CCMP winds reveals a spurious anomaly at 10°W | 11°S (Fig. 28 (e)), which is close to the location of one of the PIRATA buoys (10°W | 10°S; see section 2 c i). In the tropical Pacific, McGregor et al. (2016) observed spurious curl around the buoy locations that is

related to the procedure used in CCMP production to merge the absolute winds from the buoys with satellite-derived relative winds. Between ERAI and ERA5, differences in the filtered wind stress curl timeseries along 11°S are small and mainly related to the differences in the horizontal resolutions. While in ERAI, ERA5 and JRA55-do positive and negative anomalies of the wind stress curl tend to be more longitudinally coherent, this is not the case for NCEPNCAR and CORE II.

In overlapping years, the scatterometer products, the two ECMWF products and CCMP show similar patterns of interannually alternating positive and negative anomalies. The resemblance between those five products is expected, as the ECMWF products assimilate the scatterometer winds (Hersbach, 2010a), while CCMP relies on both, the scatterometer products as well as ERAI as the first guess field (Atlas et al., 2011). JRA55-do shows good agreement with ERAI and ERA5 in the 1980-1990s, but is dominated by more negative anomalies in recent decades. Torralba et al. (2017) found exceptionally strong trends in the underlying model JRA55, which were not found in the other reanalysis or model forcing data sets analyzed in their study. Estimates from NCEPNCAR and CORE II agree well with each other, but deviate strongly from all the other products. In contrast to the other reanalysis products, their corresponding filtered timeseries of wind stress curl anomalies along 11°S are dominated by decadal to multidecadal variations. NCEPNCAR (e.g. Hurrell & Trenberth, 1998) as well as the CORE II model forcing (e.g. He et al., 2016) have been reported to exhibit spurious multidecadal temperature and wind variability before. The only other wind product in this collection going back into the 1960-1970s, JRA55-do, does also show strong decadal to multidecadal variations in the basin-wide wind stress curl along 11°S, which, however, appear out-of-phase with the other products. Only in the 1980, when ERAI is also available, there is some agreement between NCEPNCAR, CORE II, JRA55-do and ERAI. The CORE II forcing dataset was excessively used in the past – for example within the frameworks of the Coordinated Ocean-ice Reference Experiments and the subsequent Ocean Model Intercomparison Project (e.g. Griffies et al. 2009; Griffies et al., 2016). As wind stress curl has dynamical effects on the ocean currents, the large differences in the wind stress curl variability on long timescales between CORE II and the new JRA55-do model forcing can cause substantial discrepancies in the outputs of ocean models forced with these products.

Because of existing historical and new observational estimates, Rühls et al. (2015) focused their analyses with the INALT01 model (Durgadoo et al., 2013) on the western boundary current at 6°S – the NBC. They found a major contribution of wind-driven circulation variability to the interannual to decadal NBC variability. Further, they report the northward NBC transport at 6°S to be relatively strong in the 1960s, weaker between 1970 and 1985, and stronger again in the 1990s. The wind stress curl along 11°S (Fig. 28 (g)) as well as Sverdrup transports across 3°S and 11°S (Fig. 29) derived from CORE II (NCEPNCAR) show the same decadal variations as the simulated wind-driven NBC transport at 6°S – although with opposite sign. This makes sense, as negative wind stress curl anomalies would strengthen the on average negative wind stress curl of the tropical Sverdrup gyre, thus, the anti-cyclonic circulation in the tropical South Atlantic, and, consequently increase the wind-driven transport of the northward NBUC/NBC in the tropical South Atlantic. A model forced with JRA55-do, which does not show the same decadal variations as CORE II, will probably produce different results than those from INALT01 – at least on decadal to multi-decadal timescales and in the tropical South Atlantic.

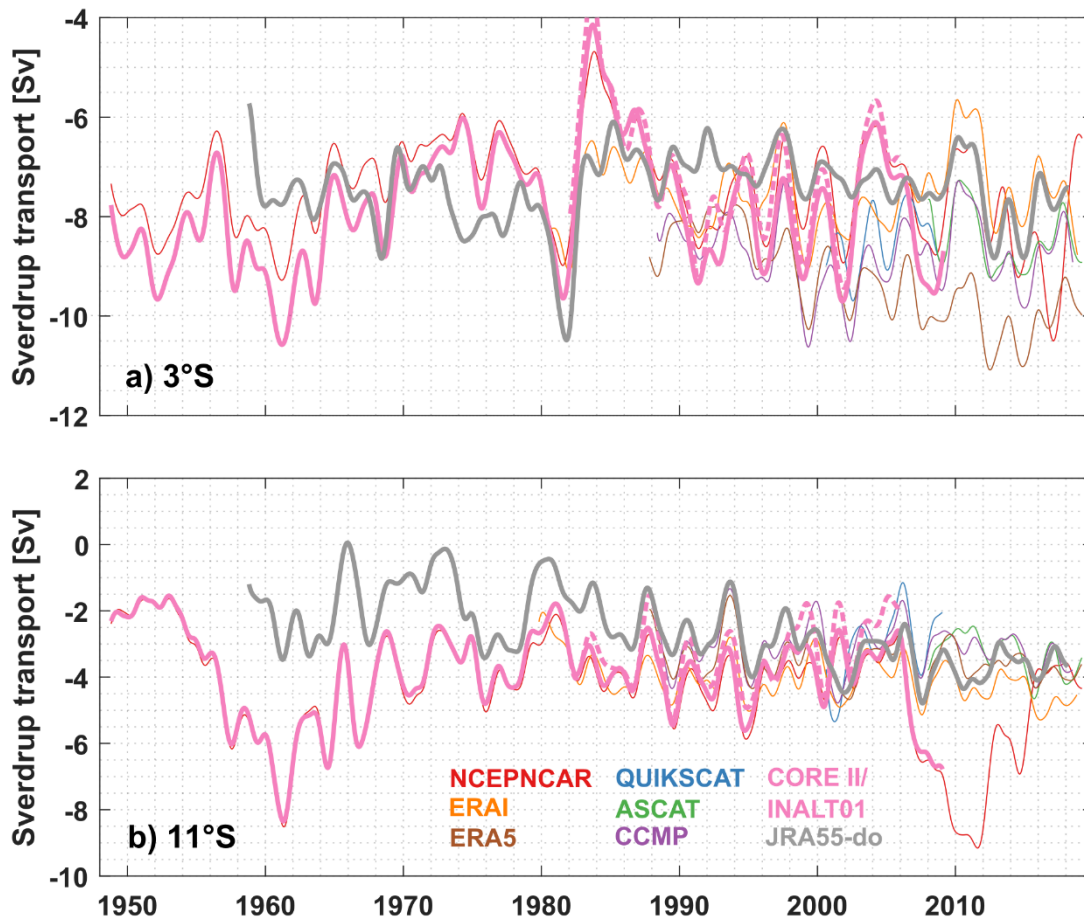


Figure 29 Basin-wide Sverdrup transport across 3°S (a) and 11°S (b). The transport time series were 700-day low-pass filtered to extract variations on interannual to decadal timescales.

The integral effect of the wind stress curl can be described by the Sverdrup transport. Therefore, we additionally show timeseries of Sverdrup transports across 3°S and 11°S (Fig. 29) calculated from the filtered wind stress curl anomalies of the different gridded products following Eq. (12). On average, the Sverdrup transport across 3°S (ranging from -7.5 Sv to -8.5 Sv) is by about a factor of 2 larger than that across 11°S (ranging from -2.5 Sv to -4.3 Sv) and southward across both latitudes. Interannual variations in NCEPNCAR and CORE II can be as large as 5.8 Sv at 3°S and 7.6 Sv at 11°S, while in JRA55-do they can have amplitudes of 4.8 Sv in at both latitudes. However, in all three products interannually variability is superseded by decadal variations. When excluding NCEPNCAR, CORE II and JRA55-do, interannual variations can range from 2 Sv to 3.5 Sv at both latitudes, which is in the same order of magnitude as the differences between individual products. As such systematic differences in the wind stress curl accumulate toward the west, these differences can add, for example, to the uncertainties of estimates meridional heat transport accomplished by the western boundary currents or other higher-order processes in model studies.

3.6. Summary and conclusions

In this study, we evaluated a comprehensive set of wind products widely used within the oceanographic community, including scatterometer winds, merged observations as well as older and newer generations of reanalysis products and model forcing datasets (Table 2). We analyzed differences between those wind products regarding their mean wind fields and variability on seasonal to decadal time scales in the tropical Atlantic (sections 5 a, b), and how these differences translate into

the local wind stress, wind stress curl or derived Ekman transport, Ekman divergence or Sverdrup transports variations (sections 5 c, d).

All of the considered wind products are able to capture the mean large-scale atmospheric circulation in the tropical Atlantic (Fig. 19). While the overall differences among products are smaller than 10 % for wind speed and 5° in wind direction almost everywhere in the region, locally, differences can be as large as 60 % in wind speed and 160° in direction. Maps of anomalies from the 2008 ensemble mean wind field (Fig. 20) reveal substantial geographic differences between individual products. We found CCMP winds, to be closest to the ensemble mean of 8 gridded wind products, which is expected as they utilize the scatterometer winds as well as ERAI in their production. The observed spatial variations are in good agreement with previous studies. They are thought to be caused by general biases, which, especially for the reanalysis products, have been described before and analyzed thoroughly in several recent studies – for example in Chelton & Freilich (2005), Praveen Kumar et al. (2012), Fujiwara et al. (2017), Taboada et al. (2019), Ramon et al. (2019) or Belmonte Rivas & Stoffelen (2019). The wind field deviations of the scatterometer products from the ensemble mean are in agreement with the accuracies, which have been investigated through comparisons with daily winds from open-ocean moored buoys in several studies (predominantly QUIKSCAT): Ebuchi et al. (2002) compared QUIKSCAT winds to a global set of moored buoys over the period 1999-2001 and found root mean square errors (RMSEs) of about 1 m s⁻¹ for wind speed. Chelton and Freilich (2005) found RMSE values of 1.2 m s⁻¹ using buoys from the National Data Buoy Center (NDBC) and only co-locations obtained in the middle of QUIKSCAT's measurement swath. For their gridded QUIKSCAT and ASCAT products, Bentamy & Croize-Fillon (2012) find RMSEs to not exceed 2 m s⁻¹ and 20° for wind speed and direction, respectively.

We correlated the variability in the gridded products to the directly observed wind data from the open-ocean moored PIRATA buoys (Fig. 21). The comparison reveals substantial differences in the abilities of the different wind products to capture the observed variability in the tropical Atlantic. Additionally, correlations between winds measured at 13 moored buoys and the 8 gridded wind products were depending on the considered timescale as well as the region or wind regime. We found winds from the CORE II forcing dataset to not be able to reproduce the observed variability on intra-seasonal timescales at all of the buoy locations. Scatterometer winds showed better agreement with the PIRATA winds on shorter timescales, however, revealed problems on interannual timescales and in the eastern tropical Atlantic. We found CCMP winds to performed best in reproducing the observed variability, closely followed by the ECMWF wind products ERAI and ERA5. The new model forcing JRA55-do performs as well as the ECMWF products on most regions, however has problems to reproduce the observed intra-seasonal to seasonal variability in the equatorial and eastern tropical South Atlantic. It should be noted, that CCMP directly incorporates data from the PIRATA buoys, which should result in a good agreement with those observations at the locations of the buoys. However, the way in which point measurements are incorporated into the CCMP winds can also lead to problems - we find, for example, spurious anomalies in spatial derivatives of the wind stress around the buoy locations,

To understand the differences among the wind products, it is crucial to consider how different wind products are produced as most of them are not independent from each other (see section 3.2). During the conduction of this study, we found a large amount of studies comparing subsets of our wind product collection with each other (e.g. Fujiwara et al., 2017; Taboada et al., 2019; Ramon et al., 2019), or with observations from open-ocean buoys (e.g. Chelton & Freilich, 2005; Bentamy & Croize-Fillon, 2012; Praveen Kumar et al., 2012; McGregor et al., 2016) and ships (e.g. Smith et al., 2001). With the

purpose of answering a certain scientific question, however, most of these studies focus only on a certain mechanism, region or timescale. Further, there seems to be a lot of insider knowledge on the benefits and caveats of different wind products and observations within the climate science community, that is not necessarily published or documented otherwise. We would like to argue, that there is a need for more comprehensive analyses – maybe in form of synthesis projects or studies, which include a more complete set of wind products evaluated on a global spatial scale and a variety of timescales. Please note, that parallel to the work on this study, we started to build a modular and open-source Python toolbox called “windeval” (<https://git.geomar.de/wind-products/windeval>) that could be used easily and to semi-automatically prepare evaluations across many different wind products in the near future.

Small uncertainties in the wind fields can translate into derived variables: Testing a set of bulk algorithms depending on wind speed (Fig. 22), we found that uncertainties from using different wind stress parametrizations can make up 15 % of the momentum flux into the ocean. In the tropical Atlantic basin interior, those uncertainties are of the same order of magnitude as the differences between individual products. In agreement with previous studies (e.g. Renault et al., 2017; Abel et al., 2017), the output from the INALT01 model, which takes into account the effect of the underlying ocean surface velocities onto the wind stress, results in larger wind stress values along 11°S.

For an integral variable like the Ekman transport across a certain latitude, the choice of wind product can result in uncertainties of ~15 % in the tropics and up to 40 % in the subtropics (Table 3). The uncertainties presented here could, for example, be of interest when comparing AMOC estimates across project and latitudes as the basin-wide Ekman contribution to the AMOC is often calculated without evaluating the choice of the chosen wind product. While all other wind products show good agreement regarding seasonal, interannual and decadal variability in the Ekman transports, we found NCEPNCAR and CORE II to be particularly problematic at 11°S. NCEPNCAR shows a weaker seasonal cycle for the Ekman transport across 11°S (Fig. 24) and both produce inconsistent equatorial upwelling exhibiting spurious decadal wind stress variations in the tropical Atlantic (Fig. 25).

For the spatial derivative of the wind stress, the wind stress curl, we find systematic differences between the wind products. Throughout the basin, the wind stress curl derived from scatterometers is characterized by small-scale information, which are not resolved in the coarser reanalysis products and emphasized by the high-pass filtering through the spatial derivatives. In the eastern and western boundary regions along 11°S, the amplitudes of the seasonal cycle of the wind stress curl in NCEPNCAR and CORE II differ noticeably from those in the other products (Fig. 26). At the eastern boundary, this could result in wrong estimates of coastal upwelling, while at the western boundary, estimates of the wind-driven contribution to the NBUC could be misrepresented. On interannual to decadal timescales, NCEPNCAR and CORE II reveal large spatial and temporal deviations from the other products, including spurious multi-decadal variations in the tropical South Atlantic (Fig. 28). The new generation wind forcing product, JRA55-do, does also show strong but different decadal to multidecadal variations in the basin-wide wind stress curl along 11°S. Torralba et al. (2017) report not only NCEPNCAR and the JRA55 reanalysis to experience spurious trends on a global scale, but also the ECMWF winds and CCMP. When used to force a model, temporal and spatial differences in the wind stress curl derived from different wind products will result in differences in the simulated ocean circulation. Therefore, the quality of wind forcing data sets are especially crucial in ocean modelling. Model results regarding wind-driven processes, especially in the tropics, should be interpreted with regard to the uncertainties in respective the wind forcing. We think, that a next step would be to investigate how the large-scale

circulation in the tropical Atlantic changes between model runs, for example, within the INALT configurations (Schwarzkopf et al., 2019), with different wind forcing. We know, that there are current efforts to investigate the zonal wind-driven current system in the tropical Atlantic as simulated with the INALT20X model under CORE II and JRA55-do forcing (Kristin Burmeister, personal communication). We would suggest to extend the effort to the tropical South Atlantic including the Western boundary current system off Brazil and the AMOC at 11°S, which are currently observed with moored observations at the boundaries. Further, one could extend the comparison adding a model run forced with ECMWF winds, which we found to perform well in the region of interest. Our results show that it is important to carefully consider the large uncertainties in individual wind products, particularly in the tropical South Atlantic region, to excessively validate global products against observations and to test the sensitivity of derived results to the choice of wind product.

3.7. Acknowledgements

I would like to sincerely thank Ezra Eisbrenner and Willi Rath for their inspiring discussions, helpful comments and making a first version of the “windeval” toolbox possible. I am thankful for the helpful comments from Kristin Burmeister and Peter Brandt. Further, I would like to thank Finn Heukamp, who helped with the development of the toolbox. His research assistant position for 6 months was funded by Research Division 1 at GEOMAR.

4. Water mass changes along 11°S from two transatlantic hydrographic sections occupied in 1994 and 2018

Abstract

The Atlantic Meridional Overturning Circulation (AMOC) is linked to the formation, transformation and advection of water masses. Water mass property changes are related to variations in the oceanic heat and freshwater transports as well as changes in the large-scale ocean circulation. Two full-depth transatlantic sections in the tropical South Atlantic, separated by 24 years, are analyzed regarding water mass property distributions and long-term water mass changes along 11°S. I found the vertical and horizontal distributions of property extrema in the Brazil and Angola Basins to be in agreement with observations reported in previous studies. I can confirm a warming of the central and lower intermediate waters in the western boundary region off Brazil between 1994 and 2018, and found those signals to extend eastward into the Angola Basin after 1994. Dissolved oxygen distributions along 11°S support a vertical expansion of the tropical South Atlantic oxygen minimum zone, but also showed a reduced westward extent between 1994 and 2018. The temperature changes in the deep and bottom waters of the Brazil Basin are in agreement with previous studies, who reported the warming of the Antarctic Bottom Water (AABW) and cooling of the lower North Atlantic Deep Water (NADW) to be mainly caused by volume changes, however, decadal temperature variations on isopycnals to also contribute to the observed signals. I found an oxygen increase of 2-3 $\mu\text{mol kg}^{-1}\text{dec}^{-1}$ within the AABW layers of the Brazil Basin, which has not been observed before and could hint towards a dominance of local mixing processes over changes in the source waters. A similar oxygen increase as well as a temperature decrease on isopycnals and isobars was observed in the lower NADW/lighter AABW layers above the western flank of the Mid-Atlantic Ridge as well as the entire abyssal Angola Basin below 2000 m, indicating that deep waters from the eastern Brazil Basin are likely to fill the abyssal Angola Basin.

4.1. Introduction

The Atlantic Meridional Overturning Circulation (AMOC) is responsible of a large fraction of the heat transport in the ocean (e.g. Talley et al., 2011) and, therefore, directly related to the Earth's climate (e.g. Rahmstorf, 2002). It consists of an upper and lower overturning cell: The upper cell is characterized by a northward transport of warm surface waters and a southward return flow of cold deep waters below. The lower overturning cell is comprised of northward flowing bottom waters, which are again incorporated into the southward flow of deep waters (e.g. Orsi et al., 1999). These overturning cells are closely linked to the formation, upwelling and advection of water masses. Changes in the major water masses of the Atlantic Ocean are related to variations in the oceanic heat and freshwater transports and can influence basin-wide zonal pressure gradients, thus, the large-scale ocean circulation.

The western tropical South Atlantic represents a “crossroad” for the different branches of the Atlantic overturning cells and, therefore constitutes a key region for the exchange of water masses, heat and salt between the Southern and Northern Hemispheres. Hence, this region was extensively investigated and found to be a good place for monitoring water mass signal propagation - for example coming from the Agulhas region, around Antarctica or from the North Atlantic. In the following, I provide a comprehensive review of the water mass distribution and observed long-term property changes in the northern Brazil Basin, which is in part based on the review presented in Herrford et al. (2017).

4.1.1. Review

Schott et al. (2002, 2005) described the local water mass distribution in the western boundary regime at 11°S based on hydrographic sections accompanying the maintenance of a moored array during 2000–2004 there. They found the upper-layer water masses along the western boundary of the tropical South Atlantic to be marked by the salinity maximum of the Subtropical Underwater (STUW) near 100 m, then by fresher values of the South Atlantic Central Water (SACW) layer down to about 400 m and by the salinity minimum of the Antarctic Intermediate Water (AAIW) near 700 m. The STUW is known to be generated in the high evaporation regions within the subtropical gyre of the South Atlantic (e.g. Tomczak & Godfrey, 1994), further subducted and transported equatorward as part of the subtropical cells (e.g. Schott et al., 2004). According to Tomczak & Godfrey (1994), SACW formation occurs in two different regions – one version of SACW is formed in the Brazil-Malvinas confluence region and transported within the subtropical gyre, the other originates from the subtropical western Indian Ocean and is brought into the Atlantic via Agulhas leakage. The two versions of SACW have similar θ -S-characteristics after being strongly transformed within the Cape Basin and, together, spread westward within the subtropical gyre (Peterson and Stramma, 1991) and is carried towards the equator with the North Brazil Undercurrent (NBUC) flowing along the Brazilian coast (Stramma & Schott, 1999). As for the SACW, two different version of AAIW have been found in the South Atlantic: A fresh variety of AAIW is thought to be generated within the Antarctic Polar Frontal Zone and its formation process linked to the excess of precipitation over evaporation in that region (Belkin and Gordon, 1996). The second version of AAIW is comprised of Intermediate Waters from the Indian Ocean entering the Agulhas/Benguela Current system via Agulhas leakage and slightly diluting the salinity minimum of the fresher AAIW version (e.g. Rusciano et al., 2012). Schott et al. (2005) also described a temperature minimum near the boundary located just below the AAIW, which is caused by upper Circumpolar Deep Water (uCDW). The uCDW is thought to be a product of mixing of deep waters from the Indian and Pacific Oceans, which spread into the Antarctic Circumpolar Current (ACC) zone and then together with the AAIW into the South Atlantic (Reid, 1989). With its strong influence on the central to intermediate water layers in the South Atlantic, the Agulhas leakage constitutes the main source of heat and salt for northward-moving upper limb of the AMOC (e.g. Biastoch et al., 2008b).

Salinity and temperature changes in the western boundary region of the tropical South Atlantic, have been described in several studies before: Based on the results from a high-resolution ocean general circulation model, Biastoch et al. (2009) reported a salinity increase of +0.028/decade between 1965 and 2005 within the NBUC region (between 100 - 600m depth; 40°W–30°W and 5°S–10°S) and associated it with an increase in Agulhas leakage due to the strengthening of the westerlies (Durgadoo et al., 2013). Later, Kolodziejczyk et al. (2014) were able to track salinity anomalies from the Agulhas region through the northward and westward branches of the South Atlantic subtropical gyre toward the NBUC. Analyzing ship-based observations within the western boundary region at 5°S and 11°S, Hummels et al. (2015) confirmed the amplitude of the salinification, but found the strongest salinity trend (+ 0.1 dec⁻¹) in layers between 100 – 250 m depth. Schmidtke and Johnson (2012) and Hummels et al. (2015) found an intrinsic cooling and freshening in the AAIW layers above its core as well as a stronger warming and salinification below. Both studies discuss the property changes in the lower AAIW layers of the tropical Atlantic to be also partly related to an enhanced export of salty Indian Ocean intermediate waters to the Atlantic (e.g. McCarthy et al. 2011; Lübbecke et al., 2015). Fu et al. (2018), on the other hand, suggested that instead a weaker northward transport in the intermediate layer could be responsible for an observed AAIW salinification in the tropical North Atlantic. A

continuous salinification and warming since the 1950s has been reported for the uCDW throughout the western South Atlantic (Arbic and Owens, 2001; McCarthy et al., 2011). Santoso et al. (2005) proposed two modes of CDW variability, which could explain the long-term trends –either salinity dipole anomalies related to the strengthening and weakening of NADW formation propagating around the AMOC multi-centennial time scales (e.g. the Southern Ocean “flip flop” oscillator described by described in Pierce et al., 1995) or localized variability in the Brazil–Malvinas confluence zone driven by fluctuations in the strength of the Western Boundary Currents on multi-decadal to centennial time scales.

The oxygen distribution at intermediate depths in the eastern tropical Atlantic is characterized by the existence of oxygen minimum zones (OMZ) found north and south of the equator. OMZs are dominant features in all tropical oceans (Karstensen et al., 2008) and the result of the balance between supply via advection, diffusion and oxygen consumption (Luyten et al., 1983; Brandt et al., 2008; 2015). Since the 1950s, a deoxygenation as well as vertical expansion of the OMZs have been observed in all tropical oceans (e.g. Stramma et al. 2008). These changes are mainly attributed to global warming - in part directly, via solubility effects, and in part indirectly, via changes in circulation, mixing and oxygen respiration (Oschlies et al., 2018). Eastward equatorial current bands along the equator have been found to supply the OMZs with high oxygen waters from the western boundary region (e.g. Schott et al. 1995; Brandt et al., 2008). Within the western boundary region at 11°S, Hummels et al. (2015) found an oxygen decrease at intermediate depths between the early 2000s and early 2010s, which they related to the increased Agulhas leakage discussed above.

Below 1200 m, the tropical Atlantic is typically occupied by North Atlantic Deep Water (NADW), which is characterized by higher salinity, temperature and oxygen concentrations than the surrounding waters (e.g. Schott et al., 2005; Herrford et al., 2017). NADW is known to originate from the subpolar North Atlantic and to be comprised of different sublayers: The formation of the denser NADW layers is related to the inflow of water masses formed in the Nordic Seas, namely Iceland–Scotland Overflow Water (ISOW) and Denmark Strait Overflow Water (DSOW), into the subpolar North Atlantic. DSOW is formed as a result of winter convection north of Iceland and overflowing the Denmark Strait sills, while ISOW originates from the Norwegian Sea and overflows the thresholds east of Iceland (e.g. Dickson & Brown, 1994). ISOW is known to be mixed and entrained by ambient waters on its way through the Iceland Basin, the Charlie Gibbs Fracture Zone and the Irminger Basin before joining the DSOW. Because of this, the DSOW in the North Atlantic can typically be identified by a deep oxygen maximum while ISOW has comparatively reduced oxygen levels in the western basin (e.g., Mantyla and Reid, 1983; van Aken and de Boer, 1995; Schott et al., 1999). The upper NADW layers are assumed to be primarily composed of Labrador Seas Water (LSW), which is formed by wintertime deep convection in the Labrador Sea and Irminger Seas (e.g. Talley and McCartney, 1982; Pickart et al., 2003; Kieke and Yashayaev, 2015). In the North Atlantic, LSW is often associated with relatively warm temperatures, low salinity values and, due to its recent exposure to atmospheric oxygen, to high oxygen concentrations (Talley and McCartney, 1982). While it is commonly assumed that NADW formation is completed when exiting the subpolar North Atlantic, several studies discuss possible contributions of saline waters from the Mediterranean Sea to the LSW layer (e.g. Arhan et al., 1998) or interactions of the southward flowing NADW and the saline waters transported within the Gulf Stream in the subtropical Atlantic (e.g. Schott et al., 1999). In the tropical and South Atlantic, it is, therefore, common to refer to the different NADW layers as upper, middle and lower NADW.

Aside from recirculation cells (e.g., McCartney, 1992) or other interior routes (e.g., Bower et al., 2009), NADW is known to enter the western tropical Atlantic as part of the southward Deep Western Boundary Current (DWBC; Schott et al. 2003). After crossing the equator, the NADW immediately bifurcates – into an eastward flow parallel to the equator and a southward flow continuing along the western slope as the DWBC (e.g. Richardson and Fratantoni, 1999; Gouriou et al., 2001; Herrford et al., 2017). At 11°S, Dengler et al. (2004) showed that the NADW transport is mainly accomplished by migrating eddies. Within the DWBC regime at 11°S, Hummels et al. (2015) found waters to become cooler and fresher on isopycnals between the two observational periods 2013–2014 and 2000–2004. They argue that the cooling and freshening could be related to changes in the source waters of the NADW in the subpolar North Atlantic. Substantial property variations have been observed for the different source water masses of the NADW over the last decades: For example, Yashayaev et al. (2003) reported an exceptionally large volume of very cold and fresh LSW to be produced in the period 1988 – 1994 and a shift towards a warmer, more saline type of LSW afterwards. Dickson et al. (2002) showed, that the ISOW and DSOW freshened over the period 1960-1990, while Hansen and Osterhus (2007) found the salinity of the ISOW to increase again from 1997 to 2004 and Jochumsen et al. (2012) found no significant trends for DSOW over the period 1996–2011. Some of these signals, for example, the signal of the very cold and fresh version of LSW formed in the 1990s, could be traced along the western boundary into the subtropical Atlantic (e.g. Rhein et al., 2004; 2015). Rhein et al. (2015) estimated travel times of about 30 years for the NADW formed at subpolar latitudes to reach the western tropical South Atlantic. On their way south, however, the different components of NADW are strongly transformed, entrained by surrounding water masses and mixed (e.g. Rhein et al., 2015; Ferreira & Kerr, 2017). Changes in the circulation have also been found to influence local property distributions on longer timescales: For example, Richardson & Fratantoni (1999) found the two pathways for the NADW layers in the northern Brazil Basin – eastward along the equator or southward within the DWBC - to alternate over the period 1989-1992 with each of them being dominant over a longer period. Steinfeldt and Rhein (2004) related CFC-poor NADW arriving at 10°S to an enhanced recirculation of the DWBC over the period 1999-2002.

The abyssal Brazil Basin is known to be filled with Antarctic Bottom Water (AABW), which is the densest water mass in the world's oceans and in the tropical Atlantic typically identified by temperatures below 2 °C (e.g. Orsi et al., 1999; Johnson, 2008; Schott et al., 2005). Its densest component is assumed to be formed around Antarctica, with the process involving the waters over the Antarctic shelf cooling due to heat loss and becoming more saline due to sea ice formation, as well as mixing of these cold and dense Antarctic Shelf Waters with warmer, more saline old deep waters from the North (Orsi et al., 1999). As these dense bottom waters with temperature of 0-0.2 °C enter the western South Atlantic, they are joined by another, slightly warmer water mass ($\theta < 2$ °C), which, according to Orsi et al. (1999), is exported from the deep levels of the ACC with the formation process including upwelled NADW that is already depleted in O₂. In the Brazil Basin, the lighter AABW component is thought to make up the larger portion of AABW (e.g. Speer and Zenk, 1993; Ferreira & Kerr, 2017), while the denser component was reported to gradually disappear north of 10°S (e.g. Reid, 1989; Sandoval and Weatherly, 2001; Herrford et al., 2017). The flow of AABW is strongly guided by bottom topography and enters the Brazil Basin from the South mainly through the Vema and Hunter channels (Hogg et al., 1999; Zenk et al., 1999). Within the Brazil Basin, Herrford et al. (2017) found mainly the lighter AABW component to be transported along the western boundary just below the DWBC, where it strongly mixes with the lower NADW layer above and gradually loses its densest end-member, and more of the denser AABW component flowing northward in the basin interior below 4500 m depth. They found the lower NADW

and the lighter AABW to form a highly interactive transition layer throughout the northern Brazil Basin and a strongly homogenized mixture of both water masses north of 5°S. Remnants of the AABW have been found to leave the Brazil Basin through the Equatorial Channel into the western tropical North Atlantic (e.g. Rhein et al., 1995; Schott et al., 2003) or through the Romanche and Chain Fracture Zones (RCHFZs) into the East Atlantic (Mercier and Speer, 1998; Demidov et al., 2007).

During the last decades, a warming of AABW has been observed along its spreading path from around Antarctica into the North Atlantic (e.g. Fahrbach et al., 2011; Purkey and Johnson, 2012; Zenk and Visbeck, 2013; Fu et al., 2018; Frajka-Williams et al., 2011). In the northern Brazil Basin, Johnson et al. (2014) and Herrford et al. (2017) reported an abyssal warming of 0.02 – 0.03 °C dec⁻¹ over the period 1989-2014 and related it to a volume loss of the dense AABW component over time with an isopycnal displacement of 60-130 dbar dec⁻¹. Besides a contraction of the dense AABW layers, both studies found the lighter AABW/lower NADW layers in the Brazil Basin to expand. Several theories exist regarding the causes of the globally occurring AABW warming - including a reduced AABW production due to a slowdown of the bottom limb of the MOC (e.g. Purkey and Johnson, 2012), a potential thermal recovery in the Weddell Sea after the Weddell Polynya closing in the 1970s (e.g. Johnson et al., 2014), restricted export of bottom waters from the Weddell Gyre due to a strengthening of westerly winds (e.g. Fahrbach et al., 2011) or the possibility of the denser AABW component being replaced by a lighter version due to reduced Antarctic Shelf Water production or enhanced CDW entrainment within the AABW formation region (e.g. Azaneu et al., 2013; van Wijk and Rintoul, 2014). Further, Herrford et al. (2017) detected decadal variations on isopycnals corresponding to the lighter AABW component and the lower NADW, which form a highly interactive layer in this region, with warming in the 1990s and cooling in the 2000s.

While water mass property changes in the northern Brazil Basin have been investigated and described in several studies, long-term observations of water masses in the northern Angola Basin are sparse. Close to the Angolan coast, hydrographic measurements from the Nansen program (1995-today) have just recently been investigated regarding the local water mass distribution in the upper 500m (Kopte et al., 2017) as well as interannual to decadal variability of the subsurface heat content, which seemed to be related to the strength of the eastern boundary current (e.g. Tchikalanga et al., 2018). In the Angola basin interior and intermediate to deep water layers, however, the only hydrographic measurements I could find were subsets of two transatlantic sections at 11°S – measured during cruise OCEANUS 133 (Warren & Speer, 1991) in 1983 and during Meteor cruise M28/1 (Zenk & Müller, 1995) as part of WOCE (World Ocean Circulation Experiment) in 1994. Analyzing the hydrographic section from 1983, Warren & Speer (1991) found temperature and salinity to be almost homogeneously distributed within the deep Angola Basin, however, higher oxygen concentrations above the eastern flank of the Mid-Atlantic Ridge (MAR) than in the eastern part of the basin. They interpreted the high oxygen waters near the MAR to be “younger” than the deep and bottom waters farther east. This is supported by Zenk & Müller (1995), who observed higher chlorofluorocarbon (CFC) concentrations at the western side than at the eastern side of the Angola basin in 1994. In their study, Warren & Speer (1991) propose a two-layer circulation scheme for deep Angola Basin along 11°S with the bottom waters below 4000 m being concentrated in a southward western boundary current and the deep waters above 4000 m flowing anticlockwise with possible sources in the North and South. Another interesting feature in the deep Angola Basin is a local oxygen minimum located on the African continental rise, that was first discovered with few observations at about 6°S by van Bennekom & Berger (1984). Later, Warren & Speer (1991) reported this deep oxygen minimum at 11°S, where it was accompanied by maxima in nutrients. Both studies interpret this oxygen-nutrient tongue to be

generated by the flux from sediments with detritus originating mainly from the Congo River plume. They argue that its appearance at 6-11°S could be explained by a deep meridional flow field in which oxygen-minimum waters are transported from the Congo River Plume southward along the eastern boundary.

Water mass property changes between the OCEANUS 133 section in 1983 and the M28/1 section in 1994 have already been described in Holfort et al. (2000) with the goal to identify long-term water mass property variations which could be related to climate change. They found a distinct temperature increase in the depth range of the uCDW and upper NADW layers, which is strongest in the western Brazil Basin and becomes weaker stretching to the African coast in the east. Besides this signal, the intrinsic temperature changes reported by Holfort et al. (2000) were within the range of their ± 0.05 °C uncertainty estimate. They argue that the observed temperature changes could, therefore, be explained by advection and mixing alone.

In 2018, a third full-depth transatlantic section was measured at 11°S within the BMBF project RACE II – Meteor cruise M148/1. As the main objective of the deep transatlantic section in 2018 was to calculate an independent and recent estimate of the total strength of the overturning at 11°S, this section also includes direct velocity observations. Concurrently, the hydrographic data collected during the M148/1 cruise allow for a direct comparison with the data from the earlier sections along 11°S. In this study, I compare the hydrographic data from the recent cruise M148/1 to the M28/1 section from 1994 regarding differences in the water mass distributions of the Brazil and Angola Basin as well as property changes along 11°S between 1994 and 2018.

4.2. Data and methods

Here, I use CTD (conductivity - temperature - depth) profiles of potential temperature (θ) in [°C], salinity (S), dissolved oxygen (O_2) in [$\mu\text{mol kg}^{-1}$] from two transatlantic sections at approximately 11°S. Meteor section M28/1 was taken in April 1994 as part of WOCE (section A8; Zenk and Müller, 1995). The CTD work during the cruise was carried out with a Neil Brown NB3 CTD system, which was additionally equipped with Clark type oxygen sensors. The salinity and oxygen sensors were calibrated against water samples collected at each station. Zenk & Müller (1995) report the accuracy for section M28/1 over the whole range to be better than 0.002 °C for temperature and 0.002 for salinity.

Meteor section M148/1 was taken in June 2018 within the BMBF project RACE II (03F0729C) and the CTD/ O_2 profiles measured with a Seabird SBE 911 plus CTD system. The accuracy of the temperature sensors was 0.002 °C and, after calibration against water samples, the accuracy of salinity and oxygen sensors was 0.003 and 1.5 $\mu\text{mol kg}^{-1}$, respectively.

The two sections were performed on different grids (see Fig. 30): In 1994 a total of 110 CTD stations were occupied along 11°20'S with a grid spacing of 0.5° along most of the section. In 2018 only 67 CTD stations were taken along 11°45'S with a grid spacing of 1-2° in the basin interiors. During both occupations the grid spacing was reduced towards the western and eastern boundaries to resolve the boundary current structures. All of the CTD profiles used here reached down to the ocean bottom within a couple of meters.

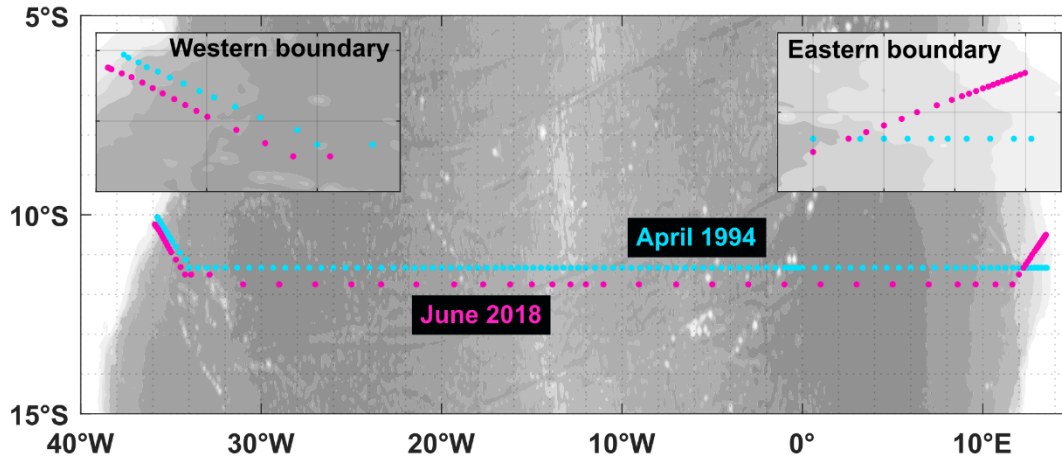


Figure 30 Bathymetric map showing the hydrographic sections occupied in April 1994 (cyan) and June 2018 (magenta) at 11°S. Every single dot marks the position of a CTD profile.

The vertical CTD profiles from both sections were sorted into a grid with 0.05° horizontal and 10 dbar vertical resolution. For the vertical sections presented in section 4.3, the variables were linearly interpolated between the profiles at each depth level and a Gaussian weighting function, with horizontal and vertical influence and cut-off radii of 0.2° and 20 dbar and 0.5° and 30 dbar, was applied for extrapolation and smoothing of excessive gradients due to irregular distribution of measurements.

Property changes are estimated as the difference between the two sections (e.g. $\theta(x, z)_{2018} - \theta(x, z)_{1994}$). On isobars, changes in temperature and salinity can have different causes: They can be due to intrinsic water mass changes along isopycnal surfaces or due to the vertical displacement of those isopycnal surfaces (Bindoff and McDougall, 1994). To separate the two contributions, I additionally show in-situ temperature (T; in [°C]) and pressure (P; in [dbar]) differences calculated on neutral density (γ^n) levels, which were, for better visualization, then converted back to pressure levels.

4.3. Water mass distribution along 11°S

While the water mass distribution in the western boundary regime at 11°S was studied extensively in the last 20 years (e.g. Schott et al., 2005; Herrford et al., 2017), the three transatlantic sections from 1983 (Warren & Speer, 1991), 1994 (Zenk & Müller, 1995) and 2018 provide, to the best of the authors' knowledge, the only CTD measurements covering the northern Angola basin interior and intermediate to deep layers. In the following, I describe and discuss the water mass distribution along 11°S, with emphasis on property differences between the western and eastern basins.

A salinity maximum ($S > 37$) at about 100m (Fig. 32 (c, d)) marks the STUW along 11°S. The subsurface salinity maximum is strongest and deepest (down to 200 m) close to the western boundary, towards the east it strongly shallows and weakens. At ~7°E, the corresponding isohalines dome to the surface and bow down to about 250 m. The subsurface layers near the eastern boundary are much fresher ($S \approx 35.7$) compared to the basin interior. This can also be seen in the θ -S-diagrams for the Angola Basin (Fig. 31 (b)), which show two separate θ -S- bands in the temperature range of 14-24 °C. In accordance with the water mass characteristics reported for the months April-June in Kopte et al. (2017), the fresher band can clearly be attributed to the eastern boundary region.

The layer below the STUW exhibits strong temperature and salinity gradients, decreasing almost linearly with depth (Fig. 31), which are typical characteristics for the central waters. The central water found at 11°S is typically SACW, which is assumed to be comprised of central waters originating from

the Brazil-Malvinas confluence region as well as from the subtropical western Indian Ocean (e.g. Tomczak & Godfrey, 1994). Close to the western boundary, the northward NBUC can clearly be seen in a deepening of the corresponding isotherms and isohalines down to 300-400 m (Fig. 32). From there towards the east the isotherms and isohalines of the SACW tilt upwards.

Below the SACW, the low salinity tongue of the Antarctic Intermediate Water (AAIW) can be seen throughout the whole 11°S section contoured by the 34.6-isohaline (Fig. 32 (c, d)). In the western boundary region of the 11°S sections, a salinity minimum of $S < 34.5$ is located at 700-800 m depth. Although extending into the western and eastern basin interiors, the salinity minimum decays towards the east. Confined to the western boundary region, a temperature minimum layer of $\theta < 4$ °C at about 1000 m can be interpreted as a signature of the uCDW. Zenk & Müller (1995) could trace high silicate concentrations related to the uCDW throughout the section until the eastern boundary. However, they also found sharp fronts in the distribution of anthropogenic tracers, like chlorofluorocarbons (CFCs), at about 5°W, indicating weaker renewal rates for the AAIW and uCDW in the eastern basin than in the western basin.

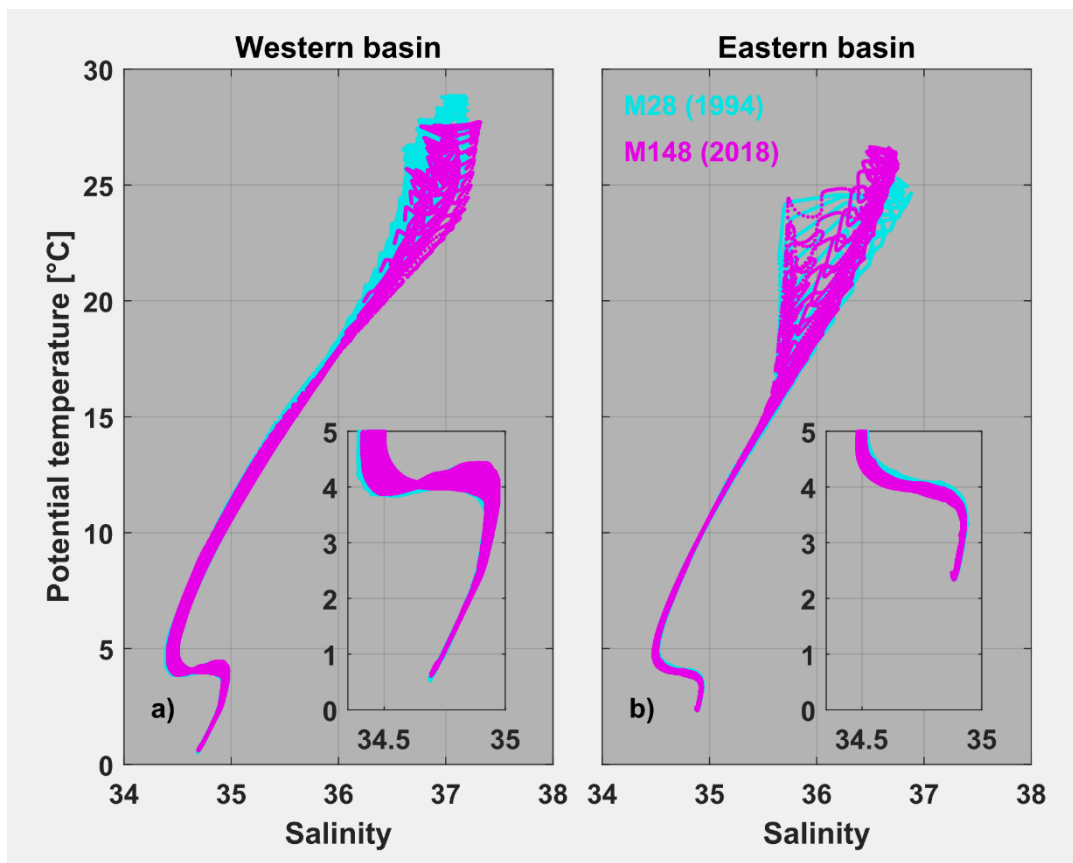


Figure 31 θ -S-diagrams for the western (a) and eastern (b) basin. Cyan dots mark measurements from cruise M28 (1994) and magenta dots from cruise M148 (2018).

As the 11°S section cuts through the tropical South Atlantic OMZ, the oxygen distribution along 11°S is characterized by low concentrations of dissolved oxygen ($O_2 < 180 \mu\text{mol kg}^{-1}$) in the thermocline to intermediate layers (Fig. 33). Along 11°S, minimum values of $O_2 < 30 \mu\text{mol kg}^{-1}$ can be found at 400 m depth close to the eastern boundary. The western boundary region, on the other hand, shows a relative oxygen maximum, which is related to the transport of high oxygen waters within the NBUC (e.g. Schott et al., 1995).

Below 1200 m, higher salinity, temperature and oxygen concentrations compared to the surrounding water masses mark the NADW (see Fig. 32 & 33). Along 11°S, the highest oxygen values can be found within the DWBC region, where the vertical stacking of S and O₂ extrema supports a division of NADW into different sublayers: The layer between 1200 – 1700 m is characterized by relatively warm temperatures ($4\text{ °C} < \theta < 4.4\text{ °C}$) and strong salinity gradients ($34.7 < S < 34.94$), which become stronger close to its upper boundary where it mixes with the fresher Intermediate waters above. I find two cores of high oxygen concentrations, which are centered around 2100 m and 3500 m in the western boundary region. The shallower oxygen maximum (O₂ > 250 μmol kg⁻¹) of the upper NADW is co-located with a salinity maximum (S > 34.94) causing the characteristic upward bulge in the corresponding θ-S-diagrams (Fig. 31 (a)). This is in contrast to the oxygen maximum of the LSW in the North Atlantic, which is typically co-located with a salinity minimum (e.g. Talley and McCartney, 1982). The second oxygen maximum located in the lower NADW layers is more pronounced with values of O₂ > 255 μmol kg⁻¹ and related to a temperature range of 2.0-2.6 °C. This characteristic vertical structure is also found in the North Atlantic and typically described as the result of the relatively low oxygen ISOW sandwiching between the two high-oxygen cores of the LSW and DSOW (e.g. Mantyla and Reid, 1983). It was found to be sustained along two major NADW routes through the Brazil Basin – along the equator up to the entries of the RCHFZs (Herrford et al., 2017) and within the DWBC as far as 11°S (Schott et al., 2005). Although gradually decreasing with distance from the western boundary, the high oxygen concentrations of the NADW layers at 11°S extend into the western basin interior as far as the MAR. There, the slightly reduced oxygen concentrations were discussed to be "older" NADW recirculating (Durrieu de Madron & Weatherly, 1994; Rhein et al., 1995) or to be water of southern hemispheric origin (Reid, 1989).

Below the NADW, the abyssal Brazil Basin along 11°S is filled with AABW, which exhibits lower oxygen (O₂ < 240 μmol kg⁻¹), salinity (S < 34.85) and temperature ($\theta < 2\text{ °C}$) values compared to the NADW above. Within the AABW layer at 11°S, salinity and potential temperature are decreasing almost linearly with depth (Fig. 31 (a); inset). This linear θ-S-relationship is the result of the cold and fresh AABW mixing with the warmer and saltier NADW. The two water masses are known to form an abyssal stratification throughout the western South Atlantic, with especially strong mixing along the western boundary as well as at sills or in channels. Upon its arrival at 11°S, the AABW has become much warmer, saltier and oxygenated (Rhein et al., 1998) and continues to do so on its way towards the equator (Herrford et al., 2017). I find the coldest temperatures (0.6-0.8 °C) along 11°S below 5000m at the foot of the Brazilian continental rise. This temperature minimum being associated with relatively low oxygen concentrations (O₂ < 230 μmol kg⁻¹) supports the predominance of the lighter AABW component over the denser component at 11°S. However, Zenk & Müller (1995) observed relatively high CFC values within that temperature minimum in 1994, which are known to mark the denser AABW component due to a more recent contact with the atmosphere.

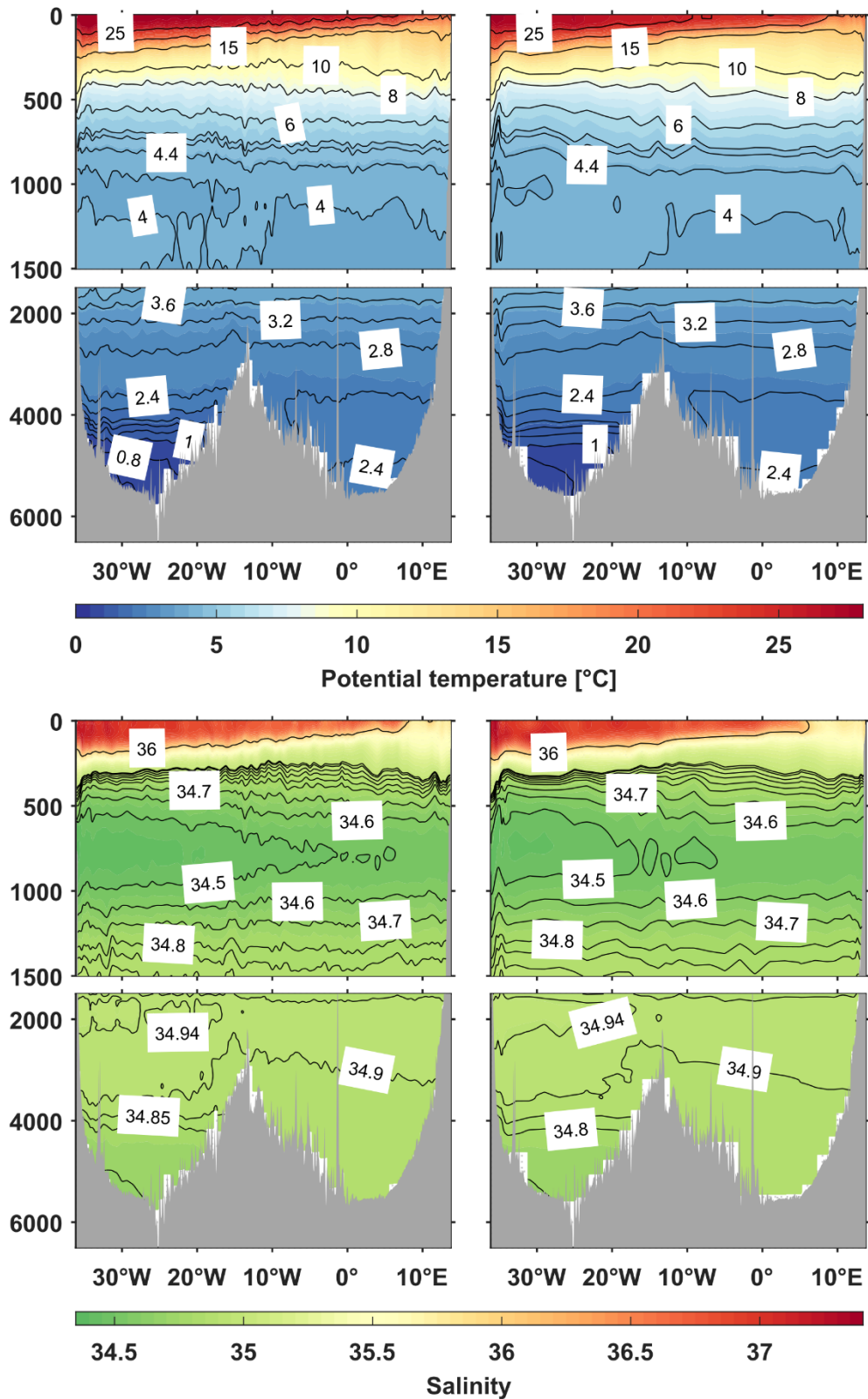


Figure 32 Vertical sections of θ (a, b; in $^\circ\text{C}$) and S (c, d) at 11°S – occupied during the transatlantic cruises M28 in April 1994 (left panels) and M148 in June 2018 (right panels).

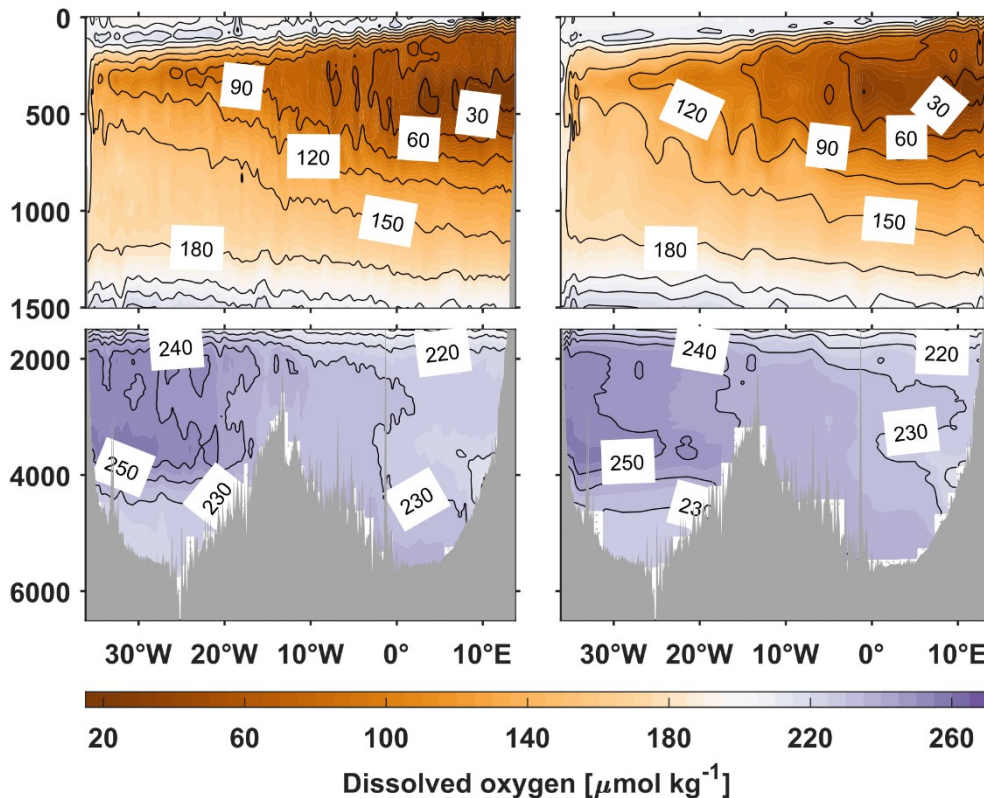


Figure 33 Vertical sections of O_2 (a, b; in $\mu\text{mol kg}^{-1}$) at 11°S – occupied during the transatlantic cruises M28 in April 1994 (a) and M148 in June 2018 (b).

The distribution of dissolved oxygen indicates that remnants of NADW fill the whole abyssal Angola Basin. Within the upper NADW layers, I find the isolines for oxygen and salinity to continuously extend from the western basin into the eastern basin, while potential temperature is slightly colder east of the MAR by about 0.4°C . Zenk & Müller (1995) reported a CFC front above the MAR along the M28/1 section, separating ‘younger’ versions of NADW in the western from ‘older’ ones of the eastern basin. The NADW entering the Brazil Basin from the North Atlantic is known to partly flow eastward along the equator towards the RCHFZs and partly southward with the DWBC (e.g. Richardson & Fratantoni, 1999; Gouriou et al., 2001; Herrford et al., 2017), which was found to split again into zonal current branches south of 19°S (Hogg & Thurnherr, 2005; Garzoli et al., 2015). The density range of the NADW layers in the Angola Basin could, therefore, be fed by NADW flows from the North and South, with the supply from the South probably being a much more transformed NADW version. The fact, that the upper NADW layer in the eastern basin is ‘older’ but colder compared to the western basin hints toward mixing of the upper NADW with the overlying uCDW in the western boundary region, which would support it being supplied from the South.

Below 2000 m, isolines do not continue across the MAR, which, as a topographic barrier, prevents any direct flow from the western into the eastern basin at those depth. Acting as a southern boundary, the Walvis Ridge blocks any flow of bottom waters below 4000 m from the South into the Angola Basin (e.g. Warren & Speer, 1991). Therefore, the only way for the AABW and lower NADW to enter the abyssal Angola Basin is through the RCHFZs near the equator (Mercier & Speer, 1998; Demidov et al., 2007) and maybe through the Rio de Janeiro and Rio Grande Fracture Zone at $22\text{--}26^\circ\text{S}$ (Mercier et al., 2000). Based on hydrographic data, Mercier et al. (2000) interpreted the latter bottom water throughflows to be a vein of the lighter AABW component originating from the deep levels of the ACC, which is lying above the western flank of the MAR in the Brazil Basin. It was found that the bottom

water entering the Angola Basin through the RCHFZs is rather a mixture of lower NADW and lighter AABW (Herrford et al., 2017) due to excessive mixing at the interface of both water masses all along their ways through the northern Brazil Basin. Ferreira & Kerr (2017) report the bottom waters filling the northern Angola Basin to be comprised of 40-50 % DSOW as it is defined in the Subpolar North Atlantic and 10-20 % AABW as defined when entering the western South Atlantic.

At 11°S, I find the waters below 4000 m to be rather homogeneous as potential temperature and salinity are almost constant with depth. Potential temperature and salinity at those depths vary by less than 0.13 °C and 0.03, horizontally and vertically. While Warren & Speer (1991) report minimum potential temperatures of 1.9 °C in 1983 pressed up against the lower flank of the MAR, I do not find potential temperature values below 2.3 °C at any of the stations in the Angola Basin in 1994 or 2018. The dissolved oxygen distribution, however, reveals differences between the western and eastern parts of the deep Angola Basin. Higher oxygen concentrations ($O_2 > 235 \mu\text{mol kg}^{-1}$) can be found above the eastern flank of the MAR and filling the abyssal plain, which is in agreement with the results from Warren & Speer (1991) or Zenk & Müller (1995). As the most source-like lower NADW would enter the Angola Basin through the RCHFZs, the high oxygen concentrations located east of the MAR support the southward flowing western boundary current at those depth as proposed by Warren & Speer (1991).

The oxygen distribution in the deep Angola Basin reveals another interesting feature- a local oxygen minimum ($O_2 < 220 \mu\text{mol kg}^{-1}$) located on the African continental rise at about 4000m depth. It is apparent in both sections, M28/1 and M148/1. This oxygen minimum extends and shallows eastward into the Angola basin interior while being diluted. Van Bennekom & Berger (1984) reported this deep oxygen minimum at about 6°S and Warren & Speer (1991) at 11°S in 1983, where it was accompanied by maxima in nutrients (e.g. silicate, phosphate and nitrate) of similar size and shape. However, they did not find a similar oxygen minimum at 24°S. Both studies interpreted this oxygen-nutrient tongue could be generated by the flux from sediments with detritus originating mainly from the Congo River plume. The fact that it is apparent at 11°S and shallowing from the continental slope into the Angola Basin interior could be explained by the deep meridional flow field of the Angola Basin, in which, according to Warren & Speer (1991), the oxygen-minimum waters are transported from the Congo River Plume southward along the eastern boundary and are then shifted upward by higher-oxygen waters from the south spreading close to the boundary at levels below 4000 m.

4.4. Water mass property changes at 11°S

In the following, I will investigate property differences between 1994 and 2018 along the two transatlantic sections at 11°S (Fig. 34). To account for property changes on isobaric surfaces due to the combined effects of changes along isopycnal surfaces, intrinsic water mass changes, and vertical displacement of the isopycnals, I separately show temperature differences calculated on pressure levels (Fig. 34 (a)) as well as temperature and pressure differences calculated on neutral density surfaces (Fig. 34 (c, d)). Note, that by definition, the spatial distribution of salinity changes on neutral density surfaces is similar to that of temperature changes and is, therefore, not shown here.

In the tropical South Atlantic, surface and subsurface waters exhibit substantial seasonal variability – as shown for the western (Stramma et al., 1995; Schott et al., 2005) and eastern (Kopte et al., 2017; Tchipalanga et al., 2018) boundaries of the 11°S section. Hence, T, S and O_2 differences in the upper ~200m between the two section are most likely related to the different seasons in which the cruises happened – M28 took place in April and M148 in June- and will not be considered.

Away from the surface, the largest difference between the two sections can be found within the SACW and AAIW layers of the Brazil Basin. I find patches of downward displacement ($20 \text{ dbar dec}^{-1} < \Delta P < 40 \text{ dbar dec}^{-1}$) of the isopycnals above 600 m, which closely resemble the distributions of the θ changes on isobars and indicate a heave contribution to the θ changes in the central water range. While temperature changes on isobars (Fig. 34 (a)) are very patchy, the signals become clearer when distinguishing between changes in spicyness (Fig. 34 (c)) and heave (Fig. 34 (d)). On isopycnals, I find a strong warming of more than $+ 0.24 \text{ }^\circ\text{C dec}^{-1}$ above 300 m in the western basin interior and reaching down to 500-600 m in the western boundary region. The layer between 300-600m, which corresponds to the interface between SACW and AAIW, rather exhibits a temperature decrease on isopycnals of about $- 0.1 \text{ }^\circ\text{C dec}^{-1}$ and, except for a narrow band at the western boundary, an oxygen increase of $20\text{-}40 \text{ } \mu\text{mol kg}^{-1} \text{ dec}^{-1}$ throughout the entire Brazil Basin. Comparing the oxygen distributions between both sections (Fig. 33) reveals that this oxygen increase is related to a reduced westward extent of the OMZ at 11°S between 1994 and 2018. Both of these signals, however, do not continue into the eastern basin. Dissolved oxygen concentrations in the eastern basin central water layers have decreased hinting towards an upward expansion of the OMZ at 11°S .

In the depth range of the AAIW and uCDW (600-1200 m), the whole western and eastern basin interiors are dominated by a warming and salinification (not shown), which are most pronounced in a patch just west of the MAR. There, temperature and salinity differences can be as large as $0.2 \text{ }^\circ\text{C dec}^{-1}$ and 0.025 dec^{-1} , respectively, and are accompanied by decrease in dissolved oxygen of $- 20 \text{ } \mu\text{mol kg}^{-1} \text{ dec}^{-1}$ (Fig. 34 (b)). The warming signal in the western basin patch is twice as large on isobars (Fig. 34 (a)) than on isopycnals (Fig. 34 (c)), which means, that it is the result of intrinsic water mass changes as well the vertical displacement of isopycnal surfaces in equal contributions. While the warming signal on isopycnals extends far into the western boundary region, the warming on isobars, however, is reduced by negative heave west of 25°W . Comparing the two θ and S sections from 1994 and 2018 (Fig. 32), it can be seen that the warming and salinification described above covers both, the base of the fresh AAIW as well as the cold uCDW layer below. Both of their characteristic minima, in salinity and temperature, show a reduced horizontal extent with the cold uCDW being almost gone in 2018. The warming signal within the AAIW density range does also extend into the eastern basin, however, is weaker on isopycnals ($+ 0.04 \text{ }^\circ\text{C dec}^{-1}$), strongly influenced by meso-scale or internal wave structures on isobars and shallows towards the east.

The warming, salinification and oxygen decrease in the central water range of the Brazil Basin are in agreement with previous studies (e.g. Biastoch et al., 2009; Kolodziejczyk et al., 2014; Hummels et al., 2015), who focused on the NBUC region and related this signal to an increase in Agulhas leakage. The intrinsic cooling and freshening in the AAIW layers above its core as well as a stronger warming and salinification and oxygen decrease below 600 m were also found by Schmidtko and Johnson (2012), Hummels et al. (2015) or Fu et al. (2018). These studies discuss the property changes in the lower AAIW layers to either be related to an enhanced export of intermediate waters from the Indian Ocean via Agulhas leakage or to local changes in the AAIW layer transports. However, they do not provide an explanation for the cooling and freshening of SACW/AAIW interface. Interestingly, comparing the transatlantic sections along 11°S from 1994 to the one in 1983, Holfort et al. (2000) found a cooling on isopycnals to span the whole depth range of SACW and AAIW in the Brazil Basin interior and a warming on isopycnals at about 1200m depth. Analyzing water property changes along 24°S , McCarthy et al. (2011) reported an overall increase in salinity on isopycnals in the thermocline waters of the South Atlantic between 1958-1983 and a freshening between 1983-2009. They confirm that half of this signal is related to an increasing proportion of Indian Ocean waters via Agulhas leakage. The other half,

however, they interpret to be the evidence of natural oscillations in the hydrological cycle. The warming and salinification of the uCDW (extending into the lower AAIW layers), on the other hand, was observed throughout the tropical and subtropical South Atlantic - since the 1950s (McCarthy et al., 2011) or even 1920s (Arbic and Owens, 2001). Being mostly caused by isopycnal change, this signal has to be transported from its source region into the tropical Atlantic via slow advection. This means that changes in the source waters of the uCDW could date back to beginning of the 1900 century and be the result of an atmospheric change on multi-decadal to centennial timescales (e.g. Santoso et al., 2005).

As described above, we find the warming signals, which are most pronounced on the isopycnals of the SACW and AAIW in the western basin, to extent into the eastern basin as well. Therefore, most of the Angola Basin is characterized by a warming on isopycnals of at least $0.01^{\circ}\text{C dec}^{-1}$ (Fig. 34 c). This is in contrast to Holfort et al. (2000), who also reported the lower AAIW/uCDW warming in the Brazil Basin, but found no temperature changes different from their uncertainty estimates in the Angola Basin between 1983 and 1994. The central to intermediate water layers of the Angola Basin are poorly ventilated and mainly supplied from western boundary via eastward zonal currents. The CFC measurements presented by Zenk & Müller (1995) indicate weaker renewal rates for the AAIW and uCDW in the eastern basin than in the western basin. could, therefore, be that signals like the warming of the AAIW/uCDW have only arrived in the Angola Basin after 1994.

While an oxygen decrease in the central water layer of the Angola Basin at 11°S (Fig. 34 (b)) is in agreement with the observed vertical expansion of both tropical Atlantic OMZs (e.g. Stramma et al. 2008), the oxygen increase in the central to intermediate water layers of the Brazil Basin at 11°S , thus, the reduction of the tropical South Atlantic OMZs horizontal extent, is not expected. Fu et al. (2018) found a similar oxygen increase and reduced horizontal extent of the tropical North Atlantic OMZ at 14.5°N between 1989-2013. They argue that the oxygen decrease in the OMZs is not spatially coherent with local processes or processes on shorter timescales, which could affect changes in dissolved oxygen. As CTD sections represent snapshots in time, the spatially and temporarily ambiguous property changes in the SACW, AAIW and uCDW layers, that are observed with a few sections, could be artifacts of aliasing. For example, interannual variations of the salinity in the NBUC region related to variations in the Agulhas leakage were reported to have similar amplitude as the observed long-term changes (Kolodziejczyk et al., 2014; Hummels et al., 2015). The southern bands of the Atlantic South Equatorial Current (SEC), which form the northern branch of the South Atlantic Subtropical Gyre and converge with the NBUC when encountering the South American continent, have also been found to exhibit substantial latitudinal shifts on seasonal to decadal timescales (e.g. Rodrigues et al., 2007; Veleda et al., 2011; Marcello et al., 2018). Further, the patchiness in the signals on isobars is probably related to internal waves or mesoscale variability, which can cause horizontal or vertical displacement of water masses on shorter timescales. Boebel et al. (1999), for example, detected elevated eddy kinetic energy in the AAIW layers east of the NBUC regime. All of these mechanisms can affect oxygen concentrations in the central to intermediate water of the Brazil Basin on shorter timescales and would manifest themselves in the differences between the two 11°S sections from 1994 and 2018.

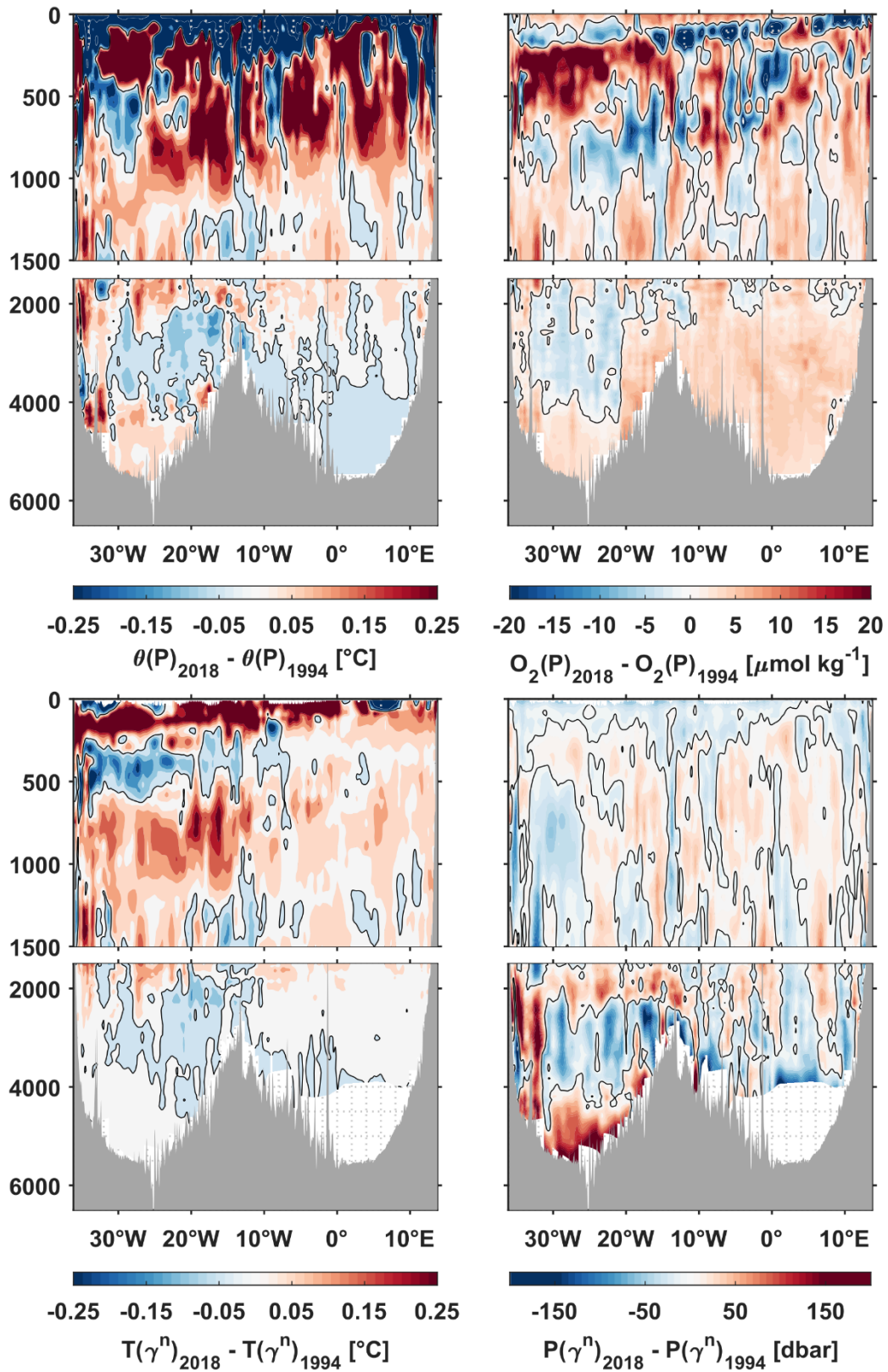


Figure 34 Vertical sections of property difference between the two sections at 11°S occupied during M28 in April 1994 and M148 in June 2018. Shown are the differences in (a) potential temperature (Θ) and (b) dissolved oxygen (O_2) on isobars, as well as (c) in-situ temperature (T) on and (d) pressure (P) of isopycnal surfaces. Red (blue) contours denote positive (negative) anomalies. Note, that positive anomalies of $P(\gamma^n)$ mean a downward displacement of isopycnals.

Most of the upper NADW layers between 1200 – 1700 m, except for a narrow band close to the continental slope, experience a warming, salinification (not shown) and an oxygen increase between 1994 and 2018 (Fig. 34). These signals are most pronounced in the western boundary region, but are also stretching into the western basin and eastern basin interiors. Reaching down to 3000 m within the DWBC, I find a warming of up to + 0.12 °C dec⁻¹ on isobars and isopycnals as well as an oxygen increase of + 4 μmol kg⁻¹ dec⁻¹.

While a general oxygen increase within the DWBC over the last decades was also reported by Hummels et al. (2015), the warming and salinification between 2018 and 1994 is different to previous findings. Comparing the 1994 section along 11°S to the one from 1983, Holfort et al. (2000) found a temperature decrease throughout the depth range of the DWBC with values of -0.05 °C, however, the contribution on isopycnals to be minor (-0.15 °C) and within their range of uncertainty. Analyzing differences between two observational periods 2013–2014 and 2000–2004, Hummels et al. (2015) also reported deep waters within the DWBC at 11°S to become cooler and fresher on isopycnals. They argue that cooling and freshening could be related to changes in the source waters of the NADW in the subpolar North Atlantic, however, could not explain the oxygen increase over the last decades. As some signals, for example the very cold and fresh version of LSW formed in the 1990s, could be traced along the western boundary into the subtropical Atlantic (e.g. Rhein et al., 2004; 2015) it could be possible that the warming I observe in the DWBC between 1994 and 2018 reflects changes in the source water masses upstream arriving at 11°S after 2014. However, interannual variations in the local NADW circulation, for example reported by Richardson & Fratantoni (1999) or Steinfeldt and Rhein (2004), as well as changes in the mixing and transformation of the different NADW components all along their way into the tropical Atlantic could also cause the observed property changes.

Below 1700m, temperature and oxygen changes on isobars (Fig. 34 (a)) as well as temperature changes on isopycnals (Fig. 34 (c)) and pressure differences of these isopycnals (Fig. 34 (d)) do all show similar patterns. While changes on isopycnals are rather small, property changes on isobars are dominated by strong ΔP (γ^n). The western boundary region exhibits a strong temperature increase on isobars between 1700-2900 m (+ 0.14 °C dec⁻¹) mainly related to an upward displacement of the corresponding isopycnals (+ 90 dbar dec⁻¹) and a temperature decrease (- 0.09 °C dec⁻¹) down to 4000 m caused by a downward displacement of isopycnals (+ 60 dbar dec⁻¹). It should be noted, that the southward transport of the DWBC at 11°S has been shown to be mainly accomplished by migrating eddies (Dengler et al., 2004), makes the interpretation of changes in ΔP (γ^n) from single ship-section rather complicated.

The NADW layers in the western basin interior exhibit a similar pattern, however, with weaker amplitudes, slightly shifted towards shallower depth and accompanied by a weak oxygen decrease of -2 μmol kg⁻¹ dec⁻¹ (Fig. 34). In contrast to the signals farther west, the cooling spanning the depth range from 2000-4500 m above the western flank of the MAR is also to at least 10 % caused by an intrinsic cooling and related to an oxygen increase of +2.5 μmol kg⁻¹ dec⁻¹. The entire western basin exhibits an increase in temperature and oxygen within the AABW layers below 4000 m. In the vicinity of the western boundary I find a warming of up to + 0.12 °C dec⁻¹ on isobars related to a downward displacement of isopycnals of + 30 dbar dec⁻¹ and an oxygen increase of +2.5 μmol kg⁻¹ dec⁻¹. Throughout the western basin interior, I find a similar oxygen increase, a warming of + 0.04 °C dec⁻¹ on isobars as well as isopycnal displacement increasing with depth from + 35 dbar dec⁻¹ at 4500 m to + 80 dbar dec⁻¹ at the bottom. The warming on isopycnals below 4000 m is of the order of + 0.01 °C dec⁻¹,

which indicates that temperature changes in the lower NADW and AABW layers of the Brazil Basin along 11°S are mainly caused by volume changes.

The whole deep to abyssal Angola Basin reveals a homogeneous oxygen increase of $+2 \mu\text{mol kg}^{-1} \text{dec}^{-1}$ (Fig. 34 (b)), which has not been observed before and is similar to the signal within the lower NADW/lighter AABW layers above the western flank of the MAR in the Brazil Basin regarding its magnitude and vertical extent. Unfortunately, I was not able to derive property changes on neutral density levels (Fig. 34 (c, d)) for the abyssal Angola Basin below 4000 m due to limitations in the hydrographic dataset used for construction of the neutral density fields. It seems, however, that the intrinsic cooling and upward displacement of lower NADW/ lighter AABW isopycnals that I observe above the western flank of the MAR is also present in the eastern basin.

The warming of the dense AABW layers and cooling of the lighter AABW/lower NADW layers on isobars along 11°S is in good agreement with the results from Johnson et al. (2014) and Herrford et al. (2017), who reported an abyssal warming of $0.02 - 0.03 \text{ }^\circ\text{C dec}^{-1}$ in the northern Brazil Basin over the period 1989-2014. They found this warming to be mainly related to a volume loss of the dense AABW component over time with an isopycnal displacement of $60-130 \text{ dbar dec}^{-1}$. Besides a contraction of the dense AABW layers, both studies also found the lighter AABW/lower NADW layers in the Brazil Basin to expand. They, as well as several other studies (e.g. Azaneu et al., 2013; van Wijk and Rintoul, 2014) discuss the possibility of the denser AABW component being replaced by a lighter version due to reduced Antarctic Shelf Water production or enhanced CDW entrainment within the AABW formation region.

Here, I found 25 % of the abyssal warming in the Brazil Basin to be related to a warming on isopycnals (Fig. 34 (c)), which explains the slightly higher amplitude of the AABW warming signal described here compared to previous studies. Comparing the 11°S section from 1994 to the one from 1983, Holfort et al. (2000) found a cooling of more than $0.05 \text{ }^\circ\text{C}$ in the region of the DWBC, however, argued that the contribution of intrinsic temperature change to this signal is just within their uncertainty estimate. Herrford et al. (2017) detected decadal variations of similar magnitude on isopycnals corresponding to the lighter AABW component and the lower NADW with warming in the 1990s and cooling in the 2000s. It could, therefore, be that the intrinsic warming of the lighter AABW and lower NADW layers between 1994 and 2018 is also part of the observed decadal variations including a warming after 2014. However, as for the NADW signals described above, it is as likely that changes in the circulation or mixing along the spreading path of the AABW into region of interest caused the observed property changes at 11°S.

As mentioned above, I find a rather homogeneous oxygen increase throughout most of the abyssal Brazil – within the DWBC, the AABW layers below 4000 m and the lower NADW/lighter AABW layers above the western flank of the MAR - as well as the entire abyssal Angola Basin below 2000 m (Fig. 34 (b)). This oxygen increase has been observed by Hummels et al. (2015) within the DWBC at 11°S, however, it has not been reported for any of the other regions before. Increasing oxygen concentrations in the AABW are in contradiction to the theories of Azaneu et al. (2013), van Wijk and Rintoul (2014) or Johnson et al. (2014), who propose that during the last decades the denser AABW components have been replaced by lighter AABW versions of which the formation process includes old NADW that is already depleted in oxygen. The oxygen increase in the AABW layers of the Brazil Basin could, however, be related to the oxygen increase observed in the DWBC at 11°S. The lower NADW/lighter AABW layers have been found to form a highly interactive layer and strongly mix along

their way, especially in the western boundary regime of the northern Brazil Basin - with the AABW becoming more saline and warmer, and the lower NADW freshening and cooling by an equal amount (Herrford et al., 2017). Higher oxygen concentration in the AABW layers at 11°S could, therefore, just be the result of local mixing with the NADW layers above, which exhibit an oxygen increase between 1994 and 2018. Another very interesting result are the rather similar property changes – a rather homogeneous oxygen increase of similar magnitude and vertical extent as well as isopycnal cooling and an upward displacement of isopycnals – that I find within the NADW layers above the western flank of the MAR and in the entire Angola Basin. A northward flow of bottom water just west of the MAR was already proposed by studies like Warren & Speer (1991) or Durrieu de Madron & Weatherly (1994). Further, bottom waters in the western part of the Brazil Basin have been discussed to be comprised of "older" NADW recirculating (e.g. Rhein et al., 1995), a strongly transformed version of lower NADW, which was mixed with lighter AABW on its way southward along the western boundary (Herrford et al., 2017), or to be water of southern hemispheric origin (Reid, 1989). It could also be, that the flanks of the MAR, similar to the counterflow arrangement at the western boundary, act as sources for strong mixing of the AABW with the overlying NADW. Analyzing microstructure data in the Brazil Basin, Polzin et al. (1997) found enhanced mixing throughout the water column above the rough flanks of the MAR. Thus, increasing oxygen concentrations in the NADW could just be mixed into the lighter AABW layers. Regardless of the mechanism causing the oxygen increase, similar property changes on the western flank of the MAR and in the deep Angola Basin indicate that it is probably the transformed NADW/AABW mixture in the eastern Brazil Basin which then enters the Angola Basin from the North through the RCHFZs and fill the abyssal eastern basin at 11°S.

4.5. Summary and conclusions

In this study, I compared ship-based hydrographic data from two transatlantic sections along 11°S taken in 1994 within the WOCE program and recently in 2018. Full-depth measurements of temperature, salinity and dissolved oxygen allowed for a thorough description of the mean water mass distributions in the Brazil and Angola Basins at 11°S.

I was able to confirm observational results from previous studies by identifying well-known property extrema in the Brazil Basin, such as the subsurface salinity maximum of the STUW, the linear θ -S-characteristic of the SACW, the salinity and temperature minima of the AAIW and uCDW, the salinity and oxygen characteristics of the different NADW sublayers within the DWBC and the temperature minimum of the AABW at the bottom. While all of the property extrema are most pronounced close to the western boundary, I found most of the isopycnals above 2000 m to extend far into the eastern basin and to shallow towards the east. Exception from that are the isohalines of the STUW, which dome to the surface east of 7°E, as well as the isotherms of the uCDW, which reveal a front above the crest of the MAR indicating weaker renewal rates in eastern basin at those depths. The oxygen distribution of the central to intermediate waters along 11°S is characterized by the tropical South Atlantic OMZ with minimum oxygen concentrations in the poorly ventilated eastern Angola Basin and a relative oxygen maximum in the western boundary current region. Below 2000 m, the MAR acts as a barrier for deep and bottom water flow. The oxygen concentrations in the deep Angola Basin indicate that it is filled with modified versions of the NADW from the Brazil Basin. While temperature and salinity are almost homogeneously distributed within the deep Angola Basin, I found higher oxygen concentrations related to "younger" versions of NADW above the eastern flank of the MAR and a pronounced oxygen minimum being located on the African continental rise at about 4000m. Both

features can be interpreted as the result of a two-layer Stommel-Arons circulation field with possible deep water sources in North and South.

As the two transatlantic sections along 11°S presented in this study are separated by 24 years, I analyzed differences between both occupations with regard to long-term water mass property changes. Thereby, I distinguished between changes along isopycnal surfaces and vertical displacement of the isopycnals. I found the largest difference between the two sections within upper 1200m of the Brazil Basin: A strong intrinsic warming (and salinification) of the central water layers is in agreement with previous studies and probably related to an increasing Agulhas leakage arriving in the NBUC region at 11°S. The intermediate water layers show intrinsic cooling above 600 m and intrinsic warming below. It is likely, that the warming being confined to the lower intermediate water layers is rather related to the continuous warming of the uCDW observed throughout the South Atlantic over the last decades than to an increased Indian Water contribution to the intermediate waters. Although weakening towards the east, both warming (and salinification) signals can also be found in the Angola Basin after 1994.

Differences in the dissolved oxygen concentrations at 11°S revealed a vertical expansion as well as reduced westward extent of the tropical South Atlantic OMZ between 1994 and 2018. While the vertical expansion is in agreement with previous observations of long-term changes in the tropical Atlantic OMZs, I can only speculate on the mechanisms causing the reduced westward extent. Further, the spatial distribution of isopycnal displacement is characterized by meso-scale or internal wave structures over most of the water column, which strongly modulates property changes on isobars.

Property changes in the deep and bottom water layers are very different between regions and, when compared to other studies, also between different periods. In the western boundary region, I find an intrinsic warming and oxygen increase in the upper NADW layers, which could be caused by decadal variations further upstream. Concurrently, changes in the lower NADW and AABW water layers in the Brazil Basin are dominated by isopycnal displacement. Below 4000 m, I found the prominent AABW warming signal, which can be traced all along its spreading paths, and can confirm that it is mainly related to a volume loss of its densest component in the Brazil Basin. The transition layer between the lower NADW and lighter AABW layers, on the other hand, is characterized by a volume increase in the Brazil Basin. Besides, the AABW layers do also exhibit an oxygen increase, which has not been observed before and I cannot explain. I found property changes above the western flank of the MAR, namely an oxygen increase as well as temperature decrease on isopycnals and isobars, to be coherent with property changes in the abyssal Angola Basin. This indicates enhanced water mass transformation above the flank of the MAR and that waters from there are likely to supply the deep northern Angola Basin.

The large-scale temperature and salinity changes, which can be seen along 11°S, have major implications: The changes in water mass properties of the central and intermediate waters at 11°S are known to be related to variations in the oceanic heat and fresh water transports into the North Atlantic, thereby influencing the preconditioning of deep convection and formation of deep waters in that region (e.g. Biastoch et al., 2008b). The warming of the uCDW, which contributes the deepest part of the northward-moving upper limb of the AMOC at 11°S, has been observed since the early 1900 century and related to variations in NADW formation on centennial time scales (e.g. Santoso et al., 2005). Furthermore, the observed AABW warming in the abyssal Brazil Basin was also found to be related to global heat, freshwater as well as sea level rise budgets. For example, Purkey & Johnson (2010) estimated the global deep-ocean warming below 4000 m to contribute about 9 % to global sea

level rise due to thermal expansion. Such signals as the warming of the uCDW or AABW can change basin-wide zonal pressure gradients along its spreading paths, the AABW warming signal is accompanied by changes in the large-scale ocean circulation. The observed volume changes at interface between the two overturning cells in the Atlantic have been associated with a weakening AABW cell (Johnson et al., 2008) and a concurrent strengthening of the upper cell of the AMOC (Patara & Böning, 2014).

It should be noted, that a third full-depth transatlantic section was measured at 11°S in 1983 (OCEANUS 133; Warren & Speer), to which I compared our results. With three occupations in 30 years, the 11°S section is one of the best sampled sections in the South Atlantic. This highlights the need for more coordinated hydrographic measurements in this region – especially the eastern tropical and subtropical South Atlantic.

5. Summary and suggestions for future research

The western tropical South Atlantic is a region with high signal-to-noise ratios and constitutes a crossroad for the different branches of the AMOC. The latitude 11°S is, therefore, considered to be a good place to monitor water mass signal propagation, changes in the boundary transports and, with that, changes in the AMOC transport. In this thesis, I investigated different contributions to the seasonal to decadal variability of the AMOC at 11°S. The following chapter summarizes the main results and provides a number of suggestions for future research.

The results presented in this thesis, heavily rely on ocean observations from or associated with the TRACOS array at 11°S. The different components of the TRACOS array developed historically. Today it is comprised of moored arrays or platforms at the western (e.g. Hummels et al., 2015) and eastern (e.g. Kopte et al., 2017) boundaries as well as 25 years of ship-based measurements in that region (e.g. Herrford et al., 2017).

In chapter 2, I present the first 4.5-year-long timeseries of AMOC variations derived from observations at 11°S. I utilized bottom pressure observations on both sides of the Atlantic basin, combined with satellite measurements of sea level anomalies to derive the upper-ocean geostrophic contribution to the AMOC for the period 2013-2018. The Ekman contribution is calculated from satellite wind stress.

Extend all timeseries at 11°S to investigate interannual to decadal AMOC variability:

In the future, when longer bottom pressure timeseries are available at 11°S, there is potential in using those and the approach described in chapter 2 to also estimate variability of the upper-ocean geostrophic transport on longer time scales. Bottom pressure recorders have the advantage, that they are less expensive and easier to deploy than full-height mooring arrays. As described in section 2.2.1., the bottom pressure sensors experience instrumental drifts, which limits their capabilities on longer time scales. Currently, the bottom pressure timeseries at 11°S are just long enough to investigate seasonal variability in that region. There is a recent study by Worthington et al. (2019) working on the calibration procedure for bottom pressure recorders, offering promising solutions for the problem mentioned above.

Until then, one could fall back on hydrographic measurements, which are already available and cover longer periods, to extend the time series of the western boundary current system and AMOC into the past. For example, a number of AMOC estimates exist using techniques combining sea surface height and Argo (e.g. Willis, 2010). This was shown to produce a reasonable mean vertical and horizontal structure of the subtropical South Atlantic circulation (Schmid, 2014). However, there are concerns regarding the spatial coverage of Argo near the coast. The capability of the Argo profiles, which are available in the northern Brazil Basin, to capture the interannual variability of the NBUC at 11°S is currently tested with the output of the INALT01 model as part of a master thesis (P. Dennert and P. Brandt, personal communication).

Interestingly, the NBUC transport timeseries derived from the moored observations off Brazil (Schott et al., 2005; Hummels et al., 2015) shows a pronounced spectral peak at periods of 22-30 months. I also found biennial variations in the depth of the neutral density surface 27.7 kg m^{-3} , which corresponds to the interface between the NBUC and DWBC below. Interannual variations in the vertical extent of the NBUC could be related to biennial variations reported for the bifurcation region of the South Equatorial Current farther upstream (Veleda et al., 2011).

More than 25 years of shipboard hydrographic measurements in the tropical South Atlantic – at the western (e.g. Hummels et al., 2015; Herrford et al., 2017) and eastern boundary (within the EAF-Nansen program; Tchipalanga et al., 2018) – would even allow to extend the NBUC and AMOC timeseries back into the 1990s. Both datasets contain irregularly distributed measurements in space and time. Therefore, it will be crucial to carefully test methods for averaging and interpolation.

The Ekman contribution to AMOC variations at 11°S is currently derived from ASCAT wind stress. Bentamy et al. (2012) illustrated and tested the process of directly matching the current ASCAT and the recent QUIKSCAT winds. Following their matching procedure would allow to extend the timeseries of the Ekman transport across 11°S presented in chapter 2 back to 1999 and make it relatively easy to quantify uncertainties. When another wind product is used, the sensitivity of the results to its choice should be tested.

Over the period 2013-2018, the timeseries of the AMOC and of its dynamical components at 11°S are dominated by strong seasonal variability. The observed seasonal variability is compared to results from the INALT01 model, which is known to reproduce the variability of the NBUC on longer timescales. On seasonal timescales, however, the model tends to underestimate bottom pressure variability at depth, especially at the western boundary. This translates into the vertical structure of the simulated geostrophic transport, which is currently used for the calculation of the observational estimate and, therefore, adding to its uncertainty.

Use PIES travel times to improve estimate of vertical AMOC structure:

Pressure inverted echo sounders (PIES) measure the travel time of an acoustic pulse from the seafloor to the surface, which can be utilized to estimate vertical profiles of dynamic height. Learning from the successful use of long-term PIES arrays at 47°N (Roessler et al., 2015) or 34.5°S (e.g. Meinen et al. 2018), I think it is worth analyzing the travel times from the PIES installed off Brazil. Those can be converted into time series of dynamic height profiles using historical hydrographic data. The resulting profiles could add information to or allow for a model-independent estimate of the vertical structure of pressure variability at the western boundary and, therefore, reduce the uncertainty of the current estimate.

In the INALT01 model, seasonal AMOC variability at 11° S is mainly wind forced and governed, besides the Ekman transport, by the geostrophic transport variability in the eastern basin. The geostrophic contribution of the western basin to the seasonal cycle of the AMOC is instead comparably weak as transport variability in the western basin interior is mainly compensated by the Western Boundary Current. Interestingly, the ratios of the NBUC and AMOC seasonal amplitudes are different between the INALT01 model (>1) and the observations (<1). Strong seasonal variability in the western and eastern basin interiors is mostly associated with the annual cycle and corresponds to patches of strong seasonal variability with westward phase propagation in the local wind stress curl. Strong seasonal variability of the upper-ocean geostrophic velocity at the eastern boundary, however, is co-located with a minimum in the seasonal variability of the wind stress curl. The annual and semi-annual harmonics of the pressure time series hint towards different baroclinic structures at the western and eastern boundaries. A higher baroclinic structure at the eastern boundary is assumed to be related to

coastal trapped waves of specific baroclinic modes that can travel from the equator towards 11° S along the African coast thereby impacting the local pressure and velocity fields (Brandt et al., 2016; Kopte et al., 2018). The analyses from chapter 2 indicate, that the seasonal variability of the geostrophic contribution to the AMOC at 11°S is modulated by oceanic adjustment to local as well as remote wind forcing.

Test ratios of locally and remotely forced AMOC variability at 11°S:

In the INALT01 model, seasonal upper-ocean geostrophic transport variability at 11°S is governed by the variability in the eastern basin as the western basin interior and the NBUC transports tend to compensate each other on seasonal time scales. This compensation could be explained by an almost equilibrium response of the circulation in the western basin at low baroclinic modes to the wind stress curl (e.g. Döös, 1999; Schott et al., 2005) as locally wind-forced annual Rossby waves would travel westward and after arriving at the western boundary directly force NBUC variability. The vertical structures in the annual harmonic of the velocity field simulated by the INALT01 model (Fig. 35) show a low baroclinic mode signal propagating westward through the western basin interior as well as another low baroclinic mode signal of opposite sign in the NBUC region and extending into the DWBC. It would be interesting to test the two theories and whether the compensation holds in different model configurations and under different wind forcing.

The seasonal variability of the upper-ocean geostrophic transport in the eastern basin interior is mainly forced by the local wind stress curl, although with a phase shift of 5-6 months compared to the western basin interior (see section 3.5.4.4). Besides, there is also a contribution about ¼ of the peak-to-peak seasonal cycle amplitude from the eastern boundary. In INALT01, the annual harmonic of the meridional velocity at the eastern boundary (east of 10°E; Fig. 35) shows a higher baroclinic structure with westward phase propagation. Kopte et al. (2018) associated the annual and semi-annual cycles of the alongshore velocity at 11°S with basin-mode resonance in the equatorial Atlantic of the fourth and second baroclinic modes, respectively (Brandt et al., 2016). Corresponding coastal trapped waves can then propagate along the African coast towards 11°S and be radiated from there into the basin as Rossby waves of similar baroclinic structure. Similar Rossby-wave radiation from the eastern boundary has been reported for the tropical North Atlantic (e.g. Chu et al., 2007) and proposed to be one of the main mechanisms for seasonal variations in the geostrophic transport there (e.g. Zhao & Johns, 2014a).

The ratios of locally and remotely forced variability in the upper-ocean geostrophic transport could either be analyzed within one of the INALT model configurations (e.g. Schwarzkopf et al., 2019) or, for example, with a set of linear shallow water model simulations (e.g. Brandt et al., 2016; Kopte et al., 2018).

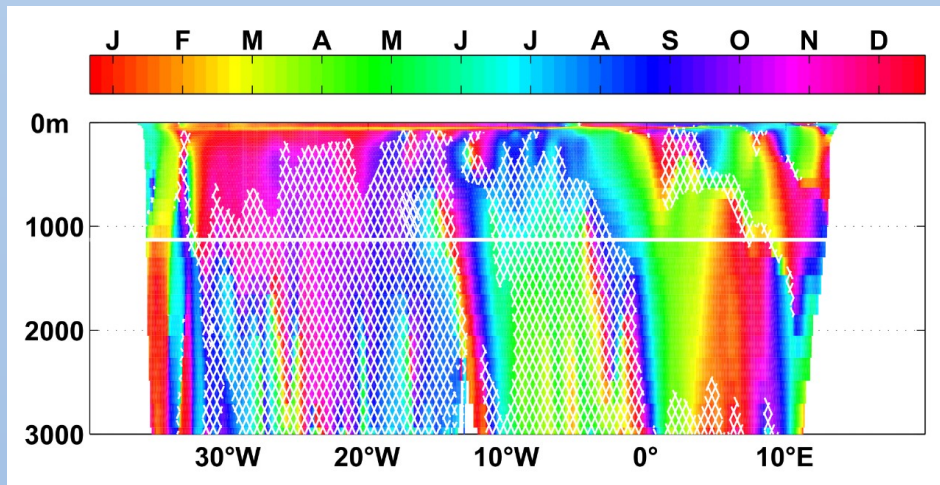


Figure 35 Zonal section of the phase of the annual harmonic of the meridional velocity in INALT01 along 11°S. White hatching overlays part of the section, where the harmonics have an amplitude $< 0.0025 \text{ m s}^{-1}$. The white line marks the level of no motion (at 1130 m) assumed for the calculation of the AMOC in INALT01.

Further, it would be interesting to test, whether some of these mechanisms and relationships also hold on other timescales. Model studies suggest, that most of the intra-seasonal ($T > 120$ days) to interannual variability at the eastern boundary is induced by the wave response to equatorial wind forcing generating equatorial Kelvin waves, which propagate eastward and transfer their energy as coastal trapped waves further to the south (Illig et al., 2004; Illig et al., 2018; Bachèlery et al., 2016; Imbol Kougue et al., 2017). At the western boundary, where the DWBC transport is known to be mainly accomplished by migrating eddies with a period of 60-70 days (Dengler et al., 2004), there seems to be a connection between seasonal variations in the generation of the eddies farther upstream and the deep seasonal variability at 11°S. (A. Brum and M. Dengler, personal communication). Analyzing transport variability associated with the horizontal branches of the subtropical cells estimated at 10°N and 10°S, Tuchen et al. (2020) found the wind-driven parts of the western boundary and basin interior transports at 10°S and 10°N to be anticorrelated and partially compensate each other on interannual to decadal timescales.

In chapter 2 I showed that uncertainties in the wind forcing are particularly relevant for the resulting uncertainties of the estimates of the Ekman as well as upper-ocean geostrophic contributions to AMOC variability at 11°S. A brief comparison of wind stress anomalies along 11°S between ASCAT and the output of INALT01, which is forced with air-sea fluxes from the CORE II data set (Durgadoo et al., 2013), revealed substantial differences in their spatial structures, as well as in the course and amplitudes of their seasonal cycles.

Chapter 3 presents a systematic assessment of a collection of different gridded surface wind products widely used within the oceanographic community. I compared their mean wind fields and their capability to reproduce the wind variability in the tropical Atlantic observed with PIRATA buoys. While all of the considered wind products captured the mean atmospheric circulation in the tropical Atlantic with overall differences of 10 % in wind speed, most of the products had problems to reproduce the wind variability in the eastern tropical South Atlantic. Further, the excessively used CORE II forcing dataset did not reproduce the observed intra-seasonal variability and scatterometer winds showed low correlations with the PIRATA winds on interannual timescales.

Further develop and use the “windeval”-tool:

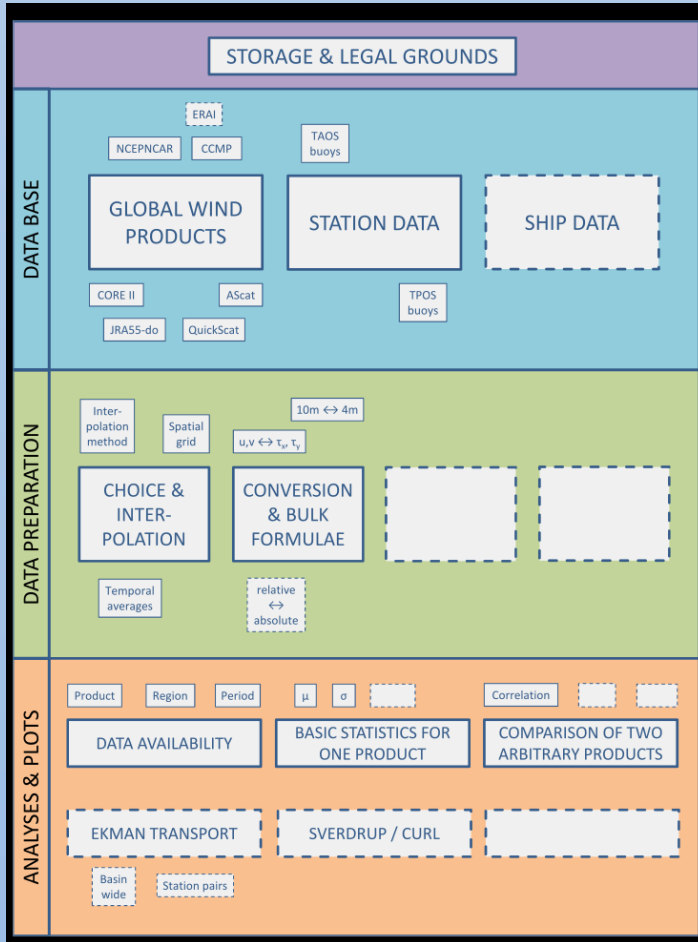


Figure 36 Modular structure of the “windeval” toolbox.

standardized reading of different wind products, standardized operations on gridded fields and station-based data, the application of common parameterizations, common diagnostics and visualizations (Fig. 36). We aim at making it as easy as possible for the scientific community to either build on or further develop the toolbox. A preliminary version can be accessed here: <https://git.geomar.de/wind-products/windeval>. Unfortunately, this work is on hold due to a lack of resources and time.

Within the ocean and climate community, there is a lot of insider knowledge on the benefits and caveats of different wind products - gridded or station-based, observational or reanalysis. There is, however, no published comprehensive and systematic evaluation of wind products. I would like to stress, that there is a need for a synthesis project or study, which includes a more complete set of wind products being evaluated on a global spatial scale and a variety of timescales. Together with some of my colleagues (W. Rath, E. Eisbrenner and F. Heukamp, we started to build a modular and open-source Python toolbox called “windeval” that could be used to easily and semi-automatically prepare evaluations across many different wind products. It is supposed to contain a data catalog,

In accordance with several recent studies related to the BMBF-RACE projects (e.g. Herrford et al., 2021; Brandt et al., 2021; Tuchen et al., 2020; Rühls et al., 2015), I tested, how the differences among products translate into derived variables, which are relevant for the large-scale circulation in the tropical Atlantic - such as the wind stress and wind stress curl, as well as Ekman transport, Ekman divergence or Sverdrup transport variations on seasonal to decadal time scales. The uncertainties from using different wind stress parameterizations can make up 15 % of the mean momentum flux into the ocean. Substantial inconsistencies were found among products regarding the seasonal wind stress curl in the eastern and western boundary regions at 11°S. For integral variables like the mean Ekman or Sverdrup transports across a certain latitude, the choice of wind product resulted in uncertainties of 15-40 % depending on the region. The more recent, higher resolution products agreed on the seasonal to decadal wind stress variability in the tropical Atlantic, while older and coarser products (NCEPNCAR and CORE II) produced spurious wind stress variations, especially on decadal to multi-decadal

timescales. These results show, how important it is to the sensitivity of derived results to the choice of wind product as well as to carefully consider or incorporate large uncertainties in wind forcing products into ocean simulation experiments.

Test the sensitivity of the tropical Atlantic large-scale circulation in INALT simulations to the choice of wind forcing:

The quality of wind forcing data sets is especially crucial in ocean modelling, as temporal and spatial differences in the wind stress derived from different wind products will result in differences in the simulated ocean circulation. I think, it is important to test the sensitivity of the large-scale circulation in the tropical Atlantic and its variability on different timescales to the choice of wind forcing product within similar simulation configurations. There are current efforts to investigate the zonal wind-driven current system in the tropical Atlantic in simulations with the new INALT20X model configuration (Schwarzkopf et al., 2019) under CORE II and JRA55-do forcing (Kristin Burmeister, personal communication). I suggest to extent this effort to the tropical South Atlantic including the Western boundary current system off Brazil and the AMOC at 11°S, for which observations are available for validation. It would also be interesting to extend the comparison with a model run forced with ECMWF winds, which performed well in the region.

Chapter 4 builds on the methods and results presented in Herrford et al. (2017), but presents new findings based on new data. This new data set consists of two full-depth transatlantic hydrographic sections along 11° S, which are separated by 24 years. One of the sections was measured in 1994 as part of the WOCE program (Zenk & Müller, 1995) and the other section in 2018 within the BMBF-project RACE II.

Estimate the absolute AMOC strength at 11°S from transatlantic sections:

The main objective of performing a deep transatlantic section during cruise M148/1 in 2018 was to calculate an independent estimate of the total strength of the overturning at 11°S while the TRACOS observing system was in place. This estimate could help to better interpret the strength and weaknesses of the different transport time series and represents a recent AMOC estimate from the southern tropical Atlantic. The only other observational estimate of absolute maximum overturning at 11°S is based on CTD data from the transatlantic WOCE ship section measured in 1994 (see section 4.2). Lumpkin & Speer (2007) derived a maximum overturning of +16.2 Sv applying an inverse box model and using a number of other hydrographic WOCE section.

During cruise M148/1, besides CTD profiles, also velocity profiles have been measured with a Lowered Acoustic Doppler Current Profiler (LADCP) at each station. These direct velocity observations (see Fig. 37) could be used to reference the geostrophic velocity derived from temperature and salinity profiles via the thermal wind relation. Dengler et al. (2002), for example, showed that using the vertically averaged velocity from the LADCP profiles as the reference velocity for the corresponding CTD station pairs resulted in an accuracy of 0.012 m s⁻¹.

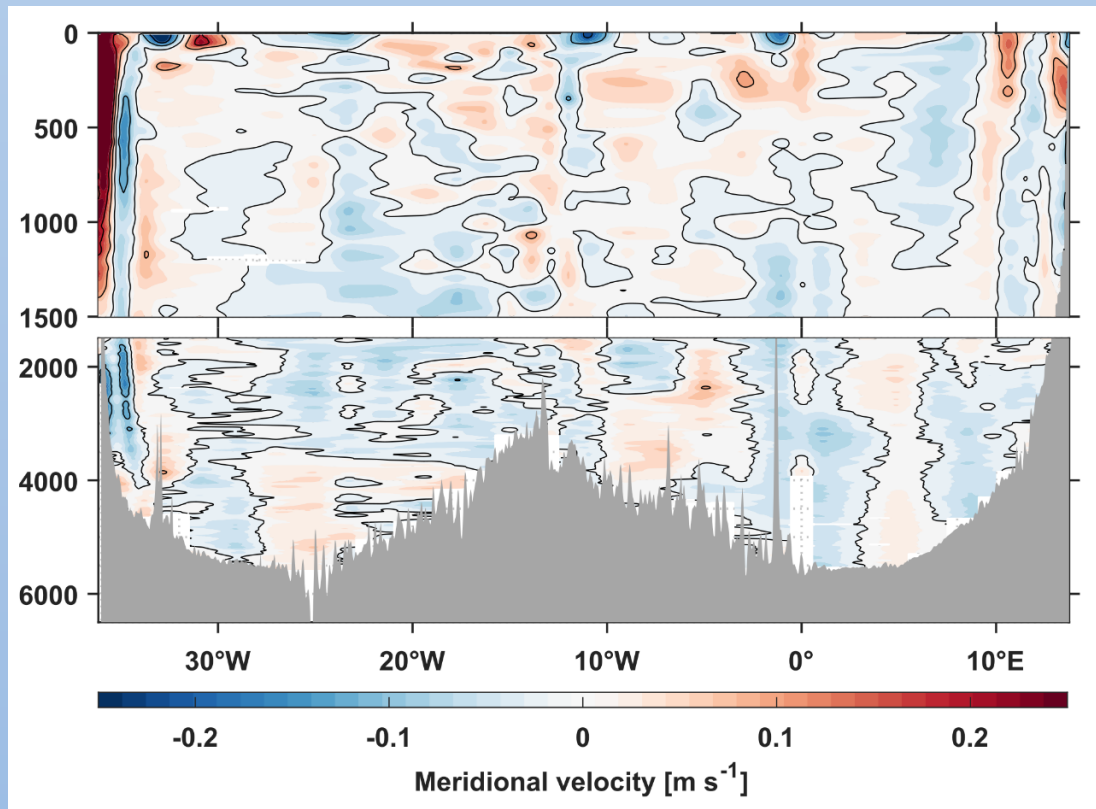


Figure 37 Vertical section of meridional velocity [m s^{-1}] along 11°S measured during METEOR cruise M148/1 in 2018. Red (blue) colors show northward (southward) velocity.

Learning from a recent study by Fu et al. (2018), I think that there is potential in applying the box inverse method to derive absolute AMOC estimates for 11°S . This method uses the thermal wind relation and the constraint of conservation of conservative properties within a predefined box, which is typically bounded by repeatedly measured hydrographic sections and landmasses. For this purpose, I suggest to combine the transatlantic sections along 11°S with repeated sections in the Subtropical South Atlantic ($30^\circ\text{S}/34.5^\circ\text{S}$) or tropical North Atlantic (14.5°N).

In chapter 4, I analyzed the two hydrographic sections along 11°S from 1994 and 2018 with regard to the local water mass property distributions in the Angola and Brazil Basins as well as property changes between the two occupations. The temperature, salinity and dissolved oxygen distributions measured during the cruises M28/1 and M148/1 confirmed several previously observed property extrema, which characterize the subsurface, central, intermediate, deep and bottom waters in the Brazil Basin. All of these property extrema are most pronounced close to the western boundary, however, when above 2000 m, also extend into the eastern basin while weakening and shallowing to the east. Below 2000 m, the Mid-Atlantic Ridge acts as a barrier for deep and bottom water flow leaving modified versions of the North Atlantic Deep Water (NADW) to fill the abyssal Angola Basin. While temperature and salinity are almost homogeneously distributed within the deep Angola Basin, there are some interesting features in the dissolved oxygen distribution being indicative of the abyssal circulation.

I analyzed water mass property changes between the two hydrographic sections from 1994 and 2018 by distinguishing between changes along isopycnal surfaces and vertical displacement of the isopycnals. The strongest signal is an intrinsic warming (and salinification) of the central water layers, which is in agreement with previous studies and probably related to an increasing Agulhas leakage

arriving in the NBUC region at 11°S. The intermediate water layers are characterized by intrinsic cooling above 600 m and intrinsic warming below. I stressed the warming in the lower intermediate water layers to be rather related to a continuous warming of deep waters from around Antarctica over the last decades than to an increased input of Indian Ocean waters at intermediate layers. Although weakening towards the east, both warming signals can also be found in the Angola Basin after 1994. Property changes in the deep and bottom water layers are ambiguous: Besides an intrinsic warming and oxygen increase in the upper NADW layers in the western boundary region, which could be caused by decadal variations further upstream, most of the changes in the lower deep and bottom water layers in the Brazil Basin are dominated by isopycnal displacement. The most prominent signal is the warming of Antarctic Bottom Water (AABW), which has been related to a volume loss of its densest component in the Brazil Basin and reported to be accompanied by a volume increase in the deep water layers above (e.g. Johnson et al., 2014; Herrford et al., 2017).

Analyze new hydrographic data from cruises along 11°S, 5°S, 35°W and 23°W:

A number of recent hydrographic sections in the northwestern Brazil Basin (see Table 5) allows for an update of the analyses of long-term water mass property changes presented in Hummels et al. (2015) or Herrford et al. (2017).

Table 5 New hydrographic measurements along four repeated ship sections with in the tropical Atlantic, which are going to full-depth and were conducted after 2014. This table represents an update of table 2 in Herrford et al. (2017).

11°S (western boundary)	11°S (eastern boundary)	5°S	35°W	23°W
M119 (2015)	M120 (2015)	M119 (2015)		M119 (2015)
M130 (2016) M131 (2016)	M131 (2016)	M130 (2016)		M130 (2016)
PIR17 (2017)				
M145 (2018) M148 (2018)	M148 (2018)	M145 (2018)		M145 (2018)
M159 (2019)		M159 (2019)	M159 (2019)	M158 (2019)

Particularly interesting is the comparison of a recent section along 35°W in 2019 to hydrographic data from previous occupations between 1990-2004. Preliminary results showed similar property changes in the upper 1200 m of the water column as observed at 11°S. In contrast to the continuous abyssal warming observed within the Vema Channel (Zenk, 2019) or at 11°S (section 4.4), however, abyssal temperatures within the Equatorial Channel along 35°W are even slightly lower in 2019 than in 2003 (see Fig. 38). In the northern Brazil Basin, Herrford et al. (2017) detected decadal variations on isopycnals corresponding to a lighter AABW component with warming in the 1990s and cooling in the 2000s. They argue, that only this lighter AABW and not the denser components are able to pass through the Equatorial Channel into the North Atlantic.

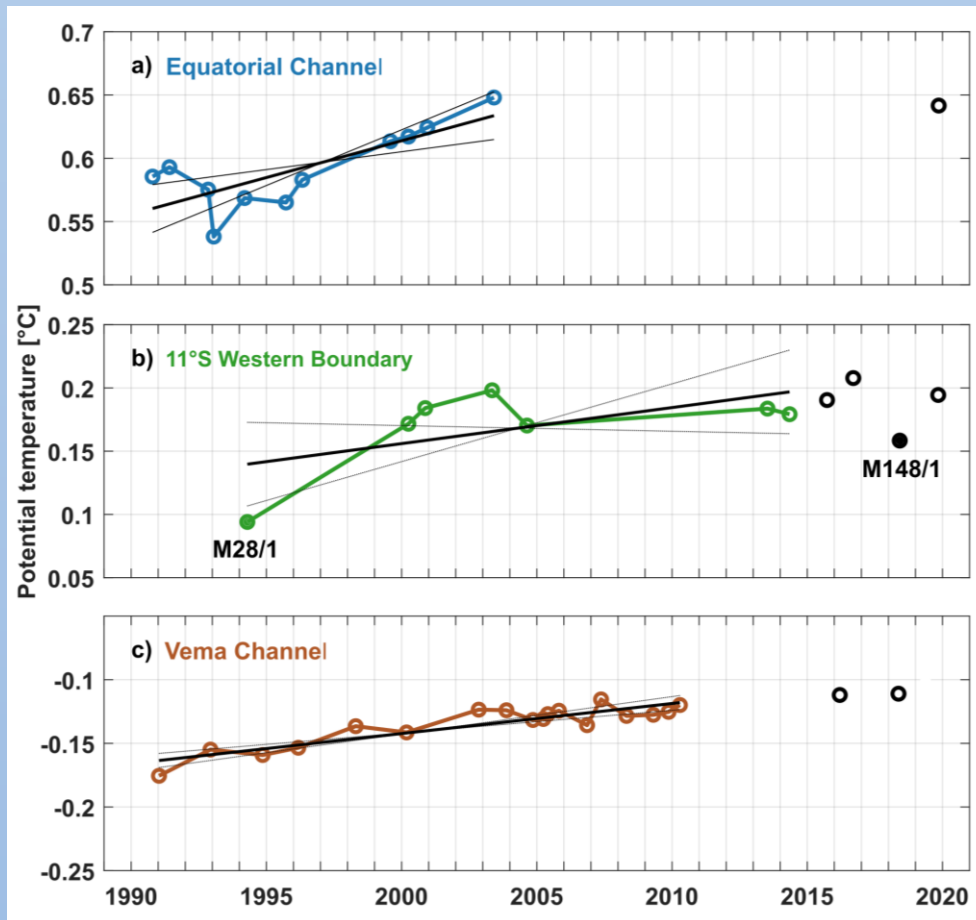


Figure 38 Evolution of θ [°C] of the coldest AABW found in the Equatorial Channel (a), at the western boundary along 11°S (b) and within the Vema Channel (c). Linear fits are shown as black solid lines and their 95% confidence estimates (the standard error of the slope of the fit multiplied by 1.96) as black dashed lines. This figure is an update of Fig. 11 in Herrford et al. (2017) as well as adapted from Fig. 18 in Zenk (2019). Linear Black circles mark new temperature measurements from recent cruises – from M159 (2019) in (a) and from M119 (2015), M130 (2016), M148 (2018), M159 (2019) in (b). Please note, that in (c), the 2016 proxy was calculated from a downstream observation at 27° S under the assumption of a given averaged horizontal temperature gradient. The data point from May 2018 was taken during Polarstern cruise PS113 and declared preliminary (Zenk, 2019).

The western boundary mooring array at 11°S is, besides current meters, also equipped with about 20 MicroCats, which measure temperature and salinity at selected depths between 500-3500 m. The available timeseries cover the periods 2000-2004 and 2013-today. I suggest to additionally analyze those in order to quantify the strength of temperature and salinity variations on hourly to interannual timescales. The difficulty in this analysis lies in finding a proper way to calibrate the MicroCat measurements for the earlier period, for which no calibration casts are available.

One of the new findings in chapter 4, is an oxygen increase of $2-3 \mu\text{mol kg}^{-1} \text{dec}^{-1}$ within the AABW layers of the Brazil Basin between 1994 and 2018, which has not been observed before. It is not clear, whether this oxygen increase is the result of changes in local circulation and/or mixing processes or changes in any of the lower NADW/AABW source waters. A similar oxygen increase was observed in the lower NADW/lighter AABW layers above the western flank of the Mid-Atlantic Ridge as well as the entire abyssal Angola Basin below 2000 m.

Investigate dissolved oxygen changes in the abyssal Brazil and Angola Basins:

The oxygen increase in the bottom water layers along 11°S has not been observed before and should be investigated further. It could directly be related to the oxygen increase reported for the NADW layers within the DWBC over the last 15 years (section 4.4; Hummels et al., 2015). Excessive mixing between the NADW and AABW along the deep western boundary (Herrford et al., 2017) in combination with a northward bottom water flow above the western flank of the Mid-Atlantic Ridge (e.g. Warren & Speer, 1991), could explain similar signals of oxygen increase there and in the deep Angola Basin. However, changes in the AABW source water advected into the region can also not be ruled out.

Too little is known about the abyssal circulation in general, as the deep ocean is not sufficiently sampled. The same lack of deep ocean observations also limits the performance of numerical models (e.g. Gasparin et al., 2019). The majority of Argo floats concentrates on the upper 2000 m of the of the water column and full-depth hydrographic measurements are rather sparse in time (e.g. Frajka-Williams et al., 2019). Currently, there are about 50 deep Argo floats in operation (McCarthy et al., 2020) – this number should be substantially increased, especially in poorly sampled regions or along important bottom water routes.

The results from my thesis contribute to the overall understanding of AMOC-related variability in the tropical Atlantic as well as possible uncertainties in the variability of different AMOC components derived from observations. Any locally forced signal of AMOC variability, that is understood and can be quantified, makes it easier to identify any large-scale coherent signals.

The TRACOS array at 11°S, as it is today, allows for monitoring AMOC variations on intra-seasonal to interannual timescales. Especially, when embedded in the PIRATA program or in combination with other AMOC arrays, however, the TRACOS arrays has also great potential for understanding mechanisms relevant for tropical Atlantic variability, as well as meridional coherence and long-term changes of AMOC variability. Maintenance cruises for the moored platforms and additional shipboard measurements within the frames of the PIRATA (Bourlès et al., 2019) and EAF-Nansen (Tchikalanga et al., 2018) programs are planned for the next years.

Provide observations to a broader range of user communities:

Following the vision of global ocean observing system that serves a broader range of communities, we should put much more effort into making our data or products “more findable, accessible, interoperable and reusable” (Wilkinson et al., 2016) as well as into communicating scientific discoveries and arguments to different public groups. I suggest to start by setting up a homepage for the observational program at 11°S or update the result from 11°S, such as the transport timeseries of the boundary currents and AMOC, on platforms like the GEOMAR-homepage or OceanSITES on a regular basis.

References

- Alley, R. B.: Wally was right: Predictive ability of the North Atlantic “conveyor belt” hypothesis for abrupt climate change, *Ann. Rev. Earth Planet. Sci.*, 35, 241–272, doi:10.1146/annurev.earth.35.081006.131524, 2007.
- Andreas, E. L, Mahrt, L., and Vickers, D.: A new drag relation for aerodynamically rough flow over the ocean, *J. Atmos. Sci.*, 69, 2520–2537, doi:10.1175/JAS-D-11-0312.1, 2012.
- Arbic, B. K., and Owens, W. B.: Climatic warming of Atlantic Intermediate Waters, *J. Climate*, 14, 4091–4108, doi: 10.1175/1520-0442(2001)014%3C4091:CWOAIW%3E2.0.CO;2, 2011.
- Arhan, M., Mercier, H., Bourlès, B., and Gouriou, Y.: Hydrographic sections across the Atlantic at 7°30N and 4°30S, *Deep Sea Res. Part I*, 45, 829–872., doi:10.1016/S0967-0637(98)00001-6, 1998.
- Atlas, R., Hoffman, R. N., Bloom, S. C., Jusem, J. C., and Ardizzone, J.: A multiyear global surface wind velocity dataset using SSM/I wind observations, *Bull. Am. Meteorol. Soc.*, 77, 869–882, doi:10.1175/1520-0477(1996)077<0869:AMGSWV>2.0.CO;2, 1996.
- Atlas, R., Ross, N., Hoffman, N., Ardizzone, J., Leidner, S. M., Jusem, J. C., Smith, D. K., and Gombos, D.: A cross-calibrated, multiplatform ocean surface wind velocity product for meteorological and oceanographic applications, *Bull. Am. Meteorol. Soc.*, 92, 157–174, doi:10.1175/2010BAMS2946.1, 2011.
- Azaneu, M., Kerr, R., Mata, M. M., and Garcia, C. A. E.: Trends in the deep Southern Ocean (1958–2010): Implications for Antarctic Bottom Water properties and volume export, *J. Geophys. Res. Oceans.*, 118, 4213–4227, doi:10.1002/jgrc.20303, 2013.
- Bachèlery, M.-L., Illig, S., and Dadou, I.: Interannual variability in the South-East Atlantic Ocean, focusing on the Benguela Upwelling System: Remote versus local forcing, *J. Geophys. Res. Oceans*, 121, 284–310, doi:10.1002/2015JC011168, 2016.
- Bakker, P., Schmittner, A., Lenaerts, J. T. M., Abe-Ouchi, A., Bi, D., van den Broeke, M. R., Chan, W.-L., Hu, A., Breadling, R. L., Marsland, S. J., Mernild, S. H., Saenko, O. A., Swingedouw, D., Sullivan, A., and Yin, J.: Fate of the Atlantic Meridional Overturning Circulation: Strong decline under continued warming and Greenland melting, *Geophys. Res. Lett.*, 43, 12252–12260, doi:10.1002/2016GL070457, 2016.
- Barker, S., Knorr, G., R. Edwards, L., Parrenin, F., Putnam, A. E., Skinner, L. C., Wolff, E., and Ziegler, M.: 800,000 years of abrupt climate variability, *Science*, 334, 347–351, doi:10.1126/science.1203580, 2011.
- Belkin, I. M., and Gordon, A. L.: Southern Ocean fronts from the Greenwich meridian to Tasmania, *J. Geophys. Res. Oceans*, 101, 3675–3696, doi:10.1029/95JC02750, 1996.
- Belmonte Rivas, M., and Stoffelen, A.: Characterizing ERA-Interim and ERA5 surface wind biases using ASCAT, *Ocean Sci.*, 15, 831–852, doi:10.5194/os-15-831-2019, 2019.
- Bentamy, A. and Croizé-Fillon, D.: Gridded surface wind fields from Metop/ASCAT measurements, *Int. J. Remote Sens.*, 33, 1729–1754, doi:10.1080/01431161.2011.600348, 2012.
- Bentamy, A., Grodsky, S. A., Carton, J. A., Croizé-Fillon, D., and Chapron, B.: Matching ASCAT and QuikSCAT winds, *J. Geophys. Res.*, 117, C02011, doi:10.1029/2011JC007479, 2012.
- Berrisford, P., Kållberg, P., Kobayashi, S., Dee, D., Uppala, S., Simmons, A.J., Poli, P., and Sato, H.: Atmospheric conservation properties in ERA-Interim, *Q. J. R. Meteorol. Soc.*, 137, 1381–1399, doi:10.1002/qj.864, 2011.

-
- Biastoch, A., Böning, C. W., Getzlaff, J., Molines, J., and Madec, G.: Causes of Interannual–Decadal Variability in the Meridional Overturning Circulation of the Midlatitude North Atlantic Ocean, *J. Clim.*, 21(24), 6599–6615, doi:10.1175/2008JCLI2404.1, 2008a.
 - Biastoch, A., Böning, C. W., and Lutjeharms, J. R. E.: Agulhas leakage dynamics affects decadal variability in Atlantic overturning circulation, *Nature*, 456, 489–492, doi:10.1038/nature07426, 2008b.
 - Biastoch, A., Böning, C. W., Schwarzkopf, F. U., and Lutjeharms, J. R. E.: Increase in Agulhas leakage due to poleward shift of Southern Hemisphere westerlies, *Nature*, 462, 495–498, doi:10.1038/nature08519, 2009.
 - Bindoff, N. L. and McDougall, T. J.: Diagnosing Climate Change and Ocean Ventilation Using Hydrographic Data, *J. Phys. Oceanogr.*, 24, 1137–1152, doi:10.1175/1520-0485(1994)024%3C1137:DCCAOV%3E2.0.CO;2, 1994.
 - Boebel, O., Schmid, C. and Zenk, W.: Kinematic elements of Antarctic Intermediate Water in the western South Atlantic, *Deep Sea Res. Part II Top. Stud. Oceanogr.*, 46, 355–392, doi:10.1016/S0967-0645(98)00104-0, 1999.
 - Böning, C., Behrens, E., Biastoch, A., Getzlaff, K., and Lamber, J. L.: Emerging impact of Greenland meltwater on deepwater formation in the North Atlantic Ocean, *Nat. Geosci.*, 9, 523–527, doi:10.1038/ngeo2740, 2016.
 - Bourlès, B., Araujo, M., McPhaden, M. J., Brandt, P., Foltz, G. R., Lumpkin, R., Giodiani, H., Hernandez, F., Lefèvre, N., Nobre, P., Campos, E., Saravanan, R., Trotte-Duhà, J., Dengler, M., Hahn, J., Hummels, R., Lübbecke, J. F., Rouault, M., Cotrim, L., Sutton, A., Jochum, M., and Perez, R. C.: PIRATA: A Sustained Observing System for Tropical Atlantic Climate Research and Forecasting, *Earth Space Sci.*, 6, 577–616, doi:10.1029/2018ea000428, 2019.
 - Bower, A. S., Lozier, M. S., Gary, S. F., and Böning, C. W.: Interior pathways of the North Atlantic meridional overturning circulation, *Nature*, 459, 243–247, doi:10.1038/nature07979, 2009.
 - Brahmananda Rao, V., Giarolla, E., Monteiro do Espírito Santo, C., and Henrique Franchito, S.: Comparison of surface wind stress characteristics over the Tropical Atlantic (10°N–40°S) in fields derived from the UWM/COADS, NCEP/NCAR and QuikSCAT datasets, *J. Oceanogr.*, 64, 551–560, doi:10.1007/s10872-008-0046-9, 2008.
 - Brandt, P., Hormann, V., Bourlès, B., Fischer, J., Schott, F. A., Stramma, L., and Dengler, M.: Oxygen tongues and zonal currents in the equatorial Atlantic, *J. Geophys. Res.*, 113, C04012, doi:10.1029/2007JC004435, 2008.
 - Brandt, P., Bange, H. W., Banyte, D., Dengler, M., Didwischus, S.-H., Fischer, T., Greatbatch, R. J., Hahn, J., Kanzow, T., Karstensen, J., Körtzinger, A., Krahnemann, G., Schmidtko, S., Stramma, L., Tanhua, T., and Visbeck, M.: On the role of circulation and mixing in the ventilation of oxygen minimum zones with a focus on the eastern tropical North Atlantic, *Biogeosciences*, 12, 489–512, doi:10.5194/bg-12-489-2015, 2015.
 - Brandt, P., Claus, M., Greatbatch, R. J., Kopte, R., Toole, J. M., Johns, W. E., and Böning, C. W.: Annual and semiannual cycle of equatorial Atlantic circulation associated with basinmode resonance, *J. Phys. Oceanogr.*, 46, 3011–3029, doi:10.1175/JPO-D-15-0248.1, 2016.
 - Brandt, P., Hahn, J., Schmidtko, S., Tuchen, F. P., Kopte, R., Kiko, R., Bourlès, B., Czeschel, R., and Dengler, M.: Upper equatorial Atlantic current intensification counteracting warming induced deoxygenation, *Nat. Geosci.*, doi:10.1038/s41561-021-00716-1, 2021.

-
- Brayshaw, D. J., Hoskins, B., and Blackburn, M.: The Basic Ingredients of the North Atlantic Storm Track. Part I: Land–Sea Contrast and Orography, *J. Atmos. Sci.*, *66*, 2539–2558, doi:10.1175/2009JAS3078.1, 2009.
 - Bryden H. L., and Imawaki, S.: Ocean heat transport, *Int. Geophys.*, *77*, 455–474, doi:10.1016/S0074-6142(01)80134-0, 2001.
 - Bryden, H. L., Longworth, H. R., and Cunningham, S. A.: Slowing of the Atlantic meridional overturning circulation at 25°N, *Nature*, *438*, 655–657, doi:10.1038/nature04385, 2005.
 - Buckley, M. W., and Marshall, J.: Observations, inferences, and mechanisms of the Atlantic Meridional Overturning Circulation: A review, *Rev. Geophys.*, *54*, 5–63, doi:10.1002/2015RG000493, 2016.
 - Burmeister, K., Lübbecke, J. F., Brandt, P., and Duteil, O.: Interannual variability of the Atlantic North Equatorial Undercurrent and its impact on oxygen, *J. Geophys. Res. Oceans*, *124*, 2348–2373, doi:10.1029/2018JC014760, 2019.
 - Caesar, L., Rahmstorf, S., Robinson, A., Feulner, G., and Saba, V.: Observed fingerprint of a weakening Atlantic Ocean overturning circulation, *Nature*, *556*, 191–196, doi:10.1038/s41586-018-0006-5, 2018.
 - Castellanos, P., Pelegrí, J., Campos, E. J. D., Rosell-Fieschi, M., and Gasser, M.: Response of the surface tropical Atlantic Ocean to wind forcing, *Prog. Oceanogr.*, *134*, 271–292, doi:10.1016/j.pocean.2015.02.005, 2015.
 - Chaudhuri, A. H., Ponte, R. M., Forget, G., and Heimbach, P.: A comparison of atmospheric reanalysis surface products over the ocean and implications for uncertainties in air-sea boundary forcing, *J. Clim.*, *26*, 153–170, doi:10.1175/JCLI-D-12-00090.1, 2013.
 - Chelton, D. B., Schlax, M. G., Freilich, M. H., and Milliff, R. F.: Satellite measurements reveal persistent small-scale features in ocean winds, *Science*, *303*, 978–983, doi:10.1126/science.1091901, 2004.
 - Chelton, D. B. and Freilich, M. H.: Scatterometer based assessment of 10-m wind analyses from the operational ECMWF and NCEP numerical weather prediction models, *Mon. Weather Rev.*, *133*, 409–429, doi:10.1175/MWR-2861.1, 2005.
 - Chidichimo, M. P., Kanzow, T., Cunningham, S. A., Johns, W. E., and Marotzke, J.: The contribution of eastern-boundary density variations to the Atlantic meridional overturning circulation at 26.5°N, *Ocean Sci.*, *6*, 475–490, doi:10.5194/os-6-475-2010, 2010.
 - Chu, P. C., Ivanov, L. M., Melnichenko, O. V., and Wells, N. C.: On long baroclinic Rossby waves in the tropical North Atlantic observed from profiling floats, *J. Geophys. Res.*, *112*, C05032, doi:10.1029/2006JC003698, 2007.
 - Clark, P. U., Pisas, N. G., Stocker, T. F., and Weaver, A. J.: The role of the thermohaline circulation in abrupt climate change, *Nature*, *415*, 863–869, doi:10.1038/415863a, 2002.
 - Codiga, D.L.: Unified Tidal Analysis and Prediction Using the UTide Matlab Functions. Technical Report 2011-01. Graduate School of Oceanography, University of Rhode Island, Narragansett, RI. 59pp. <ftp://www.po.gso.uri.edu/pub/downloads/codiga/pubs/2011Codiga-UTide-Report.pdf> (latest access: 15 March 2017), 2011.
 - Cunningham, S. A., Kanzow, T., Rayner, D., Baringer, M. O., Johns, W. E., Marotzke, J., Longworth, H. R., Grant, E. M., Hirschi, J. J.-M., Beal, L. M., Meinen, C. S., Bryden, H. L.: Temporal variability of the Atlantic meridional overturning circulation at 26.5°N, *Science*, *317*, 935–938. doi:10.1126/science.1141304, 2007.

- Cunningham, S. A.: RRS Discovery Cruise D334, 27 Oct-24 Nov 2008. RAPID Mooring Cruise Report, 2009.
- da Silveira, I. C. A., Miranda, L. B., and Brown, W. S.: On the origins of the North Brazil Current, *J. Geophys. Res.*, 99, 22501-22512, doi:10.1029/94JC01776, 1994.
- Danabasoglu, G., Yeager, S. G., Kwon, Y.-O., Tribbia, J. J., Phillips, A. S., and Hurrell, J. W.: Variability of the Atlantic Meridional Overturning Circulation in CCSM4, *J. Clim.*, 25, 5153-5172, doi:10.1175/JCLI-D-11-00463.1, 2012.
- Dee, D. P., Uppala, S. M., Simmons, A. J., Berrisford, P., Poli, P., Kobayashi, S., Andrae, U., Balmaseda, M. A., Balsamo, G., Bauer, P., Bechtold, P., Beljaars, A. C. M., van de Berg, L., Bidlot, J., Bormann, N., Delsol, C., Dragani, R., Fuentes, M., Geer, A. J., Haimberger, L., Healy, S. B., Hersbach, H., Hólm, E.V., Isaksen, I., Kållberg, P., Köhler, M., Matricardi, M., McNally, A. P., Monge-Sanz, B.M., Morcrette, J.-J., Park, B.-K., Peubey, C., de Rosnay, P., Tavolato, C., Thépaut, J.-N., and Vitart, F.: The ERA-Interim reanalysis: configuration and performance of the data assimilation system, *Q.J.R. Meteorol. Soc.*, 137, 553-597, doi:10.1002/qj.828, 2011.
- Demidov, A. N., Dobrolyubov, S. A., Morozov, E. G., and Tarakanov, R. Y.: Transport of bottom waters through the Vema Fracture Zone in the Mid-Atlantic ridge, *Dokl. Earth Sci.*, 416, 1120-1124, doi:10.1134/S1028334X07070318, 2007.
- Dengler, M., and Quadfasel, D.: Equatorial deep jets and abyssal mixing in the Indian Ocean, *J. Phys. Oceanogr.*, 32, 1165-1180, doi:10.1175/1520-0485(2002)032<1165:EDJAAM>2.0.CO;2, 2002.
- Dengler, M., Schott, F. A., Eden, C., Brandt, P., Fischer, J., and Zantopp, R. J.: Break-up of the Atlantic deep western boundary current into eddies at 8 degrees S, *Nature*, 432, 1018–1020, doi:10.1038/nature03134, 2004.
- Dickson, R. R., and Brown, J.: The production of North Atlantic Deep Water: Sources, rates, and pathways, *J. Geophys. Res.*, 99, 12319–12341, doi:10.1029/94JC00530, 1994.
- Dickson, B., Yashayaev, I., Meincke, J., Turrell, B., Dye, S., and Holfort, J.: Rapid freshening of the deep North Atlantic Ocean over the past four decades, *Nature*, 416, 832-837, doi:10.1038/416832a, 2002.
- Dong, S., Baringer, M. O., Goni, G. J., Meinen, C. S., and Garzoli, S. L.: Seasonal variations in the South Atlantic Meridional Overturning Circulation from observations and numerical models, *Geophys. Res. Lett.*, 41, 4611–4618, doi:10.1002/2014GL060428, 2014.
- Donohue, K. A., Watts, D. R., Tracey, K. L., Greene, A. D., and Kennelly, M.: Mapping circulation in the Kuroshio Extension with an array of current and pressure recording inverted echo sounders, *J. Atmos. Ocean. Technol.*, 27, 507-527, doi:10.1175/2009JTECHO686.1, 2010.
- Döös, K.: Influence of the Rossby waves on the seasonal cycle in the tropical Atlantic, *J. Geophys. Res.*, 104, 29591–29598, doi:10.1029/1999JC900126, 1999.
- Duhaut, T. H. A., and Straub, D. N.: Wind Stress Dependence on Ocean Surface Velocity: Implications for Mechanical Energy Input to Ocean Circulation, *J. Phys. Oceanogr.*, 36, 202-211, doi:10.1175/JPO2842.1, 2006.
- Durgadoo, J. V., Loveday, B. R., Reason, C. J. C., Penven, P., and Biastoch, A.: Agulhas leakage predominantly responds to the Southern Hemisphere westerlies, *J. Phys. Oceanogr.*, 43, 2113–2131, doi:10.1175/JPO-D-13-047.1, 2013.
- Durrieu de Madron, X., and Weatherly, G.: Circulation, transport and bottom boundary layers of the deep currents in the Brazil Basin, *J. Mar. Syst.*, 52, 583-638, doi:10.1357/0022240943076975, 1994.

- Ebuchi, N., Graber, H. C., and Caruso, M. J.: Evaluation of wind vectors observed by QuikSCAT/SeaWinds using ocean buoydata, *J. Atmos. Ocean. Technol.*, 19, 2049–2062, doi:10.1175/1520-0426(2002)019,2049:EOWVOB.2.0.CO;2, 2002.
- Elipot, S., Hughes, C., Olhede, S., and Toole, J.: Coherence of Western Boundary Pressure at the RAPID WAVE Array: Boundary Wave Adjustments or Deep Western Boundary Current Advection?, *J. Phys. Oceanogr.*, 43, 744-765, doi:10.1175/JPO-D-12-067.1, 2013.
- Elipot, S., Frajka-Williams, E., Hughes, C. W., Olhede, S., and Lankhorst, M.: Observed basin-scale response of the North Atlantic meridional overturning circulation to wind stress forcing, *J. Clim.*, 30, 2029–2054. doi:10.1175/JCLID-16-0664.1, 2017.
- Fahrbach, E., Hoppema, M., Rohardt, G., Boebel, O., Klatt, O., and Wisotzki, A.: Warming of deep and abyssal water masses along the Greenwich meridian on decadal timescales: the Weddell gyre as a heat buffer, *Deep Sea Res. Part II*, 58, 2509–2523, doi: 10.1016/j.dsr2.2011.06.007, 2011.
- Fairall, C.W., Bradley, E. F., Hare, J. E., Grachev, A. A., and Edson, J. B.: Bulk parameterization of air–sea fluxes: Updates and verification for the COARE algorithm, *J. Clim.*, 16, 571–591, doi:10.1175/1520-0442(2003)016,0571:BPOASF.2.0.CO;2, 2003.
- Feng, H., Vandemark, D., Quilfen, Y., Chapron, B., and Beckley, B.: Assessment of wind-forcing impact on a global wind-wave model using the TOPEX altimeter, *Ocean Eng.*, 33, 1431-1461, doi:10.1016/j.oceaneng.2005.10.015, 2006.
- Ferreira, M. L., and Kerr, R.: Source water distribution and quantification of North Atlantic Deep Water and Antarctic Bottom Water in the Atlantic Ocean, *Progr. Oceanogr.*, 153, 66-83, doi:10.1016/j.pocean.2017.04.003, 2017.
- Fore, A. G., Stiles, B. W., Chau, A. H., Williams, B. A., Dunbar, R. S., and Rodriguez, E.: Point-wise wind retrieval and ambiguity removal improvements for the QuikSCAT climatological data set, *IEEE Trans. Geosci. Remote Sens.*, 52, 51–59, doi:10.1109/TGRS.2012.2235843, 2014.
- Frajka-Williams, E., Cunningham, S. A., Bryden, H., and King, B. A.: Variability of Antarctic Bottom Water at 24.5°N in the Atlantic, *J. Geophys. Res.* 116, C11026, doi: 10.1029/2011JC007168, 2011.
- Frajka-Williams, E., Lankhorst, M., Koelling, J., and Send, U.: Coherent circulation changes in the Deep North Atlantic from 16°N and 26°N transport arrays, *J. Geophys. Res.*, 123, 3427-3443, doi:10.1029/2018JC013949, 2018.
- Frajka-Williams, E., Ansorge, I. J., Baehr, J., Bryden, H. L, Chidichimo, M. P., Cunningham, S. A., Danabasoglu, G., Dong, S., Donohue, K. A., Elipot, S., Heimbach, P., Holliday, N. P., Hummels, R., Jackson, L. C., Karstensen, J., Lankhorst, M., Le Bras, I. A., Lozier, M. S., McDonagh, E. L., Meinen, C. S., Mercier, H., Moat, B. I., Perez, R. C., Piecuch, C. G., Rhein, M., Srokosz, M. A., Trenberth, K. E., Bacon, S., Forget, G., Goni, G., Kieke D., Koelling, J., Lamont, T., McCarthy, G. D., Mertens, C., Send, U., Smeed, D. A., Speich, S., van den Berg, M., Volkov, D., and Wilson, C.: Atlantic Meridional Overturning Circulation: Observed transport and variability, *Front. Mar. Sci.*, 6, 260, doi:10.3389/fmars.2019.00260, 2019.
- Fu, Y., Karstensen, J., and Brandt, P.: Atlantic Meridional Overturning Circulation at 14.5°N in 1989 and 2013 and 24.5°N in 1992 and 2015: volume, heat, freshwater transports, *Ocean Sci.*, 14, 589-616, doi:10.5194/os-14-589-2018, 2018.
- Fujiwara, M., Wright, J. S., Manney, G. L., Gray, L. J., Anstey, J., Birner, T., Davis, S., Gerber, E. P., Harvey, V. L., Hegglin, M. I., Homeyer, C. R., Knox, J. A., Krüger, K., Lambert, A., Long, C. S., Martineau, P., Molod, A., Monge-Sanz, B. M., Santee, M. L., Tegtmeier, S., Chabrillat, S., Tan, D. G. H., Jackson, D. R., Polavarapu, S., Compo, G. P., Dragani, R., Ebisuzaki, W., Harada, Y., Kobayashi, C., McCarty, W., Onogi, K., Pawson, S., Simmons, A., Wargan, K., Whitaker, J. S., and Zou, C.-Z.:

- Introduction to the SPARC reanalysis Intercomparison project (S-RIP) and overview of the reanalysis systems, *Atmos. Chem. and Phys.*, 17, 1417–1452, doi:10.5194/acp-17-1417-2017, 2017.
- Ganachaud, A., and Wunsch, C.: Large-scale ocean heat and freshwater transports during the World Ocean Circulation Experiment, *J. Clim.*, 16, 696–705, doi:10.1175/1520-0442(2003)016<0696:LSOHAF>2.0.CO;2, 2003.
 - Garzoli, S. L., Baringer, M. O., Dong, S., Perez, R. C., and Yao, Q.: South Atlantic meridional fluxes, *Deep Sea Res. Part I Oceanogr. Res. Pap.*, 71, 21–32, doi:10.1016/j.dsr.2012.09.003, 2013.
 - Garzoli, S. L., Dong, S., Fine, R., Meinen, C. S., Perez, R. C., Schmid, C., van Sebille, E., and Yao, Q.: The fate of the deep Western boundary current in the South Atlantic, *Deep Sea Res. Part I Oceanogr. Res. Pap.*, 103, 125–136, doi:10.1016/j.dsr.2015.05.008, 2015.
 - Gibson, J. K., Kållberg, P., Uppala, S., Hernandez, A., Nomura, A., and Serrano, E.: ERA description, ECMWF Re-Analysis Project Report Series, 1, ECMWF, Reading, United Kingdom, 71 pp., 1997.
 - Gouriou, Y., Andrié, C., Boulès, B., Freudenthal, S., Arnault, S., Aman, A., Eldin, G., du Penhoat, Y., Baurand, F., Gallois, F., and Chuchla, R.: Deep circulation in the equatorial Atlantic Ocean, *Geophys. Res. Lett.*, 28, 819–822, doi:10.1029/2000GL012326, 2001.
 - Hahn, J., Brandt, P., Schmidtko, S., and Krahnemann, G.: Decadal oxygen change in the eastern tropical North Atlantic, *Ocean Sci.*, 13, 551–576, doi:10.5194/os-13-551-2017, 2017.
 - Hansen, B., and Osterhus, S.: Faroe Bank Channel overflow 1995-2005, *Progr. Oceanogr.* 75, 817-856, doi:10.1016/j.pocean.2007.09.004, 2007.
 - Hansen, B., Larsen, K., Hátún, H., and Østerhus, S.: A stable Faroe Bank Channel overflow 1995-2015, *Ocean Sci.*, 12, 1205–1220, doi:10.5194/os-12-1205-2016, 2016.
 - Herrford, J., Brandt, P., and Zenk, W.: Property Changes of Deep and Bottom Waters in the western tropical Atlantic, *Deep-Sea Res. Part I Oceanogr. Res. Pap.*, 124, 103-125, doi:10.1016/j.dsr.2017.04.007, 2017.
 - Herrford, J., Brandt, P., Kanzow, T., Hummels, R., Araujo, M., and Durgadoo, J. V.: Seasonal variability of the Atlantic Meridional Overturning Circulation at 11°S inferred from bottom pressure measurements, *Ocean Sci.*, doi:10.5194/os-2020-55, 2021.
 - Hersbach, H.: Assimilation of scatterometer data as equivalent-neutral wind, ECMWF Technical Memorandum, 629, 2010a.
 - Hersbach, H. and Dee, D.: ERA5 reanalysis is in production, ECMWF Newsletter, 147, 5-6, available at: <https://www.ecmwf.int/en/newsletter/147/news/era5-reanalysis-production> (latest access: 24 December 2020), 2016.
 - Hersbach, H., Bell, P., Berrisford, P., Horányi, A., Sabater, J. M., Nicolas, J., Radu, R., Schepers, D., Simmons, A., Soci, C., and Dee, D: Global reanalysis: goodbye ERA-interim, hello ERA5, ECMWF Newsletter, 159, 17-24, doi:10.21957/vf291hehd7, 2019.
 - Hersbach, H., Bell, B., Berrisford, P., Hirahara, S., Horányi, A., Muñoz-Sabater, J., Nicolas, J., Peubey, C., Radu, R., Schepers, D., Simmons, A., Soci, C., Abdalla, S., Abellan, X., Balsamo, G., Bechtold, P., Biavati, G., Bidlot, J., Bonavita, M., De Chiara, G., Dahlgren, P., Dee, D., Diamantakis, M., Dragani, R., Flemming, J., Forbes, R., Fuentes, M., Geer, A., Haimberger, L., Healy, S., Hogan, R. J., Hólm, E., Janisková, M., Keeley, S., Laloyaux, P., Lopez, P., Lupu, C., Radnoti, G., de Rosnay, P., Rozum, I., Vamborg, F., Villaume, S., and Thepaut, J.-N.: The ERA5 global reanalysis, *Q. J. R. Meteorol. Soc.*, 146, 1999-2049, doi: 10.1002/qj.3803, 2020.
 - Hirschi, J., Baehr, J., Marotzke, J., Stark, J., Cunningham, S., and Beismann, J.-O.: A monitoring design for the Atlantic meridional overturning circulation, *Geophys. Res. Lett.*, 30, 1413, doi:10.1029/2002GL016776, 2003.

- Hirschi, J. J., Killworth, P. D., and Blundell, J. R.: Subannual, Seasonal, and Interannual Variability of the North Atlantic Meridional Overturning Circulation, *J. Phys. Oceanogr.*, 37, 1246–1265, doi:10.1175/JPO3049.1, 2006.
- Hirschi, J., and Marotzke, J.: Reconstructing the Meridional Overturning Circulation from boundary densities and the zonal wind stress, *J. Phys. Oceanogr.*, 37, 743–763, doi:10.1175/JPO3019.1, 2007.
- Hobbs, W. R., and Willis, J. K.: Midlatitude North Atlantic heat transport: A time series based on satellite and drifter data, *J. Geophys. Res.*, 117, C01008, doi:10.1029/2011JC007039, 2012.
- Hoffman, R. N., Leidner, S. M., Henderson, J. M., Atlas, R., Ardizzone, J. V., and Bloom, S. C.: A two-dimensional variational analysis method for NSCAT ambiguity removal: Methodology, sensitivity, and tuning, *J. Atmos. Ocean. Technol.*, 20, 585–605, doi:10.1175/1520-0426(2003)20<585:ATDVAM>2.0.CO;2, 2003.
- Hogg, N., Siedler, G., and Zenk, W.: Circulation and variability at the southern boundary of the Brazil Basin, *J. Phys. Oceanogr.*, 29, 145–157, doi:10.1175/1520-0485(1999)029%3C0145:CAVATS%3E2.0.CO;2, 1999.
- Hogg, N. G., and Thurnherr, A. M.: A zonal pathway for NADW in the South Atlantic, *J. Oceanogr.*, 61, 493–507, doi:10.1007/s10872-005-0058-7, 2005.
- Holfort, J., Vanicek, M., and Siedler, G.: What causes long-term temporal changes in the South Atlantic?, *Geophys. Res. Lett.*, 27, 1187–1190, doi:10.1029/1999GLO11222, 2000.
- Hughes, C. W., and Wilson, C.: Wind work on the geostrophic ocean circulation: An observational study of the effect of small scales in the wind stress, *J. Geophys. Res.*, 113, C02016, doi: 10.1029/2007JC004371, 2008.
- Hughes, C. W., Williams, J., Blaker, A., Coward, A., and Stepanov, V.: A window on the deep ocean: the special value of ocean bottom pressure for monitoring the large-scale, deep-ocean circulation, *Prog. Oceanogr.*, 161, 19–46, doi: 10.1016/j.pocean.2018.01.011, 2018.
- Hummels, R., Brandt, P., Dengler, M., Fischer, J., Araujo, M., Veleda, D., and Durgadoo, J. V.: Interannual to decadal changes in the western boundary circulation in the Atlantic at 11°S, *Geophys. Res. Lett.*, 42, 7615–7622, doi:10.1002/2015GL065254, 2015.
- Hurrell, J. W., and Trenberth, K. E.: Difficulties in obtaining reliable temperature trends: Reconciling the surface and satellite microwave sounding unit records, *J. Clim.*, 11, 945–967, doi: 10.1175/1520-0442(1998) 011<0945:DIORTT>2.0.CO;2, 1998
- Illig, S., Cadier, E., Bachèlery, M.-L., and Kersalè, M.: Subseasonal coastal-trapped wave propagations in the southeastern Pacific and Atlantic Oceans: 1. A new approach to estimate wave amplitude. *J. Geophys. Res.*, 123, 3915–3941, doi:10.1029/2017JC013539, 2018a.
- Illig, S., Bachèlery, M.-L., and Cadier, E.: Subseasonal coastal-trapped wave propagations in the southeastern Pacific and Atlantic Oceans: 2. Wave characteristics and connection with the equatorial variability, *J. Geophys. Res.*, 123, 3942–3961, doi:10.1029/2017JC013540, 2018b.
- Imbol Koungue, R. A., Illig, S., and Rouault, M.: Role of interannual Kelvin wave propagations in the equatorial Atlantic on the Angola Benguela Current system, *J. Geophys. Res. Oceans*, 122, 4685–4703, doi:10.1002/2016JC012463, 2017.
- Jochumsen, K., Quadfasel, D., Valdimarsson, H., and Jónsson, S.: Variability of the Denmark Strait overflow: Moored time series from 1996–2011, *J. Geophys. Res. Oceans*, 117, doi:10.1029/2012JC008244, 2012.
- Jochumsen, K., Moritz, M., Nunes, N., Quadfasel, D., Larsen, K. M. H., Hansen, B., Valdimarsson, H., and Jonsson, S.: Revised transport estimates of the Denmark Strait overflow, *J. Geophys. Res. Oceans*, 122, 3434–3450, doi:10.1002/2017JC012803, 2017.

-
- Johns, W. E., Kanzow, T., and Zantopp, R.: Estimating ocean transports with dynamic height moorings: An application in the Atlantic Deep Western Boundary Current at 26°N., *Deep-Sea Res. I*, 52, 1542–1567. doi:10.1016/j.dsr.2005.02.002, 2005.
 - Johns, W. E., Baringer, M. O., Beal, L. M., Cunningham, S. A., Kanzow, T., Bryden, H. L., Hirschi, J.J., Marotzke, J., Meinen, C.S., Shaw, B., and Curry, R.: Continuous, Array-Based Estimates of Atlantic Ocean Heat Transport at 26.5°N., *J. Clim.*, 24, 2429–2449, doi:10.1175/2010JCLI3997.1, 2011.
 - Johnson, G. C.: Quantifying Antarctic Bottom Water and North Atlantic Deep Water volumes, *J. Geophys. Res.*, 113, C05027, doi:10.1029/2007JC004477, 2008.
 - Johnson, G. C., Purkey, S. G., and Toole, J.M.: Reduced Antarctic meridional overturning circulation reaches the North Atlantic Ocean, *Geophys. Res. Lett.*, 35, L22601, doi:10.1029/2008GL035619, 2008.
 - Johnson, G. C., McTaggart, K. E., and Wanninkhof, R.: Antarctic Bottom Water temperature changes in the western North Atlantic Ocean from 1989 to 2014, *J. Geophys. Res. Oceans*, 119, 8567–8577, doi:10.1002/2014JC010367, 2014.
 - Jones, P. D., Harpham, C., Troccoli, A., Gschwind, B., Ranchin, T., Wald, L., Goodess, C.M., and Dorling, S: Using ERA-Interim reanalysis for creating datasets of energy-relevant climate variables, *Earth Syst. Sci. Data*, 9, 471–495, doi:10.5194/essd-9-471-2017, 2017.
 - Kajikawa, H., and Kobata, T.: Reproducibility of calibration results by 0-A-0 pressurization procedures for hydraulic pressure transducers, *Meas. Sci. Technol.*, 25, 015008, doi:10.1088/0957-0233/25/1/015008, 2014.
 - Kalnay, E., Kanamitsu, M., Kistler, R., Collins, W., Deaven, D., Gandin, L., Iredell, M., Saha, S., White, G., Woollen, J., Zhu, Y., Chelliah, M., Ebisuzaki, W., Higgins, W., Janowiak, J., Mo, K. C., Ropelewski, C., Wang, A., Leetmaa, A., Reynolds, R., Jenne, R., and Joseph, D.: The NCEP/NCAR 40-year reanalysis project, *Bull. Am. Meteorol. Soc.*, 77, 437–471, doi:10.1175/1520-0477(1996)077<0437:TNYRP>2.0.CO;2, 1996.
 - Kanzow, T., Flechtner, F., Chave, A., Schmidt, R., Schwintzer, P., and Send, U.: Seasonal variation of ocean bottom pressure derived from Gravity Recovery and Climate Experiment (GRACE): Local validation and global patterns. *J. Geophys. Res.*, 110, C09001, doi:10.1029/2004JC002772, 2005.
 - Kanzow, T., Send, U., Zenk, W., Chave, A. D., and Rhein, M.: Monitoring the integrated deep meridional flow in the tropical North Atlantic: long-term performance of a geostrophic array, *Deep-Sea Res. I*, 53, 528–546, doi:10.1016/j.dsr.2005.12.007, 2006.
 - Kanzow, T., Cunningham, S. A., Rayner, D., Hirschi, J. J.-M, Johns, W. E., Baringer, M. O., Bryden, H. L., Beal, L. M., Meinen, C. S., and Marotzke, J.: Observed flow compensation associated with the MOC at 26.5°N in the Atlantic, *Science*, 317, 938–941. doi:10.1126/science.1141293, 2007.
 - Kanzow, T., Send, U., and McCartney, M.: On the variability of the deep meridional transports in the tropical North Atlantic, *Deep-Sea Res. I*, 55, 1601–1623, doi: 10.1016/j.dsr.2008.07.011, 2008.
 - Kanzow, T., Cunningham, S. A., Johns, W. E., Hirschi, J. J.-M., Marotzke, J., Baringer, M. O., Meinen, C. S., Chidichimo, M. P., Atkinson, C., Beal, L. M., Bryden, H. L., and Collins, J.: Seasonal Variability of the Atlantic Meridional Overturning Circulation at 26.5°N, *J. Clim.*, 23, 5678–5698, doi:10.1175/2010JCLI3389.1, 2010.
 - Kara, A. B., Wallcraft, A. J., and Bourassa, M. A.: Air-sea stability effects on the 10 m winds over the global ocean: Evaluations of air-sea flux algorithms, *J. Geophys. Res. Oceans*, 113, C04009, doi:10.1029/2007JC004324, 2008.

-
- Karstensen, J., Stramma, L., and Visbeck, M.: The oxygen minimum zones in the eastern tropical Atlantic and Pacific oceans, *Prog. Oceanogr.*, 77, 331–350, doi: 10.1016/j.pocean.2007.05.009, 2008.
 - Kelly, K. A., Dickinson, S., McPhaden, M. J., and Johnson, G. C.: Ocean currents evident in satellite wind data, *Geophys. Res. Lett.*, 28, 2469–2472, doi:10.1029/2000GL012610, 2001.
 - Kersalé, M., Meinen, C. S., Perez, R. C., Le Henaff, M., Valla, D., Lamont, T., Sato, O. T., Dong, S., Terre, T., van Caspel, M., Chidichimo, M. P., van den Berg, M., Speich, S., Piola, A. R., Campos, E. J. D., Ansorge, I., Volkov, D. L., Lumpkin, R., and Garzoli, S. L.: Highly Variable Upper and Abyssal Overturning Cells in the South Atlantic, *Sci. Adv.*, 6, eaba7573, doi:10.1126/sciadv.aba7573, 2020.
 - Kieke, D., and Yashayaev, I.: Studies of Labrador Sea Water formation and variability in the subpolar North Atlantic in the light of international partnership and collaboration, *Prog. Oceanogr.*, 132, 220–232, doi:10.1016/j.pocean.2014.12.010, 2015.
 - Kilpatrick, T., and Xie, S.-P.: Circumventing rain-related errors in scatterometer wind observations, *J. Geophys. Res. Atmos.*, 121, 9422–9440, doi:10.1002/2016JD025105, 2016.
 - Kilpatrick, T., Xie, S.-P., Tokinaga, H., Long, D., and Hutchings, N.: Systematic Scatterometer Wind Errors Near Coastal Mountains, *Earth Space Sci.*, 6, 1900-1914, doi:10.1029/2019EA000757, 2019.
 - Kim, W. M., Yeager, S., and Danabasoglu, G.: Atlantic multidecadal variability and associated climate impacts initiated by ocean thermohaline dynamics, *J. Clim.*, 33, 1317-1334. doi:10.1175/JCLI-D-19-0530.1, 2020.
 - Kistler, R., Kalnay, E., Collins, W., Saha, S., White, G., Woollen, J., Chelliah, M., Ebisuzaki, W., Kanamitsu, M., Kousky, V., van den Dool, H., Jenne, R., and Fiorino, M.: The NCEP–NCAR 50-year reanalysis: Monthly means CD-ROM and documentation, *Bull. Am. Meteorol. Soc.*, 82, 247–268, doi:10.1175/1520-0477(2001)082<0247:TNNYRM>2.3.CO;2, 2001.
 - Knight, J. R., Folland, C. K., and Scaife, A. A.: Climate impacts of the Atlantic Multidecadal Oscillation, *Geophys. Res. Lett.*, 33, L17706, doi:10.1029/2006gl026242, 2006.
 - Kobayashi, S., Ota, Y., Harada, Y., Ebata, A., Moriya, M., Onoda, H., Onogi, K., Kamahori, H., Kobayashi, C., Endo, H., Miyaoka, K., and Takahashi, K.: The JRA-55 reanalysis: general specifications and basic characteristics, *J. Meteorol. Soc. Japan Ser. II*, 93, 5–48., doi:10.2151/jmsj.2015-001, 2015.
 - Kolodziejczyk, N., Reverdin, G., Gaillard, F., and Lazar, A.: Low-frequency thermohaline variability in the Subtropical South Atlantic pycnocline during 2002–2013, *Geophys. Res. Lett.*, 41, 6468–6475, doi:10.1002/2014GL061160, 2014.
 - Kopte, R., Brandt, P., Dengler, M., Tchikalanga, P. C. M., Macuéria, M., and Ostrowski, M.: The Angola Current: flow and hydrographic characteristics as observed at 11°S, *J. Geophys. Res. Oceans*, 122, 1177-1189, doi:10.1002/2016JC012374, 2017.
 - Kopte, R., Brandt, P., Claus, M., Greatbatch, R. J., and Dengler, M.: Role of equatorial basin-mode resonance for the seasonal variability of the Angola Current at 11°S, *J. Phys. Oceanogr.*, 48, 261–281, doi:10.1175/JPO-D-17-0111.1, 2018.
 - Large, W. G., and Pond, S.: Open ocean momentum flux measurements in moderate to strong winds, *J. Phys. Oceanogr.*, 11, 324–336, doi:10.1175/1520-0485(1981)011<0324:OOMFMI>2.0.CO;2, 1981.
 - Large, W. G., McWilliams, J. C., and Doney, S. C.: Oceanic vertical mixing: a review and a model with a nonlocal boundary layer parameterization, *Rev. Geophys.*, 32, 363–403, doi:10.1029/94RG01872, 1994.

- Large, W. G. and Yeager, S.G.: Diurnal to decadal global forcing for ocean and sea-ice models: The data sets and flux climatologies, NCAR Tech. Note, NCAR/TN-460+STR, 2004.
- Large, W. G., and Yeager, S. G.: The global climatology of an interannually varying air-sea flux data set, *Clim. Dyn.*, 33, 341–364, doi:10.1007/s00382-008-0441-3, 2009.
- Lavin, A., Bryden, H. L., and Parilla, G.: Meridional transport and heat flux variations in the subtropical North Atlantic, *Global Atmos. Ocean Sys.*, 6, 269-293, 1998.
- Le Bars, D., Durgadoo, J. V., Dijkstra, H. A., Biastoch, A., and De Ruijter, W. P. M.: An observed 20-year time series of Agulhas leakage, *Ocean Sci.*, 10, 601–609, doi:10.5194/os-10-601-2014, 2014.
- Liu, W. T., Katsaros, K. B., and Businger, J. A.: Bulk parameterization of air-sea exchanges of heat and water vapor including the molecular constraints at the interface, *J. Atmos. Sci.*, 36, 1722–1735, doi:10.1175/1520-0469(1979)036<1722:BPOASE>2.0.CO;2, 1979.
- Liu, W. T., and Tang, W.: Equivalent Neutral Wind, *J. P. L. Publ.*, 96-17, 16 pp., <https://ntrs.nasa.gov/api/citations/19970010322/downloads/19970010322.pdf> (latest access: 27 July 2019), 1996.
- Liu, W. T. and Xie, X.: Measuring ocean surface wind from space, ed.: Gower, J., in: *Remote Sensing of the Marine Environment, Manual of Remote Sensing*, 6, American Society of Photogrammetry and Remote Sensing, 149–178, 2006.
- Liu, W. T., Xie, X., and Tang, W.: Scatterometer’s unique capability in measuring ocean surface stress, *Oceanography from Space*, In: Barale, V., Gower, J. and Alberotanza, L. (eds), Springer, Dordrecht, doi:10.1007/978-90-481-8681-5_6, 2010.
- Liu, W., Fedorov, A. V., Xie, S.-P., and Hu, S.: Climate impacts of a weakened Atlantic Meridional Overturning Circulation in a warming climate, *Sci. Adv.*, 6, eaaz4876 doi:10.1126/sciadv.aaz4876, 2020.
- Lozier, M. S., Li, F., Bacon, S., Bahr, F., Bower, A. S., Cunningham, S. A., de Jong, M. F., de Steur, L., deYoung, B., Fischer, J., Gary, S. F., Greenan, B. J. W., Holliday, N P., Houk, A., Houpert, L., Inall, M. E., Johns, W. E., Johnson, H. L., Johnson, C., Karstensen, J., Koman, G., Le Bras, I. A., Lin, X., Mackay, N., Marshall, D. P., Mercier, H., Oltmanns, M., Pickart, R. S., Ramsey, A. L., Rayner, D., Straneo, F., Thierry, V., Torres, D. J., Williams, R. G., Wilson, C., Yang, J., Yashayaev, I., and Zhao, J.: A Sea Change in Our View of Overturning in the Subpolar North Atlantic, *Science*, 363, 516-521, doi:10.1126/science.aau6592, 2019.
- Lübbecke, J. F., Durgadoo, J. V., and Biastoch, A.: Contribution of Increased Agulhas Leakage to Tropical Atlantic Warming, *J. Climate*, 28, 9697–9706, doi:10.1175/JCLI-D-15-0258.1, 2015.
- Lübbecke, J. F., Rodríguez-Fonseca, B., Richter, I., Martín-Rey, M., Losada, T., Polo, I., and Keenlyside, N. S.: Equatorial Atlantic variability—Modes, mechanisms, and global teleconnections, *WIREs Clim. Change*, 9:e527, doi: 10.1002/wcc.527, 2018.
- Lumpkin, R., and Speer, K.: Large-Scale Vertical and Horizontal Circulation in the North Atlantic Ocean, *J. Phys. Oceanogr.*, 33, 1902–1920, doi:10.1175/1520-0485(2003)033<1902:LVAHCI>2.0.CO;2, 2003.
- Lumpkin, R., and Speer, K.: Global ocean meridional overturning, *J. Phys. Oceanogr.*, 37, 2550–2562, doi:10.1175/JPO3130.1, 2007.
- Luyten, J. R., Pedlosky, J., and Stommel, H.: The Ventilated Thermocline, *J. Phys. Oceanogr.*, 13, 292–309, doi:10.1175/1520-0485(1983)013<0292:TVT>2.0.CO;2, 1983.
- Madec, G.: NEMO ocean engine, Note du Pôle de modélisation de l’Institute Pierre-Simon Laplace (IPSL) No. 27, France, doi:10.5281/zenodo.3248739, 2008.

-
- Mantyla, A. W., and Reid, J. L.: Abyssal characteristics of the World Ocean waters, *Deep Sea Res. Part I Oceanogr. Res. Pap.*, 30, 805–833, doi:10.1016/0198-0149(83)90002-X, 1983.
 - Marcello, F., Wainer, I., and Rodrigues, R. R.: South Atlantic Subtropical Gyre late twentieth century changes, *J. Geophys. Res. Oceans*, 123, 5194–5209, doi:10.1029/2018JC013815, 2018.
 - Marshall, J., Donohoe, A., Ferreira, D., and McGee, D.: The ocean's role in setting the mean position of the Inter-Tropical Convergence Zone, *Clim. Dyn.*, 42, 1967–1979, doi:10.1007/s00382-013-1767-z, 2014.
 - McCarthy, G., McDonagh, E., and King, B.: Decadal Variability of Thermocline and Intermediate Waters at 24°S. in the South Atlantic, *J. Phys. Oceanogr.*, 41, 157-165, doi: 10.1175/2010JPO4467.1, 2011.
 - McCarthy, G., Frajka-Williams, E., Johns, W. E., Baringer, M. O., Meinen, C. S., Bryden, H. L., Rayner, D., Duchez, A., Roberts, C., and Cunningham, S. A.: Observed interannual variability of the Atlantic meridional overturning circulation at 26.5°N., *Geophys. Res. Lett.*, 39, L19609, doi:10.1029/2012GL052933, 2012.
 - McCarthy, G. D., Smeed, D. A., Johns, W. E., Frajka-Williams, E., Moat, B. I., Rayner, D., Baringer, M. O., Meinen, C. S., Collins, J., and Bryden, H. L.: Measuring the Atlantic meridional overturning circulation at 26°N, *Prog. Oceanogr.*, 130, 91–111, doi:10.1016/j.pocean.2014.10.006, 2015.
 - McCarthy, G. D., Brown, P. J., Flagg, C. N., Goni, G., Houpert, L., Hughes, C. W., Rummels, R., Inall, M., Jochumsen, K., Larsen, K. M. H., Lherminier, P., Meinen, C. S., Moat, B. I., Rayner, D., Rhein, M., Roessler, A., Schmid, C., and Smeed, D. A.: Sustainable observations of the AMOC: methodology and technology. *Rev. Geophys.*, 58, e2019RG000654, doi:10.1029/2019RG000654, 2020.
 - McCartney, M. S.: Recirculating components to the deep boundary current of the Northern North Atlantic, *Prog. Oceanogr.*, 29, 283–383, doi: 10.1016/0079-6611(92)90006-L, 1992.
 - McGregor, S., Sen Gupta, A., Dommenges, D., Lee, T., McPhaden, M. J., and Kessler, W. S.: Factors influencing the skill of synthesized satellite wind products in the tropical Pacific, *J. Geophys. Res. Oceans*, 122, 1072–1089, doi:10.1002/2016JC012340, 2017.
 - Mears, C. A., Smith, D. K., and Wentz, F. J.: Comparison of Special Sensor Microwave Imager and buoy-measured wind speeds from 1987 to 1997, *J. Geophys. Res.*, 106, 11719–11729, doi:10.1029/1999JC000097, 2001.
 - Meinen, C. S., Johns, W. E., Garzoli, S. L., van Sebille, E., Rayner, D., Kanzow, T., and Baringer, M. O.: Variability of the Deep Western Boundary Current at 26.5°N during 2004-2009, *Deep Sea Res. II*, 85, 154-168, doi:10.1016/j.dsr2.2012.07.036, 2013.
 - Meinen, C. S., Garzoli, S. L., Perez, R. C., Campos, E., Piola, A. R., Chidichimo, M.-P., Dong, S., and Sato, O. T.: Characteristics and causes of Deep Western Boundary Current transport variability at 34.5°S during 2009-2014, *Ocean Sci.*, 13, 175-194, doi:10.5194/os-13-175-2017, 2017.
 - Meinen, C. S., Speich, S., Piola, A. R., Ansong, I., Campos, E., Kersalé, M., Terre, T., Chidichimo, M.-P., Lamont, T., Sato, O. T., Perez, R. C., Valla, D., van den Berg, M., Le Hénaff, M., Dong, S., and Garzoli, S. L.: Meridional Overturning Circulation transport variability at 34.5°S during 2009-2017: Baroclinic and barotropic flows and the dueling influence of the boundaries, *Geophys. Res. Lett.*, 45, 4180-4188, doi:10.1029/2018GL077408, 2018.
 - Meissner, T., Smith, D., and Wentz, F.: A 10-year intercomparison between collocated Special Sensor Microwave Imager oceanic surface wind speed retrievals and global analyses, *J. Geophys. Res.*, 106, 11731–11742, doi:10.1029/1999JC000098, 2001.

-
- Mercier, H., and Speer, K. G.: Transport of bottom water in the Romanche Fracture Zone and the Chain fracture zone, *J. Phys. Oceanogr.*, 28, 779–790, doi:10.1175/1520-0485(1998)028%3C0779:TOBWIT%3E2.0.CO;2, 1998.
 - Mercier, H., Weatherly, G. L., and Arhan, M.: Bottom water throughflows at the Rio de Janeiro and Rio Grande Fracture Zones, *Geophys. Res. Lett.*, 27, 1503-1506, doi:10.1029/2000GL011402, 2000.
 - Mercier, H., Lherminier, P., Sarafanov, A., Gaillard, F., Daniault, N., Desbruyères, D., Falina, A., Ferron, B., Gourcuff, C., Huck, T., and Thierry, V.: Variability of the meridional overturning circulation at the Greenland-Portugal OVIDE section from 1993 to 2010, *Prog. Oceanogr.*, 132, 250–261, doi:10.1016/j.pocean.2013.11.001, 2015.
 - Mielke, C., Frajka-Williams, E., and Baehr, J.: Observed and simulated variability of the AMOC at 26°N and 41°N, *Geophys. Res. Lett.*, 40, 1159–1164. doi:10.1002/grl.50233, 2013.
 - Orsi, A. H., Johnson, G. C., and Bullister, J. L.: Circulation, mixing, and production of Antarctic Bottom Water, *Prog. Oceanogr.*, 43, 55–109 doi:10.1016/S0079-6611(99)00004-X, 1999.
 - Oschlies, A., Brandt, P., Stramma, L., and Schmidtko, S.: Drivers and mechanisms of ocean deoxygenation, *Nat. Geosci.*, 11, 467–473, doi: 10.1038/s41561-018-0152-2, 2018.
 - Patara, L., Böning, C.: Abyssal ocean warming around Antarctica strengthens the Atlantic overturning circulation, *Geophys. Res. Lett.*, 41, 3972–3978, doi:10.1002/2014GL059923, 2014.
 - Peterson, R. G., and Stramma, L.: Upper-level circulation in the South Atlantic Ocean, *Progr. Oceanogr.*, 26, 1-73, doi:10.1016/0079-6611(91)90006-8, 1991.
 - Philander, S. G. H., and Pacanowski, R. C.: A model of the seasonal cycle in the tropical Atlantic Ocean, *J. Geophys. Res.*, 91, 14192–14206, doi:10.1029/JC091iC12p14192, 1986.
 - Pickart, R. S., Spall, M. A., Ribergaard, M. H., Moore, G. W. K., and Milliff, R. F.: Deep convection in the Irminger Sea forced by the Greenland tip jet, *Nature*, 424, 152-156, doi:10.1038/nature01729, 2003.
 - Pierce, D. W., Barnett, T. P., and Mikolajewicz, U.: Competing roles of heat and freshwater flux in forcing thermohaline oscillations, *J. Phys. Oceanogr.*, 25, 2046–2064, doi: 10.1175/1520-0485(1995)025%3C2046:CROHAF%3E2.0.CO;2, 1995.
 - Polo, I., Lazar, A., Rodriguez-Fonseca, B., and Arnault, S.: Oceanic Kelvin waves and tropical Atlantic intraseasonal variability: 1. Kelvin wave characterization, *J. Geophys. Res.*, 113, C07009, doi:10.1029/2007JC004495, 2008.
 - Polo, I., Robson, J., Sutton, R., and Balmaseda, M. A.: The Importance of Wind and Buoyancy Forcing for the Boundary Density Variations and the Geostrophic Component of the AMOC at 26°N, *J. Phys. Oceanogr.*, 44, 2387-2408, doi:10.1175/JPO-D-13-0264.1, 2014.
 - Pujol M.-I., Faugère, Y., Taburet, G., Dupuy, S., Pelloquin, C., Ablain, M., and Picot, N.: DUACS DT 2014: the new multimission altimeter dataset reprocessed over 20 years, *Ocean Sci.*, 12, 1067-1090, doi:10.5194/os-12-1067-2016, 2016.
 - Purkey, S. G., Johnson, G.C.: Warming of global abyssal and deep Southern Ocean waters between the 1990s and 2000s: contributions to global heat and sea level rise budgets, *J. Clim.*, 23, 6336-6351, doi:10.1175/2010JCLI3682.1, 2010.
 - Purkey, S.G., and Johnson, G. C.: Global contraction of Antarctic Bottom Water between the 1980s and 2000s, *J. Clim.*, 25, 5830–5844, doi: 10.1175/JCLI-D-11-00612.1, 2012.
 - Rabe, B., Schott, F. A., and Köhl, A.: Mean circulation and variability of the tropical Atlantic during 1952-2001 in the GECCO assimilation fields, *J. Phys. Oceanogr.*, 38, 177-192, doi:10.1175/2007jpo3541.1, 2008.

-
- Rahmstorf, S.: Ocean circulation and climate during the past 120,000 years, *Nature*, 419, 207-214, doi:10.1038/nature01090, 2002.
 - Rahmstorf, S., Box, J. E., Feulner, G., Mann, M. E., Robinson, A., Rutherford, S., and Schaffernicht, E. J.: Exceptional twentieth-century slowdown in Atlantic Ocean overturning circulation, *Nat. Clim. Chang.*, 5, 475–480, doi:10.1038/nclimate2554, 2015.
 - Ramon, J., Lledó, L., Torralba, V., Soret, A., and Doblás-Reyes, F. J.: What global reanalysis best represents near-surface winds?, *Q. J. R. Meteorol. Soc.* 145, 3236-3251, doi:10.1002/qj.3616, 2019.
 - Rayner, D., Hirschi, J. J.-M., Kanzow, T., Johns, W. E., Wright, P. G., Frajka-Williams, E., Bryden, H. L., Meinen, C. S., Baringer, M. O., Marotzke, J., Beal, L. M., and Cunningham, S. A.: Monitoring the Atlantic meridional overturning circulation, *Deep Sea Res. Part II: Topical Studies in Oceanography*, 58, 1744–1753, doi:10.1016/j.dsr2.2010.10.056, 2011.
 - Reid, J. L.: On the total geostrophic circulation of the South Atlantic Ocean: Flowpatterns, tracers, and transports, *Prog. Oceanogr.*, 23, 149–244, doi:10.1016/0079-6611(89)90001-3, 1989.
 - Renault, L., McWilliams, J. C., and Masson, S.: Satellite Observations of Imprint of Oceanic Current on Wind Stress by Air-Sea Coupling, *Sci. Rep.*, 7, 17747, doi:10.1038/s41598-017-17939-1; 2017.
 - Rhein, M., Stramma, L., and Send, U.: The Atlantic Deep Western Boundary Current: Water masses and transports near the equator, *J. Geophys. Res.*, 100, 2441–2457, doi:10.1029/94JC02355, 1995.
 - Rhein, M., Stramma, L., and Krahnemann, G.: The spreading of Antarctic bottom water in the tropical Atlantic, *Deep Sea Res. Part I Oceanogr. Res. Pap.*, 45, 507–527 doi:10.1016/S0967-0637(97)00030-7, 1998.
 - Rhein, M., Walter, M., Mertens, C., Steinfeldt, R., and Kieke, D.: The circulation of North Atlantic Deep Water at 16°N, 2000-2003, *Geophys. Res. Lett.*, 31, doi:10.1029/2004GL019993, 2004.
 - Rhein, M., and Stramma, L.: Seasonal variability in the Deep Western Boundary Current around the eastern tip of Brazil, *Deep Sea Res.*, 52, 1414–1428, doi:10.1016/j.dsr.2005.03.004, 2005.
 - Rhein, M., Kieke, D., and Steinfeldt, R.: Advection of North Atlantic Deep Water from the Labrador Sea to the southern hemisphere, *J. Geophys. Res. Oceans.*, 120, 2471–2487, doi:10.1002/2014JC010605, 2015.
 - Ricciardulli, L., and Wentz, F. J.: A scatterometer geophysical model function for climate-quality winds: QuikSCAT Ku-2011, *J. Atmos. Ocean. Technol.*, 32, 1829–1846, doi:10.1175/JTECH-D-15-0008.1, 2015.
 - Richardson, P. L., and Fratantoni, D. M.: Float trajectories in the deep western boundary current and deep equatorial jets of the tropical Atlantic, *Deep Sea Res. Part II Top Stud. Oceanogr.*, 46, 305–333, doi:10.1016/S0967-0645(98)00100-3, 1999.
 - Richardson, P. L.: On the history of meridional overturning circulation schematic diagrams, *Prog. Oceanogr.*, 76, 466–486. doi:10.1016/j.pocean.2008.01.005, 2008.
 - Richter, I.: Climate model biases in the eastern tropical oceans: causes, impacts ways forward, *Wiley Interdiscip. Rev. Clim. Change*, 6, 345-358, doi:10.1002/wcc.338, 2015.
 - Risien, C. M., and Chelton, D. B.: A Global Climatology of Surface Wind and Wind Stress Fields from Eight Years of QuikSCAT Scatterometer Data, *J. Phys. Oceanogr.*, 38, 2379-2413, doi:10.1175/2008jpo3881.1, 2008.
 - Rodrigues, R. R., Rothstein, L. M., and Wimbush, M.: Seasonal Variability of the South Equatorial Current Bifurcation in the Atlantic Ocean: A Numerical Study, *J. Phys. Oceanogr.*, 37, 16-30, doi: 10.1175/JPO2983.1, 2007.

- Roessler, A., Rhein, M., Kieke, D., and Mertens, C.: Long-term observations of North Atlantic Current transport at the gateway between western and eastern Atlantic, *J. Geophys. Res.-Oceans*, 120, 4003–4027, doi:10.1002/2014JC010662, 2015.
- Rühls, S., Getzlaff, K., Durgadoo, J. V., Biastoch, A., and Böning, C. W.: On the suitability of North Brazil current transport estimates for monitoring basin-scale AMOC changes, *Geophys. Res. Lett.*, 42, 8072–8080, doi:10.1002/2015GL065695, 2015.
- Rusciano, E., Speich, S., and Ollitrault, M.: Inter-ocean exchanges and the spreading of Antarctic Intermediate Water south of Africa, *J. Geophys. Res.*, 117, C10010, doi:10.1029/2012JC008266, 2012.
- Saha, S., Moorthi, S., Pan, H.-L., Wu, X., Wang, J., Nadiga, S., Tripp, P., Kistler, R., Woollen, J., Behringer, D., Liu, H., Stokes, D., Grumbine, R., Gayno, G., Wang, J., Hou, Y.-T., Chuang, H., Juang, H.-M. H., Sela, J., Iredell, M., Treadon, R., Kleist, D., Van Delst, P., Keyser, D., Derber, J., Ek, M., Meng, J., Wei, H., Yang, R., Lord, S., van den Dool, H., Kumar, A., Wang, W., Long, C., Chelliah, M., Xue, Y., Huang, B., Schemm, J.-K., Ebisuzaki, W., Lin, R., Xie, P., Chen, M., Zhou, S., Higgins, W., Zou, C.-Z., Liu, Q., Chen, Y., Han, Y., Cucurull, L., Reynolds, R. W., Rutledge, G., and Goldberg, M.: The NCEP Climate Forecast System Reanalysis, *Bull. Am. Meteorol. Soc.*, 91, 1015-1058. doi:10.1175/2010BAMS3001.1, 2010.
- Sandoval, F. J., and Weatherly, G. L.: Evolution of the deep Western Boundary Current of Antarctic Bottom Water in the Brazil Basin, *J. Phys. Oceanogr.*, 31, 1440–1460, doi:10.1175/1520-0485(2001)031%3C1440:EOTDWB%3E2.0.CO;2, 2001.
- Santoso, A., England, M. H., and Hirst, A. C.: Circumpolar Deep Water Circulation and Variability in a Coupled Climate Model, *J. Phys. Oceanogr.*, 36, 1523-1552, doi: 10.1175/JPO2930.1, 2006.
- Schlundt, M., Farrar, J. T., Bigorre, S. P., Plueddemann, A. J., and Weller, R. A.: Accuracy of Wind Observations from Open-Ocean Buoys: Correction for Flow Distortion, *J. Atmos. Ocean. Technol.*, 37, 687–703, doi:10.1175/JTECH-D-19-0132.1, 2020.
- Schmid, C.: Mean vertical and horizontal structure of the subtropical circulation in the South Atlantic from three-dimensional observed velocity fields, *Deep Sea Res. Part I*, 91, 50-71, doi: 10.1016/j.dsr.2014.04.015, 2014.
- Schmidtko, S., and Johnson G. C.: Multidecadal warming and shoaling of Antarctic Intermediate Water, *J. Clim.*, 25, 207–221, doi:10.1175/JCLI-D-11-00021.1, 2012.
- Schott, F. A., Stramma, L., and Fischer, J.: The warm water inflow into the westerntropical Atlantic boundary regime, spring 1994, *J. Geophys. Res. Oceans*, 100, 24745–24760, doi:10.1029/95JC02803, 1995.
- Schott, F., Stramma, L., and Fischer, J.: Interaction of the North Atlantic Current with the deep Charlie Gibbs Fracture Zone through flow, *Geophys. Res. Lett.*, 26, 369-372, doi:10.1029/1998GL900223, 1999.
- Schott, F. A., Brandt, P., Hamann, M., Fischer, J., and Stramma, L.: On the boundary flow off Brazil at 5-10°S and its connection to the interior tropical Atlantic, *Geophys. Res. Lett.*, 29, 1840, doi:10.1029/2002GL014786, 2002.
- Schott, F.A., Dengler, M., Brandt, P., Affler, K., Fischer, J., Bourlès, B., Gouriou, Y., Molinari, R. L., and Rhein, M.: The zonal currents and transports at 35°W in the tropical Atlantic, *Geophys. Res. Lett.*, 30, 1349-1352, doi: 10.1029/2002GL016849, 2003.
- Schott, F. A., McCreary, J. P., and Johnson, G. C.: Shallow Overturning Circulations of the Tropical-Subtropical Oceans, *Earth's Clim.*, 147, 261–304, doi:10.1029/147GM15, 2004.

- Schott, F. A., Dengler, M., Zantopp, R. J., Stramma, L., Fischer, J., and Brandt, P.: The shallow and deep western boundary circulation of the South Atlantic at 5°– 11°S, *J. Phys. Oceanogr.*, 35, 2031–2053, doi:10.1175/JPO2813.1, 2005.
- Schwarzkopf, F. U., Biastoch, A., Böning, C. W., Chanut, J., Durgadoo, J. V., Getzlaff, K., Harlaß, J., Rieck, J. K., Roth, C., Scheinert, M. M., and Schubert, R.: The INALT family – a set of high-resolution nests for the Agulhas Current system within global NEMO ocean/sea-ice configurations, *Geosci. Model Dev.*, 12, 3329–3355, doi:10.5194/gmd-12-3329-2019, 2019.
- Send, U., Lankhorst, M., and Kanzow, T.: Observation of decadal change in the Atlantic meridional overturning circulation using 10 years of continuous transport data, *Geophys. Res. Lett.*, 38, L24606, doi:10.1029/2011GL049801, 2011.
- Silva, M., Araujo, M., Servain, J., Penven, P., and Lentini, C. A. D.: High-resolution regional ocean dynamics simulation in the southwestern tropical Atlantic, *Ocean Model.*, 30, 256–269, doi:10.1016/j.ocemod.2009.07.002, 2009.
- Simmons, A.J., Poli, P., Dee, D.P., Berrisford, P., Hersbach, H., Kobayashi, S., and Peubey, C.: Estimating low-frequency variability and trends in atmospheric temperature using ERA-Interim, *Q.J.R. Meteorol. Soc.*, 140, 329–353, doi:10.1002/qj.2317, 2014.
- Sinha, B., Smeed, D. A., McCarthy, G., Moat, B. I., Josey, S. A., Hirschi, J. J.-M., Frajka-Williams, E., Blaker, A. T., Rayner, D., and Madec, G.: The accuracy of estimates of the overturning circulation from basin-wide mooring arrays, *Prog. Oceanogr.*, 160, 101–123, doi:10.1016/j.pocean.2017.12.001, 2018.
- Smith, S. D.: Coefficients for sea surface wind stress, heat flux, and wind profiles as a function of wind speed and temperature, *J. Geophys. Res.*, 93, 15467–15472, doi:10.1029/JC093iC12p15467, 1988.
- Smith, S. R., Legler, D. M., and Verzone, K. V.: Quantifying uncertainties in NCEP reanalyses using high quality research vessel observations, *J. Clim.*, 14, 4062–2072, doi:10.1175/1520-0442(2001)014<4062:QUINRU>2.0.CO;2, 2001.
- Speer, K. G., and Zenk, W.: The flow of Antarctic Bottom Water into the Brazil Basin, *J. Phys. Oceanogr.*, 23, 2667–2682, doi:10.1175/1520-0485(1993)023%3C2667:TFOABW%3E2.0.CO;2, 1993.
- Srokosz, M., Baringer, M., Bryden, H., Cunningham, S., Delworth, T., Lozier, S., Marotzke, J., and Sutton, R.: Past, Present, and Future Changes in the Atlantic Meridional Overturning Circulation, *Bull. Am. Meteorol. Soc.*, 93, 1663–1676, doi:10.1175/BAMS-D-11-00151.1, 2012.
- Srokosz, M. A., and Bryden, H. L.: Observing the Atlantic meridional overturning circulation yields a decade of inevitable surprises, *Science*, 348, 1255575, doi:10.1126/science.1255575, 2015.
- Steinfeldt, R., and Rhein, M.: Spreading velocities and dilution of North Atlantic Deep water in the tropical Atlantic based on CFC time series, *J. Geophys. Res. Oceans*, 109, C03046, doi:10.1029/2003JC002050, 2004.
- Steinfeldt, R., Rhein, M., Bullister, J. L., and Tanhua, T.: Inventory changes in anthropogenic carbon from 1997–2003 in the Atlantic Ocean between 20°S and 65°N, *Global Biogeochem. Cycles*, 23, GB3010, doi:10.1029/2008GB003311, 2009.
- Stepanov, V. N., Iovino, D., Masina, S., Storto, A., and Cipollone, A.: Methods of calculation of the Atlantic meridional heat and volume transports from ocean models at 26.5°N, *J. Geophys. Res. Oceans*, 121, 1459– 1475, doi:10.1002/2015JC011007, 2016.
- Stocker, T. F.; Qin, D.; Plattner, G.-K.; Tignor, M. M. B.; Allen, S. K.; Boschung, J.; Nauels, A.; Xia, Y.; Bex, V.; Midgley, P. M.: *Climate Change 2013: The Physical Science Basis. Contribution of Working*

-
- Group I to the Fifth Assessment Report of IPCC the Intergovernmental Panel on Climate Change. Cambridge University Press, doi:10.1017/CBO9781107415324, 2014.
- Stouffer, R. J., Yin, J., Gregory, J. M., Dixon, K. W., Spelman, M. J., Hurlin, W., Weaver, A. J., Eby, M., Flato, G. M., Hasumi, H., Hu, A., Jungclaus, J. H., Kamenkovich, I. V., Leverman, A., Montoya, M., Murakami, S., Nawrath, S., Oka, A., Peltier, W. R., Robitaille, D. Y., Sokolov, A., Vettoretti, G., and Weber, S. L.: Investigating the causes of the response of the thermohaline circulation to past and future climate changes, *J. Clim.*, 19, 1365–1387, doi:10.1175/JCLI3689.1, 2006.
 - Stramma, L., Fischer, J., and Reppin, J.: The North Brazil Undercurrent Deep Sea Research Part I, *Oceanogr. Res. Pap.*, 42, 773–795, doi: 10.1016/0967-0637(95)00014-W, 1995.
 - Stramma, L., and Schott, F. A.: The mean flow field of the tropical Atlantic Ocean, *Deep Sea Res. Part II Top. Stud. Oceanogr.*, 46, 279–303, doi:10.1016/S0967-0645(98)00109-X, 1999.
 - Stramma, L., Rhein, M., Brandt, P., Dengler, M., Böning, C., and Walter, M.: Upper ocean circulation in the western tropical Atlantic in boreal fall 2000, *Deep Sea Res. Part I Oceanogr. Res. Pap.*, 52, 221–240, doi:10.1016/j.dsr.2004.07.021, 2005.
 - Stramma, L., Johnson, G. C., Sprintall, J., and Mohrholz, V.: Expanding oxygen-minimum zones in the tropical oceans, *Science*, 320, 655–658, doi: 10.1126/science.1153847, 2008.
 - Svendsen, L., Kvamstø, N. G., and Keenlyside, N.: Weakening AMOC connects Equatorial Atlantic and Pacific interannual variability, *Clim. Dyn.*, 43, 2931–2941, doi:10.1007/s00382-013-1904-8, 2014.
 - Swingedouw, D., Fichfet, T., Goosse, H., and Fourte, M. F.: Impact of transient freshwater releases in the Southern Ocean on the AMOC and climate, *Clim. Dyn.*, 33, 365–381, doi:10.1007/s00382-008-0496-1, 2009.
 - Taboada, F. G., Stock, C. A., Griffies, S. M., Dunne, J., John, J. G., Small, R. J., and Tsujino, H.: Surface winds from atmospheric reanalysis lead to contrasting oceanic forcing and coastal upwelling patterns, *Ocean Model.*, 133, 79–111, doi:10.1016/j.ocemod.2018.11.003, 2019.
 - Talley, L. D., and McCartney, M. S.: Distribution and circulation of Labrador Seawater, *J. Phys. Oceanogr.*, 12, 1189–1205, doi:10.1175/1520-0485(1982)012%3C1189:DACOLS%3E2.0.CO;2, 1982.
 - Talley, L. D.: Shallow, intermediate and deep overturning components of the global heat budget, *J. Phys. Oceanogr.*, 33, 530–560, doi:10.1175/1520-0485(2003)033<0530:SIADOC>2.0.CO;2, 2003.
 - Talley, L. D., Pickard, G. L., Emery, W. J., and Swift, J. H.: *Descriptive Physical Oceanography: An Introduction*, 6th ed., Elsevier, Boston, 2011.
 - Tchupalanga, P., Dengler, M., Brandt, P., Kopte, R., Macuéria, M., Coelho, P., Ostrowski, M., and Keenlyside, N. S.: Eastern Boundary Circulation and Hydrography Off Angola: Building Angolan Oceanographic Capacities, *Bull. Amer. Meteor. Soc.*, 99, 1589–1605, doi: 10.1175/BAMS-D-17-0197.1, 2018.
 - The DRAKKAR Group, DRAKKAR: Developing high resolution ocean components for European Earth system models, *CLIVAR Exch.*, 65, 18–21, 2014.
 - Timmermann, A., An, S.-I., Krebs, U., and Goosse, H.: ENSO Suppression due to Weakening of the North Atlantic Thermohaline Circulation, *J. Clim.*, 18, 3122–3139, doi:10.1175/JCLI3495.1, 2005.
 - Tomczak, M., and Godfrey, J. S.: *Regional Oceanography: An Introduction*, Pergamon Press, Oxford, doi: 10.1002/joc.3370150511, 1994.
 - Toole, J. M., Andres, M., Le Bras, I. A., Joyce, T. M., and McCartney, M. S.: Moored observations of the deep western boundary current in the NW Atlantic: 2004–2014, *J. Geophys. Res.-Oceans*, 122, 7488–7505. doi:10.1002/2017JC012984, 2017.

-
- Torralba, V., Doblas-Reyes, F. J., and Gonzalez-Reviriego, N.: Uncertainty in recent near-surface wind speed trends: a global reanalysis intercomparison, *Environ. Res. Lett.*, 12, 114019, doi:10.1088/1748-9326/aa8a58, 2017.
 - Trenberth, K. E., Large, W. G., and Olson, J. G.: The mean annual cycle in global ocean wind stress, *J. Phys. Oceanogr.*, 20, 1742–1760, doi:10.1175/1520-0485(1990)020<1742:TMACIG>2.0.CO;2, 1990.
 - Trenberth, K. E., and Caron, J. M.: Estimates of meridional atmosphere and ocean heat transports, *J. Clim.*, 14, 3433–3443, doi:10.1175/1520-0442(2001)014<3433:EOMAAO>2.0.CO;2, 2001.
 - Tsujino, H., Urakawa, S., Nakano, H., Small, R. J., Kim, W. M., Yeager, S. G., Danabasoglu, G., Suzuki, T., Bamber, J. L., Bentsen, M., Böning, C. W., Bozec, A., Chassignet, E. P., Curchitser, E., Dias, F. B., Durack, P. J., Griffies, S. M., Harada, Y., Ilicak, M., Josey, S. A., Kobayashi, C., Kobayashi, S., Komuro, Y., Large, W. G., Le Sommer, J., Marsland, S. J., Masina, S., Scheinert, M., Tomita, H., Valdivieso, M., and Yamazaki, D.: JRA-55 based surface dataset for driving ocean - sea-ice models (JRA55-do), *Ocean Model.*, 130, 79-139, doi:10.1016/j.ocemod.2018.07.002, 2018.
 - Tuchen, F. P., Lübbecke, J. F., Schmidtko, S., Hummels, R., and Böning, C. W.: The Atlantic Subtropical Cells Inferred from Observations, *J. Geophys. Res. Oceans*, 124, 7591-7605, doi:10.1029/2019jc015396, 2019.
 - Tuchen, F. P., Lübbecke, J. F., Brandt, P., and Fu, Y.: Observed transport variability of the Atlantic Subtropical Cells and their connection to tropical sea surface temperature variability, *J. Geophys. Res. Oceans*, 125, e2020JC016592, doi:10.1029/2020JC016592, 2020.
 - Uppala, S. M., Kållberg, P. W., Simmons, A. J., Andrea, U., Da Costa Bechtold, V., Fiorino, M., Gibson, J. K., Haseler, J., Hernandez, A., Kelly, G. A., Li, X., Onogi, K., Saarinen, S., Sokka, N., Allan, R. P., Andersson, E., Arpe, K., Balmaseda, M. A., Beljaars, A. C. M., Van De Berg, L., Bidlot, J., Bormann, N., Caires, S., Chevallier, F., Dethof, A., Dragosavac, M., Fisher, M., Fuentes, M., Hagemann, S., Hólm, E., Hoskins, B. J., Isaksen, L., Jansse, P. A. E. M., Jenne, R., McNally, A. P., Mahfouf, J.-F., Morcrette, J.-J., Rayner, N. A., Saunders, R. W., Simon, P., Sterl, A., Trenberth, K. E., Untch, A., Vasiljevic, D., Viterbo, P., and Wollen, J.: The ERA-40 Re-Analysis, *Q. J. R. Meteorol. Soc.*, 131, 2961–3012, doi:10.1256/qj.04.176, 2005b.
 - van Aken, H. M., and de Boer, C. J.: On a synoptic hydrography of intermediate and deepwaters masses in the Iceland basin, *Deep Sea Res. Part I Oceanogr. Res. Pap.*, 42, 165–189, doi: 10.1016/0967-0637(94)00042-Q, 1995.
 - van Bennekom, A. J., and Berger, G. W.: Hydrography and silica budget of the Angola Basin, *Neth. J. Sea Res*, 17, 149–200, doi: 10.1016/0077-7579(84)90047-4, 1984.
 - van Wijk, E. M., and Rintoul, S. R.: Freshening drives contraction of Antarctic Bottom Water in the Australian Antarctic Basin, *Geophys. Res. Lett.*, 41, 1657–1664. doi: 10.1002/2013GL058921, 2014.
 - Veleda, D .R. A., Araújo, M., Silva, M., Montagne, R., and Araújo, R.: Seasonal and interannual variability of the southern south equatorial bifurcation and meridional transport along the eastern Brazilian edge, *Tropical Oceanogr.*, 39, 27-59, doi: 10.5914/tropocean.v39i1.5176, 2011.
 - Veleda, D .R. A., Araújo, M., Zantopp, R., and Montagne, R.: Intraseasonal variability of the North Brazil Undercurrent forced by remote winds, *J. Geophys. Res.*, 117, C11024, doi:10.1029/2012JC008392, 2012.
 - Vignudelli, S., Kostianoy, A. G., Cipollini, P., and Benveniste, J.: *Coastal Altimetry*, Springer-Verlag, 2011.
 - Voldoire, A., Exarchou, E., Sanchez-Gomez, E., Demissie, T., Deppenheimer, A.-L., Frauen, C., Goubanova, K., Hazeleger, Q., Keenlyside, N., Koseki, S., Prodhomme, C., Shonk, J., Toniazzo, T., and

- Traoré, A.-K.: Role of wind stress in driving SST biases in the Tropical Atlantic, *Clim. Dyn.*, 53, 3481–3504, doi: 10.1007/s00382-019-04717-0, 2019.
- Warren, B. A., and Speer, K. G.: Deep circulation in the eastern South Atlantic Ocean, *Deep-Sea Res.*, 38, 281-322, doi: 10.1016/S0198-0149(12)80014-8, 1991.
 - Watts, D. R., and Kontoyiannis, H.: Deep-ocean bottom pressure measurement—Drift removal and performance, *J. Atmos. Ocean. Tech.*, 7, 296–306, doi: 10.1175/1520-0426(1990)007<0296:DOBPM>2.0.CO;2; 1990.
 - Wentz, F. J., Scott, J., Hoffman, R., Leidner, M., Atlas, R., and Ardizzone, J.: Remote Sensing Systems Cross-Calibrated Multi-Platform (CCMP) 6-Hourly Ocean Vector Wind Analysis Product on 0.25 Deg Grid, Version 2.0, Remote Sens. Syst., Santa Rosa, USA, 2015.
 - Wilkinson, M., Dumontier, M., Aalbersberg, I. J., Appleton, G., Axton, M., Baak, A., Blomberg, N., Boiten, J.-W., da Silva Santos, L. B., Bourne, P. E., Bouwman, J., Brookes, A. J., Clark, T., Crosas, M., Dillo, I., Dumon, O., Edmunds, S., Evelo, C. T., Finkers, R., Gonzales-Beltran, A., Gray, A. J. G., Groth, P., Goble, C., Grethe, J. S., Heringa, J., 't Hoen, P. A. C., Hooft, R., Kuhn, T., Kok, R., Kok, J., Lusher, S. J., Martone, M. E., Mons, A., Packer, A. L., Persson, B., Rocca-Serra, P., Roos, M., van Schaik, R., Sansone, S.-A., Schultes, E., Sengstad, T., Slater, T., Strawn, G., Swertz, M. A., Thompson, M., van der Lei, J., van Mulligen, E., Velterop, J., Waagmeester, A., Wittenburg, P., Wolstencroft, K., Zhao, J., and Mons, B.: The FAIR Guiding Principles for scientific data management and stewardship, *Sci. Data*, 3, 160018, doi: 10.1038/sdata.2016.18, 2016.
 - Willis, J. K.: Can in situ floats and satellite altimeters detect long-term changes in Atlantic Ocean overturning?, *Geophys. Res. Lett.*, 37, L06602, doi:10.1029/2010GL042372, 2010.
 - Worthington, E. L., Frajka-Williams, E., and McCarthy, G. D.: Estimating the deep overturning transport variability at 26°N using bottom pressure recorders, *J. Geophys. Res. Oceans*, 124, 335–348. doi:10.1029/2018JC014221, 2019.
 - Wüst, G.: Schichtung und Zirkulation des Atlantischen Ozeans, *Die Stratosphäre*. ed.: Emery, W. J. in: *Wissenschaftliche Ergebnisse der Deutschen Atlantischen Expedition auf dem Forschungs- und Vermessungsschiff 'Meteor' 1925-1927*, 6(1), E. Translation. Amerind Publishing Co. (1978), 1935.
 - Xu, X., Chassignet, E. P., Johns, W. E., Schmitz Jr., W. J., and Metzger, E. J.: Intraseasonal to interannual variability of the Atlantic meridional overturning circulation from eddy-resolving simulations and observations, *J. Geophys. Res. Oceans*, 119, 5140–5159, doi:10.1002/2014JC009994, 2014.
 - Yang, J.: Local and remote wind stress forcing of the seasonal variability of the Atlantic Meridional Overturning Circulation (AMOC) transport at 26.5°N, *J. Geophys. Res. Oceans*, 120, 2488–2503, doi:10.1002/2014JC010317, 2015.
 - Yashayaev, I., Lazier, J. R. N., and Clarke, R. A.: Temperature and salinity in the central Labrador Sea, *ICES Mar. Sci. Symp.*, 219, 32– 39, 2003.
 - Yelland, M., and Taylor, P. K.: Wind Stress Measurements from the Open Ocean, *J. Phys. Oceanogr.*, 26, 541-558, doi:10.1175/1520-0485(1996)026<0541:WSMFTO>2.0.CO;2, 1996.
 - Zantopp, R., Fischer, J., Visbeck, M., and Karstensen, J.: From interannual to decadal: 17 years of boundary current transports at the exit of the Labrador Sea, *J. Geophys. Res. Oceans*, 122, 1724–1748. doi:10.1002/2016JC012271, 2017.
 - Zenk, W., and Müller, T. J.: WOCE studies in the South Atlantic: Cruise No. 28, 29 March- 14 June 1994, *METEOR-Berichte*, University Hamburg, 95, 193 pp., 1995.

-
- Zenk, W., Siedler, G., Lenz, B., and Hogg, N. G.: Antarctic Bottom Water flow through the Hunter Channel, *J. Phys. Oceanogr.*, 29, 2785–2801, doi: 10.1175/1520-0485(1999)029%3C2785:ABWFTT%3E2.0.CO;2, 1999.
 - Zenk, W., and Visbeck, M.: Structure and evolution of the abyssal jet in the Vema Channel of the South Atlantic, *Deep Sea Res. Part II*, 85, 244–260, doi: 10.1016/j.dsr2.2012.07.033, 2013.
 - Zenk, W.: Abyssal currents, ed.: Cochran, J. K., Bokuniewicz, H. J., Yager, P. L., *Encyclopedia of Ocean Sciences (Third Edition)*, Elsevier Inc., 3, 189–203, doi: 10.1016/B978-0-12-409548-9.11343-0, 2019.
 - Zhang, R., and Delworth, T. L.: Simulated Tropical Response to a Substantial Weakening of the Atlantic Thermohaline Circulation, *J. Clim.*, 18, 1853–1860, doi:10.1175/JCLI3460.1, 2005.
 - Zhang, R., and Delworth, T. L.: Impact of Atlantic multidecadal oscillations on India/Sahel rainfall and Atlantic hurricanes, *Geophys. Res. Lett.*, 33, L17712, doi:10.1029/2006GL026267, 2006.
 - Zhang, D., Msadek, R., McPhaden, M. J., and Delworth, T.: Multidecadal variability of the North Brazil Current and its connection to the Atlantic meridional overturning circulation, *J. Geophys. Res.*, 116, C04012, doi:10.1029/2010JC006812, 2011.
 - Zhang, R., Sutton, R., Danabasoglu, G., Kwon, Y.-O., Marsh, R., Yeager, S. G., Amrhein, D. E., and Little, C. M.: A review of the role of the Atlantic meridional overturning circulation in Atlantic Multidecadal Variability and associated climate impacts, *Rev. Geophys.*, 57, 316–375, doi:10.1029/2019RG000644, 2019.
 - Zhao, J., and Johns, W. E.: Wind-Driven Seasonal Cycle of the Atlantic Meridional Overturning Circulation, *J. Phys. Oceanogr.*, 44, 1541–1562, doi:10.1175/JPO-D-13-0144.1, 2014a.
 - Zhao, J., and Johns, W. E.: Wind-forced interannual variability of the Atlantic Meridional Overturning Circulation at 26.5°N, *J. Geophys. Res. Oceans*, 119, 2403–2419, doi:10.1002/2013JC009407, 2014b.
 - Zhao, J., Bower, A., Yang, J., Lin, X., and Holliday, N. P.: Meridional heat transport variability induced by mesoscale processes in the subpolar North Atlantic, *Nat. Commun.*, 9, 1124, doi:10.1038/s41467-018-03134-x, 2018.

Acknowledgements

Zuallererst möchte ich mich bei Peter Brandt für diese Möglichkeit bedanken – das waren ein paar äußerst spannende Jahre. Ich bin ihm sehr dankbar für sein Vertrauen und die viele Freiheit bei der Umsetzung und Durchführung meines Projektes, sowie seinen konstanten wissenschaftlichen Rat in vielen hilfreichen Diskussionen.

Vielen Dank auch an Torsten Kanzow und Arne Biastoch, die mir vor allem im Rahmen meiner ISOS-Komitee-Treffen, aber auch darüber hinaus, mit ihrem Rat zur Seite standen.

Ganz besonders bedanken möchte ich mich bei Kerstin Jochumsen, Walter Zenk und Willi Rath - für ihre Unterstützung und den richtigen Input zur richtigen Zeit.

Vielen Dank auch an meine Kollegen in der PO - Kristin, Johannes H., Yao und Jan für nette Gespräche und Beratung zu diversen Themen, sowie Marcus Dengler, Rebecca Hummels and Gerd Krahnmann für spannende Diskussionen, viel Textarbeit und gute Ratschläge. Ich möchte mich außerdem bei den Technikern und der Assistenz der PO sowie den Kapitänen und Mannschaften auf den Forschungsschiffen bedanken, die unsere wissenschaftlichen Arbeit verziert mit ein wenig Abenteuer überhaupt erst möglich machen.

In meiner Zeit am GEOMAR habe ich ein paar sehr gute Freunde gewonnen, die für mich sowohl ein starkes Sicherheitsnetz als auch immer wieder eine außergewöhnlich gute Gesellschaft sind. Vielen Dank an Christina, Ezra, Thea, Meike, Annika, Swantje, Sabine, Katha und Siren. Ich bin gespannt zu sehen, wo es jeden von euch hin verschlägt und wer an welchem Rädchen drehen wird!

Ich möchte aus ganzem Herzen meiner Mama danken, die fast immer alles möglich macht. Neben vielem anderem, hat sie mir eine hohe akademische Ausbildung ohne jeglichen finanziellen oder anderweitigen gesellschaftlichen Druck ermöglicht. Gleichzeitig erinnert sie mich hartnäckig daran, dass es auch noch viele andere Dinge im Leben gibt, für die man Zeit haben oder für die man kämpfen sollte. Merci, Mommy!

Herzlichen Dank auch an den Rest meiner kleinen Familie - Oma, Opa, Papa, Thomas – für die Unterstützung entlang meines Weges, aber auch für die Hilfe beim „Füße auf dem Boden“ und „Öhrchen steif“ halten.

Zum Schluss möchte ich Philipp danken – dafür, dass er mir in den besonders stressigen Zeiten den Rücken frei und mich gesund gehalten hat, für seine Geduld und den Spaß, den wir zusammen haben. Ich freue mich auf all die Herausforderungen, die da noch kommen!

*“If you want to build a ship,
don’t drum up the men to gather wood, divide the work and give orders.
Instead, teach them to yearn for the vast and endless sea.”*

Antoine de Saint-Exupère

